What made the quasar blush?

Emission mechanisms in optically red quasars

Matthew Thomas Whiting

Submitted in total fulfilment of the requirements
of the degree of Doctor of Philosophy

School of Physics
University of Melbourne

December 2000

Abstract

Quasars selected at radio frequencies have been shown to exhibit a much broader range of optical colours than the canonical blue colours of optically-selected quasars. This thesis sets out to explain this observation by the presence of optical non-thermal synchrotron emission, connected with the relativistic jet that powers the radio emission in these quasars.

In the first part of this thesis, we investigate the properties of synchrotron emission. This is firstly done from the perspective of observed optical synchrotron jets. The measured spectral indices of these jets show good evidence that the synchrotron spectrum is turning over at optical frequencies, indicating that the energy distribution of the emitting particles has a cutoff at some maximum energy. Secondly, we investigate analytic solutions for synchrotron emission from both ordered and tangled magnetic fields, and find that the emitted flux in the ordered field case exhibits a strong dependence on the viewing angle. This is compared with the expected dependence due to Doppler boosting caused by some bulk flow that would occur in a relativistic jet, and the implications for real jets are discussed.

The second part of the thesis is concerned with flat-spectrum radio quasars taken from the Parkes Half-Jansky Flat-spectrum Sample. We present an extensive data-set of optical and near-infrared photometry for > 100 objects, and fit theoretical models to these observations. We find that $\sim 40\%$ of the sources have power-law SEDs, while a similar number show evidence for two primary components: a blue power law and optical synchrotron emission. The blue power law is similar to the dominant component observed in the spectra of optically-selected QSOs. There is strong evidence that the synchrotron component has a turnover in the rest frame UV-optical region of the spectrum. In the remaining sources it is likely that the synchrotron peaks at longer wavelengths, while peaks at shorter wavelengths appear to be ruled out. The relative strengths of these two components show variations of more than four orders of magnitude. The sources with power law SEDs show evidence for an excess number of red power law slopes compared to optically-selected quasars.

Analysis of polarisation data, both optical (from the literature) and near-infrared (new observations), supports the presence of an optically red, highly polarised component, which is consistent with the fitted synchrotron component.

The properties of the BL Lacertæ objects in the sample are examined. It is found that, aside from having much lower emission line equivalent widths (by definition), the BL Lacs are indistinguishable from the other synchrotron-dominated sources in the sample. This suggests that the BL Lac phenomenon is caused primarily by a relative lack of emission line gas, rather than an excessively boosted synchrotron component.

Finally, observations of variability on timescales of hours in a source with no optical synchrotron emission demonstrates that the blue power law emission can exhibit short-timescale variations, a property which is often ascribed to synchrotron emission. This indicates that both components are important for modelling the optical emission from flat-spectrum radio quasars.

Declaration

This is to certify that:

① This thesis entitled "What made the quasar blush? Emission mechanisms in optically red quasars" comprises only my original work, except where indicated in the preface.

② Due acknowledgement has been made in the text to all other material used.

③ The thesis is less than 100,000 words in length, exclusive of tables, maps, bibliographies and appendices.

. . . .

Matthew Thomas Whiting

Preface

While most of the work presented herein is my own, there is some that is the result of collaborative work, or the result of the work of others. Any data that is used is cited accordingly in the text, and other specific details are listed here:

- Chapter 1 and a large part of Chapter 2 are reviews of the literature. References are quoted in the text.
- The derivation of the tangled-field synchrotron emission in Chapter 3 is taken mostly from Longair (1994). The ordered-field derivation, however, is my own work.
- The data set described in Chapter 4 is taken from Francis, Whiting, and Webster (2000). Paul Francis performed the bulk of the observations (although I did assist for nearly half the nights) and all the reduction. The discussion of the new systematic errors, while not in Francis et al. (2000), is presented in Whiting et al. (2001).
- Most of the modelling presented in Chapter 5 is also presented in Whiting et al. (2001). All the modelling is my own work.
- The optical polarisation data used in Chapter 6 comes from the literature, primarily Wills et al. (1992), and is cited accordingly in the text. Some of the near-infrared polarimetry was originally presented in Masci (1997), while the rest represents my new work.
- The analysis and its interpretation in Chapter 7 is my own work. Data used is cited accordingly in the text.
- The work in Chapter 8 is original and entirely my work.

Additionally, this research has made use of the NASA/IPAC Extragalactic Database (NED)[1] (which is operated by the Jet Propulsion Laboratory, California Institute of Technology, under contract with the National Aeronautics and Space Administration), as well as NASA's Astrophysics Data System Abstract and Article Services[2]. Some routines from Numerical Recipes (Press et al. 1997) were used in the analysis of the modelling.

[1]http://nedwww.ipac.caltech.edu/
[2]http://adswww.harvard.edu/

Acknowledgements

No undertaking of the magnitude of a Ph.D. thesis can be accomplished without help from many sources, and I have benefited over the past four years from the help and efforts of many people.

The first to be thanked must be Rachel Webster. She has been of immense help throughout the course of my studies, both in giving me direction when I needed it, and in being able to ask the questions that made me think about the deeper issues. That, surely, is the role of any good supervisor, and Rachel has excelled in that role.

Paul Francis, as well, deserves much praise. The compilation of the data set detailed in Chapter 4 is largely thanks to his hard work, in doing most of the observing and nearly all the reduction (which, when you have of the order of 1000 images, is a considerable effort!). I also thank Paul for his counsel and help throughout the Ph.D., particularly for his many comments during the development and analysis of the modelling.

I am most grateful to the University of Melbourne, for awarding me the Grimwade Scholarship. This scholarship has provided me with assistance in travelling to conferences and the like, and so has been invaluable in helping the progress of my research. I am also grateful for the hospitality shown me by Sr. Deirdre Rofe and the community of St. Mary's College, in my three enjoyable years as residential tutor there.

I have benefited from discussions and interactions with many people over the past four years, that have helped me develop my knowledge on the field of quasars and AGN, including Stefan Wagner, Matthew Baring, Ian McHardy, Dick Hunstead, and Patrick Leahy. Locally, Alicia Oshlack (my fellow Parkes partner-in-crime!), Matt O'Dowd and Frank Masci have all been invaluable. I also thank those who have helped with the observing that has formed part of this thesis, namely Paul Francis, Frank Masci, Michael

Drinkwater, Tori Ibbetson and Alicia Oshlack. The groovy title for this thesis is courtesy of Matt Tilling.

More generally, I thank all the members of the Melbourne Uni Astro group from the past four years, for their friendship, support and the many and assorted forms of cricket! This sentiment extends to my non-astro friends – I thank them all for their love, support, and their wonderful abilities to provide distractions from work!

Lastly, in the place of honour, I wish to thank my beloved family. Their love and support has been wonderful, particularly in this last year when things have been so hectic.

This thesis is dedicated to the memory of my beloved grandmother,
Mavis Simpson,
a loving soul who so dearly wanted to see the final version.
I hope she is reading it even now and is well pleased.

Contents

List of Figures

List of Tables

Chapter 1

Quasars and Blazars

1.1 Quasars

This thesis is concerned with the optical emission properties of quasars. The advent of quasar research has been one of the most important advances in astronomy in the past half-century. These advances have helped to revolutionise the way we think of our universe, provided us with insights into many areas of exotic physics (from black holes to ultra-high energy gamma rays), and provided sources for every kind of astronomical detector. This chapter takes the form of a review of quasars and their (apparently) more extreme cousins the blazars. First, a note of clarification: the word "quasar" was traditionally used only for the radio-loud version, while radio-quiet quasars were known as QSOs (Quasi-Stellar Objects). It is becoming more common now to use quasar as a general term to refer to both types, and that practice is followed in this thesis.

1.1.1 The discovery of quasars

The discovery of quasars is an interesting tale in itself. The first radio surveys (such as the 3C or 3rd Cambridge survey) had poor angular resolution, so many sources were unable to be associated definitely with a particular optical source. In a classic piece of observational radio astronomy, a group of Australian astronomers (Hazard et al. 1963) used the lunar occultation of the radio source 3C 273[1] to pin down its location, by means of the diffraction pattern produced when the source disappeared behind the moon's limb.

[1] The 273rd object in the 3C or 3rd Cambridge catalogue of radio sources

The Caltech-based astronomer Maarten Schmidt was then able to locate the optical counterpart (using the 5m telescope at Mt. Palomar Observatory), and, in the position indicated by the radio observation, found two sources: a blue star and "a faint wisp, or jet" (Schmidt 1963).

This blue star, however, was obviously not an ordinary star. Its spectrum showed strong broad emission lines that Schmidt identified with the Hydrogen Balmer series, redshifted by $z = 0.16$. Schmidt concluded that this either made it a very compact star with a high gravitational redshift, or put it well outside the galaxy. This discovery prompted Greenstein and Matthews (1963) to look again at the spectrum of another radio source – 3C 48 – and they similarly found a redshift of $z = 0.3675$, based on lines of Mg II (until then only seen in UV spectra of the sun) and forbidden lines of Oxygen and Neon.

1.1.2 Quasars in the optical

After their detection at radio wavelengths, it was in the optical part of the spectrum that quasars were first recognised to be something peculiar. First of all, they had a very small size on the sky – the angular size of both 3C 273 and 3C 48 was $< 1''$. This similarity to the appearance of stars lead to the descriptive names of quasar (from quasi-stellar radio source) and QSO (quasi-stellar object). Besides this morphological description though, there were two other important observations.

Spectra

The first key feature that was noticed was the emission line spectrum that had initially so puzzled astronomers. The lines are very strong in emission (something not seen except in the hottest stars), featuring the elements of Hydrogen (the Balmer and Lyman series are prominent), Helium, Carbon and Magnesium, amongst others. The emission lines are also very broad. It was realised early on (Greenstein and Schmidt 1964) that this implied very large velocity widths for the line emitting gas – several thousand km s^{-1}. Together with the broad lines are narrow, forbidden lines (the strongest are [O III], [O II] and [N II]). These types of emission line features are seen also in the active nuclei of some local galaxies – the Seyfert galaxies. These are the low-luminosity analogues of quasars, where the host galaxy is visible. The different name comes from the different historical classification, although it is now widely accepted that type 1 Seyfert nuclei and quasars are the same type of object, in the sense that they are continually connected in luminosity. (The galaxies surrounding quasars are generally not seen due to their greater distance and the greater luminosity of the central object.)

The host galaxies of Seyferts are observed to be nearly always spirals, while quasars can occur in either spiral or elliptical galaxies. The exception are the radio-loud quasars and radio galaxies, which are predominantly in ellipticals. For example, approximately 89% of the low-redshift 3CR sources are in ellipticals (Martel et al. 1999).

The Seyfert galaxies come in two forms: type 1 and type 2 (also known as Sy1s and Sy2s). In both cases the galaxy has a bright, dominant nucleus. It is the optical spectrum of this nucleus that determines the difference between the two classes. The Sy1s show both broad and narrow emission lines, in a similar manner to quasars, while all the emission lines in Sy2s are narrow. The explanation for this difference will be discussed in Section 1.3. Collectively, quasars and Seyferts (as well as radio galaxies and low-luminosity galaxy nuclei called LINERs[2]) are known as AGN, or Active Galactic Nuclei.

Colour

The second key observation regarding the optical emission from quasars was the very blue nature of it. The first quasar identified, 3C 273, was found (Oke 1963; Schmidt 1963) to have a very blue optical continuum ($f_\nu \propto \nu^{0.28}$). This was found to be a general property of quasars and AGN, which distinguished them from stars: the hottest main sequence stars have $U - B \simeq 0.4 - 0.5$ mag, while typical AGN have $U - B \simeq -1$ mag (Krolik 1999). This proved to be a relatively efficient way to search for quasars – the so-called "UVX", or UV-excess method. A major example of this type of survey is the Palomar-Green (PG) Catalog (Green et al. 1986), which was the source catalogue for the Palomar Bright Quasar Sample (BQS) (Schmidt and Green 1983).

Another prominent optically-selected catalogue of quasars is the Large Bright Quasar Survey (LBQS, Hewett et al. (1995) and references therein).

[2]LINER = Low Ionisation Nuclear Emission line Region (Heckman 1980)

This is a catalogue of 1055 quasars, selected on the basis of their non-starlike appearance on objective prism photographic plates. The quasars had either strong emission (or absorption) lines, blue colour, or strong continuum breaks (i.e. utilising the two main optical features of quasars discussed above). This survey is therefore sensitive to all types of quasars except red quasars with featureless optical spectra (such as red BL Lacs – see next section).

Additionally, there is a major quasar redshift survey currently underway at the Anglo-Australian Observatory – the 2dF Quasar Redshift Survey (2QZ). This survey uses the 2 Degree Field multi-fibre spectrograph that is capable of taking spectra of 400 objects simultaneously. It thus is able to observe many more sources than previous surveys. The input catalogue contains over 46,000 objects, selected according to their $U-B/B-R$ colours (from APM scans of UK Schmidt plates), and the survey is expected to find some 25,000 quasars. As the survey is on-going, there is no final published catalogue, but see Boyle et al. (2000) for descriptions of the survey, as well as the first results on the optical luminosity function.

An interesting result of these large optical quasar surveys was the finding that only about 10% of all quasars are "radio-loud". The first quasars that were discovered were very bright in the radio (since that was the region of the spectrum in which they were found), but the vast majority of quasars that are now known are in fact radio-quiet. These quasars have a ratio of radio to optical flux of $\nu f_{\nu_r}/\nu f_{\nu_o} \sim 10^{-6} - 10^{-5}$, (note that although they are radio-quiet, they are not radio-silent!) while the radio-loud quasars have radio fluxes three to four orders of magnitude greater (Sanders et al. 1989). However, note that even in the radio-loud quasars, the radio emission comprises only about 0.1% of the total luminosity emitted over the entire electro-magnetic spectrum (Krolik 1999).

1.2 Blazars

There is a subset of the radio-loud quasars that have apparently extreme properties that set them apart from the rest of the population. These properties include rapid variability (at all frequencies and on all timescales), high polarisation (at both optical and radio frequencies), and, in some objects, a lack of any strong optical emission lines. The collective name that is usually applied to these objects is "blazar".

The name blazar originated, of all places, in an after-dinner speech by Ed Spiegel, at the Pittsburgh Meeting on BL Lac objects. The name is a combination of quasar and BL Lac, and has connotations of the characteristic optical variability and flaring that is seen in these objects. The use of the name in the literature is most likely due to the review of optical polarisation in extragalactic objects by Angel and Stockman (1980). However, the use today is still somewhat non-standardised. It has become quite common to describe the class of such objects as blazars, while it is probably more accurate to use "blazar" to describe the nature of the activity (i.e. "Source X exhibits blazar properties").

1.2.1 BL Lacertæ objects

Possibly the most famous sub-class of the blazars are the BL Lacertæ objects, or BL Lacs. These are named after their progenitor BL Lacertæ, which was originally classified as a blue variable star, and found to be the optical counterpart to the radio source VRO 42.22.01 (Schmitt 1968). Their defining feature is the lack of strong emission lines in their optical spectra. The commonly used definition (Stocke et al. 1991) is that the equivalent width satisfies $W_\lambda < 5$ Å. Additionally, if the Ca II H&K break (also termed the "4000Å break") due to the host galaxy is present, then the contrast[3] must be $\leq 25\%$. Marchã et al. (1996) modified this definition slightly to include sources with contrasts of up to 40%, with a relaxed restriction on the equivalent widths.

The cause of the lack of emission lines in BL Lacs has been the subject of much debate for the past twenty to thirty years. The most commonly used explanation (Blandford and Rees 1978, surely the most cited conference proceedings paper ever!) is that BL Lacs are viewed close to the axis of a relativistic jet. The (synchrotron) emission from this jet is Doppler boosted, increasing its intensity so that it swamps the continuum and line emission that would otherwise be visible.

The question of how exactly to define a BL Lac was complicated somewhat by the discovery by Vermeulen et al. (1995) and Corbett et al. (1996) of a broad Hα line in the progenitor of the class, BL Lacertæ. This observation

[3] The relative depression blueward across the Ca II break, so that a normal elliptical galaxy has a contrast of 50%.

was made at a time when the overall flux of the object was at a relatively low level (Maesano et al. 1997). These observations raise the prospect of there being a Seyfert-like accretion disk in the centre of BL Lacertæ, although present data is not quite suitable for discrimination between an accretion disk model or photo-ionisation by the synchrotron jet (Corbett et al. 2000).

For many years, BL Lacs were divided into two categories: radio-selected (RBLs) and X-ray selected (XBLs). The two categories had very different broad-band spectral energy distributions (SEDs): the RBLs peaked[4] in the IR to optical part of the spectrum, and were generally brighter at radio frequencies than XBLs; while the XBLs peaked at higher energies – into the X-ray part of the spectrum. The division into two categories was supported by a bi-modal distribution of the ratio of radio to X-ray flux. However, recent deeper surveys (such as the RGB, or *ROSAT* – Green Bank survey (Laurent-Muehleisen et al. 1999)) have filled in the gap between the two parts of the distribution, and the RBL/XBL terminology has made way for one that is less governed by the manner of selection. Instead, BL Lacs are more commonly referred to as LBLs or HBLs (low- or high-peaking BL Lac objects respectively) – referring to the location of the peak of the broad-band SED. Generally speaking (although by no means exclusively), sources that were known as RBLs are LBLs, and similarly for XBLs and HBLs. This categorisation has been used as part of attempts at BL Lac unification schemes (Fossati et al. 1998; Ghisellini et al. 1998).

1.2.2 Other blazars

As well as BL Lacs, the blazar class contains those quasars variously described as OVVs (Optically Violent Variables), HPQs (High Polarisation Quasars) or FSRQs (Flat-Spectrum Radio Quasars). These are quasars that share many of the same properties of BL Lacs (such as high polarisation and rapid variability), but with quasar-like emission lines. The different names come from the different classification schemes used: either by optical variability, optical polarisation or radio spectral index.

The name FSRQ is quite common, as it derives from the important fact that nearly all blazar sources have compact radio structure (i.e. are core-dominated) and tend to have flat radio spectra. A flat spectrum is typically

[4]This is a peak in a plot of νF_ν against ν, which gives the energy flux per logarithmic bandwidth.

defined as satisfying $\alpha > -0.5$, with $F_\nu \propto \nu^\alpha$.

1.2.3 Optical emission in blazars

The optical emission in blazars tends to be highly polarised, with levels of at least a few percent, and often much higher. This gives the first important clue as to the nature of this optical emission. A form of radiation that is naturally quite highly polarised is synchrotron radiation. This is radiation that is emitted when relativistic particles (such as electrons) move through a magnetic field. The particles spiral around the field lines, and as they do so they emit photons. The spectrum of synchrotron radiation covers a very broad range of frequencies – it can extend from radio frequencies (where it is found most often) up to optical and even X-ray energies. In blazars, the synchrotron emission is most likely to come from a relativistic jet that extends out from the centre of the source (although this is not always where synchrotron emission comes from – supernova remnants emit most of their radio emission in the form of synchrotron). A more complete discussion of synchrotron emission can be found in Chapter 3.

From examining the multi-wavelength SEDs of blazars (for example, Impey and Neugebauer 1988), it is found that a continuous, perhaps slightly curved, spectrum connects the radio, IR, and optical data points (and in some cases, the X-ray points as well). This, and the observed polarisation of the IR and optical, has led to models that invoke a single synchrotron component to explain the emission over this entire wavelength range. A further argument for synchrotron emission at optical wavelengths is the featureless continuum seen in BL Lacs. A continuum with no emission lines is precisely what you would expect when the emission is dominated by synchrotron.

What other components are there in the optical emission of blazars? For many objects, the synchrotron emission accounts very well for the continuum emission. In some, however, there is good evidence for emission from an accretion disk, which, as we shall see, is the dominant emission component in "normal" quasars. One example is the study by Malkan and Moore (1986) on two HPQs: PKS 1510−089[5] and PKS 0736+017. In both these cases, emission that is likely to be from an accretion disk was found to make up a quarter to a half of the visual light. There is also the case of the broad Hα

[5]This source, 1510−089, is part of the sample of quasars studied in this thesis

line in the spectrum of BL Lacertæ, which possibly indicates the presence of an ionising continuum from a Seyfert-like accretion disk (Corbett et al. 2000).

This brings us to the topic of emission lines in blazars. BL Lacs, by definition, have little to no emission lines present in their spectra, while HPQs have emission lines of the same strength as "normal" (that is, low polarisation) quasars. Scarpa and Falomo (1997) found that BL Lacs and HPQs had similar distributions of emission line luminosities, and suggested that the difference between the two classes was that BL Lacs had a stronger continuum. However, it is possible instead that BL Lacs have systematically weaker emission lines, due to a relative dearth of emission line gas. A further alternative (which may be the case with BL Lacertæ) may be that the accretion disk (if it is present) is weak, and so the ionising continuum is not sufficient to produce emission lines that are observable over the non-thermal (synchrotron) continuum. In other words, the lines are there, but they are just very weak. This is similar to the beaming hypothesis, but without requiring the stronger continuum. These issues will be discussed further in Chapter 7.

Finally, a word or two about the higher energy emission from blazars. The Energetic Gamma Ray Experiment Telescope (*EGRET*), on board the Compton Gamma Ray Observatory, detected gamma rays (at energies of > 100 MeV) from at least 93 blazars (66 blazars were detected with high confidence, and the remaining 27 were low confidence detections) (Hartman et al. 1999). It was found that these "*EGRET* blazars" emitted more energy in the gamma ray region of their spectrum than any other. (See the figures in Appendix D for examples of these types of sources.) Also, a small number of blazars have been detected at even higher energies ($\gtrsim 1$ TeV), using Čerenkov detectors such as Whipple and HEGRA (see Petry (1999) for a review of the HEGRA detections).

The source of this gamma ray emission appears to be inverse Compton radiation, whereby highly relativistic particles interact with photons and "up-scatter" them, increasing the photon energy by a factor of $\sim \gamma^2$ (where γ is the Lorentz factor of the particle). If there is a significant amount of synchrotron emission, particularly at optical wavelengths, then the radiating particles are sufficiently relativistic to up-scatter any ambient photons to very high energies. The ambient photons can be the synchrotron photons emitted by the relativistic particles (in which case the up-scattered radiation is termed Synchrotron Self-Compton radiation, or SSC), or they can originate from some other source, such as the accretion disk, the broad line region, or even the cosmic microwave background (in which case it is termed External Compton radiation, or EC). This theory is able to explain quite well the broad-band spectra of blazars in terms of two broad peaks: the synchrotron peak, at low (i.e. IR to optical to soft X-ray) energies; and the Inverse Compton peak, at high (i.e. gamma ray) energies (see, for example, Fossati et al. (1998) or Ghisellini et al. (1998)).

1.3 The unified picture of quasars

From the observed properties of quasars and blazar AGN, we are able to construct a model for the structure of the central regions. Three key properties of quasars, that were recognised very early on (Greenstein and Schmidt 1964), give us a good insight into what is required to power quasars:

Luminosity: The large redshifts of quasars, if taken to be cosmological (a notion almost universally accepted now), imply very high luminosities. These luminosities can be as great as 10^4 times the total luminosity of a typical galaxy.

Size: Firstly, quasars are noted (indeed, often selected) to have a star-like appearance, i.e. unresolved to optical telescopes. This puts a limit of a few kpc to their size (depending on redshift and your choice of cosmology). However, the variability that is seen in many sources puts a far more stringent limit on the size. By converting the variability timescale into a physical size (from light travel time arguments), it is found that the emitting region (including the region from which the broad emission lines originate) must be ~ 1 parsec in size.

Emission lines: One of the defining features of quasars are the broad emission lines. These have velocity widths of thousands of km/s. As noted above, these emission lines originate within a few parsecs of the centre of the quasar.

The only model that has been successful at explaining how so much energy can be produced in such a small region has been accretion of matter onto a very compact, massive body – a black hole. The high velocities of the broad line region imply that they are orbiting a very massive object, and the only stable object so compact is a black hole.

The basic inferred structure of a quasar is then (starting at the centre and moving out):

① A massive black hole. The masses of these black holes range up to at least $10^9 M_\odot$. The massive elliptical galaxy M87 (not a quasar, but certainly the host of an AGN – see Chapter 2) has a black hole that has been measured at $(2.4 \pm 0.7) \times 10^9 M_\odot$ (Ford et al. 1994; Harms et al. 1994).

② An accretion disk. As matter falls in towards the black hole, it forms a disk which is heated by friction to quite high temperatures ($\gtrsim 10^5$K). This is believed to be the source of the strong continuum seen in (non-blazar) quasars.

An accretion disk is not the only method of creating the strong continuum. Barvainis (1993) proposed that free-free emission, from large numbers of small clouds of gas at high (10^5K–10^6K) temperatures. However, observations of broad Fe Kα emission lines in the X-ray from a few Seyferts (and possibly at least one quasar (Yaqoob and Serlemitsos 2000)) indicates that accretion disks may be necessary (the broadening fits that expected due to general relativistic effects originating in an accretion disk near a massive black hole).

③ Broad line region (BLR). A region extending from a few to hundreds of light days from the central black hole (known from reverberation mapping studies – see Netzer and Peterson (1997) for a review of the field). This is the location of the high-velocity gas ($\sim$ few thousand km/s) that is the source of the broad emission lines (Doppler broadened due to the high velocities) seen in the optical spectra.

④ Narrow line region (NLR). This region is much further out: $\sim$ 1kpc. This may be associated with the host galaxy, although it is illuminated by the central continuum source.

This basic structure is thought to be the same for Seyferts, although with an additional feature. The difference between Sy1s and Sy2s is explained very well by the presence of extra obscuration in Sy2s that blocks out the light from the BLR, leaving only narrow lines in the optical spectrum. This obscuration is thought to take the form of a "dusty torus" surrounding the BLR. Thus, Sy2s are viewed at an angle that intersects the torus, while Sy1s are viewed through the hole, enabling both the BLR and NLR to be seen. Whether such a torus exists for quasars is unclear. It has been postulated that a quasar analogue of Sy2s exists (the so-called type 2 quasar) (for instance, Halpern et al. 1999), and one or two may indeed have been detected by the X-ray telescopes *Chandra* (Fabian et al. 2000) and *BeppoSAX* (Franceschini et al. 2000).

Finally, the other key feature that is present, particularly in radio-loud objects (and, indeed, is very important for this thesis) is a jet. Radio galaxies (the other major extragalactic radio source aside from quasars) often show large radio lobes that extend up to megaparsecs away from the host galaxy. These lobes are connected to the host by a (usually thin) jet that, as seen in VLBI studies, reaches in to the innermost parsec of the galaxy. Such features are also seen in radio quasars, and are the source of the bulk of the radio emission. Also, some jets have been observed at higher frequencies, up to optical or even X-ray energies (see Chapter 2 for full details). The jets seem to emerge at right angles to the accretion disk, and thus impart a degree of axisymmetry to the structure of the nuclear region (a good example is the jet of the nearby AGN NGC 4258, which exhibits a sub-parsec radio jet elongated along the rotation axis of the disk (Herrnstein et al. 1997)).

This basic structure of a quasar (or, more generally, of an AGN) has formed the foundation for viewing angle unification schemes. The essence of these schemes is to explain the different observed properties of different types of AGN by the variation of the line-of-sight angle to the system (in other words, generalising the Sy1/Sy2 unification scheme).

This is particularly useful for radio-loud objects, due to the presence of the jet. The jet is relativistic[6], and so, if viewed close to its direction of

[6]This is known from observed superluminal motion seen with VLBI and *HST* in the inner parts of jets. Superluminal motion (i.e. motion at an apparent speed faster than c) requires reasonably relativistic speeds towards the observer at a small angle to the line of sight, and is a purely geometric effect caused by the features in the jet almost keeping up with the light that they emit.

propagation, the jet emission will be Doppler boosted (i.e. amplified) – this is known as Doppler beaming. Thus, the closer the observer is to the jet axis, the more dominant the jet emission will be relative to the emission from the accretion disk region. This is essentially the explanation for BL Lacs – that they are simply radio galaxies viewed close to the jet axis and the jet emission is far more dominant than the emission from the nucleus (which includes the emission lines).

This sort of unification scheme (Urry and Padovani 1995) unites BL Lacs with the low luminosity radio galaxies (Fanaroff-Riley type I, or FR I: Fanaroff and Riley (1974)), and FSRQs (or blazars with emission lines – generally more luminous than BL Lacs) with the more luminous FR IIs. These unification schemes are discussed further in Chapter 7.

1.4 This thesis

This thesis focuses on a sample of radio-loud quasars and AGN, with particular interest in their optical properties. The overall aim is to come up with consistent models that explain the optical/near-infrared emission, and examine the implications of these models for the study of radio-loud quasars in general.

Much of the modelling done is concerned with emission (more specifically, synchrotron emission) from the jet. Since we are looking at optical emission, Chapter 2 contains a review of those (few) sources that have observed optical jets (that is, optical counterparts to radio jets) and summarises the properties of those jets.

In Chapter 3, the theory behind synchrotron emission is examined, and is applied to a particular form of jet that may be expected to exist in the sources under consideration. The effects of relativistic boosting of the emission from the jet are also considered.

The remainder of the thesis contains the data and the results of the modelling. The sample of quasars used – the Parkes Half-Jansky Flat-spectrum Sample (Drinkwater et al. 1997) – is introduced, and the data (broad-band optical and near-infrared photometry) is presented for approximately one-third of the sample.

The models that are fitted to this data are presented in Chapter 5, as are the results of the model fitting. These results are then tested against the polarisation in Chapter 6 (since synchrotron emission is highly polarised, and many of the sources are HPQs). Chapter 7 contains an examination of the BL Lac objects in the sample, and how their properties are related to the rest of the sample's quasars. Chapter 8 contains an investigation of short-timescale variability of three objects from the sample at near-infrared wavelengths.

The key results of the thesis are summarised in Chapter 9, and the implications of the results in the context of other studies of radio-loud quasars and blazars are discussed.

Chapter 2

Optical jets and their properties

An important feature in the unified model of AGN, particularly radio-loud AGN, is the jet. This is a relativistic outflow from the central regions of the AGN, and is a major source of radio frequency emission (through the synchrotron process) in radio-loud objects. The other major sources are the large lobes often seen in radio galaxies, although these are stronger at low radio frequencies than high.

Since the work in this thesis is concerned primarily with the optical and near-infrared emission of radio-loud quasars, the amount of optical emission that comes from the jet is of considerable interest. This chapter contains a review of observations of optical counterparts to radio jets, and a summary of the relevant properties, particularly the spectral indices of the jet and the angle the jet makes with the line of sight.

2.1 Observed optical jets

Only a small number of optical counterparts to radio jets in active galaxies have been observed, despite the large number of radio jets that are known. The main reason for this is that, with a couple of notable exceptions, they are faint and small (in breadth, if not length). The rapid increase in the number of optical jets known in the past decade has been primarily due to the advent of the *Hubble Space Telescope (HST)*, with its unsurpassed resolution, although some have been discovered via ground based telescopes,

Name	Other names	Redshift of host	Host type
3C 15	PKS 0034−014	0.073	E1
3C 66B	0220+424	0.0215	E
3C 78	0305+039 NGC 1218	0.0289	S0/Sa
3C 120	PKS 0430+052 II Zw 14	0.033	S0
PKS 0521−365		0.055	E
3C 200	0824+294	0.458	?
3C 212	0855+143	1.049	?
3C 245	1040+123	1.029	?
3C 264	1142+198 NGC 3862	0.0216	E
3C 273	1226+023	0.16	E4
M87	1228+126 3C 274 Virgo A NGC 4486	0.004	E1
3C 346	1641+173	0.161	E
3C 371	1807+698	0.051	E
3C 380	1828+487	0.692	E
PKS 2201+044		0.028	E

Table 2.1: Sources that exhibit optical jets that are coincident with radio synchrotron jets. Other names lists common names by which the sources are known (positions are B1950). The redshift and morphological type (where known) of the host galaxy is also shown (generally taken from NED, the NASA/IPAC Extragalactic Database).

notably several using the *Nordic Optical Telescope (NOT)* on La Palma. Those sources with optical jets are listed in Table 2.1, and descriptions of the individual sources follow.

M87: The famous jet in M87 is the oldest known and most studied of all optical jets, primarily because of its high surface brightness and proximity to Earth. In 1918, the astronomer Heber Doust Curtis observed it during a study of M87, describing it as a "curious, straight ray" (Curtis 1918). M87 was later discovered to be a strong radio source (Virgo A), and the non-thermal nature of the jet was confirmed by Baade (1956), by detecting its strong optical polarisation. It was already known to have a blue featureless continuum and to be associated with radio emission – in the same manner as the Crab Nebula.

M87 itself is a giant elliptical (in fact, one of the most massive known – it has a mass of up to $\sim 10^{14}M_\odot$ (Mathews 1978)) at the heart of the Virgo cluster. It was first discovered by Charles Messier, in his famous catalogue of Nebulae and Star Clusters (Messier 1781), and has been the subject of much study throughout this century.

Narrow-band imaging and spectroscopy by the *HST* have revealed the presence of a disk of ionised gas, surrounding a black hole of mass $2.4 \pm 0.7 \times 10^9 M_\odot$ (Ford et al. 1994; Harms et al. 1994). This mass is actually obtained from the velocities of the disk and is the mass internal to a radius of $0\farcs24$ (or 18–20 pc), which, with a mass to light ratio of $M/L \sim 170$, implies the presence of a black hole.

The jet itself shows remarkably similar structure at both optical and radio frequencies, which is seen in both continuum images and polarisation images. The brighter knots in particular show evidence for a steepening of the spectrum in the optical (Meisenheimer et al. 1996), indicating that the spectrum turns over at optical frequencies.

3C 273: The jet in 3C 273 is the second oldest known optical jet. It was first noted by Schmidt (1963) (describing it as "a faint wisp or jet") in the paper that first reported 3C 273's large redshift.

The structure of the 3C 273 jet is atypical for optical jets. The radio emission is much more extended, both laterally and longitudinally, than the optical emission, with the optical jet running along the ridge line of the radio emission (Morrison and Sadun 1992; Thomson et al. 1993). The radio features generally coincide with the optical knots, although the bright radio head of the jet is not seen in the optical (Bahcall et al. 1995). It is possible that the optical jet emission is not pure synchrotron (Thomson et al. 1993), but may include either some scattered quasar light or starlight.

The host galaxy has been shown (Bahcall et al. 1997) to be a bright E4 elliptical. Indeed, at $M_V = -22.1$, it is brighter than the brightest galaxy of a rich cluster. It seems to be in a group of several galaxies.

3C 15: This source is an elliptical galaxy, classified as an intermediate FR I / FR II. The optical counterpart to the jet was discovered by Martel et al. (1998), using *HST*. The optical jet matches the inner part of the radio jet, although the two radio knots are undetected in the optical.

Interestingly enough, the nucleus of 3C 15 appears to lack a sharp point-like AGN, possibly indicating that the source is in an inactive state. What is seen, however, are three ridges of emission extending out from the nucleus, along with a dark dust band, which seem to point to a merger event.

3C 66B: This optical jet was detected by Butcher et al. (1980) using a vidicon video camera on the 4m Mayall telescope at Kitt Peak. At *HST* resolution (Macchetto et al. 1991a), the jet shows filamentary structure, with evidence for two strands. This has not been seen in any other optical jet except M87, which shows a more tightly bounded structure, possibly indicating a different interaction with the medium. Fraix-Burnet (1997) found evidence for an optical counter-jet (3C 66B is the only optical jet source that shows a radio counter-jet), which, if confirmed, would cast some doubt on the beaming model for jets.

3C 78: The optical jet in 3C 78 was discovered by Sparks et al. (1995). The jet shows a "remarkable" coincidence between the radio and optical morphologies and direction (that is, the position angles are the same). The host galaxy is notable for being a spiral (an S0 at least), as well as showing Seyfert 1 characteristics.

3C 120: 3C 120 is classed as a Seyfert 1 galaxy, and so is rare in not being an elliptical host. It has a variable AGN, is a powerful X-ray source (Maraschi et al. 1991), and has a radio jet with superluminal motion (Walker et al. 1988). A faint optical counterpart to the jet was detected using the *NOT* (Hjorth et al. 1995). One of the "condensations" was found to be polarised ($p = 12\% \pm 4\%$), thus linking it with the radio jet. The overall structure of the optical jet coincided with the radio, although no counterparts to the radio knots could be discerned. It is possible that the optical emission is not pure synchrotron (similar to 3C 273) – there could be some scattered starlight present as well.

PKS 0521−365: This is an elliptical radio galaxy that exhibits a bright radio nucleus, along with extended radio emission. In *HST* observations (Macchetto et al. 1991b), a bright knot was seen at the same place as in *VLA* data. After this, the jet has roughly constant surface brightness.

However, in *HST* snapshot survey observations (Scarpa et al. 1999), this bright knot is not seen. In these observations, the jet has an almost constant width along its length, which implies that the plasma is moving in a well-defined cylindrical funnel. There is also a general one-to-one correspondence between the radio and optical morphologies.

3C 200: In their *HST* snapshot survey of 3CR sources, de Koff et al. (1996) detected a narrow feature extending southeast from the core of this quasar. The direction and morphology of the radio jet is "practically identical", and so they suggest this is a very strong candidate for an optical jet. However, a longer exposure image than that taken in the snapshot survey would be required to obtain better analysis of this jet.

3C 212: This is one of the highest redshift sources known to exhibit optical counterparts to radio jet structures. With an absolute magnitude of $M_V < -24$, it is more accurately described as a quasar, rather than a radio galaxy. It was imaged with *HST* and Keck by Ridgway and Stockton (1997). It shows a peculiar morphological structure, with a number of blue optical components lying along the radio jet axis. It also shows an extended structure that Ridgway and Stockton speculated could be the optical counterpart to the radio lobe, but was shown (Stockton and Ridgway 1998) to more likely be a neighbouring galaxy.

3C 245: This, too, is a bright, high redshift quasar ($M_V < -26$), also imaged by Ridgway and Stockton (1997). These images show a linear feature that coincides exactly with the radio jet, and since there is good correspondence between the optical and radio structure, it is likely the optical emission is due to synchrotron radiation.

3C 264: This optical jet was discovered by Crane et al. (1993). The radio and optical jets show a very good spatial coincidence. There is also a 'ring' of enhanced optical emission at a radius of 300-400 pc from the nucleus, which Baum et al. (1997) interpret as most likely due to the presence of a face-on dusty disk. The jet widens dramatically after passing through this disk and becomes turbulent, changes direction, and fades rapidly. This is most likely due to decreased pressure in the ambient medium outside the disk/ring.

Lara et al. (1999) have shown that the optical emission is most likely due to synchrotron emission (and not Inverse Compton or scattering), but that likely explanations of re-acceleration have some problems. In particular, well defined knots are required along the jet, and these are not seen. Also, it is unclear how the radio-optical spectral index is kept approximately constant along the jet.

3C 346: Optical emission associated with a radio knot was discovered (Dey and van Breugel 1994) in this FR II radio galaxy, using ground based imaging in the optical/ultraviolet. *HST* snapshot imaging by de Koff et al. (1996) resolves this knot into a curved jet and a triple hot spot that coincides perfectly with the radio emission.

3C 371: 3C 371 is classed as a BL Lac object and exhibits a one-sided radio jet. The optical jet was discovered using the *NOT* by Nilsson et al. (1997). The radio and optical morphologies do not exactly coincide, with the radio jet being several times longer than the optical (Scarpa et al. 1999), in a manner somewhat reminiscent of the jet of 3C 273, and unlike other jets such as those of M87 and PKS 0521−365.

3C 380: This object is a radio-loud quasar, classified as a compact steep-spectrum source by Fanti et al. (1990). The radio jet shows two prominent knots that are seen in the optical (O'Dea et al. 1999). There is a good one-to-one correspondence between the optical and radio emission in both the knots. Due to the large redshift of the source, these knots are the most luminous known.

PKS 2201+044: The optical jet in this source was discovered (Scarpa et al. 1999) during the *HST* snapshot survey of BL Lac objects, and so the exposure time was less than ideal. However, the jet was able to be resolved, and the association with the radio jet was established. A final point to note is that, although 2201+044 is classified as a BL Lac, it shows broad emission lines in its spectrum, and so the beaming cannot be very strong (perhaps due to a large angle to the line of sight).

There are a number of other sources that are possible candidates for optical jets. De Koff et al. (1996) found a further 8 candidates for optical synchrotron jet emission, including 3C 20 (the optical counterpart of a hot spot was detected by Hiltner et al. (1994)), 3C 133 and 3C 410. As these observations were made with *HST* in snapshot mode (which involves shorter exposures than are ideal), longer exposure imaging may be expected to resolve these jets. In addition to these sources, a number of sources have been shown to exhibit optical emission associated with a radio hot spot (Dey and van Breugel 1994; Meisenheimer et al. 1989).

2.2 Observed properties of optical jets

In this section we list and discuss some of the observed properties of the optical jets, in particular their length and viewing angle, and the spectral indices (both optical and ratio-optical). All of these parameters are important in constraining the models that will be used for the synchrotron emission from the Parkes quasars, as well as beaming models for quasars and BL Lacs (Chapter 7).

2.2.1 Power law indices

A relatively easy parameter of optical jets to measure is the spectral index, which is defined (for this discussion) as α, where $F_\nu \propto \nu^{-\alpha}$. This is usually determined on the basis of two points: a radio and an optical observation, giving the radio–optical slope α_{ro}, or two different optical wavelengths for the optical slope α_o. The spectral index gives one an idea of the average slope of the continuum over the frequency range under consideration, which allows the emission mechanisms to be constrained.

Since all the optical jets have radio counterparts, α_{ro} gives information on how the optical emission is connected to the radio emission, and this can help determine whether the optical emission is synchrotron as well (since the radio emission is widely accepted to be due to the synchrotron process). The optical slope can also give information on the emission processes at the higher optical frequencies, without worrying about the radio emission.

Table 2.2 lists the measured spectral indices for all optical jets as taken from the literature. At first glance, several things are immediately apparent. The average values for the spectral indices are $\langle\alpha_o\rangle = 1.41 \pm 0.33$ and $\langle\alpha_{ro}\rangle = 0.79 \pm 0.13$. Even though there is some scatter in the values, it is clear that the α_o values are steeper than the α_{ro} values.

This is consistent with a synchrotron component that cuts off or turns over at some maximum frequency. This in fact has been postulated as one reason for the low number of sources seen with optical jets (as compared to the number of sources with radio jets), as most of the sources without optical jets have this cut off at a frequency lower than optical frequencies.

We note that, from Table 2.2, the values of α_o, while there are a couple above 2.0, are mostly clustered around values of 1.3 – 1.4. Is this significant? If the optical slopes were much steeper, the jet emission would be harder to detect, since they will in general be fainter, and so jets with steeper optical indices will tend to be selected against. On the other hand, a flatter optical slope would not be selected against, and so the absence of flat optical slopes (i.e. slopes that are closer to or the same as the radio–optical slope) appears

Name	α_o	α_{ro}	ref
3C 15	1.2	—	8
	—	0.95	7
	—	0.86	10
3C 66B	1.6	0.80	1
	2.4	—	8
3C 78	1.2	—	8
	—	$\sim$ 0.69	3
	—	0.81	10
3C 120	1.3	0.65–0.69	2
	—	0.69	10
3C 200	—	0.74	10
PKS 0521−365	2.0	0.76	1
	1.4	—	8
	—	0.73	7
3C 212	1.4	—	8
	—	1.06	10
3C 245	1.2	—	8
	—	1.03	10
3C 264	1.4	0.58	1
	1.34	0.63	6
	1.4	—	8
	—	0.85	10
3C 273	1.33	0.90	1
	1.3	—	8
	—	1.07	10
M87	1.2	0.66	1
	0.97	0.65	4
	1.2	—	8
	—	0.71	10
3C 346	1.8	—	8
	—	0.87	10
3C 371	—	0.81	5
	—	0.75	9
	—	0.74	10
3C 380	1.2	—	8
PKS 2201+044	—	0.85	9

Table 2.2: Table showing spectral indices α (where $S_\nu \propto \nu^{-\alpha}$). The indices given are the optical (α_o) and the radio–optical (α_{ro}). References: (1) Crane et al. (1993); (2) Hjorth et al. (1995); (3) Sparks et al. (1995); (4) Meisenheimer et al. (1996); (5) Nilsson et al. (1997); (6) Lara et al. (1999); (7) Martel et al. (1998); (8) O'Dea et al. (1999); (9) Scarpa et al. (1999); (10) Scarpa and Urry (2001)

to be a real one. That is, there are not significant numbers of jets with synchrotron spectra extending to UV and X-ray energies.

2.2.2 Jet length and viewing angles

The length of observed optical jets can be a difficult parameter to measure. Quite obviously, it depends on the capabilities of the telescope being used, as the end of the jet needs to be able to be resolved and detected significantly above the background. Even when the end of the jet is able to be defined, the apparent length of the jet is still only the projected length – that is, the jet is seen projected onto the plane of the sky. For this reason, jet length and the viewing angle, or the angle that the jet makes to the line of sight, are tied together.

The length of the jet can provide information on both the power of the central source (depending on models of how jets are formed and therefore how they connect to the central black hole), as well as the nature of the interstellar and intergalactic medium. A list has been compiled of jet lengths (in both arcseconds and kiloparsecs) in Table 2.3. The lengths span nearly two orders of magnitude, with the powerful quasar 3C 273 having the longest. However, these lengths are of course projected lengths, so viewing angle effects have not been accounted for.

Since the jets are seen in projection against the plane of the sky, this viewing angle is quite a difficult parameter to measure. As well as being important for determining the correct lengths of jets, this angle is also important for determining the Doppler factor, and hence the amount of relativistic beaming that is occurring (see Chapter 3 and Chapter 7). The viewing angle, therefore, is very important in understanding the overall energetics of the jet. Often, determinations of the viewing angle will be coupled with determinations of the Lorentz factor Γ. This is the "bulk Lorentz factor" (rather than the Lorentz factor of the individual radiating particles), which comes from the speed at which the "blobs" or features in the jet are moving.

One determination of the angle (and in this case, Γ) was made by Scarpa and Urry (2001). They discussed the energy budget of the known optical jets, and found that the above parameters lay in a "most probable" region centered around $\Gamma \sim 7.5$ and $\theta \sim 20°$. These values were reached by requiring the jets to transport enough kinetic energy to power an average radio lobe, since the kinetic power of the jet depends on Γ. The "most probable"

Name	Length (arcsec)	Length (kpc)
3C 15	4.2	5.3
3C 66B	8.0	3.2
3C 78	1.5	0.8
3C 120	15.0	24.8
PKS 0521−365	6.5	6.4
3C 200	0.8	3.6
3C 212	2.2*	12.5
3C 245	1.6*	9.1
3C 264	2.2	0.9
3C 273	23.0	56.2
M87	25.0	2.1
3C 346	3.6	9.0
3C 371	4.5	4.1
3C 380	1.4	8.5
PKS 2201+044	2.1	1.1

Table 2.3: Projected lengths of optical jets, in both arcseconds and kiloparsecs. The kiloparsec lengths are calculated using $H_0 = 75$ km s^{-1} Mpc^{-1}. Note that an * indicates that the length shown was calculated by the author from published images.

region was found by considering the amplification or de-amplification of the jet emission due to relativistic beaming (a de-amplified jet is less likely to be detected), which depends on both Γ and θ.

An alternative method is that used by Sparks et al. (2000). They imaged the nearest five 3CR galaxies that host optical jets, and found evidence for almost circular dust disks in four of them. They interpreted these disks as being face-on, so that the optical jets emerge close to perpendicular to these disks. From this, they find a critical line of sight angle of 30°– 40°, above which an optical jet is not seen. Taking the beam angular width to be $\sim 1/\Gamma$, this implies a minimum value of $\Gamma \sim 1.4 - 2$.

A somewhat different way of obtaining viewing angles for jets has been the approach of Ghisellini et al. (1993). They used observations of superluminal motion of radio jets to obtain an upper limit on the viewing angle. To do this, the Doppler factor δ needs to be found, and then the angle can be calculated from the apparent transverse speed β_a. The Doppler factor is calculated by comparing the predicted self-Compton flux at X-rays with that observed – this gives an expression for δ in terms of the radio and

X-ray fluxes, and the angular size of the radio core. The derived angles, for those sources with optical jets (only four of them have calculated values), are typically $\lesssim 10°$ (although one source, 3C 345, has $\theta = 17°$). We do note, however, that these Doppler factors are derived using non-simultaneous data, which may lead to erroneous results (particularly for the more variable sources).

Superluminal motion has also been observed in the optical for one optical jet – that of M87. Biretta et al. (1999) observed M87 with *HST* at five different epochs from 1994 to 1998, and found superluminal motion with apparent speeds from $4c$ to $6c$. For the fastest features, they find that the orientation angles must satisfy $\theta \lesssim 19°$ and the Lorentz factors must be $\Gamma \gtrsim 6$ (with the sense that larger angles require larger Lorentz factors and produce smaller Doppler factors – an angle of $\theta = 19°$ requires $\Gamma = 40$ and gives $\delta = 0.5$, compared with $\theta = 10°$ requiring $\Gamma = 6$ and $\delta = 5.7$ (see Table 3 of Biretta et al. (1999))).

2.3 X-ray jets

Finally, we will move from the optical region to briefly discuss jets at X-ray energies. The two best-known optical jets, those of M87 and 3C 273, have both been detected in X-rays, as has a knot in the jet of 3C 120. The detection of the M87 jet was first reported by Schreier et al. (1982), based on observations with the *Einstein* satellite, and were further developed by Biretta et al. (1991). Due to the comparatively poor resolution of this satellite, the detection of the jet was dominated by the emission from the core and from the strongest of the emission knots. A similar detection was made with *ROSAT* (Neumann et al. 1997). The emission process may be synchrotron, although it is likely to be due to a different population of electrons to that emitting the radio–optical spectrum. Alternatively, it may be due to some other X-ray process (such as thermal bremsstrahlung or inverse Compton scattering) (Biretta et al. 1991; Meisenheimer et al. 1996).

The *ROSAT* satellite also detected X-ray emission from a radio knot in 3C 120 (Harris et al. 1998). Since this radio knot has not been detected at optical frequencies (the optical jet is much closer in to the core), it is unlikely that the X-ray emission is due to synchrotron. However, since no simple thermal bremsstrahlung or inverse Compton model fits the data, Harris et al. speculate on the existence of a separate, high-energy population of electrons that radiate a flat-spectrum X-ray component.

The launch last year of the *Chandra* X-ray Observatory provided a startling new example of an X-ray jet. The first target for the observatory was the radio quasar PKS 0637−752, a point source (so it was believed) that was to be used to calibrate the telescope optics. However, it was immediately apparent that there was an X-ray jet (Schwartz et al. 2000), which was coincident with the known radio jet (Tingay et al. 1998). At the source redshift of $z = 0.651$, the jet has a length of some 100kpc.

The origin of the X-rays is not certain (Chartas et al. 2000). A single-component power law synchrotron model does not work, as the optical emission is several orders of magnitude below the interpolation between the radio and X-ray data. Other models, such as inverse Compton, are difficult to fit effectively (Schwartz et al. 2000).

The jet of 3C 273 has also been imaged with *Chandra* (Marshall et al. 2000). Morphologically, the X-ray emission is strongest at the end of the jet closest to the core, and then decreases as the jet gets further away. This is the opposite sense to the radio emission, which is strongest at the head of the jet. The spectrum of the first knot in the jet (i.e. the one closest to the core) is consistent with a single power law extending from radio to X-ray energies, which may be due to synchrotron emission (although it is also possible that at least some of the X-ray emission originates from inverse-Compton scattering of the microwave background by relativistic motion in the jet). The likelihood of synchrotron emission being responsible for the X-ray flux decreases the further along the jet you go.

Chapter 3

Synchrotron radiation

The purpose of this chapter is to introduce the phenomenon of synchrotron radiation, and its place in studies of radio-loud AGN. The derivations presented in Section 3.2 are not original – they owe much of their form to Longair (1994) – while those presented in later sections are the author's own developments starting from the work in Section 3.2.

First, a note: the derivations that follow are aimed at calculating the luminosity of synchrotron emission. This should (unless stated otherwise) be taken to mean the spectral luminosity, or luminosity per unit frequency, with SI units of W Hz^{-1}.

3.1 Introduction

In the 1940s, the development of experimental particle physics led to the development of various types of particle accelerators, which were used to accelerate particles such as electrons to high enough energies to observe particular interactions. One such form of accelerator that was common was the *synchrotron*, which used circular magnets to accelerate particles up to high energies – an early example was the General Electric 70 MeV synchrotron.

When these synchrotrons were first constructed and utilised, it was noticed (Elder et al. 1947, 1948) that an intense light (polarised in the plane of the electrons' orbit) was emitted from the high energy electrons. The theory of this radiation was investigated by Schwinger (1949), who first derived the spectrum of radiation that is emitted.

It was a few years later that its application to astrophysics was realised. Shklovsky (1953) showed that the radio and at least part of the optical emission of the Crab Nebula could be explained by synchrotron emission. It soon became accepted as the dominant component of the radio emission from the Galaxy, from supernova remnants, and from radio galaxies. The natural polarisation of synchrotron emission was used in a number of instances to confirm its presence, particularly at optical wavelengths (for example, Baade (1956) observed the polarisation of the jet in M87). A good review of the early studies of synchrotron emission is that by Ginzburg and Syrovatskii (1965), who, in this and their later review (Ginzburg and Syrovatskii 1969), tried to coin the term "magnetobremsstrahlung" as an alternative to "synchrotron". However, they did note that *"it hardly seems possible at this late stage to change the accepted terminology"*, and sadly, they proved to be correct.

3.2 Tangled magnetic fields

3.2.1 Introduction

The first derivation presented will be the derivation most commonly used in the literature. The method followed is that detailed in Longair (1994), which has the advantage of being done in S.I. units (unlike other derivations such as those found in Pacholczyk (1970) or Rybicki and Lightman (1979)).

The physical model for this derivation is a jet that has a tangled magnetic field. This means that there is no preferred angle to the magnetic field lines, and so we integrate over all viewing angles. The viewing angle is important because the radiation from each particle is strongly beamed in the direction in which that particle is travelling, since the particle is relativistic.

This relativistic motion means that the dipole radiation pattern that is emitted in the rest frame of the particle is Lorentz-transformed into a strongly beamed pattern in the observer's, or lab, frame (see Fig. 3.1). The way this pattern transforms is governed by the aberration formulae:

$$\sin\phi = \frac{\sin\phi'}{\gamma(1+\beta\cos\phi')}, \quad \cos\phi = \frac{\cos\phi'+\beta}{1+\beta\cos\phi'} \tag{3.1}$$

where a prime ($'$) indicates the particle's rest frame. In the rest frame, there is zero power emitted at angle $\phi' = \pi/2$, and so in the lab frame we have

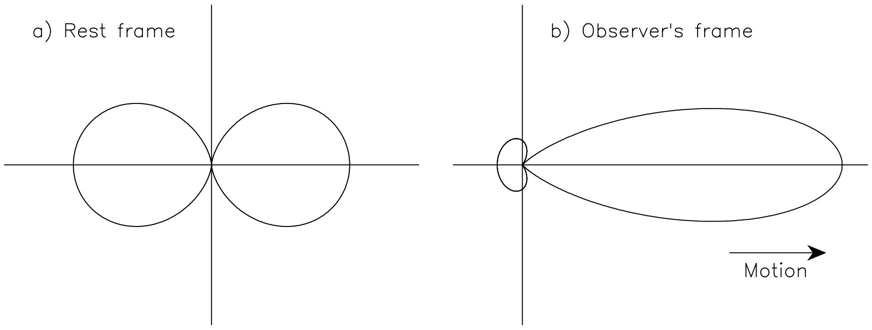

Figure 3.1: Diagram showing the effect of relativistic motion at right angles to acceleration. a) Dipole radiation pattern from a non-relativistic accelerated charge (i.e. in the particle's rest frame). b) Beamed radiation pattern from particle observed to be moving to the right. In this case, the particle is moving at a velocity of $0.4c$ (i.e. a Lorentz factor of just $\gamma = 1.091$), and the scale in both the x and y directions has been shrunk by a factor of two.

$\sin\phi = 1/\gamma$, which, for large γ (i.e. for a more relativistic particle), gives $\phi \sim 1/\gamma$. Thus all the forward power is radiated in a beam of angle $2/\gamma$. The emitted power as a function of angle is also affected by the relativistic motion of the particle. The full expression is not shown here, but it results in very strong power emitted in the forward direction, and much less power in the opposite direction (see Fig. 3.1).

3.2.2 Derivation

We first consider the case of a single particle (of mass m, energy $E = \gamma mc^2$, and charge e) moving with velocity v in a uniform magnetic field of strength B. The trajectory of this particle makes an angle of α_p with the direction of the magnetic field – this angle is called the "pitch angle". The particle's trajectory forms a spiral, or helix, centred on the field line, due to the $\vec{v} \times \vec{B}$ force. This spiral has a radius of curvature, with respect to the central line, of $a = v/(\omega_r \sin\alpha_p)$, where $\omega_r = eB/m\gamma$ is the relativistic gyro-frequency.

The emission can be expressed in terms of components in two polarisations: both perpendicular and parallel to the projected direction of the magnetic field. A rather complete derivation of these two components is given in Longair (1994) – here we simply give the final result. Defining two variables to be used in the equations:

$$\theta_\gamma^2 = 1 + \gamma^2\theta^2 \qquad \eta = \omega a \theta_\gamma^3 / 3c\gamma^3,$$

we can write these two emission components as:

$$\frac{\mathrm{d}I_\perp(\omega)}{\mathrm{d}\Omega} = \frac{e^2\omega^2}{12\pi^3\epsilon_0 c}\left(\frac{a\theta_\gamma^2}{c\gamma^2}\right)^2 K_{\frac{2}{3}}{}^2(\eta) \tag{3.2}$$

$$\frac{\mathrm{d}I_{||}(\omega)}{\mathrm{d}\Omega} = \frac{e^2\omega^2\theta^2}{12\pi^3\epsilon_0 c}\left(\frac{a\theta_\gamma}{c\gamma}\right)^2 K_{\frac{1}{3}}{}^2(\eta) \tag{3.3}$$

where $K_{\frac{1}{3}}$and $K_{\frac{2}{3}}$are the modified Bessel functions of order $\frac{1}{3}$ and $\frac{2}{3}$ respectively.

The next step is to integrate over solid angle. Since nearly all the radiation is emitted within very small angles of the pitch angle (due to the relativistic beaming of the radiation pattern), and the elemental solid angle varies little over $\mathrm{d}\theta$, the solid angle becomes $\mathrm{d}\Omega = 2\pi\sin\alpha_p\mathrm{d}\theta$. We can then integrate Eqns. 3.2 & 3.3 with respect to θ. Also, since the radiation is concentrated in a small angle about α_p, we can take the integral limits to $\pm\infty$ (as this makes finding an analytic solution that much easier!). Thus:

$$I_\perp(\omega) = \frac{e^2\omega^2 a^2\sin\alpha_p}{6\pi^2\epsilon_0 c^3\gamma^4}\int_{-\infty}^{+\infty}\theta_\gamma^4 K_{\frac{2}{3}}{}^2(\eta)\mathrm{d}\theta \tag{3.4}$$

$$I_{||}(\omega) = \frac{e^2\omega^2 a^2\sin\alpha_p}{6\pi^2\epsilon_0 c^3\gamma^2}\int_{-\infty}^{+\infty}\theta^2\theta_\gamma^2 K_{\frac{1}{3}}{}^2(\eta)\mathrm{d}\theta \tag{3.5}$$

[Note that by integrating over solid angle, we are evaluating the total power radiated by the particle, in all directions, which, while useful for the case of a tangled field, is not necessarily what is desired when calculating observed synchrotron spectra from a uniform field. This point will be addressed in Section 3.3.]

By using analytic integrals (Westfold 1959), these two quantities can be written in terms of the functions

$$F(x) = x\int_x^\infty K_{\frac{5}{3}}(z)\mathrm{d}z \qquad \text{and} \qquad G(x) = xK_{\frac{2}{3}}(x) \tag{3.6}$$

(where $x = 2\omega a/3c\gamma^3 = 2\eta/\theta_\gamma^3$). We therefore obtain

$$I_\perp(\omega) = \frac{\sqrt{3}e^2\gamma\sin\alpha_p}{8\pi\epsilon_0 c^3}(F(x)+G(x))$$

$$I_{||}(\omega) = \frac{\sqrt{3}e^2\gamma\sin\alpha_p}{8\pi\epsilon_0 c^3}(F(x)-G(x))$$

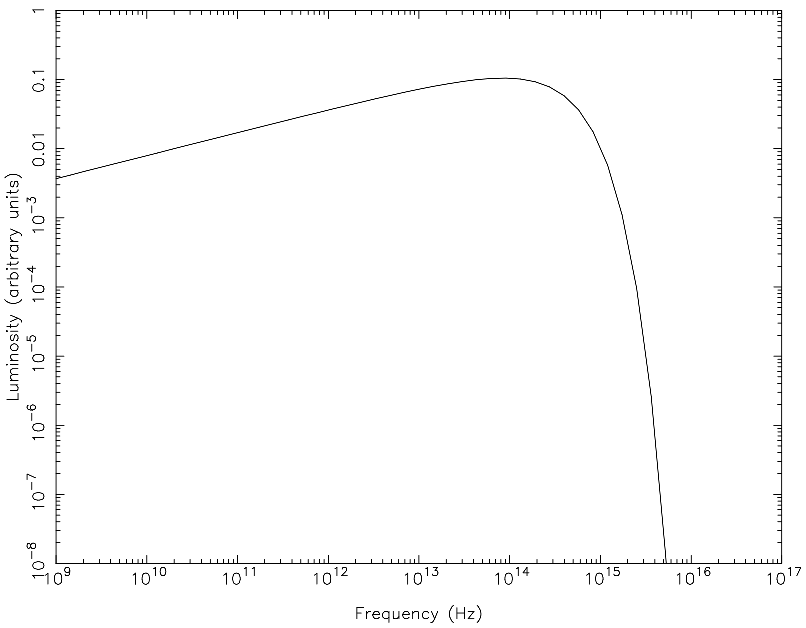

Figure 3.2: Synchrotron spectrum of a single particle in a tangled magnetic field. Values of the parameters are: $B = 10^{-4}$T, $\gamma = 10^4$, and $\alpha_p = 45°$.

The next and final step in deriving the single particle emission function is to add these terms and divide by the time over which the radiation was emitted. Since we have integrated over solid angle, the above expressions give the energy emitted during one period of the particle's orbit, i.e. in a time $T_r = \nu_r^{-1} = 2\pi\gamma m/eB$. Thus, the total luminosity (i.e. radiated power) of the particle in both polarisations is:

$$L(\omega) = \frac{I_\perp + I_\parallel}{T_r} = \frac{\sqrt{3}e^3 B \sin\alpha_p}{8\pi^2\epsilon_0 cm} F(x) \tag{3.7}$$

This flux is shown in Fig. 3.2, for $B = 10^{-4}$T, $\gamma = 10^4$, and $\alpha_p = 45°$.

3.2.3 Populations

This equation gives the emission spectrum for a single particle in a magnetic field. More interesting, from an astronomical point of view, is the spectrum from a *population* of particles. Such a population will have a distribution of energies (and hence Lorentz factors) and pitch angles. The two most commonly used distributions are a power law distribution of energies, $N(E)\mathrm{d}E = \kappa E^{-p}\mathrm{d}E$, and an isotropic probability distribution of pitch angles, $p(\alpha_p) = \frac{1}{2}\sin\alpha_p$.

We can then integrate over energy and pitch angle to obtain the total emission from such a population. This is done in detail by Longair (1994), but we just quote here the result for the dependence of the resulting flux on both frequency and magnetic field strength:

$$L_{\rm pop}(\nu) \propto B^{(p+1)/2}\nu^{-(p-1)/2} \tag{3.8}$$

This is a very important result, as it links an observable parameter (i.e. the spectral index of the emission) to the power law slope of the particle energy distribution, in the sense that $\alpha = (p-1)/2$ (where we use α to represent the spectral index, as is standard in the literature). We will come back to this result in the next section.

Note that a power law distribution of energies produces a power law emission. In physical systems, however, the energy distribution can often either cut off, or change slope at some energy. A good example for this comes from the modelling done by Meisenheimer et al. (1996) on the radio to optical emission from the jet of M87. They found that the best fit to the flux measurements was for an energy distribution of the form $N(\gamma) \propto \gamma^{-2.31}$, with an abrupt cut off at some maximum energy.

In general, if the energy distribution has a cut off, then the resulting emission spectrum will have a critical frequency ν_c where the power law spectrum has an exponential cutoff (in the same manner as the single particle spectrum – see Fig. 3.2). It can be shown (for example, Blandford 1990) that this critical frequency scales like $\nu_c \propto \gamma_+^2 B$, where γ_+ here is the maximum value of the γ distribution.

3.3 Ordered jets

The derivation in Section 3.2 integrates over all the possible viewing angles. This is valid if the magnetic field in which the particles are moving is tangled (i.e. there is no preferred direction of the magnetic field), or if you are interested in the total energy radiated from a region. In the former case, there will be particles moving in many different directions, and so the observer will see contributions from many different values of the viewing angle θ.

However, if the magnetic field is not tangled, but is instead quite uniform, the observer will only see emission in a small range of θ values, those close to the angle between the line of sight and the magnetic field direction. Such a physical set-up may be similar to that seen in the collimated jets of FR II radio galaxies, or in the high-polarisation regions of both radio and optical jets. To find the observed spectrum for this case, we need to take into account only that radiation which is beamed in the direction of the observer.

The total energy emitted as a function of viewing angle is given by the sum of Eqns. 3.2 & 3.3. To obtain the observed luminosity (that is, the emitted power per unit frequency) of a single particle, we divide this by the orbital time $T_r = \nu_r^{-1} = 2\pi\gamma m/eB$. We use this time since the observer will see a pulse of emission (corresponding to the beamed radiation pattern) once in every orbit of the helical path of the emitting particle. This gives the following:

$$\begin{aligned} L_{1p}(\omega,\theta,\gamma) &= \frac{eB}{2\pi\gamma m}\frac{e^2\omega^2}{12\pi^3\epsilon_0 c}\left(\frac{a\theta_\gamma}{c\gamma}\right)^2\left[\frac{\theta_\gamma^2}{\gamma^2}K_{\frac{2}{3}}{}^2(\eta)+\theta^2K_{\frac{1}{3}}{}^2(\eta)\right] \\ &= \frac{e^3B\omega^2}{24\pi^4\epsilon_0 cm\gamma}\left(\frac{m\beta\gamma}{eB\sin\alpha_p}\right)^2\frac{\theta_\gamma^4}{\gamma^4}\left[K_{\frac{2}{3}}{}^2(\eta)+\frac{\theta^2\gamma^2}{\theta_\gamma^2}K_{\frac{1}{3}}{}^2(\eta)\right] \\ &= \frac{e\ m\ \omega^2}{24\pi^4\epsilon_0 Bc\sin^2\alpha_p}\frac{\beta^2\theta_\gamma^4}{\gamma^3}\left[K_{\frac{2}{3}}{}^2(\eta)+\frac{(\theta_\gamma^2-1)}{\theta_\gamma^2}K_{\frac{1}{3}}{}^2(\eta)\right] \end{aligned}$$

So, if for simplicity we let $\zeta = em/(24\pi^4\epsilon_0 c)$, then the power per unit frequency for a single particle, as a function of frequency ($\nu = \omega/2\pi$), angle ($\theta = \phi - \alpha_p$, where ϕ is the line-of-sight angle to the magnetic field direction) and energy ($E = \gamma mc^2$) is given by:

$$L_{1p}(\omega,\theta,\gamma) = \frac{\zeta\,\omega^2}{B\sin^2\alpha_p}\frac{\beta^2\theta_\gamma^4}{\gamma^3}\left[K_{\frac{2}{3}}{}^2(\eta)+\frac{(\theta_\gamma^2-1)}{\theta_\gamma^2}K_{\frac{1}{3}}{}^2(\eta)\right]. \qquad (3.9)$$

3.3.1 Populations

Once again, we want to look at the emission from a population of particles, rather than just a single particle. We use the distributions of energy and pitch angle used for the previous case.

Energy

The energies of the particles in the population are assumed to be distributed according to a power law (here we write it in terms of γ, rather than E). In this case, however, the power law is assumed to cut off at some maximum energy γ_+:

$$N(\gamma)\ \mathrm{d}\gamma = \begin{cases} \kappa\gamma^{-p}\ \mathrm{d}\gamma & 1 \leq \gamma \leq \gamma_+, \\ 0 & \gamma > \gamma_+. \end{cases} \tag{3.10}$$

Pitch Angle

The pitch angles are assumed to have an isotropic distribution. This is given by the probability distribution

$$p(\alpha_p)\ \mathrm{d}\alpha_p = \frac{1}{2}\sin\alpha_p\ \mathrm{d}\alpha_p$$

In general, the distribution of pitch angles will be defined by (or at least related to) the process by which the particles are accelerated.

Due to the beaming of the emission, an observer is only going to see emission from particles with pitch angles very close to $\alpha_p = \phi$. That is, the range of α_p values is restricted to a small range $\alpha_{p_1} - \alpha_{p_2}$, where $\alpha_{p_1} = \phi - \delta\alpha_p$ and $\alpha_{p_2} = \phi + \delta\alpha_p$. In practice, since these integrals are calculated computationally, we can determine the value of $\delta\alpha_p$ empirically by finding where the flux drops below some cutoff level. We find that $\delta\alpha_p$ is roughly proportional to the inverse square-root of the frequency (at higher frequencies, the emission becomes slightly more beamed, and so the width of the integration does not need to be as great), so that

$$\delta\alpha_p = 10^{-3}\left(\frac{\nu}{(10^{10}\mathrm{Hz})}\right)^{-\frac{1}{2}}, \tag{3.11}$$

where $\delta\alpha_p$ is measured in radians.

Total emission

To obtain the total emission from such a population, we integrate over both the energy and the pitch angle, to find:

$$\begin{aligned} L_{\text{tot}}(\omega, \phi) &= \int_{\alpha_{p_1}}^{\alpha_{p_2}} \frac{1}{2} \sin \alpha_p \left(\int_1^{\gamma_+} \kappa \gamma^{-p} L_{1p}(\omega, \gamma, \phi - \alpha_p) \, \mathrm{d}\gamma \right) \, \mathrm{d}\alpha_p \\ &= \frac{\zeta \, \omega^2 \kappa}{2B} \int_{\alpha_{p_1}}^{\alpha_{p_2}} \int_1^{\gamma_+} \frac{\beta^2 \theta_\gamma^4 \gamma^{-p-3}}{\sin \alpha_p} \left[K_{\frac{2}{3}}{}^2(\eta) + \frac{(\theta_\gamma^2 - 1)}{\theta_\gamma^2} K_{\frac{1}{3}}{}^2(\eta) \right] \mathrm{d}\gamma \, \mathrm{d}\alpha_p, \end{aligned} \tag{3.12}$$

where $\theta = \phi - \alpha_p$. See the following section for example spectra.

3.4 Exploring parameter space

Examination of Eqn. 3.12 shows that the luminosity at frequency ω of a population of particles depends on a number of factors: the viewing angle ϕ (that is, the angle the line of sight makes with the direction of the magnetic field); the particle energy distribution (governed in this case by the parameters p and γ_+); and the magnetic field strength B in the region of emission. In this section, we will examine each of these individually, to try to determine the dependence the luminosity has on each of them.

3.4.1 Variation of viewing angle

The viewing angle, or angle of the $\vec{B}$ vectors to the line of sight, is an important physical quantity, since jets are long, thin structures and will be inclined at some angle to the line of sight. See Section 2.2.2 for some typical values for jets that have been observed at optical wavelengths. Note that in measuring the viewing angle with respect to the direction of the jet, we are assuming that the magnetic field lies along the jet (i.e. parallel to the jet's direction). While this is obviously going to be a simplification of real jets, observations of M87 (Perlman et al. 1999) indicate that the magnetic field does tend to be parallel to the jet direction, particularly in the inter-knot regions.

In Fig. 3.3, we see the variation of the spectrum with changing viewing angle ϕ. Shown are spectra in units of both L_ν (luminosity per unit frequency) and L_λ (luminosity per unit wavelength), in arbitrary luminosity units.

Because the L_λ spectra rise to a peak and then decrease (this peak is related to the critical frequency ν_c mentioned earlier), we can use the location of the peak to find dependencies on ϕ of both the normalisation of the flux, and the location of the peak wavelength. We find that both these quantities depend on $\sin\phi$ in the following manner:

$$\lambda_{\text{peak}} \propto (\sin\phi)^{-1} \tag{3.13}$$

$$L_{\lambda,\text{peak}} \propto (\sin\phi)^{2.5} \tag{3.14}$$

Also, the shape of the spectrum is independent of the viewing angle, so that the entire curve has the same flux–angle dependence.

3.4.2 Variation of magnetic field strength

Another important physical quantity is the magnetic field strength B. A strong magnetic field will increase the strength of the synchrotron emission, as well as affect the location of the turnover. Magnetic fields in jets are often estimated assuming "equipartition", where the energy densities of the electrons and the magnetic field are equal. Typical values obtained are $\sim 10^{-4}$G $= 10^{-8}$T, although it is thought that values less than this are required to account for observed synchrotron cooling (e.g. in the M87 jet Heinz and Begelman (1997)). The value of the magnetic field is likely to increase as you move in towards the compact core.

In Fig. 3.4, we see the variation in the spectra as the magnetic field strength varies from 10^{-4}T to 10^{-11}T. The peak wavelength varies with B as

$$\lambda_p \propto B^{-1} \tag{3.15}$$

The peak flux, however, does not show a simple power law variation with B, but rather shows some curvature over the range of values explored. At large values of B ($B > 10^{-7}$T), the flux goes like $L_p \propto B^{2.5}$, while at lower values ($B < 10^{-8}$T), the relationship is $L_p \propto B^3$.

3.4.3 Variation of energy distribution

The energy distribution (Eqn. 3.10), being a power law up to a maximum energy, has two parameters: γ_+, the maximum energy, and p, the slope of

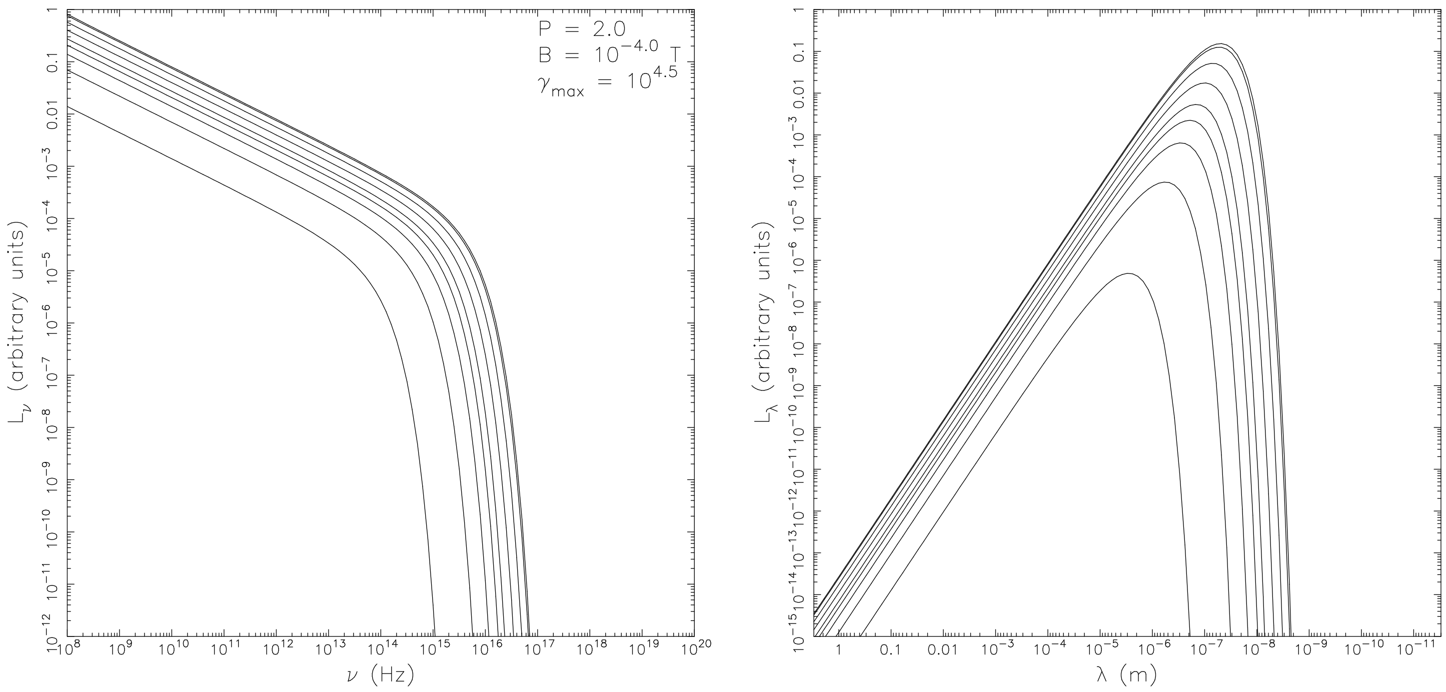

Figure 3.3: Variation of luminosity with changing viewing angle ϕ, which takes the values 90°, 70°, 45°, 30°, 20°, 15°, 10°, 5°and 1°(with larger ϕ values giving larger fluxes). The values of the other key parameters are indicated.

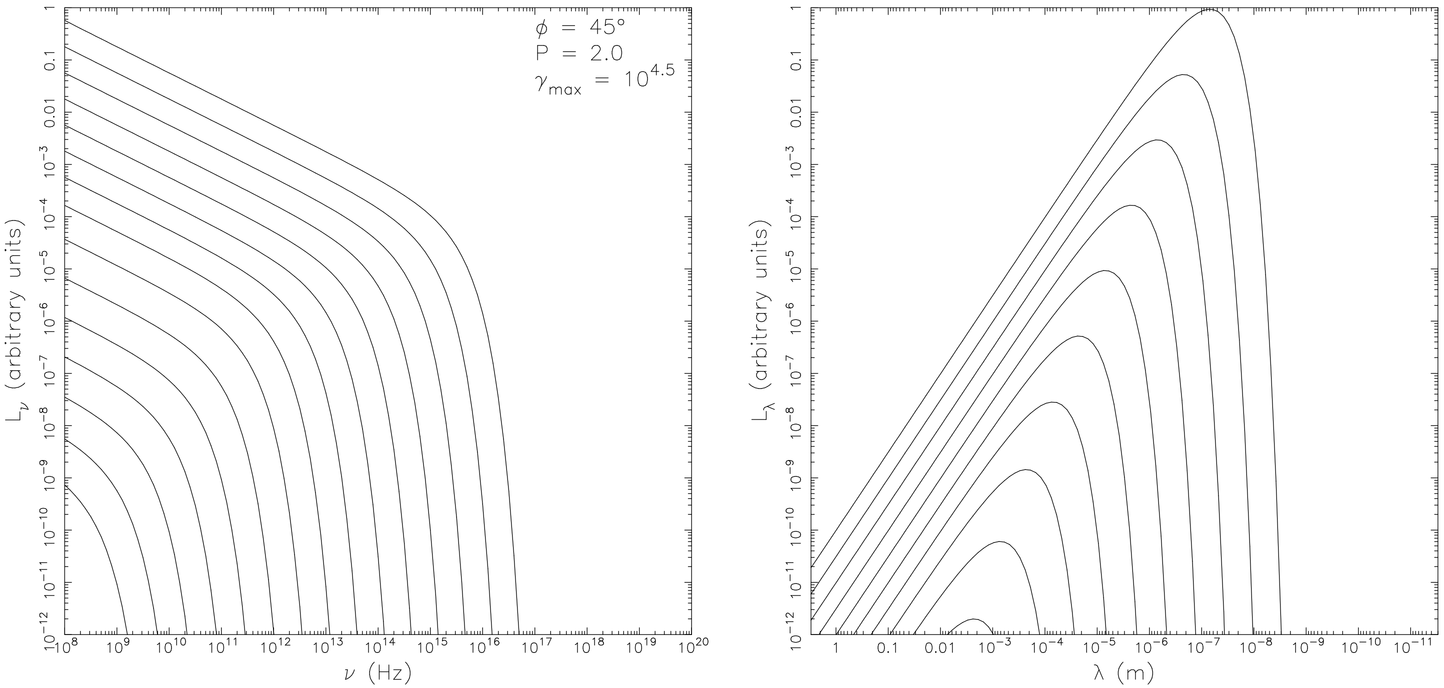

Figure 3.4: Variation of synchrotron spectrum with changing magnetic field strength B. The values of B considered are every half-dex in the range 10^{-4}T to 10^{-11}T, with higher B values giving higher fluxes. The values of the other key parameters are indicated.

the power law. We need to investigate what dependence the spectrum has on both of these parameters.

Maximum energy

The maximum energy of the energy distribution will strongly affect the resulting synchrotron emission, as the higher energies will contribute at the high-frequency end. A lack of high energy particles, therefore, will result in a spectrum that turns over at lower frequencies.

A range of synchrotron spectra with different γ_+ values are shown in Fig. 3.5. Note that, for wavelengths longer than the peak, the power law slope is the same, but the different γ_+ values cause the spectrum to turn over at different points. Once again, we can look at how the peak wavelength and flux vary with γ_+, and we find (looking at the L_λ spectra):

$$L_{\lambda,\mathrm{peak}} \propto \gamma_+^3 \tag{3.16}$$

$$\lambda_{\mathrm{peak}} \propto \gamma_+^{-2} \tag{3.17}$$

Slope of power law

The slope of the power law determines how rapidly the energy spectrum drops off with increasing energy. A large value of p means a steeper power law slope, which means that the higher energies are less prominent in the particle population. The value of p will affect the slope of the synchrotron spectrum at frequencies $\nu \ll \nu_c$.

The spectra for different values of p are shown in Fig. 3.6, from $p = 1$ (the one with the largest luminosity) up to $p = 4.5$ (the least luminosity). As can be seen, the synchrotron power law index α gradually steepens as p increases, and we find that the relationship between the two indices is $\alpha = (p-1)/2$, which is the same as that for the tangled field case (Section 3.2).

Also worth noting is the fact that the location of the peak does not change with the different values of p. This removes one degree of freedom in choosing the location of the peak/turnover frequency of the synchrotron emission.

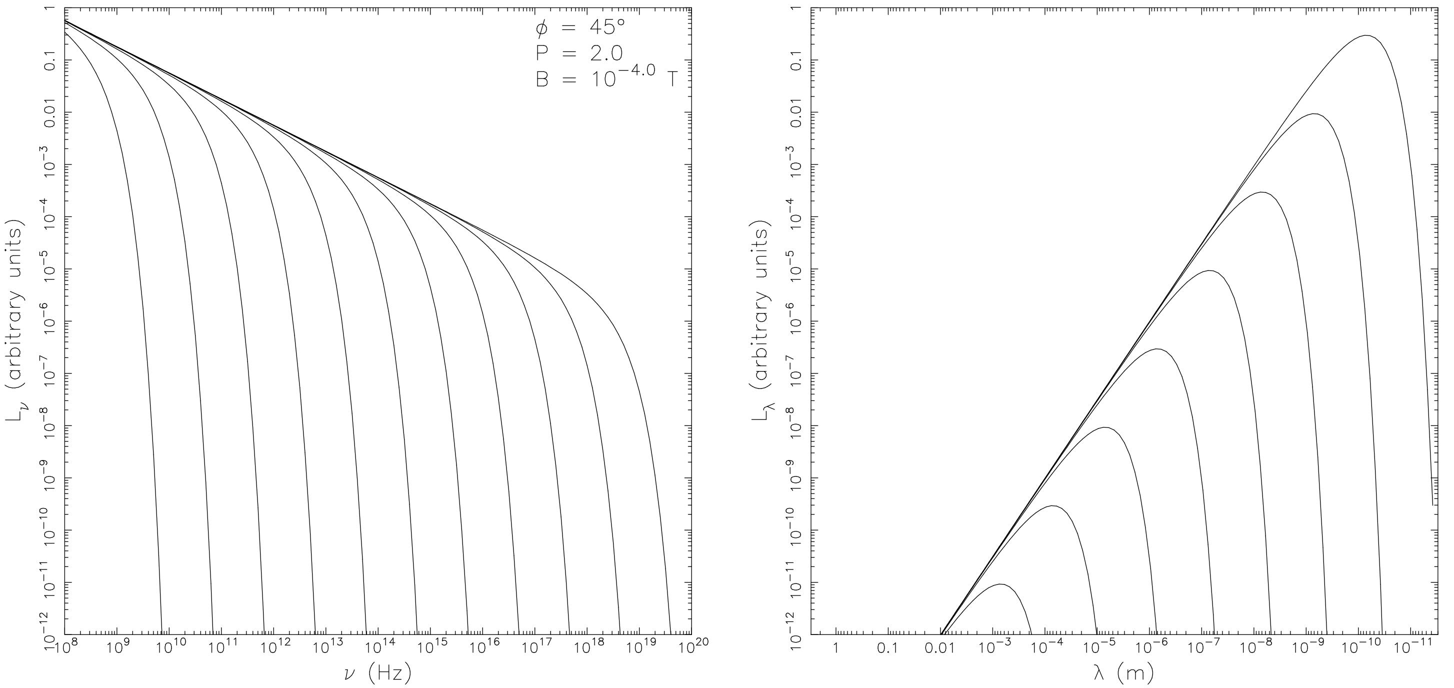

Figure 3.5: Variation of synchrotron spectrum with changing maximum energy γ_+. The values of γ_+ considered are every half-dex in the range 10 to 10^6, with the higher γ_+ values giving spectra extending to higher frequencies. The values of the other key parameters are also indicated.

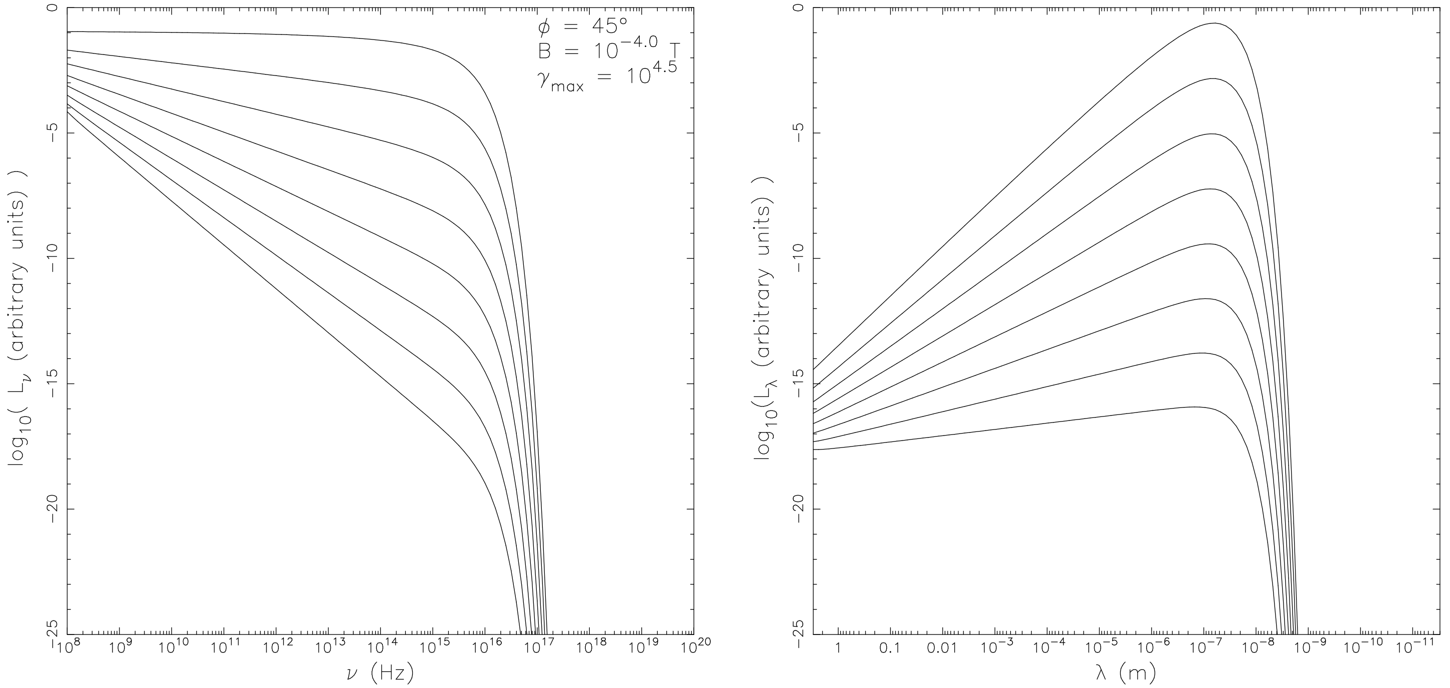

Figure 3.6: Variation of synchrotron spectrum with changing p. The values of p are spaced every 0.5 in the range 1 to 4.5, and the larger the value of p, the steeper and lower in flux is the resulting spectrum. The values of the other key parameters are also indicated. Note that this graph has a vertical axis that is different from the other graphs.

3.4.4 Overall variation

If we combine all these variations together, we can find how the peak wavelength and the peak flux vary with all the physical parameters. The net dependency is:

$$\lambda_{\mathrm{peak}} \propto \gamma_+^{-2} B^{-1} \sin\phi^{-1} \tag{3.18}$$

or, in terms of frequency:

$$\nu_c \propto \gamma_+^2 B \sin\phi$$

This has the same dependency as the tangled field derivation, although with the added dependence on the line of sight angle. This angle is also crucial in determining the overall luminosity, due to the strong dependence found: $L \propto (\sin\phi)^{2.5}$. This is worth noting carefully, since for small angles to the line of sight the overall luminosity will decrease quite rapidly. This is the opposite effect that you get from Doppler boosting, an enhancement of intensity coming from a source moving relativistically towards the observer. This effect is discussed in the following section.

3.5 Relativistic Doppler boosting

The calculations up to now have been made in the rest frame of the jet, i.e. there is no bulk motion present. However, in real jets, relativistic bulk motion has been postulated to exist, mainly from observations of superluminal motion in radio jets. Various models have been developed (Lind and Blandford 1985; Urry and Padovani 1995) to explain how the observed emission from a jet with bulk motion is affected, and we investigate two of the standard models in this section.

For a relativistic source moving at an angle ϕ to the line of sight, with a Lorentz factor $\Gamma = 1/\sqrt{1-\beta^2}$ (where $\beta = v/c$), the observed flux is enhanced by the Doppler factor

$$\delta = \frac{1}{\Gamma(1-\beta\cos\phi)} \tag{3.19}$$

The degree of enhancement depends on the nature of the source, but, in the case of a continuous, collimated jet (such as is modelled in Section 3.3), it takes the form

$$F_\nu(\nu) = \delta^{2+\alpha} F'_{\nu'}(\nu),$$

where a $'$ indicates a quantity is measured in the rest frame, $\nu = \delta\nu'$, and $F_\nu \propto \nu^{-\alpha}$. The other basic model for beaming is the case where, instead of a continuous jet, the outflow occurs in discrete "blobs". The beaming then has the form

$$F_\nu(\nu) = \delta^{3+\alpha} F'_{\nu'}(\nu).$$

Note that here, Γ is the *bulk* Lorentz factor, which relates to the velocity of features moving along the jet, not the velocities of the individual particles (which have Lorentz factors γ). This may be due to some bulk flow of plasma, or, in the latter case, the velocities of the individual "blobs".

Note that as $\phi \to 0$, the value of δ increases, reaching a maximum value at $\phi = 0$ of $\delta_{\max} = 1/\Gamma(1-\beta) \approx 2\Gamma$ for $\beta \approx 1$. The effect of Doppler boosting is shown in Fig. 3.7, for two extreme cases: $\delta^{2.5}$, corresponding to a continuous jet with $\alpha = 0.5$; and δ^4, corresponding to a jet made up of discrete blobs with $\alpha = 1.0$. The flux in these plots are normalised to the $\Gamma = 1$ curve, corresponding to isotropic emission. Note that for increasing Γ, the flux at small angles rapidly increases, whereas the large angle flux decreases below the un-boosted flux (the so-called "de-beaming"). The case of a larger dependence on δ (the discrete blob case) shows a much larger dependence on angle.

However, in the case of synchrotron emission from an ordered field, this dependence is counteracted by the angular dependence of the emission itself. To find the angular dependence of the observed flux, we need to take into account the fact that beaming changes the observed angle (in the manner of the aberration formulae Eqn. 3.1). The flux observed at an angle ϕ in the observer's frame will depend on both the Doppler beaming factor and the flux emitted at angle ϕ' in the rest frame of the blob/jet. These angles are related by (inverting Eqn. 3.1):

$$\begin{aligned} \sin\phi' &= \frac{\sin\phi}{\Gamma(1-\beta\cos\phi)} \\ &= \delta\sin\phi \end{aligned}$$

Thus, the observed flux at angle ϕ is

$$\begin{aligned} F(\phi) &\propto \delta^p (\sin\phi')^{2.5} \\ &\propto \delta^{p+2.5} (\sin\phi)^{2.5} \end{aligned}$$

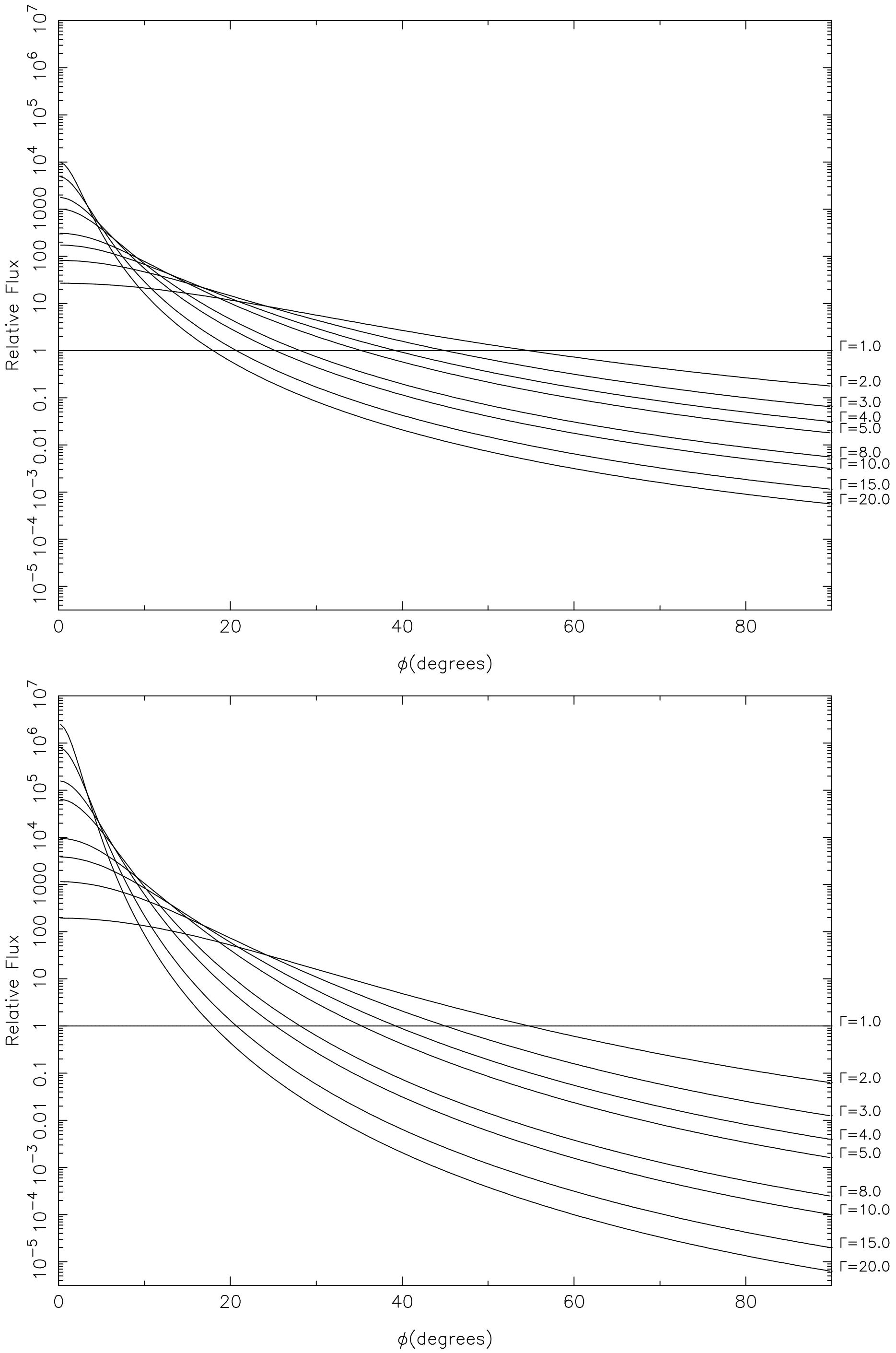

Figure 3.7: The effect of Doppler boosting on isotropic emission, for two different dependencies on δ: $\delta^{2.5}$ in the top plot and δ^4 in the bottom. The amount of Doppler boosting for each curve is shown by the value of the bulk Lorentz factor Γ next to the terminating point of the curve. A value of $\Gamma = 1$ represents no Doppler boosting.

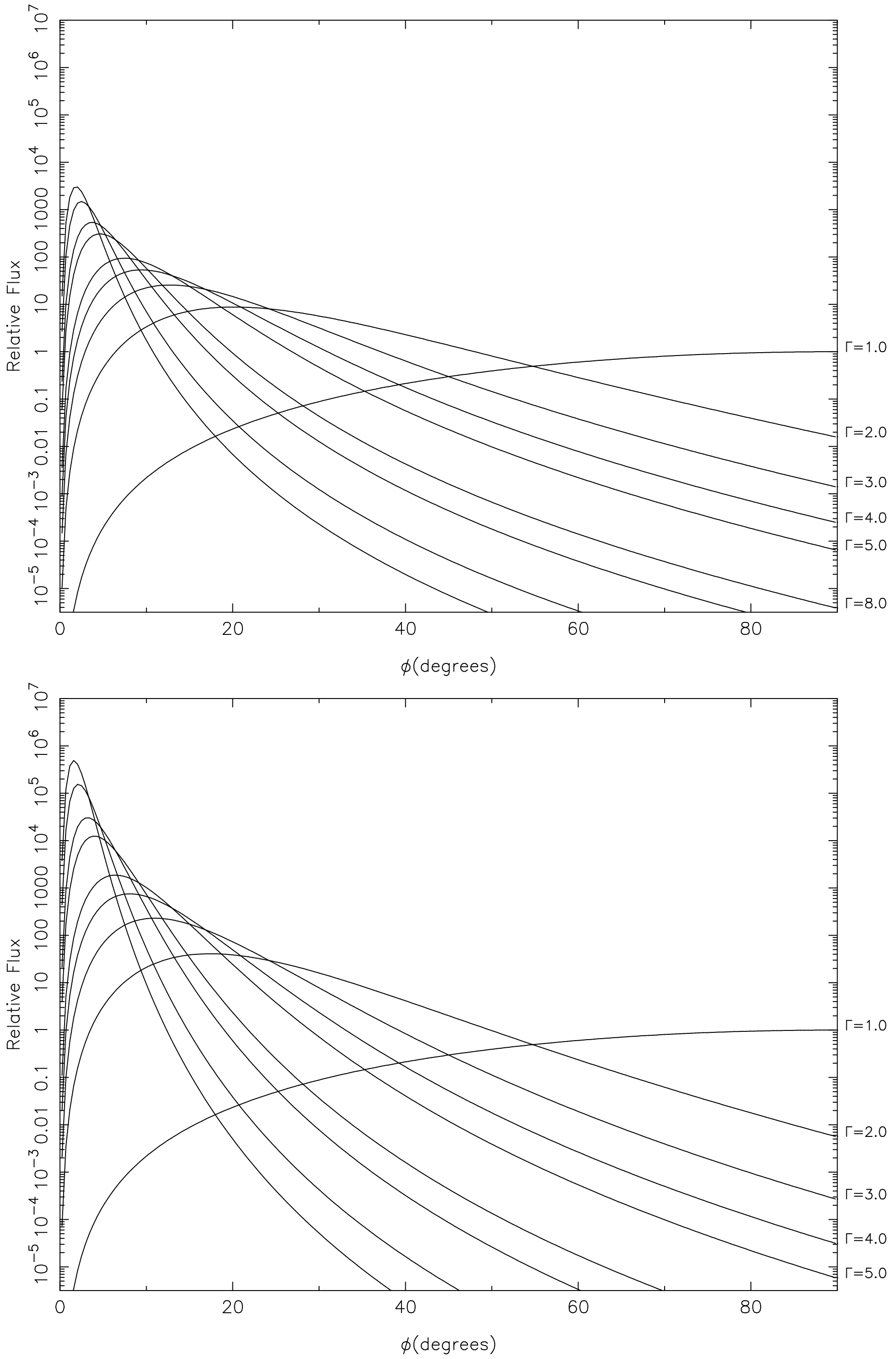

Figure 3.8: The effect of Doppler boosting combined with the angular dependence of the ordered field synchrotron emission (Section 3.3), for two different dependencies on δ: $\delta^{2.5}$ in the top plot and δ^4 in the bottom. The Γ values are the same as for Fig. 3.7. A value of $\Gamma = 1$ represents no Doppler boosting.

where p is either $2+\alpha$ or $3+\alpha$ depending on the nature of the source (see above).

Fig. 3.8 shows the angular dependence of the flux for various amounts of boosting, parametrised by the Lorentz factor Γ, for the same two cases of Fig. 3.7. The flux is normalised to the observed flux at an angle of 90°with no boosting (that is, with $\Gamma = 1$). As can be seen, when the angular dependence is considered by itself, the flux rapidly decreases for small ϕ. As more and more Doppler boosting is added, the flux at small angles increases, due to both the intensity enhancement and the angular aberration. The boosted flux approaches that of the isotropic emission case near the peak of the curve, but drops rapidly at low angles. Also noticeable is that the de-beaming effect is more pronounced for this case, so that most of the flux is observed in a small range of angles. As Γ increases, this angular range gets smaller, and moves to smaller ϕ values

3.6 Discussion

There are a number of key points to arise from this analysis. Firstly, consider the effect that the angular dependence of the synchrotron emission has on the observed flux. In the case of pure Doppler boosting (Fig. 3.7), the flux at small angles to the line of sight is boosted by factors of up to several orders of magnitude (depending on the bulk velocity, the spectral slope and the physical makeup of the jet). However, when this is combined with the angular dependence of synchrotron emission from an ordered magnetic field (Fig. 3.8), the observed flux at small angles decreases rapidly. The angles at which this occurs become smaller for larger values of the bulk velocity Γ. The flux at large angles is also reduced more, due to enhanced de-beaming.

Thus, for an ordered jet to be viewed at angles close to its direction of motion (assuming the magnetic field is parallel to that direction), a reasonably large bulk velocity (i.e. large Γ) is required. A jet with a low value of Γ will still have a significant decrease in flux at low values of ϕ due to the strong angular dependence of the emission.

Secondly, we note that jets, particularly those seen in double-lobed radio sources (i.e. such as those in FR IIs), are seen at large angles to the line of sight. At large angles, the Doppler beaming becomes, in effect, de-beaming, since the observed flux is reduced. This observation, then, puts a strong restriction on how large the values of Γ can be in the jet. For large enough Γ, the de-beaming will be sufficient to reduce the jet flux to levels too small to be observed. Also, this effect applies for both types of synchrotron emission (both tangled and ordered fields – in fact it is more pronounced for the ordered field case), and for all types of beaming (i.e. different dependences on δ).

Finally, since much of the work presented in this chapter has been concerned with synchrotron emission from an ordered magnetic field, is there any observational evidence that such emission will be important in astrophysical contexts? There are two particular observations that point to there being magnetic fields that are quite highly ordered in the jets of AGN.

The first of these observations is the measurement of high values of polarisation in both the radio and optical – parts of the M87 jet have $P \sim 40\% - 50\%$. Such high polarisations imply that the magnetic field is highly ordered. Further examples are the high optical and NIR polarisations measured from quasars ($P \sim 20\%$ – see Chapter 6). These measurements are made by integrating over the entire source, and so imply the existence of regions of highly ordered magnetic fields.

The second observation is that some jets, particularly those in the powerful FR II radio galaxies, are highly collimated. Collimation of a jet can be caused by either pressure from the ambient medium, or magnetohydrodynamic confinement. While the ambient medium is likely to be important for the weakly confined jets in FRI radio galaxies, it is unlikely that it can provide the necessary collimation seen in the thin jets in FR II sources. This collimation can most likely only be provided by highly structured magnetic fields that confine the jet to its thin, well collimated shape. Both this observation and that of high polarisation point to ordered magnetic fields being important in the jets of radio-loud AGN.

Chapter 4

Sources and Data

This chapter serves two purposes. Firstly, we introduce the Parkes Half-Jansky Flat-spectrum Sample, a catalogue comprising 323 radio-loud flat-spectrum objects first published by Drinkwater et al. (1997). This catalogue forms the basis for the modelling and analysis that will be done in this thesis. Secondly, we present the optical photometry that will be used in the actual modelling. This data has already been published (Francis, Whiting, and Webster 2000), but it is presented here also, together with additions and alterations specific to the modelling performed later in the thesis.

Additionally, a note for completeness: whenever names of sources from the sample are presented in this thesis, they are specified in the standard form HHMM±DDD, where "HHMM" is the right ascension of the source in hours and minutes, and "DDD" is the declination to the nearest tenth of a degree. Both right ascension and declination are in B1950 coordinates. In the literature, sources from the Parkes Catalogue (as all these sources are) have the prefix "PKS". For the purposes of brevity, however, this has been omitted from all the source names for the remainder of this thesis.

4.1 The Sample

During the 1960s and 1970s, the 64m radio telescope near Parkes in New South Wales surveyed the entire sky (as visible from the telescope) at 2.7 GHz, generating a catalogue that numbered nearly 11,000 sources. Many of these sources are AGN or quasars, and so this catalogue represents a huge resource of possible candidates for radio-selected quasars.

This was taken advantage of in the creation of the Parkes Half-Jansky Flat-Spectrum Sample (hereafter PHFS) (Drinkwater et al. 1997). This is a sample of bright radio sources, taken from the machine-readable version of the Parkes Catalogue (PKSCAT90, Wright and Otrupcek 1990), that have a flat radio spectrum based on the fluxes from the catalogue. The criteria for selection are:

Observed:	Fluxes at both 5.0 GHz and 2.7 GHz exist in the Parkes Catalogue (PKSCAT90).
Radio loud:	$S_{2.7\mathrm{GHz}} > 0.5\mathrm{Jy}$
Flat spectrum:	Radio spectral index $\alpha_{2.7/5.0} > -0.5$, where $S_\nu \propto \nu^\alpha$.
Position:	Galactic latitude: $\|b\| > 20°$
Position:	Declination (B1950.0): $-45° < \delta < +10°$

Note that the spectral index is derived from the 2.7 and 5 GHz fluxes from the catalogue. However, these fluxes were taken at different times – sometimes up to more than a year apart – and so, if the source in question had varied in flux between these observations, this spectral index will not be the true radio continuum slope of the quasar. More recent contemporaneous observations[1] using the Australia Telescope Compact Array, have shown that $\sim 10\%$ of the sources are incorrectly included in the PHFS (a greater number than predicted by Drinkwater et al. (1997)), as their true radio spectral index is steeper than -0.5. Additionally, a similar number will have been excluded for having an apparently steep index.

The Galactic latitude requirement was included to exclude those sources close to the Galactic plane, where increased optical extinction by dust, as well as the increased density of sources, would pose a problem in the identification and study of the optical counterparts of the sources. The declination limits were imposed purely to limit the size of the sample. These criteria resulted in a total of 323 sources.

The resulting sample of radio sources is quite heterogeneous. The sources included range from low redshift radio galaxies (including narrow-line radio galaxies and steep (radio) spectrum galaxies), through the spectrum of traditional quasars – both optically bright and optically faint – with a number

[1]These observations are currently ongoing, and have involved many people at the University of Melbourne.

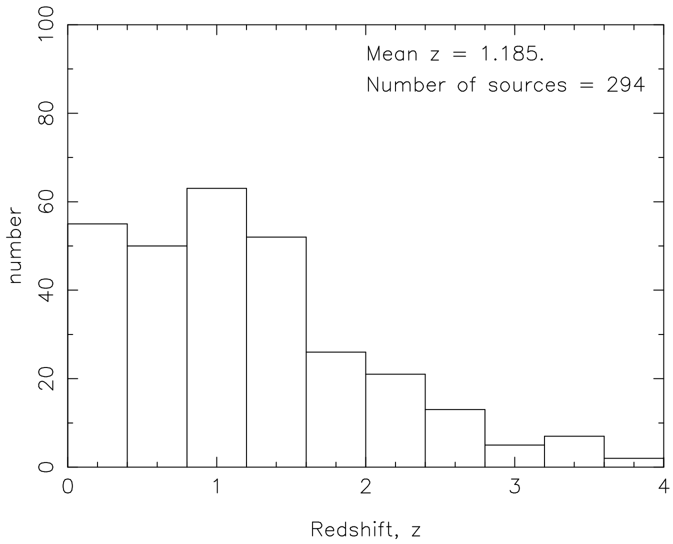

Figure 4.1: Distribution of redshifts for sources from the PHFS.

of BL Lac objects, up to some very high redshift quasars. The redshift distribution for those sources with measured redshift (a total of 294 sources out of 323) is shown in Fig. 4.1. The 29 sources that do not have a measured redshift generally fall into two distinct classes: BL Lac objects, with no measurable emission lines from which to deduce the redshift; or optically faint sources that are too faint to get a suitable spectrum from which to measure a redshift.

While the radio properties of the objects are all very similar (by virtue of the selection process), the optical properties vary considerably. The most obvious effect, first pointed out by Webster et al. (1995), is that there is a very large dispersion in their $B-K$ colours (that is, the ratio of flux in the K band (infrared: 2.2μm) to the B band (blue: 0.4μm)). This range, $2 < B-K < 8$, is much greater than that seen in typical optically-selected samples of quasars (for instance, the Large Bright Quasar Survey, or LBQS, has a range of $2 \lesssim B-K \lesssim 4$).

Webster et al. interpreted this range of optical-NIR colours as being due to the presence of large amounts of dust, that obscures the quasar at optical wavelengths. This had the implication that, if similar amounts of dust were present in radio-quiet quasars (as suggested by X-ray observations), then optical surveys of bright quasars may be missing up to 80% of quasars for a given intrinsic magnitude.

Serjeant and Rawlings (1996), however, suggested the alternative interpretation that the red optical colours are due to the presence of a red, optical synchrotron component. This component would likely be an extension of the beamed radio emission. This idea will be tested by the modelling in Chapter 5.

Finally, we note that a further alternative explanation was offered by Benn et al. (1998). They investigated a sample of radio-selected quasars (the B3-VLA quasar sample, Vigotti et al. (1997)), and found that many of them exhibited an excess of light in the K band. They argued that this light mostly came from star-light from the host galaxy. The B3 sample is dominated by steep radio-spectrum sources, and, according to unified schemes, the central AGN source should be subject to more obscuration than for flat-spectrum sources, making it easier to detect the galactic emission. This explanation, however, was tested by Masci et al. (1998), and rejected as an explanation for the spread in optical colours of the PHFS sources.

4.2 Observational data

To attempt to solve the puzzle of the red optical-NIR colours, it was decided to make observations of the PHFS quasars at seven wave-bands, covering the optical and NIR wavelength ranges: B ($\lambda \sim 0.44\mu$m), V ($\lambda \sim 0.55\mu$m), R ($\lambda \sim 0.7\mu$m), I ($\lambda \sim 0.88\mu$m), J ($\lambda \sim 1.24\mu$m), H ($\lambda \sim 1.65\mu$m), and K ($\lambda \sim 2.19\mu$m). Having this many data points in the optical and NIR range of the spectrum makes it far easier to accurately model the spectral energy distributions (SEDs) of the Parkes quasars, and hopefully determine the nature of the reddening mechanism. The results of these observations have been published by Francis et al. (2000). However the method and results of observations are discussed here, as well as the choice of data that is used in this thesis.

4.3 The new observations

Over the course of 26 nights in 1997, a total of 157 sources from the PHFS were observed, using the Australian National University's 1 metre[2] and 2.3

[2] Or, as it is traditionally known, the "40 inch".

metre telescopes. The optical observations were made using either the 1m or the imager on the 2.3m telescope, while the NIR observations were made with the *CASPIR* 256×256 InSb array camera (McGregor et al. 1994) on the 2.3m telescope. The methods of the observations and data reduction are explained in detail in Francis et al. (2000), so they will not be repeated here.

To minimise the effects of variability, the optical and NIR observations for each object were made as close as possible in time to each other (the largest spread in time for a single object was six nights, and most sources had a spread much shorter than this).

It should be noted that variability has been seen on timescales less than this. So-called "intra-day variability" (IDV) has been commonly seen at radio frequencies in many radio loud quasars, including many of the objects observed here (see, for example Kedziora-Chudczer (1998), or the review of IDV properties by Wagner and Witzel (1995)). Such variability has also been seen at optical and NIR wavelengths (Heidt and Wagner 1996; Romero, Cellone, and Combi 1999), mainly in sources such as BL Lac objects and flat-spectrum radio quasars (i.e. the sort of object found in the PHFS). While the radio variations could be due to scintillation of an intrinsically small source by the interstellar medium, this cannot explain the variability at infrared and optical frequencies. Instead, these variations are thought to be due to relativistic shocks propagating down jets, or the interactions of these shocks with features in the jets. This model is preferred to one where the variations are due to flares or hot spots on the accretion disk, primarily because of the low incidence of optical intra-day variability seen in radio-quiet quasars (which either have very weak jets or are without them) (Jang and Miller 1997; Romero et al. 1999). However, see Chapter 8 for a result that challenges this. Amplitudes of this variation can be up to 0.1 magnitudes over the course of one night.

For the purposes of modelling and plotting the data, the magnitudes need to be converted into fluxes. The assumed fluxes for objects of zero magnitude are listed in Table 4.1. In the optical, the filter sets used approximate the Johnson & Cousins system (the calibration was done using Graham standards, which also approximate this system), and the zero magnitude fluxes are taken from Bessell, Castelli, and Plez (1998). The NIR observations were made using the *CASPIR* filter set, calibrated with *IRIS* standards, and the

Band	Mean λ (μm)	Zero magnitude flux (F_λ, W m^{-2} μm^{-1})
B	0.440	6.32×10^{-8}
V	0.550	3.63×10^{-8}
R	0.700	2.18×10^{-8}
I	0.880	1.13×10^{-8}
J	1.239	3.11×10^{-9}
H	1.649	1.15×10^{-9}
K	2.192	4.10×10^{-10}

Table 4.1: Assumed fluxes of a star with zero magnitude, for each of the wave-bands used.

zero magnitude fluxes used are those calculated by P. McGregor[3] assuming that the star Vega is well represented in the NIR by a black body of temperature 11200 K and normalisation $F_\lambda(555\text{nm}) = 3.44 \times 10^{-12}$ W cm^{-2} μm^{-1} (Bersanelli, Bouchet, and Falomo 1991). The observations were made with the *CASPIR* K_n filter, but were calibrated using the K magnitudes of the *IRIS* system without a colour correction term applied. They have thus been normalised using a K-band zero point (Table 4.1).

4.4 Photometry

The photometry confirms the result presented in Webster et al. (1995), namely that there is a large spread in $B-K$ colours in the PHFS quasars. This distribution is shown in Fig. 4.2, along with the distribution of colours for a small representative sample of quasars from the LBQS. As can be clearly seen, the PHFS distribution is much broader and contains many quite red objects. Also note that the lower envelope of the PHFS distribution is approximately the same as that of the LBQS quasars – i.e. there are not really any sources in the PHFS that are significantly bluer than the optically selected quasars. (The one outlying source in Fig. 4.2 is 0232−042, which has a very blue SED: $B-K=1.45$.)

In Fig. 4.3 is plotted a histogram of the absolute magnitudes of the PHFS sources with simultaneous photometry. The absolute magnitude is

[3]CASPIR manual, Mount Stromlo & Siding Spring Observatories, Australian National University. http://msowww.anu.edu.au/observing/teldocs/2.3m/CASPIR/

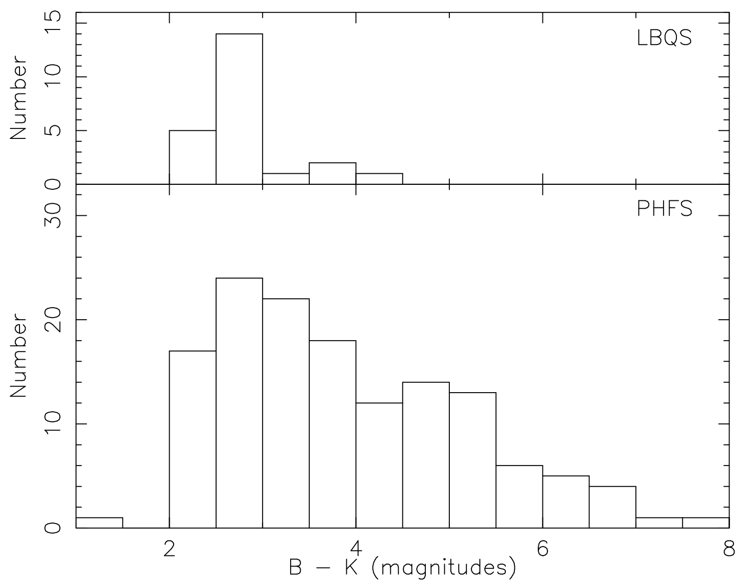

Figure 4.2: Distribution of $B-K$ colours for the PHFS sources with quasi-simultaneous photometry. The top panel shows a small representative sample of sources from the LBQS – the photometry is taken from Francis (1996) and Francis et al. (2000).

calculated by

$$M_V = m_V - 5\log_{10}(d_L) + 2.5(1+\alpha)\log_{10}(1+z) - 25 \qquad (4.1)$$

where m_V is the apparent V magnitude, d_L is the luminosity distance, in Mpc, to redshift z, and α is the spectral index ($F_\nu \propto \nu^\alpha$). In calculating M_V, we used the best-fit spectral index to the optical photometry (that is, B, V, R, and I magnitudes). The term $K(z) = -2.5(1+\alpha)\log_{10}(1+z)$ is the K-correction term (Peterson 1997).

One can use the absolute magnitude to discriminate between sources of quasar and Seyfert luminosity. The dividing line is traditionally given by

$$M_V = -21.5 + 5\log_{10} h \qquad (4.2)$$

where $H_0 = 100h$ km s^{-1} Mpc^{-1}. As can be seen in Fig. 4.3, there are 16 sources in this sub-sample of the PHFS that are of Seyfert luminosity. These sources are either low-redshift galaxies, or optically faint sources (that are not necessarily at a low redshift). We note that the distribution from quasar to Seyfert luminosities is continuous, demonstrating that the division

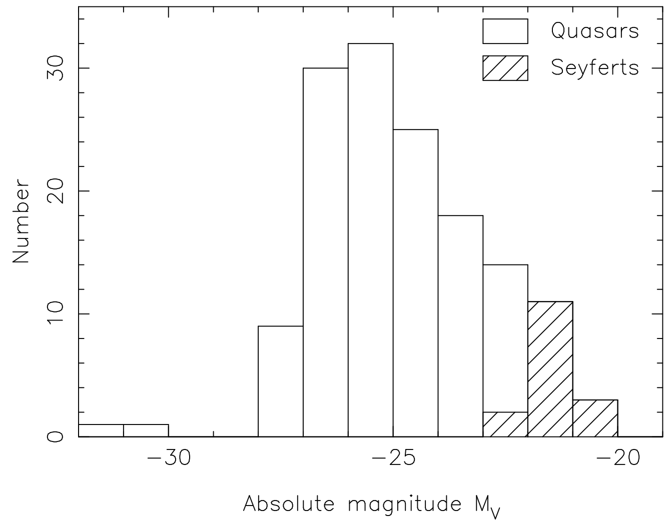

Figure 4.3: The distribution of absolute magnitudes for sources in the PHFS with quasi-simultaneous photometry. In calculating M_V, we used $H_0 = 75$ km s^{-1} Mpc^{-1} and $q_0 = 0.5$, and the spectral index α was calculated from the optical photometry. The open histogram shows those sources of quasar luminosity, while the hatched histogram shows those with Seyfert luminosity (see text for definition).

between the two classes is largely an arbitrary one (although we also note that even the low-redshift sources here are not true Seyferts, due to their strong radio emission – Seyfert galaxies are not generally radio-loud objects).

4.5 Errors

When the observational data was published (Francis et al. 2000), the quoted error for each object was the sum (in quadrature) of random errors (determined from the root-mean-squared pixel-to-pixel variation in the sky regions) and an assumed 5% systematic error in the photometric zero points (determined from the scatter in the zero points from different standard star measurements over the course of a night). The rms scatter in the zero points was typically $\leq 3\%$, so a somewhat conservative value of 5% was adopted as the systematic value.

However, for the purposes of the modelling to be done in this thesis, there are a number of potential systematic errors not considered in Francis et al. (2000) that may be important. These include:

① The optical zero magnitude fluxes (Bessell et al. 1998) were derived for an A0 star, and so will be slightly incorrect for a quasar spectrum. This has the effect of introducing small colour terms into the photometry, the size of which will depend on the spectral index of the object being observed. A similar effect will of course be present in the NIR. Bersanelli et al. (1991) found that spectral shape differences could produce systematic errors of at least a few percent in the NIR flux.

② The zero point fluxes in the optical and the NIR are taken from different references (see above). These different zero points may not be exactly equivalent, which will produce small offsets between the optical and NIR parts of the SED.

③ If the sky conditions at Siding Spring Observatory were not completely photometric for all observations for a given source (particularly if the transparency changed between different bands), then the measured photometry will have small band-to-band errors present.

④ The observations for each source were taken quasi-simultaneously (indicating all observations were made within at most a six-day period), to minimise the effects of variability. However, as discussed above, a number of the sources in the PHFS have been found to exhibit intraday variability in the optical (Heidt and Wagner 1996; Romero et al. 1999), and a larger number no doubt have similar properties to these. Therefore, variability on timescales of the order of those separating our observations is likely for some of the sources. Such variability can be up to 0.1 mag over the period of a night.

A possible example of a source that has undergone variability between the two sets of observations is the BL Lac 0537−441. This source has been shown to be quite variable on very short timescales (amplitudes of $\sim$ 0.3 mag on timescales of 2 days were seen by Romero et al. (2000)). Its SED is shown in Fig. 4.4, where it appears as if the NIR emission (which was observed after the optical) has been boosted – note that the slope of the NIR is approximately that of the optical (excluding the B band point), but with a different normalisation. This difference corresponds to a variation of $\sim$ 0.5 mag over the course of 4–5 nights. For further examples (although not as extreme) of such

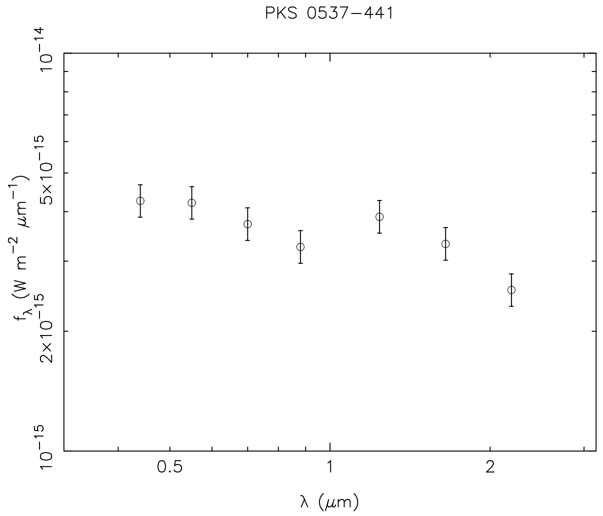

Figure 4.4: The SED of the BL Lac object 0537−441. Note that the three NIR points appear to be displaced upwards from the extrapolation of the optical points. Error bars are 1σ.

"micro-variability", see Chapter 8.

⑤ Finally, the presence of strong emission lines in the quasars' spectra could boost the flux of a band above the level of the continuum. The amount of this effect is investigated for a small number of objects in Section 5.9.

To account for all these extra effects, which will be present in all the objects in different amounts, we have increased the systematic error from 5% to 10%, while leaving the random error the same. These updated errors are shown in the tables of photometry (Tables B.1 & B.2).

4.6 Sources used

For the purposes of the modelling done in this thesis, not all of the sources that were observed will be used. The sources that are not are excluded for a number of reasons.

Firstly, we have excluded those sources that were not observed or detected in at least six bands. The reasoning behind this was to make sure that there were more points than free parameters in the model fitting (i.e. that the number of degrees of freedom in the fitting is significantly more

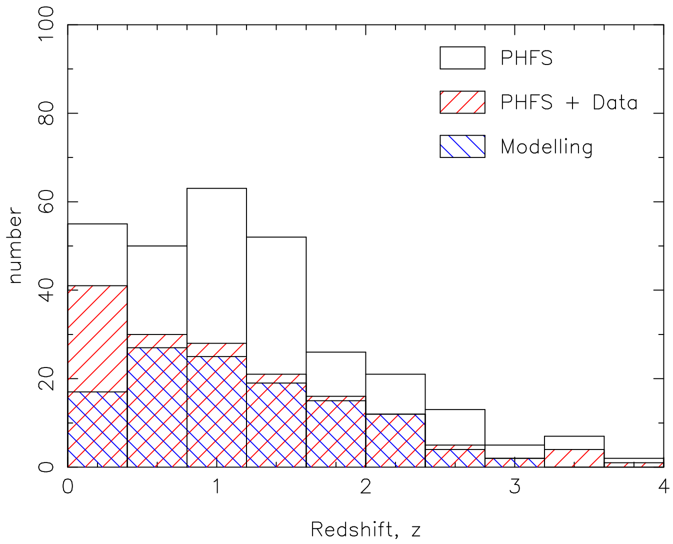

Figure 4.5: Redshift distribution, showing sources with photometry ("PHFS + Data") and those sources selected for modelling ("Modelling") (see text for criteria). The entire PHFS sample is shown for comparison ("PHFS").

than zero).

Secondly, sources without a measured redshift were excluded. The redshift is needed to accurately obtain the observed shape of the model (in particular those parts that are not a power law). Also, it is preferable to be able to use rest-frame quantities (such as wavelength), as these are intrinsic to the source and not dependent on the observer. One source that had an unknown redshift in Drinkwater et al. (1997), PKS 0829+046, has a published redshift of $z = 0.18$ (Falomo 1991) (found by fitting to the host galaxy emission), which is used herein.

Finally, also excluded from the main analysis were those sources with prominent additional spectral components. One class of these objects were the low-redshift galaxies, which show a prominent 4000Å break between the B and V bands. These sources show strong evidence for significant flux from the underlying galaxy in their spectra (Masci, Webster, and Francis 1998), and thus would need an additional galaxian component to be modelled accurately – this is beyond the scope of this thesis. The other class of sources to be excluded were the high-redshift (i.e. $z > 3$) quasars. These sources have strong Lyα breaks present between the B and V bands.

Once all these exclusions were made, the number of sources decreased from 157 to 117. For completeness, the redshift distribution of the selected sources, compared to that of the PHFS as a whole, and the sources with any optical/NIR photometry from Francis et al. (2000), is shown in Fig. 4.5. Note the large number of sources with small redshift that have been excluded (due to the criterion for removing galaxy-dominated sources). The only source with $z < 0.1$ is the BL Lac 1514−241 ($z = 0.0486$) – this source is dominated by its smooth continuum, so that no 4000Å break from the host galaxy is visible. The next highest redshift source is 0829+046 at $z = 0.18$. The photometry is listed in Table B.1, with the new errors, while the photometry for the excluded sources is listed in Table B.2, together with the reason for each source's exclusion.

Chapter 5

Model fitting

The photometry described in the preceding chapter is an impressive dataset, in both the breadth and density of its coverage of the optical/NIR spectrum. This, coupled with its quasi-simultaneous nature, makes it an excellent resource for modelling the optical emission of the PHFS quasars. In this chapter we will endeavour to construct physical models for the optical emission that are consistent with the data. Much of the analysis and results presented in this chapter is presented in a paper (Whiting, Webster, and Francis 2001) that is currently in press.

5.1 Power law fitting

In searching for physical models, it is usually best to start with the simplest models and work up in complexity. One of the simplest models to fit to data is that of a power law. Francis et al. (2000) found that about 90% of the PHFS have approximately power law SEDs. We first wish to test this more rigorously. As a starting point, we choose to fit (naively) a simple power law, with an unconstrained spectral index. This will separate out the sources that have power law SEDs from those that show some curvature in their spectrum.

This power law can be parametrised as $f_{PL}(\lambda) = c\lambda^{\alpha}$, with the normalisation c and the spectral index α free parameters (which will be fit to the data). Note that this model implies $f_\nu \propto \nu^{-2-\alpha}$, but we will be working in terms of λ and f_λ.

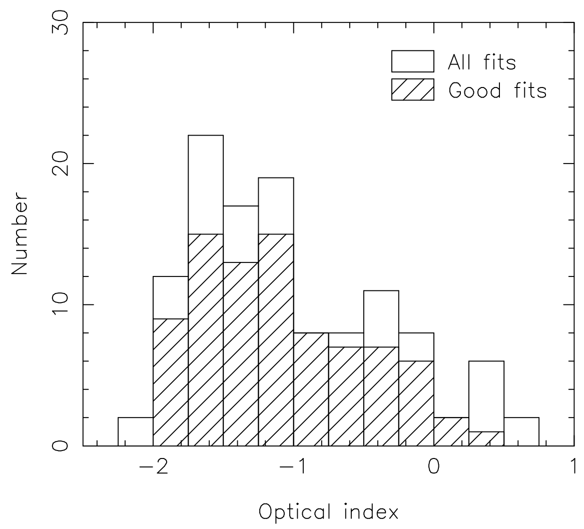

Figure 5.1: Histogram of fitted power law indices. Hatched histogram indicates good fits, while open histogram indicates all fits.

5.1.1 Fits to data

To fit this model, the magnitudes in Table B.1 were converted into fluxes according to the zero-magnitude fluxes listed in Table 4.1. This model is fit to these fluxes using a least-squares method. This generates a χ^2 value:

$$\chi^2 = \sum_{i=1}^{7} \frac{(y_i - f_{PL}(\lambda_i))^2}{\sigma_i^2}, \tag{5.1}$$

which indicates the goodness of fit. A fit to a source will be deemed to be "good" when the value of χ^2 is less than the cut-off value corresponding to the 99% confidence level of the χ^2 distribution. For a source with 5 degrees of freedom (as is the case for most sources with this power law model), this cutoff level is 15.09. (Note that increasing the value of this cutoff is equivalent to increasing the confidence level – for example, the 99.5% cutoff is 16.75 for 5 degrees of freedom.) If the χ^2 value is greater than this cutoff level, then the null hypothesis that the power law model fits the data is rejected.

When this power law model is fitted to the data, we find that 83 sources (or 71% of the total) have good fits. The distribution of resulting power law indices, both for the good fits and for all sources, is shown in Fig. 5.1.

The spectral indices of these good fits span a wide range of values. At one extreme there are the sources with relatively blue SEDs ($\alpha \lesssim -1.4$). These sources are characterised by their blue continuum, the presence of moderate to strong emission lines, and generally low X-ray flux (most were not detected by *ROSAT* (Siebert et al. 1998)).

At the other extreme are the sources with redder SEDs (that is, flatter in f_λ), with $-1 \lesssim \alpha \lesssim 0$. These sources are blazar type objects, with high optical polarisation (Wills et al. 1992) – see Section 6.3 – as well as relatively weak (or even absent) emission lines – in fact, all the BL Lac objects in our sample are in this region of the power law index distribution.

5.1.2 Interpretation of power laws

So, we have fit a power law to a large majority of the sources in our sample, spanning a wide range of spectral indices. Are the physical processes that generate this power law the same for all sources? That is, does the power law in the blue sources have the same origin as that in the red sources?

The first class of sources – the blue sources – are being fit by a blue power law, which has similar colours to the blue power law emission seen in optically-selected quasars (Francis 1996). This is likely to be the optical part of the continuum emission from the accretion disk (often termed the big blue bump).

However, the power law being fit to the redder sources is most likely of different origin to that seen in the blue sources. These objects exhibit characteristics commonly associated with optical synchrotron emission (such as high optical polarisation and lack of prominent emission lines), and so we postulate that this emission is, at least in part, some form of synchrotron emission. The slope of the power law can then be used to determine p, the power law index of the electron energy distribution (i.e. defined such that $N(E) \propto E^{-p}$: see Chapter 3). Using the values shown in Fig. 5.1, we obtain $2 < p < 6$ (using $-1.5 < \alpha < 0.5$ and $p = 2\alpha + 5$).

If synchrotron emission is present in the spectra of at least some of these quasars, then this raises the question "Is the synchrotron component best modelled by this power law?" The synchrotron component will be present in one of two forms, as discussed in Chapter 3: a power law caused by an unbroken (power law) electron energy distribution, or a turning-over component caused by a break or a cut-off in the electron energy distribution.

(Note that the power law can also be produced by a synchrotron spectrum turning over at higher frequencies than those observed.)

Both of these forms can be tested. The power law model must produce power law indices that are consistent with slopes of plausible energy distributions. The presence or otherwise of a turnover can be evaluated by examining the sharpest possible turnover (caused by an abrupt cut-off in the energy distribution at some maximum energy). This will provide the maximum contrast with the power law, and is consistent with modeling done by other authors (for example, Meisenheimer et al. 1996).

Many of the sources, while they have power law fits that can not be rejected at the 99% confidence level, show evidence for curvature in their SEDs. This curvature can be 'n'-shaped (higher in the middle than at either end), 'u'-shaped (lower in the middle) or perhaps take the form of an inflection (e.g. the flux decreases, levels off and possibly decreases again). (See Fig. 5.3 for illustrations of the different types.) Most of the sources classed as BL Lac objects are 'n'-shaped, and so we postulate that these sources are dominated by a synchrotron component that is turning over in the optical.

Other sources, however, are bluer in the optical than in the NIR (i.e. show an inflection, without the turn-up seen in 'u'-shaped sources). This is a possible indication of the presence of excess emission in the NIR, in addition to a blue power law. We propose that this excess emission is due to a synchrotron component that has turned over in the NIR, and so does not dominate in the optical, where the dominant emission is instead a blue power law similar to that observed in the bluest sources.

5.2 Physical models

In response to this phenomenological classification, we next propose the following two-component physical model: one component is a blue power law, representing continuum emission from the accretion disk region; and the second is synchrotron emission, representing emission from the relativistic jet (that is known to be present due to the flat-spectrum radio emission seen in these objects).

5.2.1 Accretion disk emission

We have found, from the simple power law fitting, that the bluest sources have power law continua. The slopes of these power laws are consistent with them being the same component as that seen in optically-selected quasars, commonly termed the "Big Blue Bump" (BBB). This component, then, is taken to represent the underlying quasar continuum in the UV-optical part of the rest-frame spectrum – that is, the "un-reddened" quasar continuum.

Over the wavelength range of our observations, the BBB is modelled as a simple power law, $f_\lambda \propto \lambda^{\alpha_B}$ or $f_\nu \propto \nu^{-2-\alpha_B}$. Francis (1996) found the median slope for a subsample of quasars from the Large Bright Quasar Survey (LBQS), taken from optical/NIR photometry, was $f_\nu \propto \nu^{-0.35\pm0.3}$, and noted that the observations were consistent with an intrinsic continuum slope of $f_\nu \propto \nu^{-0.3}$ that is reddened by various amounts of dust. We therefore take the value of α_B to be -1.7. The effects of allowing the value of α_B to vary are considered in Section 5.7.

5.2.2 Synchrotron emission

Rationale

All the PHFS sources are radio-loud flat-spectrum sources, and thus very likely have relativistic jets that emit synchrotron radiation, at least at radio frequencies. Could this synchrotron emission extend up to the optical/NIR part of the spectrum? Our power law fitting from the previous section provides circumstantial evidence for this: the redder sources in the optical tend to be the ones with higher polarisation (a good sign of synchrotron emission) and less prominent emission lines (possibly a sign that the emission lines are being swamped by the presence of a synchrotron component).

As discussed above, the synchrotron spectrum could take the form of either a power law, from a power law distribution of electron energies, or a power law with a break or turn-over, due to an electron energy distribution that exhibits a break or even a cut-off. These types of spectra are discussed in Chapter 3. The latter type of spectrum is seen in optical synchrotron jets (see Section 2.2.1 and references therein), where the optical spectrum is like $\nu^{-1.2}$–$\nu^{-3.0}$, compared to a radio–optical spectrum of $\nu^{-0.6}$–$\nu^{-1.0}$.

Additionally, a synchrotron spectrum that has a turn-over will, when combined with the blue power law, be able to reproduce an inflection-like

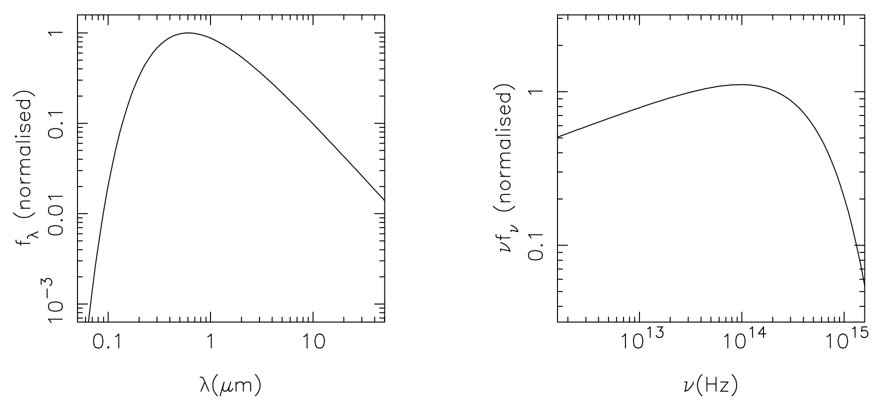

Figure 5.2: The synchrotron model used in the analysis, in both f_λ and νf_ν units. Both plots have been normalised so that the peak flux in f_λ is 1. Note that the vertical scale is different in the two plots.

SED, which is seen in a number of the PHFS sources. Also, such a spectrum, particularly in the region of the turn-over, will be quite red, and will thus be able to account for the red colours of many of the SEDs.

Analytic modelling

We consider here synchrotron emission from a population of electrons with an energy distribution that has the form of a power law up to some maximum energy and zero beyond this (i.e. an energy spectrum with an abrupt cutoff, as modelled in Section 3.3). This can be expressed as a distribution of the Lorentz factor γ of the radiating electrons:

$$N(\gamma)\ \mathrm{d}\gamma = \begin{cases} \kappa\gamma^{-p}\ \mathrm{d}\gamma & 1 \le \gamma \le \gamma_+ \\ 0 & \gamma > \gamma_+ \end{cases}$$

This is consistent with modelling done by Meisenheimer et al. (1996) on the jet of M87. They found that the overall synchrotron spectrum of the brightest parts of the jet was best described by a spectrum that had a sharp cutoff at $\nu_c \approx 10^{15}\,\mathrm{H}z$, and modelled this with an energy distribution of the form of a straight power law $N(\gamma) \propto \gamma^{-2.31}$, with a rather abrupt high energy cutoff. We consider the effect of using a power law synchrotron spectrum without a cutoff in Section 5.5.

Such a synchrotron spectrum is straightforward to model analytically.

We use the synchrotron model from Section 3.2, for the case of a disordered field. This model is somewhat more general than the ordered field model, and the wavelength dependence of the two are the same. The single particle luminosity for a radiating electron is given by

$$L_{1\mathrm{p}}(\omega) = \frac{\sqrt{3}e^3 B \sin\theta}{8\pi^2\epsilon_0 c m_e} F(x)$$

where $\omega = 2\pi\nu$ is the angular frequency, and $F(x)$ is given by Eqn. 3.6. Since we are interested in the luminosity of a population of particles, so we need to integrate $L_{1\mathrm{p}}(\omega)$ over suitable distributions of energies and pitch angles. The energy distribution is that given above, while the pitch angle distribution that we use is an isotropic one, where the probability distribution is $p(\theta)\mathrm{d}\theta = \frac{1}{2}\sin\theta\,\mathrm{d}\theta$. Thus, the integrated luminosity from such a population is

$$L(\omega) = \frac{\sqrt{3}e^3 B\kappa}{16\pi^2\epsilon_0 c m_e} \int_0^\pi \sin^2\theta \left(\int_1^{\gamma_+} \gamma^{-p} F(x)\ \mathrm{d}\gamma \right) \mathrm{d}\theta$$

An example of such a spectrum is shown in Fig. 5.2, for $\gamma_+ = 10^6$ and $B = 10^{-8}\mathrm{T} = 10^{-4}\mathrm{G}$ (the value of κ has been taken to be 1). The peak frequency ν_c depends on these two values, and can be shown by simple arguments (Blandford 1990) to be approximated by $\nu_c \sim \gamma_+^2 B$ MHz (where B is measured in Gauss).

The slope of the power law tail (at frequencies $\nu \ll \nu_c$) is related to the energy power law index by $\alpha_S = (p-5)/2$ (where $f \propto \lambda^{\alpha_S}$). The energy distribution for the spectrum in Fig. 5.2 is taken to be $N(\gamma) \propto \gamma^{-2.5}$ (i.e. $p = 2.5$), giving a power law of $f_\lambda \propto \lambda^{-1.25}$.

We consider here a range of p values from $p = 2.0$ to $p = 3.0$, which gives a range of long-wavelength power law slopes of $\alpha_S = -1.5$ to $\alpha_S = -1.0$. This range covers the distribution of radio-to-optical slopes for the PHFS sources (this distribution can be seen in Fig. 7.7c), as well as the distribution of radio-to-optical slopes observed in optical synchrotron jets (i.e. $\nu^{-0.5}$ to $\nu^{-1.0}$: see Table 2.2 or Scarpa and Urry (2001)). Allowing p to vary does not significantly alter the results of our analysis – see Section 5.7 for further discussion.

We also note here that a value of $p > 3$ means that the νf_ν flux will increase towards longer wavelengths (since $f_\nu \propto \nu^{-(p-1)/2}$ and so $\nu f_\nu \propto \nu^{-(p-3)/2}$) and this results in the radio flux being severely overestimated by the fitted synchrotron component, since observationally the radio emission always has a lower νf_ν flux than the optical. This assumes that the same synchrotron component is responsible for both the optical and radio emission, which is an assumption commonly made, particularly for the modelling of optical synchrotron jets (Meisenheimer et al. 1996).

5.3 Fitting technique

These two components (the blue power law and the synchrotron component) are combined linearly to form a model $f_C(\lambda) = a\lambda^{-1.7} + bf_{synch}(\lambda)$ that is fit to the data in the same way as the power law model (that is, minimising the χ^2 value as given by Eqn. 5.1). The reduced χ^2 value (that is, χ^2/ν) for each of the two models (combined and power law) are compared, and the model with the lowest χ^2/ν is chosen to be the best fit model. Here, ν is the number of degrees of freedom. This is defined as the number of data points minus the number of parameters in the fit.

In fitting the combined model, the location of the peak wavelength of the synchrotron spectrum, λ_p, was allowed to vary. This variation was allowed to occur over a range of rest frame wavelengths, such that the curvature of the spectrum caused by the turn-over affected the synchrotron flux in the region of the data points (in other words, we did not want to just be fitting the power law part of the synchrotron spectrum). Quantitatively, the minimum peak wavelength was taken to be half a decade shorter than the B band (0.44μm) shifted to the rest frame, and then 20 λ_p values per decade (evenly spaced in $\log_{10} \lambda_p$) were considered, up to a maximum peak of 10μm. For each of these synchrotron functions, a best fit to the data was found, and then the best of these was chosen, giving the best fit λ_p value for that source.

A selection of fits are shown in Fig. 5.3, for sources best fit by a range of both power law and combined models. Fits for all the sources are shown in Appendix D.

5.4 Results

This section discusses the results and implications of the fitting, from the point of view of the different parameters and variables.

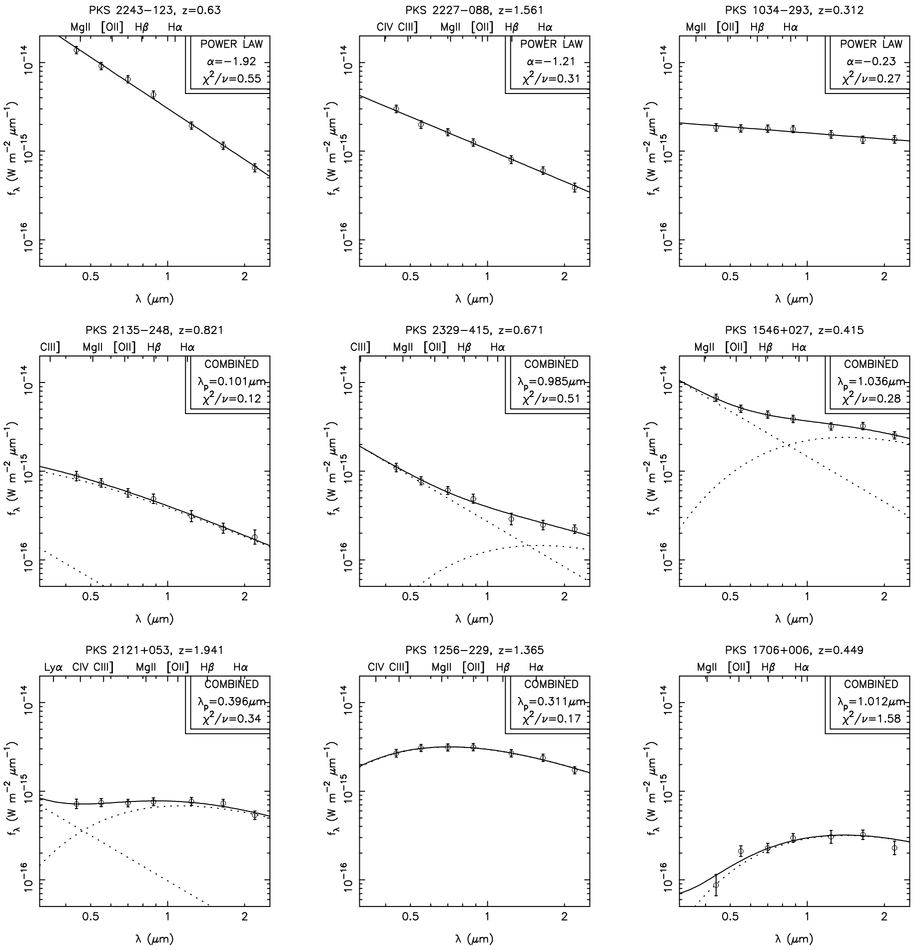

Figure 5.3: Examples of the various types of photometry, and the fits to them. The horizontal axis on each plot is wavelength, in μm, and the vertical axis is f_λ in $\mathrm{Wm}^{-2}\mu\mathrm{m}^{-1}$. Error bars on the fluxes are 1σ. The locations of notable emission lines are shown, based on the redshift of each quasar. For the combined fits, the individual components – the power law ($\alpha_B = -1.7$) and the synchrotron component ($p = 2.5$) – are shown as dotted lines. The λ_p value, where given, is for the quasar rest frame. See Appendix D for the complete set of sources and their fits.

5.4.1 χ^2/ν distributions

The combined model was fit to the data in the method detailed above, and the fits were compared to those of the power law model. The best fitting model (based on the χ^2/ν values) was chosen for each source. For the "default" values of the model parameters ($p = 2.5$ and $\alpha_B = -1.7$), we find that 93 sources (or 79% of the total) are well fit by one of the models. Of these, 48 are best fit by the power law model, and 45 by the combined model. The results for each source are summarised in Table C.1, which gives, for those sources with good fits, the χ^2/ν values for each models, as well as the power law index, synchrotron peak wavelength (λ_p) and the ratio of synchrotron to total flux at a rest-frame wavelength of 0.5μm.

The first result to look at is the distribution of χ^2/ν values, as this will give a good indication of how good the fits are for each model, and how the two models compare to each other. Fig. 5.4 shows the distributions of χ^2/ν values for all sources, divided on the basis of which model fit each source best. It also shows the distribution of best-fit χ^2/ν values for all sources. As can be seen, the distribution for the sources best fit by the combined model is noticeably broader than that for the power law sources, with more sources having very low χ^2 values.

To directly compare the two models, one can plot, for each source, the fitted χ^2/ν from each model against one another. This is done in Fig. 5.5, where the resulting best fit is indicated by the symbol used. The colour of the point indicates the power law index from the power law model fit. Two points can be drawn from this plot. Firstly, those sources best fit by the combined model tend to be a long way from the line of equality – that is, when the combined model is fit best, it is generally much better than the power law model. These are the sources that exhibit significant curvature in their SEDs. Secondly, the bluer sources tend to be best fit by the power law model, while the intermediate and redder sources are more likely to be best fit by the combined model. We note that the power law model has one more degree of freedom than the combined model, and so a source with equal χ^2 for both models will give a slightly lower χ^2/ν for the power law model.

So, one can see that the blue sources are most likely to be best fit by the power law, but not by a big margin, indicating that the two models give very similar fits. This indicates that the assumption of the presence of a power law in the combined model is accurate, as it is this power law that

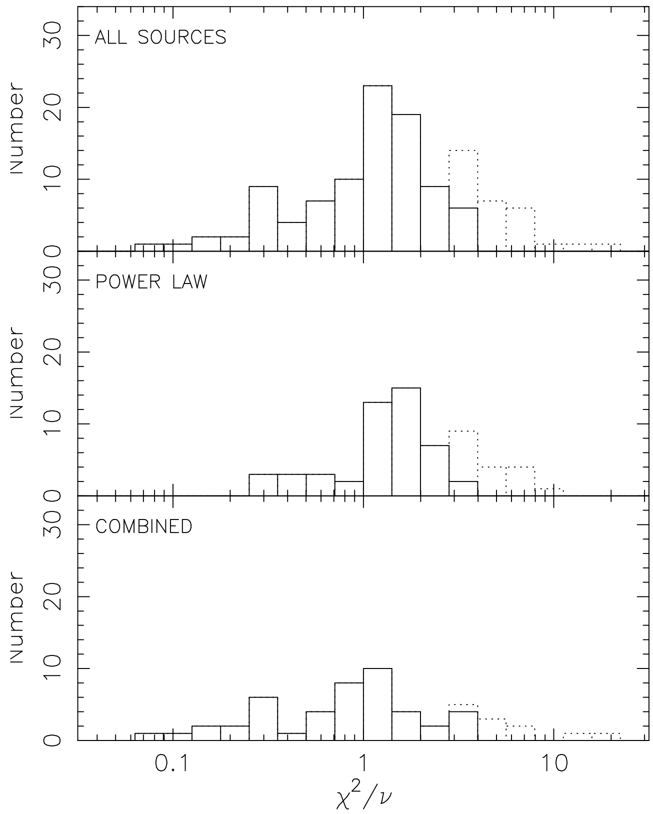

Figure 5.4: Histograms of the reduced χ^2 values, for all sources and for each of the best-fit models. The dotted histogram shows those sources whose fits are rejected at the 99% confidence level.

means the combined fits are close to the power law fits (which in turn means that the points are close to the line of equality on Fig. 5.5).

5.4.2 Synchrotron components

The properties of the synchrotron components that are fitted as part of the combined model are of particular interest. As can be seen in Fig 5.6, the peak wavelengths are restricted to a relatively narrow range of values (approximately a decade in wavelength). However, this is likely to be largely a reflection of the distribution of the wavelengths of the photometric points.

The strength of the fitted synchrotron component varies considerably from source to source. In Fig. 5.7, the ratio of the synchrotron and power law components at a rest-frame wavelength of 0.5μm is shown for all sources best fit by the combined model. The main bulk of this distribution spans nearly

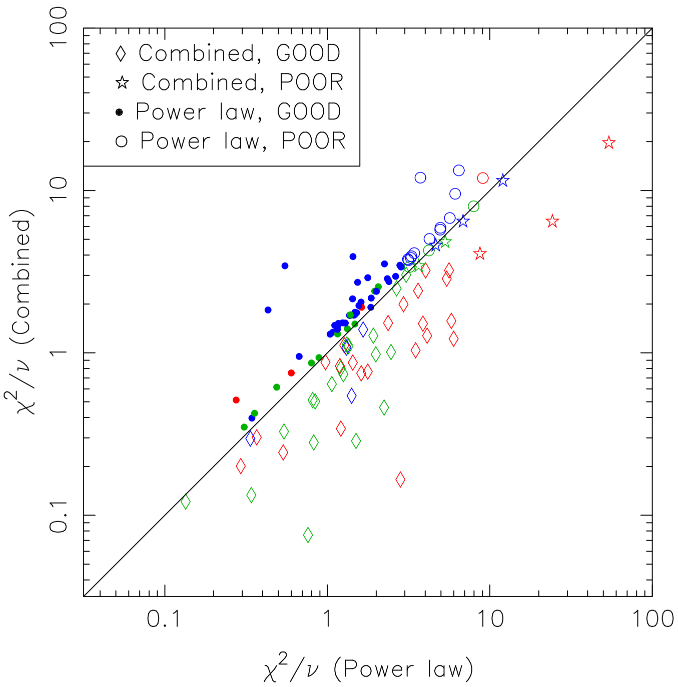

Figure 5.5: Comparison of the χ^2/ν values for the power law model and the combined model. The symbols indicate which source fits best, and whether that fit is accepted at the 99% confidence level. The colours of the points indicate the slope of the power law from the power law fit (regardless of whether that fit was the best or not): red – $\alpha > -0.5$; green – $-1.3 < \alpha < -0.5$; blue – $\alpha < -1.3$. The line shown is the line of equal χ^2/ν.

four orders of magnitude. This large range of values, which is also seen in the normalisations of the individual components, indicates that a continuum of variations of these components is seen, probably due to variations in the strengths of the inner jet and emission from the accretion disk and/or surrounding regions.

We also note that a small number of the sources at the high-ratio end of the distribution are faint, red sources, that are likely to be significantly dust-reddened. They are thus fit with a dominant synchrotron component, as the synchrotron spectrum has the approximate form of a power law with an exponential cut-off (which is the same as a power law with dust extinction).

5.4.3 Power law sources

While many sources have been fitted better with the combined model, a large number are still preferentially fit with the power law. If we plot a

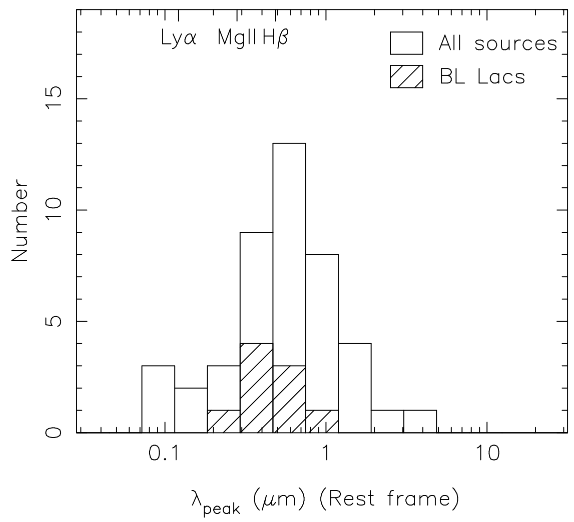

Figure 5.6: Histogram of peak wavelengths, showing all sources fit best with the combined model, in the rest frame. The solid histogram shows all sources with combined fits accepted at 99% confidence, while the hatched histogram shows the BL Lac objects. The locations of three prominent emission lines are given for reference.

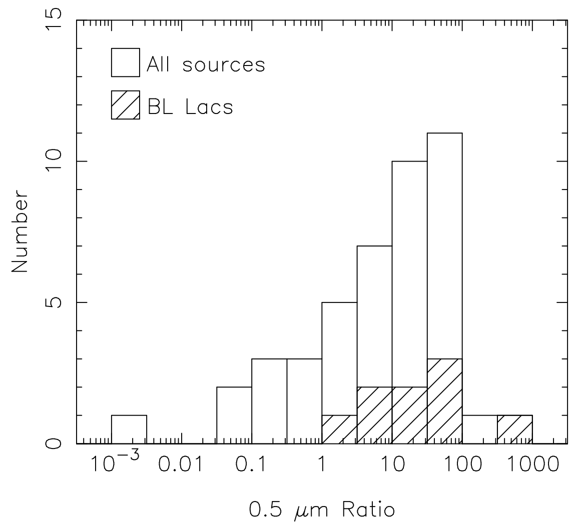

Figure 5.7: Histogram of ratios of the synchrotron component to the power law component of the combined model, for those sources best fit by the combined model. The ratio is calculated at a rest-frame wavelength of 0.5μm. The hatched histogram shows the BL Lac objects.

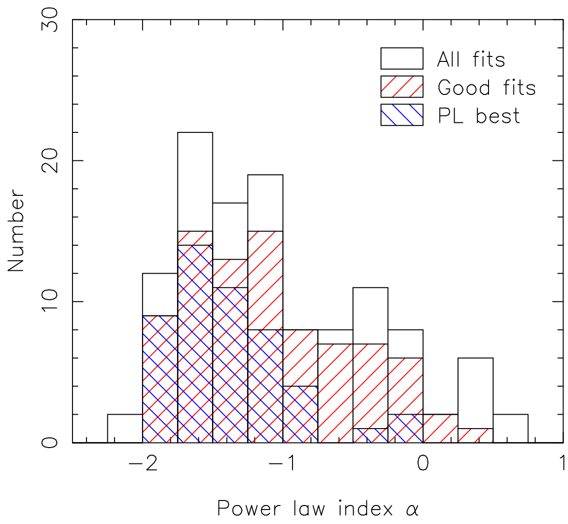

Figure 5.8: Distributions of the fitted power index α. The open histogram shows all 117 sources, the hatched histogram shows which of those fits are accepted at 99% confidence, while the cross-hatched histogram shows which of those sources have power law fits better than the combined fit.

histogram (Fig. 5.8) of the power law indices of those still fit by the power law model, it can be seen that most of those sources that are preferentially fit by the power law model are the bluer sources, while the majority of the sources with indices $\alpha > -1$ are fit better by the combined model.

It is worth noting here that there are a significant number of power law sources with what might be termed "intermediate" slopes (that is, slopes with $\alpha \sim -1.2$, which are redder than the blue power law from the combined model) and a few red ($\alpha > -0.5$) sources. These latter sources are often high polarisation sources (see Chapter 6), and so are likely to be synchrotron dominated (they of course show no evidence for a turn-over similar to that being fit by the synchrotron model, although their slope could be due to a very steep energy distribution (i.e. large p) or a more gradual turn-over).

The presence of the intermediate power law slopes raises interesting issues. Are similar sources seen in optical quasar surveys? Fig. 5.9 shows the power law index distributions for the sources best fit by the power law model, together with the LBQS quasars from Francis (1996). While the two data sets cannot be said to come from different parent distributions (the Kolmogorov-Smirnov test probability for the null hypothesis that the parent distributions are the same is 11.3%), there does appear to be an excess

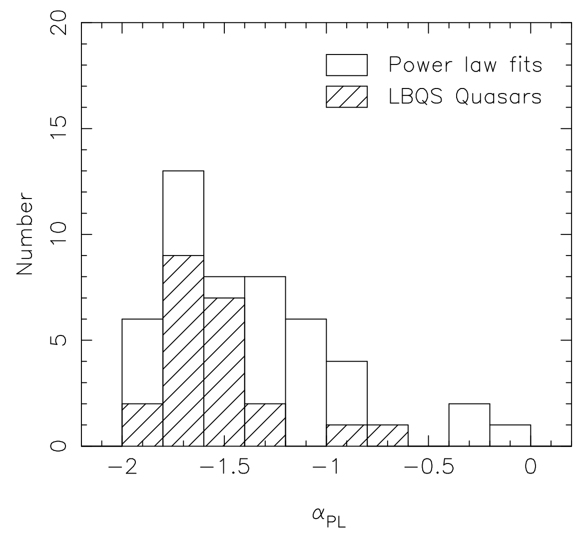

Figure 5.9: Histograms of power law indices for the power law sources in this paper and for the LBQS quasars from Francis (1996).

of quasars in our sample for $-1.4 \lesssim \alpha \lesssim -0.8$. This may indicate that the accretion disk emission in radio loud quasars has a broader range of colours, which would have implications for models of accretion disk emission. This effect may be related to the interaction between the jet outflow and the disk.

5.4.4 Redshift distributions

To give an indication of what sources are being fit by which model, Fig. 5.10 shows the redshift distributions of the sources best fit by both the combined model and the power law model.

The two distributions are different at the 99.9% level, with the average redshifts being $z = 1.51$ (power law sources) and $z = 0.90$ (combined model sources). The combined model tends to fit sources at lower redshift, while the higher redshift sources are nearly always fit by the power law model. For example, of the 17 sources with $z > 2$, only three are best fit by the combined model, compared with 12 out of the 18 sources with $z < 0.5$.

This may be an indication of the fact that the fixed observation band (0.4μm to 2.5μm) corresponds to different rest frame wavelength ranges at different values of z: at $z = 0.5$ this is 0.27μm to 1.67μm, while at $z = 2.5$ it is 0.11μm to 0.71μm. This shorter wavelength pass-band will result in less synchrotron emission being observed, due to the turnover of the synchrotron

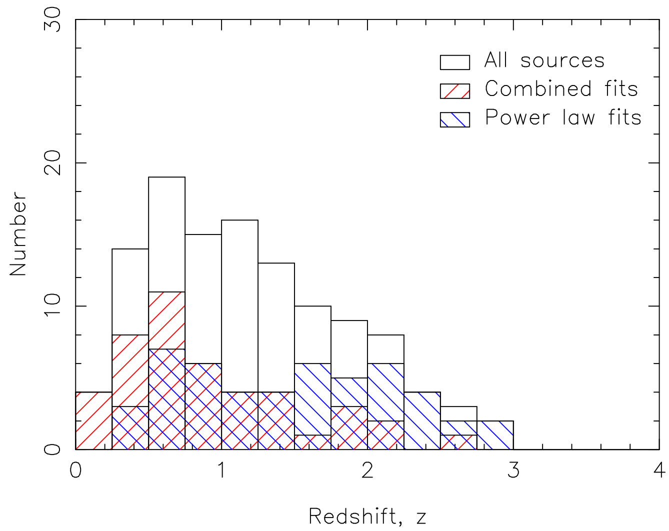

Figure 5.10: Redshift distributions of sources best fit by each model. The redshift distribution of all sources that had models fit to them is also shown for comparison.

component. If this is the case, this is evidence that there is an upper limit to the distribution of λ_p values, in the sense that there are fewer sources with λ_p short enough to give significant synchrotron emission in the redshifted pass-band.

This is reminiscent of the observation made in Section 2.2.1 that, despite being preferred by selection, almost no jets are seen in AGN with their synchrotron spectra extending up to X-ray energies. This indicates that the optical region is about as energetic as significant synchrotron emission from AGN/quasar jets can get.

We also note that, as well as this effect, the shorter rest frame wavelengths that are observed will result in a stronger big blue bump (should one be present), and so even if the synchrotron were the same level, its relative strength will be decreased.

5.4.5 Colour-colour diagram

Finally, the consistency of the model fits can be checked by plotting the sources on a colour-colour diagram. An optical colour vs. NIR colour diagram was used by Francis et al. (2000) to graphically show the range of different SEDs present amongst the sample. In Fig. 5.11 the $J-K$ colours of all sources that have good model fits are plotted against their $B-I$ colours.

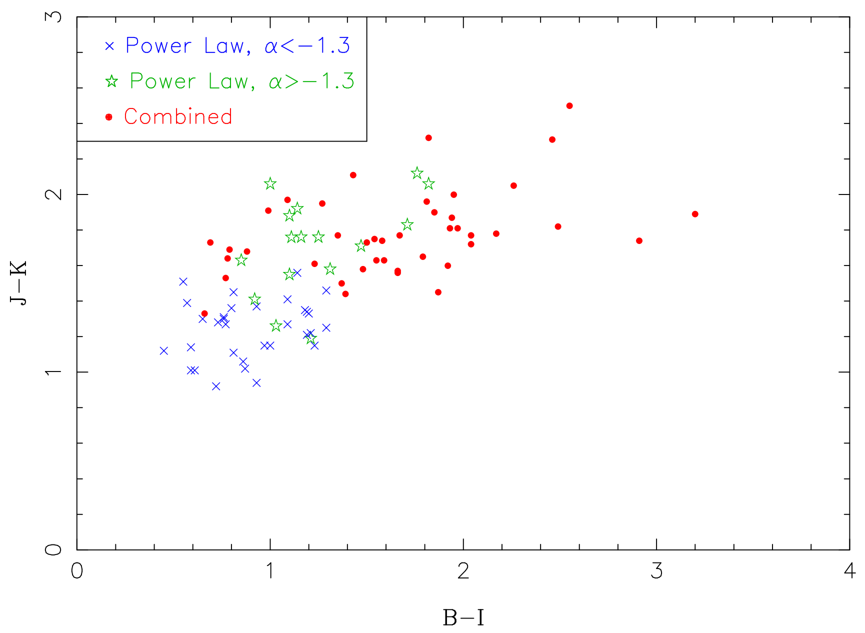

Figure 5.11: Infrared $(J-K)$ colour versus optical $(B-I)$ colour for all quasars with good model fits. The best fit model is indicated by the symbol used.

The sources are also separated into their fitted model types, with the power law sources divided into red and blue power laws according to their fitted slope (using $\alpha = -1.3$ as the dividing line).

Clear distinctions can be made between the different model types. The blue power law sources lie at the bottom left corner, indicating blue colours in both optical and infrared, while as the power law becomes redder, the sources move towards the upper-right. Many of the combined fits are in the optically-red region of the plot, indicating that the SED is turning over in the optical (similar to 1256−229 in Fig. 5.3, for example). The reddest sources in $B-I$ are sources with optical continua that drop towards the blue, in the manner of 1706+006 (see Fig. 5.3), which are typical of dusty sources, or sources dominated by host galaxy emission, and are fit by a dominant synchrotron component. Note that 1706+006 is the faintest of the sources shown in Fig. 5.3, and is a good candidate for dust extinction. Other combined sources, however, are among the bluer sources in the optical, but have redder NIR colours than the power law sources. These are the sources that show an inflection, similar to 2329−415 in Fig. 5.3, where the synchrotron component is dominant in the NIR but turns over and has less effect in the optical.

5.5 Other models: Power law synchrotron

Thus far, we have been considering a synchrotron model that peaks at some λ_p and then turns over sharply (i.e. exponentially). This model was chosen for consistency with other modelling done for optical synchrotron emission (Meisenheimer et al. 1996), and to provide the maximum contrast with the power law model. However, synchrotron emission could alternatively be present in the form of a power law. What if we consider a model of the same form as the combined model, but with this power law synchrotron model instead? Is this any better at fitting the observations?

Such a model was constructed, being a linear combination of the blue (BBB) power law from earlier, and a power law of variable index: $f(\lambda) = a\lambda^{-1.7} + b\lambda^{\alpha_S}$. To distinguish it from the BBB power law, the indices were restricted to the range $-1.6 < \alpha_S < 1.5$. This model was then fitted to the photometry in the same way as previously. Note that the special case of $a = 0$ is simply the power law fit from Section 5.1 (with the index restricted to lie in the above range).

We do note, briefly, that by restricting the index of this power law to lie in the above range, we are imposing an implicit bias against fitting blue synchrotron power laws. Should there be any synchrotron spectra with a slope bluer than $\lambda^{-1.5}$, this fitting routine will not fit them correctly (although such slopes are bluer than any of the observed radio-to-optical slopes seen in the PHFS sources – see Fig. 7.7c). However, due to the nature of the fitting routine, this cannot be remedied (if the routine tries to fit two power laws of too similar slopes, it will reach a singularity and fail to work).

The χ^2/ν values for this model are plotted in Fig. 5.12 against those for the combined model detailed in Section 5.2. The symbols used indicate which model is preferred, and whether it is a good or bad fit. For sources that are bluer than $\lambda^{-1.7}$, the best fit is always with no synchrotron component (for both forms of the synchrotron model), as the presence of the second component will redden the blue power law. Hence, for these sources, both the original combined model and the two power law model give the same fit, consisting of just the $\lambda^{-1.7}$ (i.e. BBB) power law. These sources are indicated by the "Equal fit" symbols on Fig. 5.12.

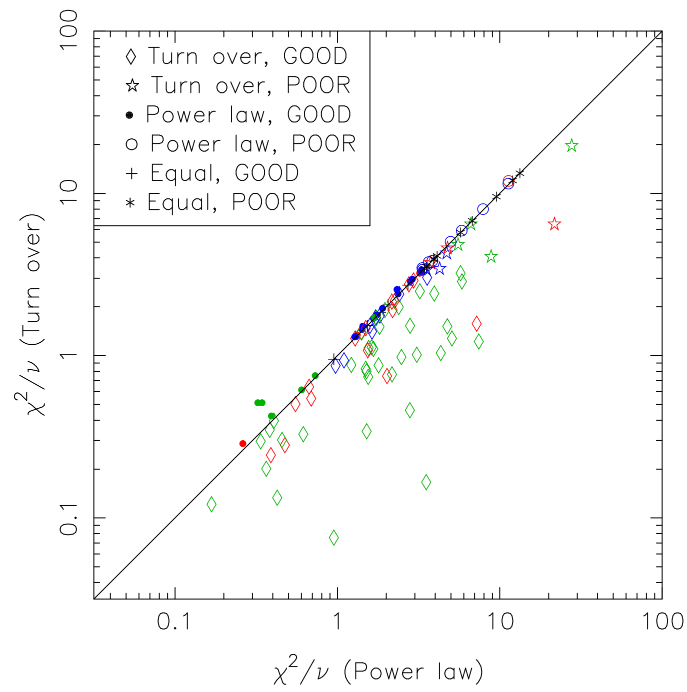

Figure 5.12: Values of χ^2/ν for the combined models featuring either power law synchrotron models or synchrotron models with a turn-over. The symbols relate to which model is preferred, and whether the fit is accepted at the 99% confidence limit or not (i.e. good or poor). The line shown is the line of equal χ^2/ν. The colours relate to the location of λ_p from the fit with the turn-over synchrotron model: red – $\lambda_p > 1\mu$m; green – $0.1\mu\text{m} < \lambda_p < 1\mu$m; blue – $\lambda_p < 0.1\mu$m.

The power law synchrotron model obviously does not do as well at explaining the optical/NIR SEDs of the quasars as the model with a turn-over. Only 22 sources have a good power law synchrotron fit that is better than their fit from the synchrotron model with a turn-over, and only two of these (1034−293 and 2329−415, with indices of $\alpha_S = -0.21$ and $\alpha_S = 0$ respectively) are significantly better. These power law synchrotron sources may have turn-overs at shorter wavelengths, beyond our currently available data. The only way to tell would be to obtain UV photometry (ideally contemporaneous with the optical/NIR).

We note that many of the sources from Fig. 5.8 that are in the cross-hatched histogram (that is, had better single power law fits than combined fits) and had $\alpha > -1.6$, also had fits with the two power law model that were better than those with the turnover synchrotron model. (This is not always the case, however, since going from one power law to two decreases the degrees of freedom, so the χ^2/ν value will be greater.) In most of these cases, the blue power law (the $\lambda^{-1.7}$ component) is either absent or has a very low normalisation.

For most sources, however, the synchrotron model with a turn-over gives a much better fit to the observed optical/NIR SEDs (many of these sources show large ratios of synchrotron to blue power law flux). This result provides clear evidence that there is a break or a cutoff present in the energy distribution of the radiating particles. Additionally, it shows that there are few, if any, sources with turn-overs at shorter wavelengths (i.e. in the UV or X-ray). This is in accord with the finding from the redshift distributions (see the discussion in Section 5.4.4).

5.6 Other models: Hot dust

So far, it has been shown that, for a number of sources, the optical–NIR photometry is well fit with a power law plus a curved component, which we have assumed to be the turnover of a synchrotron component. However could another model be used instead of synchrotron? One possible alternative is blackbody emission resulting from hot dust.

To test this model, we used a blackbody emission spectrum due to dust at a temperature of 1750 K (the sublimation temperature characteristic of dust grains consisting of graphite and silicates, e.g. Laor and Draine (1993)) emitted in the quasar's rest frame. A blackbody curve at this temperature would have its peak, in the quasar rest-frame, at 1.66μm. This blackbody spectrum was combined with the same $\lambda^{-1.7}$ power law used in the combined model to produce a model that was fit to the data.

The fits generated by this model were almost always worse than those of the synchrotron model, as seen in Fig. 5.13. This was due to the peak of the blackbody occurring at much longer observed wavelengths than the K band. Discounting the case where only the $\lambda^{-1.7}$ component was fit (the "Equal" points in Fig. 5.13), in only 12 cases was the χ^2/ν value from the dust model less than that of the synchrotron model, and in most cases this was because the dust model had one more degree of freedom. For each of these objects, the SED took the form of a blue power law (one object was $\lambda^{-1.4}$, and the rest were bluer than $\lambda^{-1.54}$) that had a slight amount of reddening at the H and K bands, which was fit by the presence of the dust blackbody

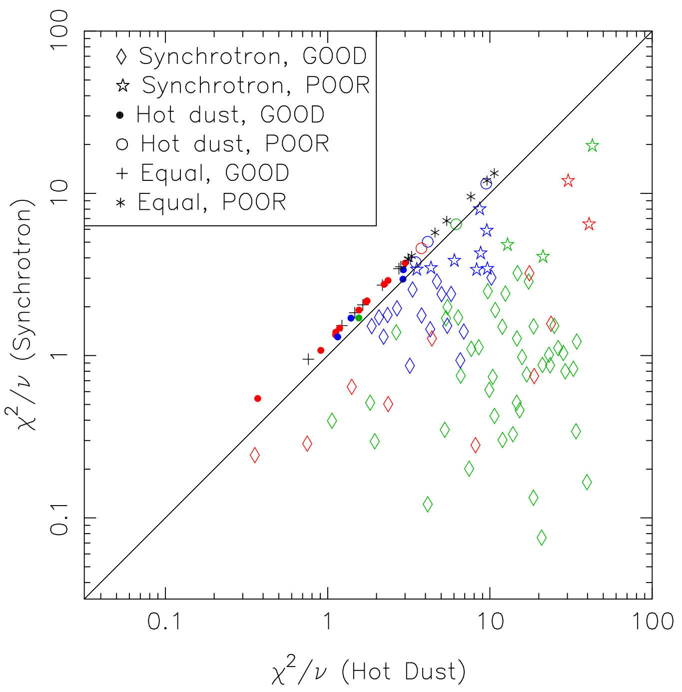

Figure 5.13: Values of χ^2/ν for the combined models featuring either a synchrotron model or a hot dust model. The symbols relate to which model is preferred, and whether the fit is accepted at the 99% confidence limit or not (i.e. good or poor). The line shown is the line of equal χ^2/ν. The colours relate to the location of λ_p from the synchrotron model fit: red – $\lambda_p > 1\mu$m; green – $0.1\mu\text{m} < \lambda_p < 1\mu$m; blue – $\lambda_p < 0.1\mu$m.

curve (in other words, the synchrotron fit had a long-wavelength peak, as evidenced by the colour of the points in Fig. 5.13). For the majority of the sources, however, the hot dust model was a lot worse than the synchrotron model, and so can not provide the peak in the optical/NIR that is required to explain many of the observed SEDs.

A number of authors (for example, Sanders et al. 1989, and references therein) have argued for the existence of a near-IR bump, somewhere around 3μm, corresponding to blackbody emission from hot dust. Sanders et al. also mention the presence of a local minimum at 1μm, which they note for its "universality" in their sample of bright quasars from the Palomar-Green (PG) survey. They interpret this to be due to the finite sublimation temperature of dust, causing a drop in the blackbody emission, combined with the rise in flux of thermal emission from hot ($T \gtrsim 10{,}000$K) gas. However, any dip observed in the data presented here occurs at wavelengths which are too short to be attributed to hot dust. To observe a 1μm dip, photometry at longer wavelengths would need to be used.

5.7 Alternative parameter values

Throughout this chapter, we have used values for the electron energy index of $p = 2.5$, and for the BBB spectral index of $\alpha_B = -1.7$. We consider here the effect that changing these values has on the results. Table 5.1 lists the numbers of sources best fit by each of the two models, for each set of parameters, as well as the total number of sources fit by one of the models.

Reducing the value of p means that the synchrotron spectrum has a bluer slope, which enhances the effect of the turn-over. Using a lower value of p in the combined model results in some sources, otherwise fit by the power law, being instead fit by the combined model. This is indeed seen in Table 5.1, where the number of sources fit by a power law decreases as you move from $p = 3$ to $p = 2.5$ to $p = 2$ (if the value of α_B is kept constant), while the number of sources fit by the combined model increases. Note also that more sources have good fits for the lower values of p.

The λ_p distributions are also affected by a changing p value. For lower p values, there are more sources with shorter λ_p values (that is, close to 0.1μm). This is due to the slope of the power law tail of the synchrotron spectrum: for higher p values the slope is redder, and so a synchrotron spectrum peaking around 0.1μm would contribute too much at the longer wavelengths.

For the spectral index of the blue optical power law used in the combined model, we considered both steeper and flatter values than the one mentioned in Section 5.2.1. The dispersion found by Francis (1996) for the slopes of LBQS quasars is $\pm \sim 0.3$, and so we consider here slopes in f_λ of $\alpha_B = -1.4$ and $\alpha_B = -2.0$.

Changing the slope of this power law (while keeping p constant) has a much less drastic effect than changing the value of p. As the slope becomes steeper in f_λ (that is, bluer), only a couple of sources fit by the power law change to be fit by the combined model. The distribution of λ_p values is not changed considerably by the variation of the α_B values.

In summary, reasonable changes to the fiducial values of α_B and p make little difference to the fits, both in the λ_p distribution and the numbers fitted by each model, although the difference will be accentuated if the values of α_B and p are both taken to extremes.

5.8 Fits to excluded sources

As explained in Section 4.6, there are a number of sources that were excluded from the sample. Some of these were excluded for the sole reason that they did not have a measured redshift (i.e. those sources with "no z" in the final column of Table B.2). These sources are generally quite red and optically faint (thus explaining their undetermined redshift), with the exception of the BL Lac object 0048−097, which has a power law SED. The models were fitted to the observed wavelengths of these objects, to investigate the bias created by excluding them. Note that this fitting does not take into account the change in shape of the synchrotron spectrum due to the redshift of the source. The results are summarised in Table 5.2.

As can be seen, all but three of the sources are fit with the combined model, and the three that aren't are fit with quite red power laws (that is, red compared to the power laws fit to the sources with measured redshifts). The location of the peak wavelengths are generally into the NIR, which are longer than the bulk of the distribution of the sources with redshifts (see Fig. 5.6). Also, the synchrotron component that is fitted is generally fairly dominant, as evidenced by the fraction values $F_{0.5}$. However, it is unlikely that many of these sources would truly be synchrotron sources, since they show more the characteristic shape of dust absorption and are quite faint in the optical (again, with the exception of 0048−097, which was fit with the power law tail of a dominant synchrotron model). We propose that these sources are dust-dominated rather than synchrotron-dominated.

5.9 Effect of emission lines on photometry.

As mentioned in Section 4.5, the presence of a strong emission line in the wavelength range of one of the filters will raise the SED level above that of the continuum, which will increase the systematic error in the photometry.

To test this effect, and to see how the fits to the photometry are affected, we examined several sources whose spectra showed significant emission lines. To calculate the contribution of the emission line, we define the total flux in

p	2.0	2.0	2.0	2.5	2.5	2.5	3.0	3.0	3.0
α_B	−1.4	−1.7	−2.0	−1.4	−1.7	−2.0	−1.4	−1.7	−2.0
Power law	46	44	45	49	48	48	53	52	52
Combined	49	51	50	44	45	44	39	40	40
Total	95	95	95	93	93	92	92	92	92

Table 5.1: Number of sources fitted best by each model, for different values of the parameters p and α_B. Only those fits accepted at the 99% confidence level are shown. Values of the parameters used are $p = 2.0$, $p = 2.5$ and $p = 3.0$, as well as $\alpha_B = -1.4$, $\alpha_B = -1.7$ and $\alpha_B = -2.0$.

Source name	B (mag)	$B - K$	Best fit model	α	$\lambda_p(\mu\mathrm{m})$	$F_{0.5}$	good/bad fit
0048−097	16.12	3.61	Combined	–	0.15	0.97	good
1110−217	24.41	7.67	Combined	–	1.85	0.88	good
1156−094	21.95	5.08	Combined	–	1.04	0.69	good
1648+015	21.87	5.31	Combined	–	1.17	0.82	bad
1732+094	$B > 23.5$, $V = 21.15$	> 7.13	Power law	−0.39	–	0.00	bad
2056−369	$V > 23.5$, $R = 23.45$	$> 5.39^*$	Power law	0.59	–	0.00	good
2245+029	21.71	6.22	Combined	–	1.85	0.41	good
2337−334	22.93	6.54	Power law	0.36	–	0.00	good
2344−192	23.52	6.27	Combined	–	1.65	0.83	bad

Table 5.2: Fitting results for sources that were excluded from the sample purely due to their undetermined redshift. The best fit model is given along with either the peak synchrotron wavelength (for combined fits) or the power law index (for power law fits). $F_{0.5}$ denotes the fraction of the total flux made up by the synchrotron component, at an observed wavelength of 0.5μm. Note that a * denotes a $V - K$ measurement, not $B - K$, since a B measurement was not made (due to the faintness of the source).

the line as $F_{\rm line}$ and the total continuum flux *under* the line as $F_{\rm cont}$. Then the change in magnitude is given by

$$\begin{aligned}\Delta m &= 2.5\log_{10}\left(\frac{F_{\rm line}+F_{\rm cont}}{F_{\rm cont}}\right)\\ &= 2.5\log_{10}\left(\frac{W_\lambda+\Delta\lambda}{\Delta\lambda}\right)\end{aligned}$$

where W_λ is the equivalent width of the line, and $\Delta\lambda$ is the wavelength range over which the flux is measured. The equivalent widths and fluxes were computed using the *splot* routine in the data reduction package IRAF.

Note that we are able to do this analysis only for a small number of sources, as not all sources have spectra, and those spectra that do exist are often poor quality, and in all cases non-simultaneous.

The values of the change in magnitude, when considered over the same wavelength range as that of the broad-band filters ($\Delta\lambda \sim 1000 - 2400$Å for the optical bands), ranged from 0.05 – 0.25 magnitudes. By artificially reducing the flux in the relevant band by this amount, the change in χ^2 due to the presence of the emission line could be evaluated. This was done for several sources that had strong emission lines present in their spectra (the spectra for a large number of PHFS sources will be presented elsewhere (Francis et al. 2001)). A few specific examples are listed here, and are shown in Fig. 5.14 (with the adjusted photometry in red):

- ★ 1510−089 has a strong Hα line in the I band ($\Delta m = 0.14$), as well as a combination of a strong Hβ line and prominent Fe II emission in the R band ($\Delta m = 0.11$). The removal of flux corresponding to these lines caused a reduction in χ^2/ν of nearly 50% (1.28 – 0.68), without greatly changing the resultant fit, although the fitted synchrotron peak was at a slightly longer wavelength.

- ★ 1725+044, similarly, has Hα in I band ($\Delta m = 0.13$) and Hβ + [O III] in R band ($\Delta m = 0.07$), and removal of these more than halves χ^2/ν from 2.49 to 1.17, without changing the location of the peak of the synchrotron.

- ★ 1036−154 has a large Mg II line in the B band ($\Delta m = 0.17$), which causes a noticeable upturn in the SED. Removal of this line reduces the χ^2/ν from 0.77 to 0.56, without changing the location of the peak

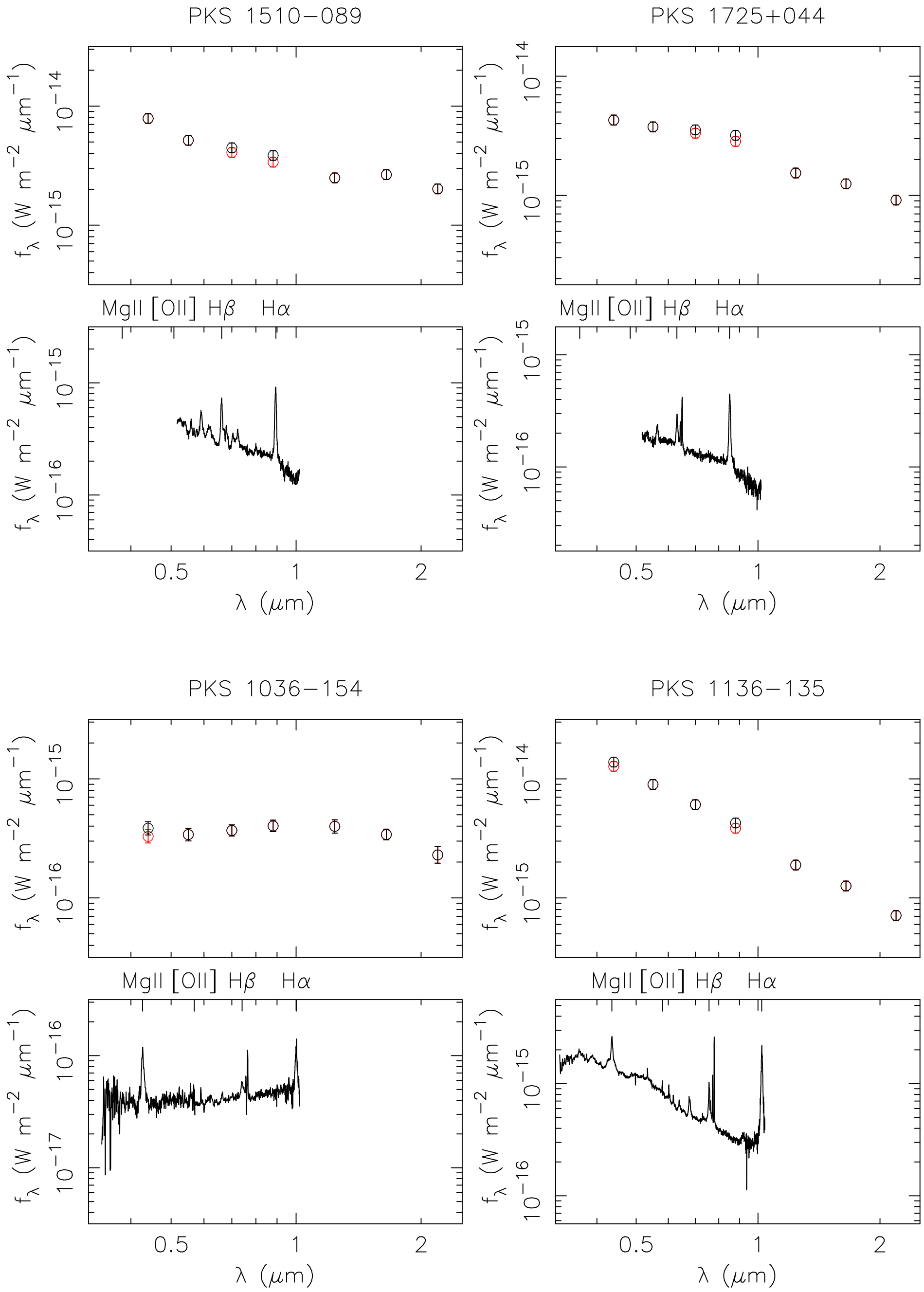

Figure 5.14: The effect of removing strong emission lines from the photometry. The adjusted photometry (as described in the text) is shown in red. The spectra are given for comparison, showing the location of prominent emission lines.

wavelength, although the 0.5μm ratio increases slightly (from 5.3 to 7.2).

★ 1136−135 is initially fit with a pure power law, and this remains the case after removal of the Mg II line ($\Delta m = 0.09$ in B) and both the Hβ and the strong [O III] (total $\Delta m = 0.11$ in I). The power law index softens slightly (from -1.85 to -1.81) and the χ^2/ν value decreases from 0.43 to 0.29.

In conclusion, by selecting quasars with strong emission lines, we have demonstrated that the largest changes to the SED are $\Delta m \sim 0.25$ in one wave-band. In most cases investigated, removal of the line flux improved the χ^2/ν value of the model fit, but did not significantly alter the nature of the fit. When good quality long-wavelength spectra (preferably at least quasi-simultaneous with the photometry, which is not the case here) are available for these quasars, it should be possible to recalculate the fits, taking the emission line contributions into account, although the general conclusions are not expected to change.

5.10 Sources without good fits

Up to this point, we have only discussed the results for the sources with good (i.e. acceptable at the 99% confidence level) fits. A total of 24 sources (or 21 per cent of the total) are not fit well by either the power law model or the combined model. What sort of sources are these?

A few sources ($\sim$ 8) have roughly power law SEDs, but with a little curvature ('n'-shaped) in the blue end of the optical. This may be indicative of a small amount of dust attenuation or extinction.

Most of the other sources have one or more photometric points that do not smoothly connect with the rest of the SED. It is possible that, for these points, at least one of the systematic errors discussed in Section 4.5 is dominating, over and above the level that was assigned. In some sources, there may also be further emission processes present that have not been modelled.

Chapter 6

Optical Polarisation

6.1 Background

One of the key features of synchrotron radiation is its high intrinsic degree of polarisation. The highest possible polarisation comes from a completely ordered $\vec{B}$ field, where the polarisation can reach $\sim 70\%$ (Longair 1994). If there is significant synchrotron emission at optical and NIR wavelengths, then one would expect to be able to detect a corresponding polarisation. Indeed, this has been used as a way to confirm the presence of synchrotron emission in optical jets. A good example was the confirmation by Baade (1956) (using photographic plates and a polaroid filter) that the optical emission from the jet of M87 was strongly polarised, and so was likely to be synchrotron emission.

Although we are primarily interested in synchrotron radiation in this thesis, we do note here that there are other methods for producing polarised light. The most common effect seen in low-luminosity AGN such as Seyferts is that of scattering or reflection from dust. The classic example is that of Seyfert 2s, such as NGC 1068 (Miller et al. 1991), that show only narrow lines in their total flux spectrum, but show broad lines in their polarised flux spectrum. This situation arises because the light from the broad line region (BLR) is obscured from the direct line of sight by a thick torus of dust and gas. Instead, light from the BLR is scattered into the line of sight by either clouds above the torus, or the inside edge of the torus itself, and, in doing so, becomes polarised. In the PHFS objects, however, the line of sight to the nucleus is not expected to pass through this torus (should one be present in these higher luminosity objects), since flat-spectrum objects are preferentially face-on (as opposed to edge-on). Thus, we do not consider here the effect of scattering in the analysis of the polarisation.

Radio-quiet quasars generally have very little optical polarisation. The measured values are usually a few tenths of a percent, and objects with a polarisation of more than about 2% are rare (Stockman, Moore, and Angel 1984, who used the BCS, or Burbidge, Crowne, and Smith (1977) catalogue). Only about 1% of bright optically-selected quasars show high polarisation (i.e. $P > 3\%$), and these have radio and optical continua that resemble BL Lac objects. In other words, the optical emission in the high polarisation quasars seems to be due (at least in part) to a different process to that in the low polarisation objects.

The combined model used in Chapter 5 allows this possibility. It is made up of two components: a synchrotron component, which can be very highly polarised (exactly how much depends on the particle distributions and the geometry of the emitting region); and a blue power law, which represents emission from a "normal" blue quasar (most likely emission from the accretion disk). The latter component is assumed here to be unpolarised, which is a good approximation, as $P < 1\%$ for most optically-selected quasars (Antonucci 1988; Stockman et al. 1984). Hence, the degree of polarisation predicted by the modelling will be governed by the amount of synchrotron emission fit to the data. This, of course, will change with wavelength, as the proportion of total flux made up by the synchrotron emission changes.

6.2 Existing studies

The polarisation properties of quasars and blazars have been investigated previously by a number of different authors, some for samples that include some sources considered here. Wills et al. (1992) studied a large sample of bright, flat-spectrum core-dominant quasars, measuring their optical polarisation. An interesting result is that they found that the fraction of quasars with $P > 3\%$ in a fixed observed passband decreased with increasing z, possibly indicating that the percentage polarisation decreases towards shorter rest frame wavelengths. This would be consistent with the presence of a synchrotron component turning over in the optical region.

Impey and Tapia (1990) present radio and optical data for a slightly larger sample of radio-selected quasars, including optical polarisation measurements. They find strong statistical links between strong optical polarisation and properties such as compact radio structure, superluminal motion and weak emission lines (properties common to the blazar class of objects). They explain this by requiring the optical emission, as well as the compact radio emission, to be relativistically beamed. In a similar study, Impey, Lawrence, and Tapia (1991) compared VLBI structure of 50 strong radio sources with their optical properties. They found strong correlations between the strength of the unresolved core at 5GHz and optical polarisation, emission line equivalent widths and line-to-continuum ratio, and flux variability.

Smith et al. (1988) obtained multicolour ($UBVRI$) polarisation measurements of 11 highly polarised quasars, and found that three of these exhibited decreasing polarisation toward shorter wavelengths, which they modelled as a combination of polarised synchrotron emission, and two unpolarised components, from the broad-line region and the accretion disk. None of these sources, however, are part of this sample.

Finally, Smith et al. (1994) studied the optical polarisation properties of 1546+027, by using both broad band polarimetry and spectropolarimetry. They were able to decompose the optical spectrum into a polarised synchrotron component, of wavelength-independent intrinsic polarisation of 15%, and an unpolarised "LPQ" (or low-polarisation quasar – in other words, a "normal" un-polarised quasar) component (to account for the emission lines).

6.3 Optical polarisation

Firstly, we wish to compare the photometry and the predictions of the modelling with published optical polarisation measurements. We use in particular the large catalogue of measurements compiled by Wills et al. (1992). These measurements were made using a photo-multiplier tube polarimeter on the 2.1m telescope at the McDonald Observatory, in Texas, USA. The observations were taken using white light – that is, without a filter. The particular values for the polarisation that will be used are the median values of Wills et al. – these are the median of their measurements, together with any taken from the literature (provided the errors were not too large: i.e. they excluded those with $\sigma_P > 2.4\%$). By taking the median of several observations, the resulting value is less sensitive to variability, which is a particular problem for the high-polarisation objects.

We first compare the percentage polarisation with the optical–NIR continuum slope. The values of the slope (α, where $f_\lambda \propto \lambda^\alpha$) are obtained from the fitting of the power law model to the photometry (Section 5.1). The resulting plot is shown in Fig. 6.1, together with the line of best fit (determined by linear regression). The equation of this line is $\log_{10}(P) = (0.62 \pm 0.10)\,\alpha + (1.13 \pm 0.20)$, and a correlation is present at the 99.9% confidence level (the Kendall's τ probability that a correlation is not present is 3.4×10^{-4}).

This regression line can be compared with that found by Scarpa and Falomo (1997) in their study of 73 blazars: $\log_{10}(P) = (0.40 \pm 0.08)\,\alpha + (1.40 \pm 0.10)$. We find a stronger α dependence, although the difference in the two slopes is not quite significant at the 95% level. A possible explanation for the stronger dependence on α found here is the fact that our sample contains many low polarisation and blue objects. The fact that Scarpa and Falomo consider optical indices only (as opposed to optical-NIR indices) can be discounted as an explanation, as we find a regression line slope of 0.60 ± 0.12 when the optical indices are considered instead.

It is clear from Fig. 6.1 that the redness of the optical continuum is strongly correlated with the degree of optical polarisation. This confirms the statements made about the different types of sources in Section 5.1, indicating that the optical emission in the redder sources is likely to be of a different origin to that in the blue sources. A possible explanation for the observed correlation is that the polarisation decreases with decreasing wavelength. Blue sources will then have a relatively smaller contribution from wavelengths with larger polarisations. Such a scenario is given by the model of a synchrotron component turning-over at some peak wavelength in the optical region, then decreasing rapidly – exactly what is fitted in the modelling.

We now test whether the models fit in Chapter 5 are consistent with the polarisation measurements. In other words, is the amount of polarisation related to the amount of synchrotron that is fit to the quasar's SED? This can be tested by comparing the polarisation measurements from Wills et al.

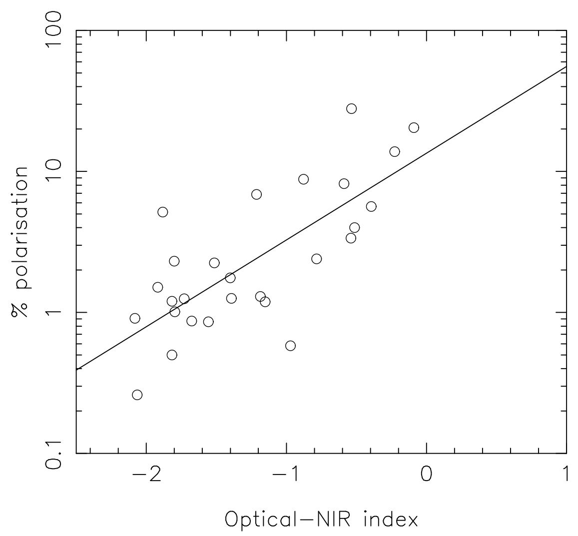

Figure 6.1: Polarisation from Wills et al. (1992) as a function of the optical-NIR spectral index, as derived from fitting the power law model in Section 5.1. The solid line is the line of best fit.

(1992) with the fractional amount of flux due to the fitted synchrotron component. However, since the observations of Wills et al. were made without a filter, the average synchrotron fraction is determined by integrating over the range 0.3μm – 1μm. This is given by

$$\langle F \rangle = \frac{\int f_S(\lambda)\,\mathrm{d}\lambda}{\int f_T(\lambda)\,\mathrm{d}\lambda}, \tag{6.1}$$

where $f_S(\lambda)$ and $f_T(\lambda)$ are the synchrotron flux and the total flux at wavelength λ.

Fig. 6.2 shows the percentage polarisation as a function of this average synchrotron fraction. For those sources that were best fit by the power law model, the fraction is calculated from the combined model fit, and these sources are indicated by a different symbol. All the power law sources with polarisation measurements had relatively red power law indices (i.e. $\alpha > -1.3$). (The bluest sources seen in Fig. 6.1 are not shown in Fig. 6.2 because they are too blue to be fit by the synchrotron model.)

The spread in polarisation measurements at large synchrotron fractions is much greater than at low fractions, indicating that the high polarisation sources generally have large amounts of synchrotron fitted to them (at the

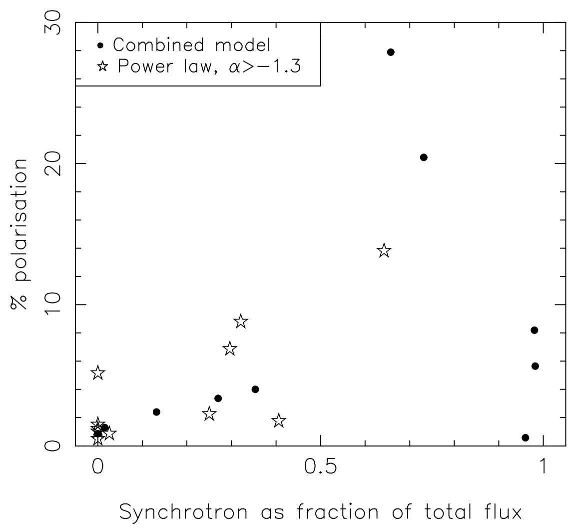

Figure 6.2: Polarisation from Wills et al. (1992) as a function of the proportion of the total flux made up by synchrotron. The sources are given different symbols according to the nature of their best fit model.

wavelengths at which the polarisation is measured). Additionally, all but one of the sources at zero (or near-zero) synchrotron fraction have low optical polarisation.

The two exceptions to this picture are 0202−172 and 1020−103. Firstly, 1020−103 has a very high synchrotron fraction ($\sim 95\%$), but has very little optical polarisation ($P = 0.58\%$). In this case, the source has a power law continuum with a slight curvature, which is fit well by an almost pure synchrotron curve (giving the high synchrotron fraction). It may be that this curvature is due to effects other than synchrotron, which would explain the lack of polarisation. A possible candidate is contamination from the very strong Hα line, which would boost the continuum level in the centre of the SED.

Secondly, 0202−172 has a measured polarisation of $P = 5.15\%$, but also has a very blue power law continuum ($\alpha = -1.85$). This continuum slope is possibly too steep to attribute to synchrotron (it implies a value of $p = 1.3$ – in turn implying a rather flat energy distribution). However, the location of the synchrotron peak may have shifted in the period since the polarisation measurements were made (the polarisation measurements were taken 8 years prior to the photometry observations).

This raises the main caveat for this sort of study. There is a long gap in time between the polarisation measurements and the observations that obtained the photometry (which was used to derive the synchrotron fractions). The flux and polarisation of the sources may well have varied in that period, particularly for the high-polarisation sources.

6.4 Near-infrared polarisation

6.4.1 The data

To try to avoid the problem of non-simultaneity of the photometry and polarisation observations, it was decided to obtain polarisation measurements of a number of PHFS objects in the NIR, closer in time with optical photometry observations. This would enable the photometry measurements to be nearly simultaneous with the data used in the model fitting, and thus better able to predict the wavelength dependence of the polarisation from the model fitting results.

The polarisation measurements that are used in this thesis come from two observing runs on the Anglo-Australian Telescope, using the *IRIS* instrument. The first set of observations were made on the nights of February 27 – March 2, 1997, by Frank Masci, Paul Francis and the author. The sources observed were selected according to brightness in K band (from previous observations). An object with $K \sim 15$ would have required ~ 3 hours integration time, and considerably more at J band, so only sources with $K < 14$ were chosen.

The polarimetry observations and reduction are described in detail in Frank Masci's Ph.D. thesis (Masci 1997), and the results are given in Table 6.1. (Note that 1510−089 was not observed in the H band.) For all of these sources, the observations were between 41 and 49 days earlier than the optical and NIR observations from Francis et al. (2000) used for the model fitting.

Does the fact that the two sets of data are not exactly simultaneous matter? Obviously, one would prefer them to be so. However, what we are looking for here is the wavelength dependence of the polarisation, or, equivalently, the wavelength dependence of the proportional amount of synchrotron flux. The wavelength dependence itself is governed primarily by the location of the synchrotron peak (the relative normalisations of the synchrotron and power law components will affect the normalisation of the polarisation curve, but we are primarily interested in the wavelength dependence). If the source has varied in the period between the two sets of observations, it is more likely to vary in flux (i.e. in normalisation), rather than having the peak wavelength vary (although we do note that the latter type of variation has also been observed – see, for instance, Pian et al. (1998)). The latter case would involve a change in the energetics of the emitting particles, and so would be less likely to occur on short timescales. Thus, the wavelength dependence of the polarisation should be the same for the two sets of data.

The second set of observations were made on the nights of October 12 – 14 1997, by the author and Michael Drinkwater. The sources presented here are those that are consistent with the sample definition given in Section 4.6: namely 0118−272, 0454+066 and 2210−257. We also observed 0118−272 and 0454+066 at optical wavelengths (using the ANU's 1m telescope), to obtain B, V, R and I magnitudes, since these were not observed in the sample of Francis et al. (2000). These observations were made during the three nights immediately preceding the AAT observations. 2210−257, on the other hand, is in the Francis et al. (2000) sample, and so we use that data for the modelling (this results in a difference of either 32 or 35 days between the photometry and the polarimetry). The reduction of the optical images was performed in the same way as described in Chapter 4.

6.4.2 Data reduction and measuring the polarisation

Each of the images made with *IRIS* were made up of multiple dithered 60 second images, each in turn made up of twelve averaged 5 sec exposures in H and K, and one 60 sec exposure in J. The initial part of the reduction was performed using FIGARO software specifically designed for the *IRIS* detector. This step accounted for the bias and dark current, and corrected for non-linearity between the number of photons incident on the chip and the number of electrons produced. The flat field was created from the difference of dome exposures with the lamps on and off – this removes any telescope emission, improving greatly the photometric accuracy. The effects of known bad pixels were removed by interpolating over them. The sky emission was removed by using a median of the five or seven data frames taken closest together in time. This median sky frame was then subtracted off the images to produce data frames with improved signal-to-noise. The resulting data frames were then aligned and median combined, to produce the final images. An example

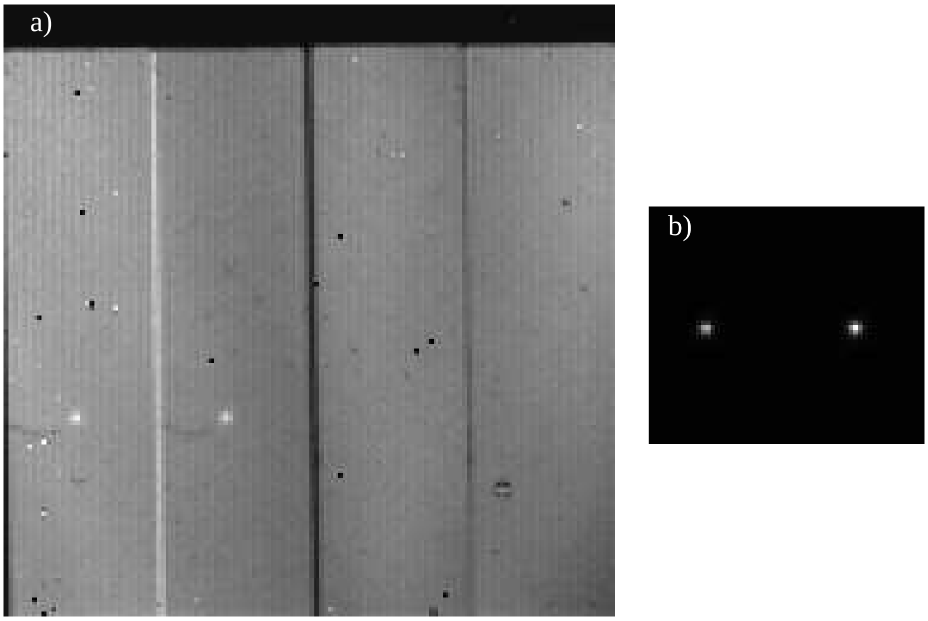

Figure 6.3: Example output from the *IRIS* detector, before and after reduction. a) The output from the whole chip, after bias subtraction and linearisation. Note the large number of bad pixels, as well as the noticeable structure in the sky background. b) The reduced image, showing just the source (0118−272) in two orthogonal polarisations. The polarisation of this source is noticeable in the different brightness of the two images (the right-hand one is brighter than the left).

of a single image after the linearisation stage (but before flat-fielding and bad-pixel removal) is shown in Fig. 6.3a, and the final image is shown in Fig. 6.3b.

The *IRIS* detector measures two orthogonal polarisations simultaneously, using a Wollaston prism. This prism produces two images next to one another on the detector, one in "ordinary" light and the other in "extraordinary" light (polarised in the direction orthogonal to the ordinary light). The chip actually has four images, two of a given part of the sky, and two of an adjacent part. For a given object, however, only two are of relevance. See Fig. 6.3a for an example.

From each of these two images, an intensity can be measured, giving I_1 and I_2. From these intensities we can find one of the Stokes parameters, say U:

$$U = \frac{I_1 - I_2}{I_1 + I_2}. \tag{6.2}$$

Thus, we can in principle find one of the Stokes parameters from a single image. In practice, however, there will be some instrumental polarisation present. This can be removed by taking a second image with the plane of polarisation rotated by 90°(done with a half-wave plate located before the Wollaston prism). The ordinary and extraordinary images then swap positions on the chip, producing intensities I_1' and I_2'. We then use the "ratio technique"(from Frank Masci's Ph.D. thesis (Masci 1997)) to calculate the Stokes parameter without the effects of instrumental polarisation. First, we find the ratio

$$r = \sqrt{\left(\frac{I_1 I_2'}{I_1' I_2}\right)}, \tag{6.3}$$

and then calculate the Stokes parameter according to

$$U = \frac{r-1}{r+1} \tag{6.4}$$

The second Stokes parameter, Q, is measured in the same way, but with the plane of polarisation at 45°to the initial orientation. The total percentage polarisation (i.e. the fraction of the total light in the polarised component) is then given by

$$P = 100\sqrt{U^2 + Q^2}\ \% \tag{6.5}$$

and its angle of orientation is given by

$$\theta_P = \frac{1}{2}\tan^{-1}\left(\frac{Q}{U}\right). \tag{6.6}$$

The errors in P are calculated assuming Poisson errors in the measured intensities I_1 etc. The resulting values $P \pm \sigma_P$ are listed in Table 6.1.

To find the photometry, each pair of ordinary and extraordinary images were added together, then all four summed images were combined to create the final image for each source and filter. The photometry was then performed with the *apphot* package in IRAF, using circular apertures with the sky background level determined by the median flux in an annulus around the source.

The photometry was calibrated with standard stars observed at the beginning and end of the night. These standard star observations, however, yielded differing flux levels across the different nights, and so the fluxes were bootstrapped from observations of the radio galaxy 2206−237 (on the basis that this source was the least likely of those observed to have varied in the month since it was observed by Francis et al. (2000)). This provided NIR SEDs that were in better agreement with the optical SEDs from the observations a few nights earlier. The optical and NIR photometry for 0118−272 and 0454+066 are listed in Tables 6.2 and 6.3 respectively.

6.4.3 The modelling

Since the synchrotron component is the only polarised component, and its degree of polarisation does not change with wavelength, one would expect the percentage polarisation to be directly related to the amount of synchrotron flux present. In fact, the percentage polarisation will be directly proportional to the ratio of synchrotron flux to total flux. In Fig. 6.4, the polarisation of each of these quasars is plotted as a function of wavelength, together with the synchrotron ratio normalised (arbitrarily, as it is the wavelength dependence we are interested in, not the precise normalisation) to the K-band polarisation point (which is always the longest wavelength point). For completeness, a line of constant polarisation is shown, again normalised to the K-band point. All these sources are best fit with the combined model (see Appendix D for the model fits).

The fits to 0454+066 and 0118−272 were as follows:

★ 0454+066: Best fit by the combined model, with $\chi^2_S/\nu = 3.08$ compared to $\chi^2_P/\nu = 5.92$. The synchrotron component had $\lambda_p = 0.66\mu$m, and a ratio of synchrotron to power law at 0.5μm of $R_{0.5} = 8.45$.

★ 0118−272: Best fit by the combined model, with $\chi^2_S/\nu = 2.10$ compared to $\chi^2_P/\nu = 2.85$. The synchrotron component had $\lambda_p = 0.94\mu$m, and a ratio of synchrotron to power law at 0.5μm of $R_{0.5} = 1.10$.

Polarisation measurements from Wills et al. (1992) have also been included, where they exist. Once again, an allowance needs to be made for the fact that these observations were made without a filter. In a similar way as before, the mean wavelength for each object can be calculated:

$$\langle\lambda\rangle = \frac{\int \lambda f_T(\lambda)\mathrm{d}\lambda}{\int f_T(\lambda)\mathrm{d}\lambda} \tag{6.7}$$

The polarisation measurement is then plotted at this wavelength. These measurements are included with the caveat that they are *not* simultaneous

Source Name	$P \pm \sigma_P(\%)$ J	H	K	$P_{\rm opt}(\%)$ (Wills et al.)
0537−441	8.0 ± 0.5	8.7 ± 0.4	10.8 ± 0.8	—
0829+029	12.0 ± 0.4	12.5 ± 0.2	13.6 ± 0.1	8.2
1020−103	1.7 ± 0.2	2.5 ± 0.4	1.8 ± 0.6	0.6
1036−154	2.8 ± 1.3	3.1 ± 1.5	5.4 ± 2.0	—
1313−333	12.7 ± 0.3	12.9 ± 0.5	13.6 ± 0.5	—
1510−089	3.6 ± 0.2	—	2.7 ± 0.2	2.4
1546+027	6.2 ± 0.2	8.5 ± 0.2	8.6 ± 0.2	3.4
0118−272	17.2 ± 0.8	16.5 ± 0.5	17.0 ± 0.4	—
0454+066	5.1 ± 1.8	5.9 ± 1.0	2.9 ± 1.0	—
2210−257	3.4 ± 1.2	6.9 ± 1.5	4.0 ± 0.9	—

Table 6.1: Near-infrared polarisation measurements for ten PHFS sources, for the J, H and K bands. Errors given are 1σ. The data in the top section of the table are from the March 1997 observing run (Masci 1997), while the data in the bottom section are from the October 1997 run, detailed in the text. Also given are optical polarisation measurements from Wills et al. (1992).

Name	B	V	R	I
0118−272	16.59 ± 0.10	16.32 ± 0.10	15.89 ± 0.10	15.29 ± 0.10
0454+066	19.38 ± 0.13	18.74 ± 0.11	18.12 ± 0.10	17.45 ± 0.10

Table 6.2: Optical photometry of extra sources used for NIR polarimetry. The errors given are 1σ errors, with a 10% systematic error, as described in Section 4.5.

Name	J	H	K
0118−272	13.70 ± 0.10	12.79 ± 0.10	12.11 ± 0.10
0454+066	15.79 ± 0.10	14.95 ± 0.10	14.42 ± 0.10

Table 6.3: NIR photometry of extra sources used for NIR polarimetry. The errors given are 1σ errors, with a 10% systematic error, as described in Section 4.5.

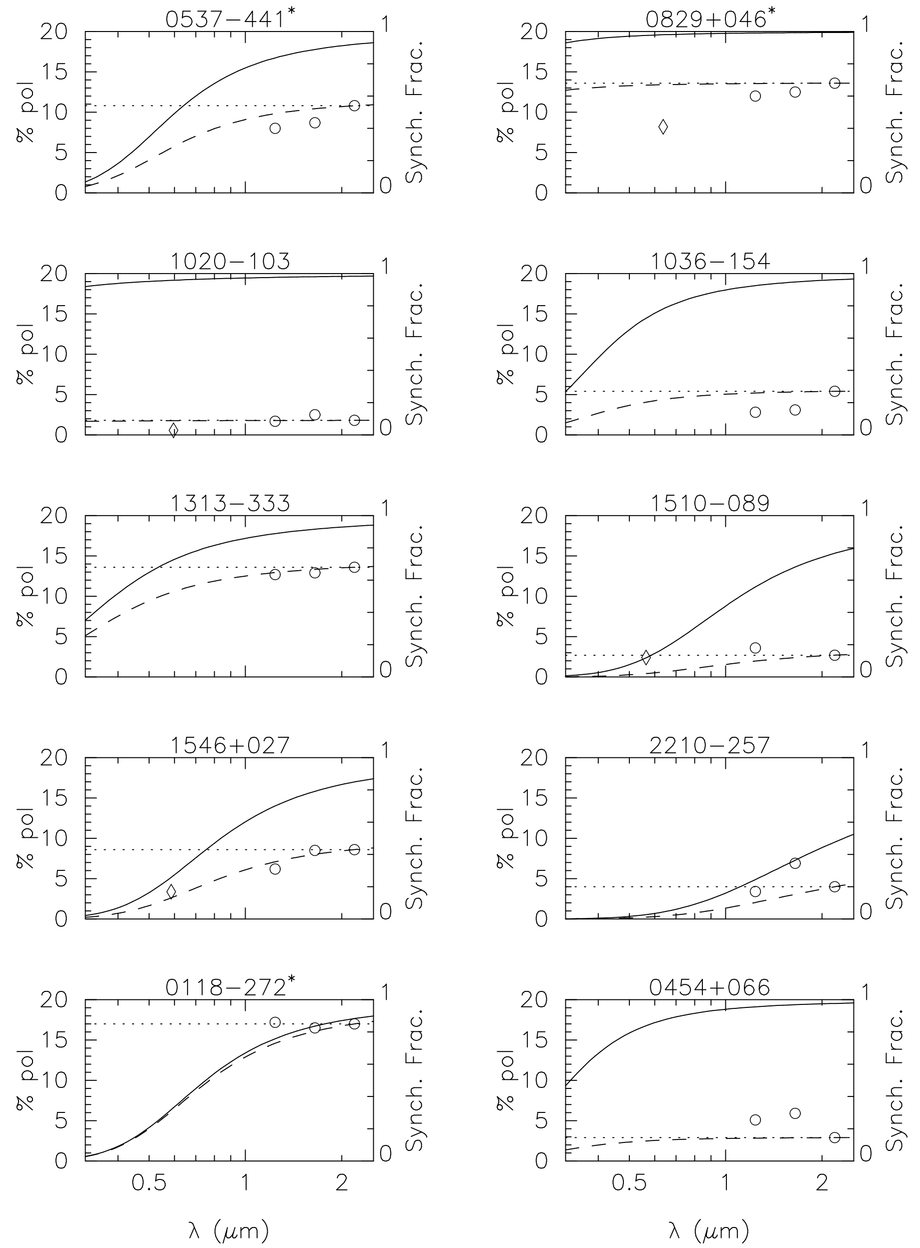

Figure 6.4: Near-infrared polarisation of a selection of quasars as a function of wavelength. Also shown are optical measurements from Wills et al. (1992) (plotted with a diamond). The solid lines show the fraction of the total flux made up by the synchrotron component (right-hand axis), while the dashed line shows this normalised (see text) to the K-band data point, and is in polarisation units (left-hand axis). The dotted line shows constant polarisation, normalised to the K-band data point as well. A * denotes the object is a BL Lac.

with the photometry (and hence the fitted model), nor with the NIR polarimetry. They are included merely as a guide, and should not be expected to agree with the fitted model.

The fitting gives mixed results for different sources. For some, such as 1546+027, the fitted synchrotron component replicates well the wavelength dependence of the polarisation. However, for some sources, such as 1313−333, the points are equally well given by a constant polarisation component. This is what you would expect from a pure synchrotron component, and these sources are typically BL Lac objects, from which you would expect to see a synchrotron-dominated SED.

A notable exception to this is the BL Lac 0537−441, whose polarisation is not fit well by a constant synchrotron component, but is fit better by a combination of a synchrotron and a significant power law component (although we do note that this source is suspected of having varied over the course of obtaining all the photometry observations – see Fig. 4.4 and Section 4.5 for a discussion of this variability).

Another source worth noting is 0118−272 (another BL Lac). Its polarisation appears to be better fit by a constant polarisation model, indicating a dominant synchrotron component. However, its optical SED (Appendix D) shows an upturn in flux at the blue end, leading to the fit of a strong power law component at short wavelengths.

It is apparent from these plots that having simultaneous optical polarisation measurements would better help discriminate between the combined model and a constant polarisation model. Unfortunately the NIR points by themselves do not provide enough wavelength range to distinguish the two models. The obvious next step in studying the polarisation of the PHFS sources would be to obtain simultaneous (or at least quasi-simultaneous) optical and NIR polarisation measurements of a number of sources, using *TAURUS* on the AAT in the optical, and either *IRIS2* (*IRIS'* replacement on the AAT) or *CASPIR* (on the ANU 2.3m) in the NIR (once they have polarimetry capability).

6.5 Summary

The optical and NIR polarisation properties of the PHFS quasars provides a very good way to test the fitted models from Chapter 5. Since the synchrotron component is the only significantly polarised component in the modelling, one would expect the amount of polarisation at a given wavelength to be related to the amount of synchrotron emission present in the SED at that wavelength.

This is certainly supported by the correlation between the optical–NIR spectral index and the polarisation, where the redder sources have much larger polarisations than the blue sources. This can be interpreted as the redder sources having additional red, polarised emission over the top of the blue emission seen in the bluer sources. This qualitative analysis is realised in the combined model, where the polarised synchrotron component is added to a blue, unpolarised power law, making it redder. As an illustration of this point, see Fig. 5.8, where the combined sources have clearly redder power law slopes than the power law sources.

It is also seen that the amount of polarisation is related to the amount of synchrotron that is fit to the SED, so that the more highly polarised a sources is, the more synchrotron tends to be present in its spectrum.

Finally, by looking at the polarisation in different wave-bands, the wavelength-dependence of the polarisation can be deduced. For a number of sources, this is consistent with the predictions of the fitted models, however it was found that the wavelength range covered was a bit too restrictive to provide conclusive support (or otherwise) for the models. Optical polarisation measurements would thus be needed to make confident statements about the relationship between the models and the degree of polarisation.

Chapter 7

BL Lacs in the PHFS

7.1 Introduction

BL Lacertæ objects, or BL Lacs, are a class of AGN that are defined by their lack of any prominent emission lines in their optical spectra. Most theories to explain this lack involve the presence of an extra continuum component that helps to mask emission lines (although these lines may already be weak). From the shape of the radio–IR–optical SED (Impey and Neugebauer 1988), as well as high optical and radio polarisation, this extra component is thought to be synchrotron emission, which comes from the relativistic jet (such as those seen in the optical that are discussed in Chapter 2). Due to the relativistic nature of the jet, Doppler beaming will be important (see Section 3.5), an effect strongly dependent on the viewing angle, or the orientation angle of the jet.

Hence, since the orientation to the line of sight is important for the appearance of most of these flat-spectrum radio quasars and BL Lacs, it follows that there must be objects with similar properties but a different appearance due to a different orientation. If the angle at which we view the radio quasars or BL Lacs is small (as seems likely), this other group of objects must be much more numerous. Such a group is termed the “parent population” of the closely aligned objects.

7.1.1 Radio galaxies

Clear candidates for the parent populations of radio quasars and BL Lacs are the radio galaxies. These are galaxies that exhibit large amounts of radio emission, most often in the form of jets or lobes that can extend far beyond the boundaries of the (optical) host galaxy.

Radio galaxies are separated into two distinct classes based on their radio luminosity: Fanaroff-Riley type I and type II (Fanaroff and Riley 1974). FR Is, the low luminosity galaxies, have their radio emission peaking closer to the central nucleus, and exhibit fainter, more diffuse lobes. FR IIs, always at high radio luminosities, have their dominant radio emission from the bright parts of their lobes, which are usually connected to the nucleus by a thin collimated jet.

The division in luminosity is strongest at lower radio frequencies (e.g. 178 MHz, where the dividing luminosity is $\sim 2 \times 10^{25}$ W Hz^{-1}). At higher frequencies, however, there is considerable overlap in the luminosities of the two classes. The low frequency emission is dominated by the lobes, so this indicates that the lobes of the two types of radio galaxies are significantly different. The higher frequency emission, on the other hand, comes from the inner jet and core region, indicating that these regions in FR Is and FR IIs are more similar.

Aside from the differences in their radio properties, the two classes of radio galaxies differ in a number of ways. The division between the two classes appears to also be a function of optical luminosity. If one plots the radio luminosity against the optical luminosity (that is, the optical magnitude down to a fixed surface brightness in the rest frame), then one finds that the two classes are well separated (with mixing only occurring over a factor of ~ 10 in radio luminosity), and that the dividing radio luminosity increases roughly as $L_{\rm opt}^2$ (Owen and Ledlow 1994).

The emission line properties of the two classes are also different. It has been shown that, in FR IIs, the narrow emission line (particularly [O III] 4959,5007) luminosities are correlated with that of the radio (Baum and Heckman 1989; Rawlings et al. 1989). This may be related to the optical luminosity relationship, in the sense that a bigger, brighter galaxy will have more emission-line gas. This gas is found to be extended, usually spatially located near the radio source axis (in both radio galaxies and steep-spectrum radio quasars) (Baum and Heckman 1989). The total emission line luminosities (that is, broad plus narrow) are less correlated with the radio power, indicating either that only the narrow line gas is associated with the radio source, or that the viewing-angle dependence of the broad lines is important (not all sources of a given power will have the same range of line luminosities due to their different viewing angles). Meanwhile, the emission line luminosities of FR Is are also correlated, but are typically 5–30 times less than those of FR IIs with the same total radio power (Zirbel and Baum 1995). The correlation for the FR Is is dominated by a correlation between line luminosity and host galaxy optical magnitude – no similar correlation exists for FR IIs. Finally, optical spectra of FR IIs are reasonably heterogeneous, as some show quite strong emission lines, whereas others only show weak, low-excitation lines, similar to FR Is (Laing et al. 1994).

7.1.2 Unification Schemes

FR I and FR II radio galaxies have been proposed (Urry and Padovani 1995, and references therein) as the parent populations of radio-loud AGN. Under this scheme, radio quasars are aligned versions of FR II galaxies (with flat-spectrum quasars possibly more aligned than steep-spectrum quasars). BL Lacs, on the other hand, have lower luminosities than quasars (particularly when the effects of beaming are removed), and so are believed to be aligned versions of FR I galaxies.

The supporting evidence for these unified schemes generally involve radiation (or some property) that is assumed to be isotropic. Good evidence for this is found in the study by Antonucci and Ulvestad (1985), who studied the extended radio emission of a sample of blazars (including both BL Lacs and OVV quasars). They found that they had similar extended radio powers to radio galaxies from the 3C (mainly FR IIs with some FR Is) and B2 (predominantly FR Is) samples. It is uncertain, however, whether the clear morphological dichotomy between FR Is and FR IIs is reflected in the extended emission of quasars and BL Lacs.

If one assumes that the narrow emission lines are emitted isotropically, then it is found that quasars and FR IIs have [O II] luminosities that span the same range of values (Hes et al. 1993). BL Lacs, on the other hand, show somewhat larger [O III] luminosities than FR Is. This may, however be due to either underestimation of the FR I fluxes due to a strong stellar continuum, or a (relatively) small slit that may not have included all the emission line region (Tadhunter et al. 1993). Also, there is some evidence that [O III] in quasars and FR IIs is emitted anisotropically (at least in comparison to [O II]) (Hes et al. 1993; Urry and Padovani 1995), and this

Name	Jet flux (μJy)	Source magnitude	Source flux (mJy)	Flux ratio (Jet/Source)
3C 15	5.9	V=15.8	1.75	3.37×10^{-3}
3C 66B	5.9	V=15.0	3.66	1.61×10^{-3}
3C 78	33	R=12.5	35.63	0.93×10^{-3}
3C 120	14	V=14.8	4.40	3.18×10^{-3}
3C 200	18	V=20.0	0.04	4.91×10^{-1}
0521−365	60	R=14.6	5.15	1.17×10^{-2}
3C 212	0.19	V=19.1	0.08	2.26×10^{-3}
3C 245	0.17	V=17.3	0.44	0.38×10^{-3}
3C 264	33	R=12.5	35.63	0.93×10^{-3}
3C 273	57	V=12.8	27.79	2.05×10^{-3}
M 87	1960	B=9.6	589.88	3.32×10^{-3}
3C 346	11	V=17.5	0.37	3.00×10^{-2}
3C 371	15	V=14.4	6.37	2.36×10^{-3}
2201+044	0.57	V=15.2	3.05	0.19×10^{-3}

Table 7.1: Ratios of jet flux to central source flux at optical wavelengths for known optical jets. Jet fluxes taken from Table 1 of Scarpa and Urry (2001), while central source fluxes are converted from magnitudes taken from NED. Where possible, the magnitudes are taken to be at approximately the same wavelength as the jet observation.

could also account for the difference between BL Lacs and FR Is.

7.2 Orientation of the PHFS quasars

The integral part of the Urry and Padovani (1995) unification scheme is orientation, in that BL Lacs are beamed FR Is and quasars are beamed FR IIs, due to the viewing angle being close to the direction of the relativistic jet. Can we estimate the amount of beaming that is present in the PHFS sources, and thereby deduce their orientation? The synchrotron emission fit by the modelling in Chapter 5 provides the means for doing this.

From the model fitting, we found that many of the PHFS quasars have significant synchrotron emission at optical wavelengths. This synchrotron emission is assumed to come from the relativistic jet that provides the radio emission – that is, from an optical jet. It can be noted that if the synchrotron component in the fit is taken to be representative of the optical jet emission, and the blue power law component representative of the central source (i.e. accretion disk) emission, then the ratio of jet flux to central source flux takes a wide range of values (see Fig. 5.7).

This can be compared to those sources that have been observed to have optical jets. Scarpa and Urry (2001) have compiled a list of optical fluxes of the optical jets in each of these sources, and we have used these values, together with optical magnitudes of the sources taken from the literature[1] to compile a list of jet-to-central-source flux ratios for the optical jet sources. Where available, the magnitudes are at approximately the same wavelength as the observation of the jet. When just a single magnitude was given, it has been taken to be V band. These data are listed in Table 7.1, and the ratios are plotted as a histogram in Fig. 7.1, where they are compared with the synchrotron to power law flux ratio for the PHFS quasars (calculated at an observed wavelength of 0.5μm). Although there are three optical jet sources that are in the PHFS (3C 273, 0521−365 and 3C 120), none of these sources are in the sub-sample with optical/NIR photometry, and so there is no overlap between the two plots.

It can be seen in Fig. 7.1 that the PHFS quasars have much higher ratios of jet to central source flux. If, as discussed previously, the PHFS quasars are viewed at a smaller angle to the jet axis, then this difference in flux ratios will be due to different amounts of Doppler beaming.

Recall from Chapter 3, for a relativistic source viewed at an angle θ to the direction of motion, the observed flux is enhanced by the Doppler factor

$$\delta = \frac{1}{\Gamma(1-\beta\cos\theta)} \tag{7.1}$$

where $\beta^2 = 1 - 1/\Gamma^2$. The degree of enhancement depends on the nature of the source, but in general takes the form

$$F_\nu(\nu) = \delta^p F'_{\nu'}(\nu) \tag{7.2}$$

where a $'$ indicates a quantity is measured in the rest frame. (Note that $\nu = \delta\nu'$.) If $F_\nu \propto \nu^{-\alpha}$, then the values for p are either $p = 2+\alpha$ for a smooth, continuous jet, or $p = 3+\alpha$ for discrete moving blobs (or spheres). The amount of enhancement as a function of θ for two different p values is shown in Fig. 3.7. (Note that here we are simply using the standard Doppler formulae, not the versions altered to account for an ordered magnetic field

[1] The magnitudes were found using NED, the NASA/IPAC Extragalactic Database, http://nedwww.ipac.caltech.edu/

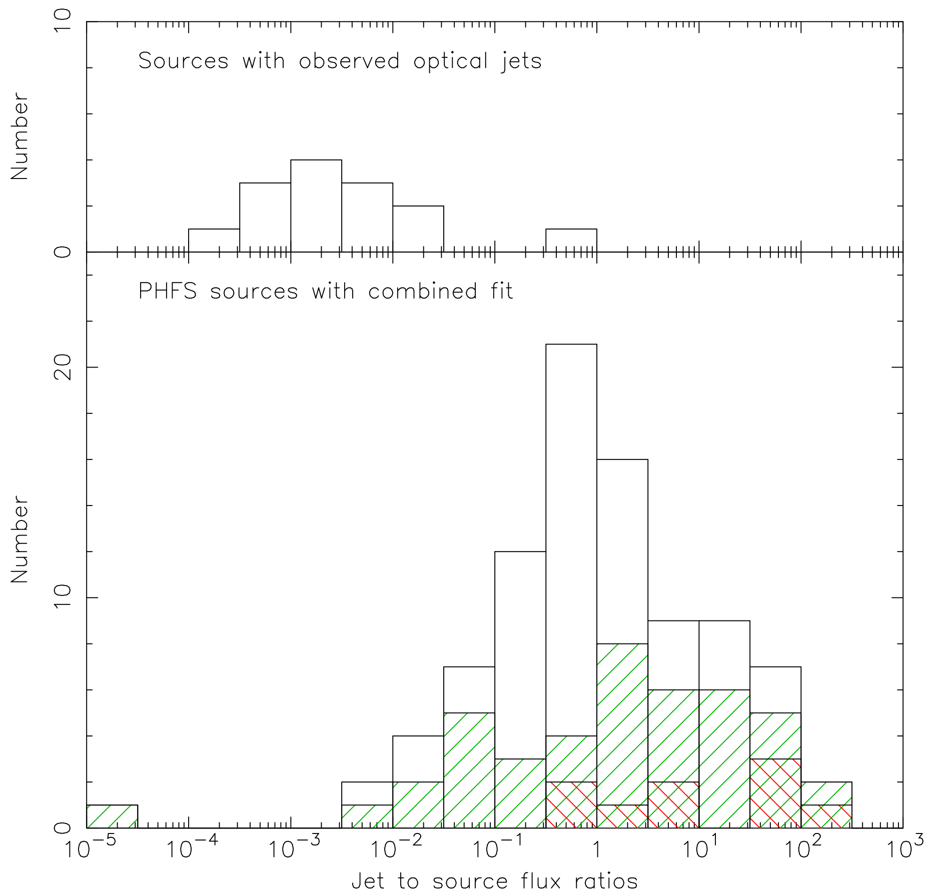

Figure 7.1: Histogram of jet-to-central-source flux ratios for both sources that have observed optical jets, and the PHFS sources based on the fitting. In the PHFS plot, the open histogram shows all sources that were able to be fit by the combined model, while the green hatched histogram shows those sources *best* fit by the combined model (in preference to the power law model – see Chapter 5 for details on the fits). The red hatched histogram shows the BL Lac objects.

– Chapter 3.)

Now, the case of the optical jets can be considered in this light. By comparing jets from both those sources with known optical jets and the PHFS quasars (based on the modelling from Chapter 5), the viewing angle for the PHFS quasars can be determined by making a number of assumptions:

① The jets in both types of objects are, on average, the same, particularly the bulk Lorentz factors (Γ).

② The intrinsic (unbeamed) jet flux scales the same way as the core flux. This means that the ratio of intrinsic jet flux to core flux is a constant. In other words, the apparent differences in this ratio are purely due to Doppler amplification (or de-amplification) of the jet flux.

③ The viewing angle θ and the Lorentz factor Γ are known for the sources with known optical jets. These values are needed to derive the parameter values for the PHFS sources.

Since the ratios of jet-to-core flux have been measured (Fig. 7.1), one can define R as the ratio of the jet-to-core ratios in two different sources. Now, let F'_j and F'_c represent the unbeamed jet and core fluxes respectively, and $F_j = \delta F'_j$ and $F_c = F'_c$ the observed jet and core fluxes (note that the core flux is assumed to be unbeamed). Then, assuming that the Doppler beaming in sources 1 and 2 is given by δ_1^p and δ_2^q, R can be defined by

$$R = \frac{F_{j1}/F_{c1}}{F_{j2}/F_{c2}} = \frac{\delta_1^p F'_{j1}/F'_{c1}}{\delta_2^q F'_{j2}/F'_{c2}} = \Gamma^{q-p}\frac{(1-\beta\cos\theta_2)^q}{(1-\beta\cos\theta_1)^p}, \tag{7.3}$$

since the ratio of unbeamed jet flux to core flux is assumed to be constant across all sources. So, given that the value of R is determined observationally, and that Γ and θ_2 are known, then θ_1 can be calculated:

$$\cos\theta_1 = \frac{R^{1/p} - \Gamma^{(q-p)/p}(1-\beta\cos\theta_2)^{q/p}}{\beta R^{1/p}} \tag{7.4}$$

This is not defined for all values of R, however. If R is sufficiently large, then even making θ_1 as small as possible will not provide the necessary boosting. Similarly, R cannot be too small either. These limits can be calculated from Eqn. 7.4, setting $\theta_1 = 0°$ and $\theta_1 = 180°$ respectively, and are defined as

$$\Gamma^{q-p}\frac{(1-\beta\cos\theta_2)^q}{(1+\beta)^p} \leq R \leq \Gamma^{q-p}\frac{(1-\beta\cos\theta_2)^q}{(1-\beta)^p} \tag{7.5}$$

To use this method to estimate viewing angles for the PHFS quasars, the values of Γ and θ_2 need to be defined for the sources with known optical jets (i.e. point ③ above). We use the two results detailed in Section 2.2.2: those of Scarpa and Urry (2001) and Sparks et al. (2000). The two sets of (θ, Γ) values used were $(20°, 7.5)$ (from Scarpa and Urry (2001)), and $(30°, 3)$ (since the angles and Γ factors given by Sparks et al. (2000) are limiting values, we choose a slightly more extreme case, taking their lower angle limit and a slightly higher Γ value).

To calculate the viewing angle for the PHFS quasars, one must also assume a jet-to-core ratio for the optical jet sources. This was taken to be the median value of the ratios measured in Table 7.1. In calculating this value, however, we have excluded those sources that are either in the PHFS or have a blazar nature: 3C 120, 0521−365, 3C 273, 3C 371, and 2201+044. The median jet-to-source ratio of the remaining objects was found to be 2.26×10^{-3}. (The median value in this case is slightly more robust than the average, as it is not affected greatly by the outliers.) For each PHFS source, the value of R is found by taking the ratio, at 0.5μm, of the fitted synchrotron component (representing the emission from the optical jet) to the fitted blue power law (representing the emission from the central source), and dividing that by the above median value. (Note that finding this 0.5μm ratio is equivalent to finding the ratio of the total jet flux to total central source flux at 0.5μm, since both are unresolved in our images.) This value of R is then used in Eqn. 7.4 to find the PHFS quasars' viewing angles. This is done for each of the two different sets of (θ, Γ) parameters detailed above.

We can make a brief comment here about the effect of the host galaxy emission. The optical jet sources are generally at low redshift, and the host galaxy is well resolved. The source fluxes listed in Table 7.1 for these cases are the integrated fluxes over the entire galaxy. Thus, the jet-to-source ratios are really $f_{\rm jet}/(f_{\rm core}+f_{\rm gal})$ (since the central source flux will be included in the integrated flux). Now, for the PHFS sources, the host galaxy is generally unresolved and at a much lower flux level than the central continuum (Masci et al. 1998). This can be expressed as $f_{\rm gal} \ll f_{\rm core}$, which implies that

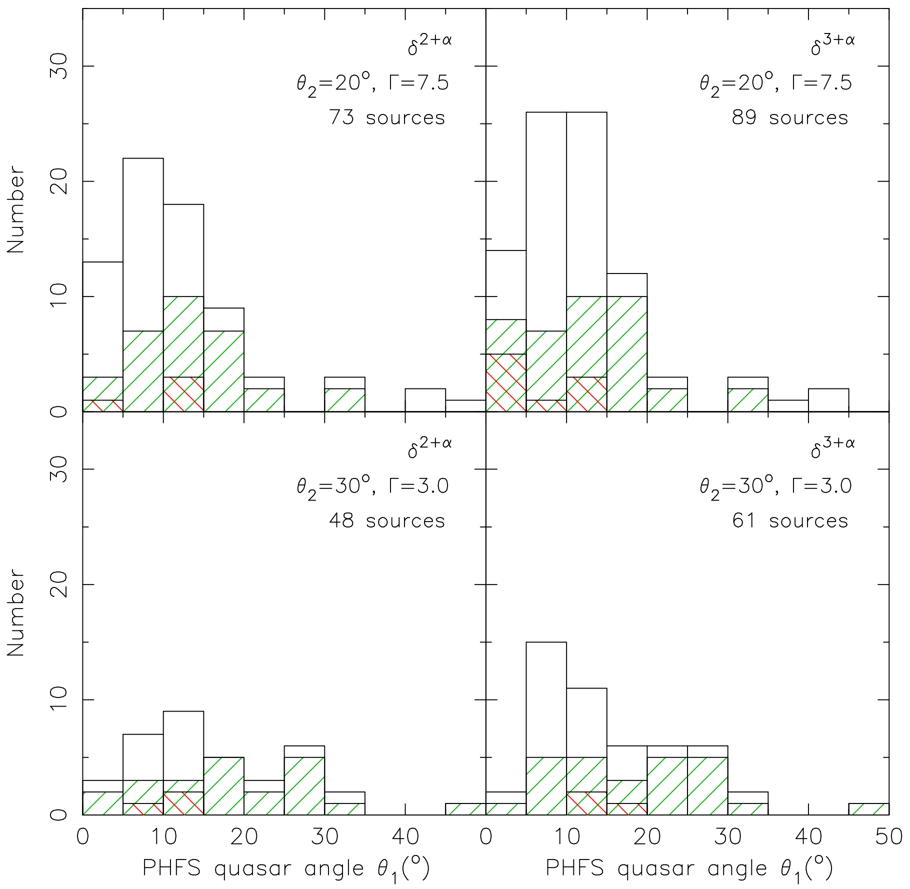

Figure 7.2: Viewing angles for the PHFS quasars, for different Γ and θ assumptions, as well as different Doppler boosting dependencies. The open histograms are all sources with combined model fits, while the green hatched histograms are those sources best fit by the combined model (in preference to the power law model – see Chapter 5 for details on the fitting). The red hatched histograms are the BL Lac objects.

$f_{\rm jet}/f_{\rm core} \approx f_{\rm jet}/(f_{\rm core} + f_{\rm gal})$. Hence, the ratios used are consistent with each other, assuming the host galaxy emission in the PHFS sources is much less than the emission from the central source.

Also needed to calculate the viewing angle is the value of the Doppler index p. The calculations are performed for the two cases of $p = 2 + \alpha$ and $p = 3 + \alpha$. For the optical jet sources, α is taken to be 1.4 (the average value for optical jets as calculated from published values – see Section 2.2.1). For the PHFS sources, α is calculated from the observed fitted synchrotron component by taking the average slope of just the synchrotron component (since it is just the jet emission we are concerned with here), between the

p	(θ_2,Γ)	θ_1 (°) (All)		θ_1 (°) (Combined fits)	
		Average	Median	Average	Median
$2+\alpha$	(20°,7.5)	14.0	10.6	13.8	12.7
$3+\alpha$	(20°,7.5)	13.4	10.6	12.5	11.9
$2+\alpha$	(35°,3)	30.8	20.8	22.4	19.5
$3+\alpha$	(35°,3)	26.5	16.8	21.4	20.2

Table 7.2: Table showing the average and median viewing angles for the PHFS quasars, for a range of different (θ,Γ) values and options for the Doppler index p.

observed wavelengths of 0.4μm to 0.8μm (simulating a power law index calculated from two measurements made at these wavelengths).

The resulting viewing angles are plotted in Fig. 7.2, for all sources that have a combined fit (recall that some sources are not able to be fit by the combined model as their SED is bluer than the assumed blue power law), and also for those sources that are best fit by the combined model when compared to the power law model. The angles for the BL Lacs (which are all fit best by the combined model) are also shown. The average and median angles are shown in Table 7.2.

Not all sources are plotted on any graph. This is due to some sources having an R value outside the range specified in Eqn. 7.5. Either Doppler beaming alone cannot explain these large (or small) ratios of jet flux to core flux, or the assumed values of Γ or θ_2 do not apply.

Note that for the smaller angle – high energetic case for the optical jets, the PHFS angles are smaller, with the distribution concentrated below $\sim 15°$. For the less energetic case, the distribution is more spread out, and there are fewer sources for which the beaming model works (i.e. for which the value of R is within the allowed range).

An interesting point to draw out of Fig. 7.2 is that the BL Lacs are not preferentially at the low angles, as might be expected from the pure beaming hypothesis (i.e. that the BL Lac phenomenon is due to a relativistic jet viewed at a small angle to the line of sight). Instead, they are consistent with having the same distribution as the non-BL Lac synchrotron sources. This is largely due to the spread in values of R seen in Fig. 5.7.

This raises an interesting point: are the BL Lacs significantly different from the non-BL Lacs in the PHFS, for any of their properties? The model fitting performed in Chapter 5 provides an excellent basis to do this, and this will be discussed in the following section.

7.3 Modelling results for the PHFS BL Lacs

We can use the modelling results to explore the differences (and similarities) between the quasars and BL Lacs in the PHFS, since the sample contains both types of objects. In determining which sources in the PHFS are BL Lacs, we have used two particular catalogues. The first is that of Padovani and Giommi (1995), which was used as the primary source of classification as either a BL Lac or a BL Lac candidate (more on this classification below). The second is Table 2 of Véron-Cetty and Véron (2000) – this was used if a source was not listed in Padovani and Giommi (1995).

It should be noted that whether a source is a BL Lac or not is subject to some uncertainty, as it depends on the quality of the optical spectra used for the determination, and also on the source itself. Some BL Lacs have been shown to exhibit broad emission lines when they are at a low overall flux level, including BL Lacertæ itself! (Corbett et al. 1996; Vermeulen et al. 1995) (We do note, however, that these lines, when seen, do have quite small equivalent widths – albeit greater than the 5Å cutoff for BL Lacs.) Another example is the BL Lac 0537−441 (see the spectrum, taken by Wilkes et al. (1983), in the plot in Appendix D, which exhibits a significant Mg II line). Often sources that may be BL Lacs are classed as "BL Lac Candidates", which generally means that the spectrum used shows no significant emission lines, but that the spectrum itself was not of sufficient quality to confidently declare the object a BL Lac.

7.3.1 Parameters from modelling

Are the BL Lac objects physically different from the other PHFS quasars, or do they represent just one extreme of a continuum of variations (in this case, in emission line strength)? The distributions for a number of key parameters from the fitting (the power law slope, the peak synchrotron wavelength and the relative strength of the synchrotron component at 0.5μm) are shown in Fig. 7.3, along with the distribution of both the absolute magnitudes and the equivalent widths of the Mg II 2798 and Hβ lines. These equivalent widths are taken from Francis et al. (2001) – details of the measurements can be found therein. Note that the spectra are not simultaneous with the

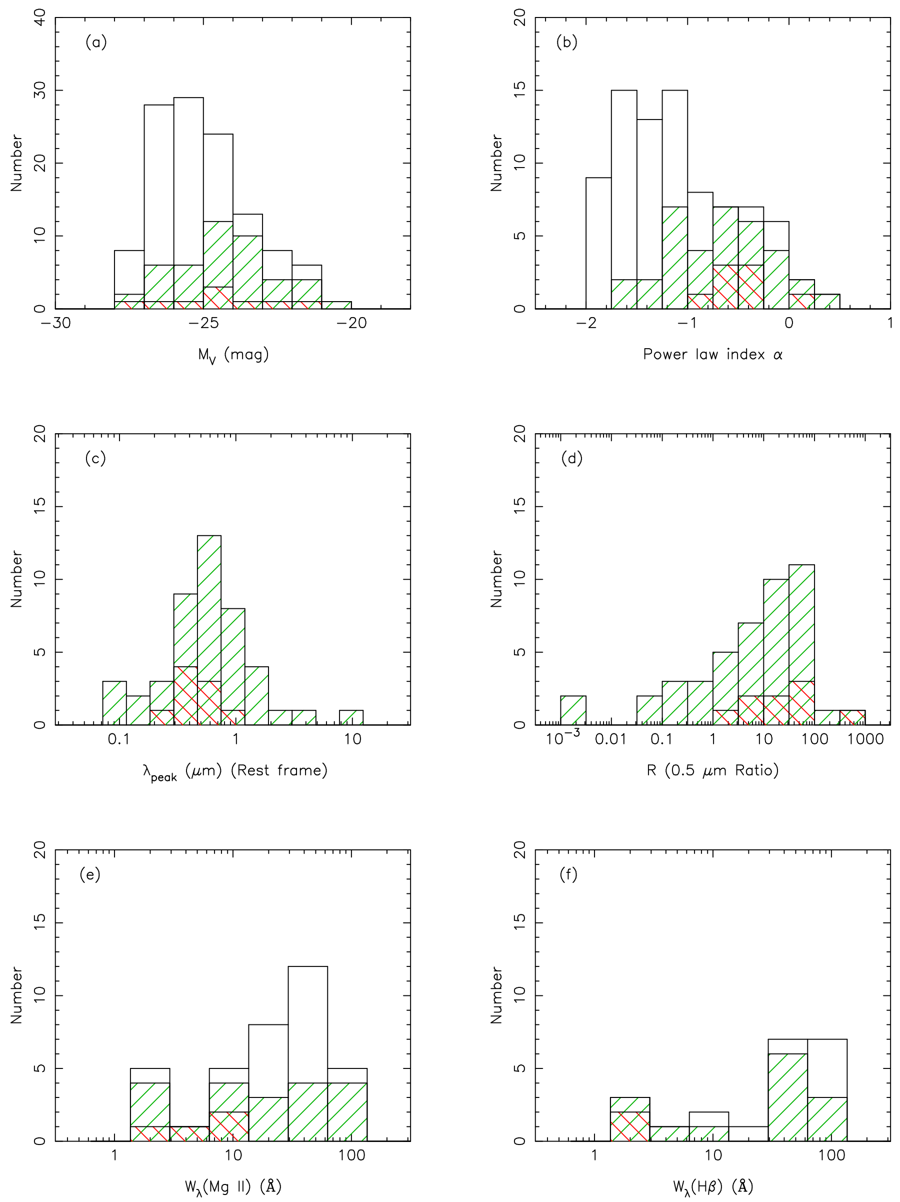

Figure 7.3: A summary of the modelling (and other) results, showing where BL Lacs are in relation to the rest of the PHFS. For all plots, the open histogram shows all sources with a good power law fit (with the exception of (a), where it is all sources that are used in the model fitting – i.e. from Table B.1), the green shows those sources best fit by the combined model, while the red shows the BL Lacs. (a) Absolute V magnitudes of the sources, calculated from the photometry using $H_0 = 75$ km s^{-1} Mpc^{-1} and $q_0 = 0.5$. (b) Power law index from the power law fit of Section 5.1. (c) The peak wavelength λ_p from the combined fit of Section 5.2 (for sources best fit by the combined model). (d) The ratio of synchrotron to power law flux for the combined model at 0.5μm (again, for sources best fit by the combined model). (e) Equivalent widths of Mg II. (f) Equivalent widths of Hβ.

photometry observations. The median values for each parameter are listed in Table 7.3, for BL Lacs as well as the non-BL Lacs (including all the non-BL Lacs and those best fit with a synchrotron component).

Firstly, how do the luminosities of the BL Lacs compare to the rest of the sample? Fig. 7.3a shows the values of M_V (calculated in the same way as in Section 4.4, with $H_0 = 75$ km s^{-1} Mpc^{-1} and $q_0 = 0.5$), for all sources that have been modelled. Also shown are the distributions of the synchrotron-dominated sources (i.e. those best fitted with the combined model), and the BL Lac objects. There is no statistical difference between the BL Lac objects and the rest of the synchrotron-dominated sources, and minimal difference (still not statistically significant) between the BL Lacs and the rest of the sample as a whole.

The next point to note is that, in comparison to the whole PHFS, the BL Lacs are redder (Fig. 7.3b). They are also, in fact, redder as a group than the objects that are best fitted by the combined model, although the difference here is significant only at the 95% level – see Table 7.3.

If just the synchrotron fits for the combined model sources are considered, there is very little difference between BL Lacs and non-BL Lacs. The median λ_p (Fig. 7.3c) is slightly shorter for BL Lacs (0.44μm compared to 0.67μm), but this is not significant – the two distributions are consistent with being from the same parent distribution. Similarly, there is no statistical difference between the two synchrotron ratio distributions (Fig. 7.3d), although the BL Lacs do have a larger median ratio (15.7 compared to 6.1 for the non-BL Lacs). In Table 7.3 are also listed the Kolmogorov-Smirnov probabilities that the BL Lac and non-BL Lac distributions come from the same parent distribution – a low probability indicates that the parent distributions are likely to be different.

7.3.2 Emission lines and BL Lacs

If one looks at the equivalent widths of both the Mg II and Hβ emission lines (Fig. 7.3e,f), it can be seen that the BL Lac objects are at the lower extreme of the distribution, consistent with their definition. Note also that the non-BL Lac synchrotron sources have a large range of equivalent widths: some have very small emission lines, while others have quite large ones.

Does the synchrotron component that has been fitted to the optical/NIR continuum decrease the equivalent width of the emission lines, as expected

Parameter	Median values			K.-S. Prob. (%)	
	All	Comb.	**BL Lacs**	(All)	(Comb.)
M_V (mag)	-25.30	-24.07	**-24.34**	20.25	81.92
α_{PL}	-1.22	-0.78	**-0.42**	0.01	4.60
λ_p (μm)	—	0.67	**0.44**	—	24.21
$R(0.5\mu\mathrm{m})$	—	6.10	**15.67**	—	97.82
W_λ(Hβ) (Å)	46.67	45.59	**2.59**	2.73	4.26
W_λ(Mg II) (Å)	31.79	30.33	**5.33**	0.46	2.54

Table 7.3: This table shows the median values of the distributions in Fig. 7.3 for BL Lacs compared to the non-BL Lac sources (All = all non-BL Lacs with a good power law fit; Comb. = all non-BL Lacs best fit with the combined model). Also shown are the Kolmogorov-Smirnov probabilities that the BL Lac and non-BL Lac distributions are from the same parent distribution.

under the "swamping hypothesis"? One would expect that adding a non-ionising synchrotron component to the continuum will have the effect of reducing the equivalent width of the emission lines from the BLR, due to the fact that the flux in the emission lines is not changed but the continuum flux is increased.

To test this prediction, we compared the equivalent widths of five emission lines (C IV 1549, C III] 1909, Mg II 2798, Hβ, and the doublet [O III] 4959,5007) with the ratio of synchrotron to continuum flux at the line wavelength, to see if some form of an anti-correlation is present. The details of the spectral dataset will presented elsewhere (Francis et al. 2001). Objects that had spectra taken were essentially a random sample of the PHFS (subject to visibility during the observing runs).

Fig. 7.4 shows the results of this comparison for the Mg II and Hβ lines, which are the two broad lines with the longest wavelength (and hence the two lines most likely to show a reduction in equivalent width). Those sources best fit with the power law model are also shown: the value of the ratio used for these sources was taken from fitting the combined model, and so are upper limits to the ratio.

The Mg II line does not show much relationship to the synchrotron ratio, while the Hβ line does show a reduction in equivalent width with increasing amount of synchrotron. This lends some support to the hypothesis that excess synchrotron light is present. The difference in the two plots is likely due to the presence of the turnover in the synchrotron flux, so that it has less

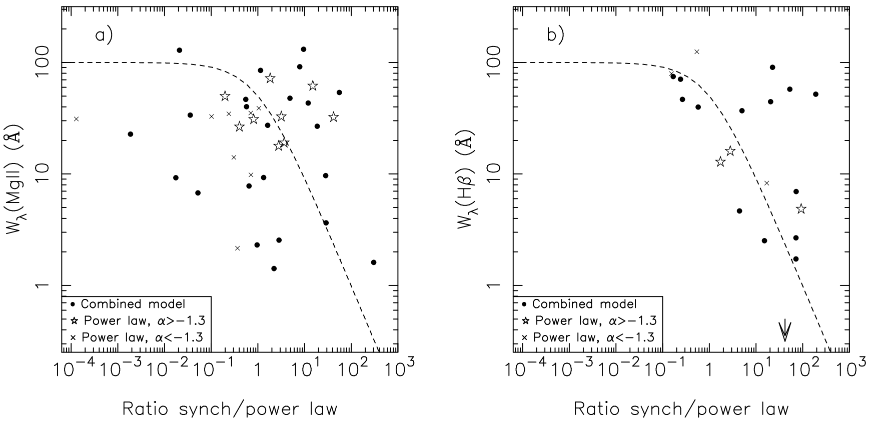

Figure 7.4: The equivalent width of a) the Mg II and b) Hβ lines as a function of the ratio of synchrotron to power law flux at the emitted wavelengths. The sources are given different symbols according to the nature of their best fit model (the arrow indicates an upper limit for a source that was best fit with the combined model). Ratios for sources best fit by the power law model are calculated from the combined model fits, and so are upper limits to the ratios (for the crosses and stars). The dashed lines represent the expected change in equivalent width with increasing amount of synchrotron, for an emission line with intrinsic equivalent width of 100Å.

effect at the shorter wavelength of Mg II. There are, however, several sources that have high synchrotron ratios together with high equivalent widths.

7.4 Implications for the nature of BL Lacs

What do the results of the modelling for the BL Lacs tell us? Firstly, the fitted values of λ_p and R indicate that the BL Lacs, as a group, are not statistically different from the rest of the sources with synchrotron-dominated spectra. They are generally redder than the population as a whole, and slightly (but not significantly) redder than the synchrotron-dominated sources. The bulk of the difference in this latter case seems to be made up by the sources with a blue optical SED and a redder NIR – i.e. where the synchrotron component turns over in the optical range.

The main difference between BL Lacs and non-BL Lacs is, not surprisingly, the equivalent widths of the emission lines. By selection, the BL Lacs are preferentially the objects with low equivalent widths. The median Hβ equivalent widths for the BL Lacs and non-BL Lacs are 2.6Å and 46.7Å respectively (or 45.6Å if just the synchrotron-dominated non-BL Lacs are used).

7.4.1 Emission lines

Why do the emission lines have such small equivalent widths? The equivalent width is calculated by dividing the integrated line flux that is above the continuum by the average continuum level over the extent of the line. Thus, a comparatively low equivalent width means that either the continuum level is comparatively high, or the flux in the line is comparatively low.

We note first that there is evidence from the literature that the level of the continuum is important, as emission lines have been seen in BL Lacs when they are at a low flux level (e.g. BL Lacertæ). However, even in these cases, the lines are still relatively weak (BL Lacertæ's Hα equivalent width was measured by Vermeulen et al. (1995) to be 15.3Å, and only 5.6Å by Corbett et al. (1996)). So it seems that a large continuum cannot be the whole story, although it is undoubtedly important in many sources.

If a large continuum is important for the PHFS BL Lacs, could this be accounted for by the synchrotron component? Fig. 7.4b partially supports this hypothesis, as there is a trend for the equivalent widths of Hβ to decrease with increasing amount of synchrotron. However, there does appear to be a large dispersion in the distribution of equivalent widths, particularly at high synchrotron ratios, with sources present that have relatively high ratios at Hβ, as well as large equivalent widths.

Also, there is little evidence that the level of the continuum in BL Lacs is larger than that in the non-BL Lac sources. Certainly the ratios of synchrotron to power law appear to be larger (although statistically they are consistent with being the same as the rest of the synchrotron-dominated sample), and this accounts for the slightly redder colour of the BL Lacs when compared to the rest of the synchrotron-dominated sources. However, the continuum levels are not very much larger than those of the non-BL Lacs. This is seen in Fig. 7.5, where the equivalent widths of the Mg II and Hβ lines are compared with the luminosity of the fitted SED (i.e. approximately the continuum level) at the line wavelength. The luminosities of the BL Lacs have the same range of values as the non-BL Lacs, and there is no correlation between the luminosity of the continuum, represented by the value of the fitted SED, and the equivalent width of the emission lines. We do add the standard caveat here that the spectra and the photometry (to which the models are fitted) are non-simultaneous, so there is always the possibility that the source has varied in between the two observations.

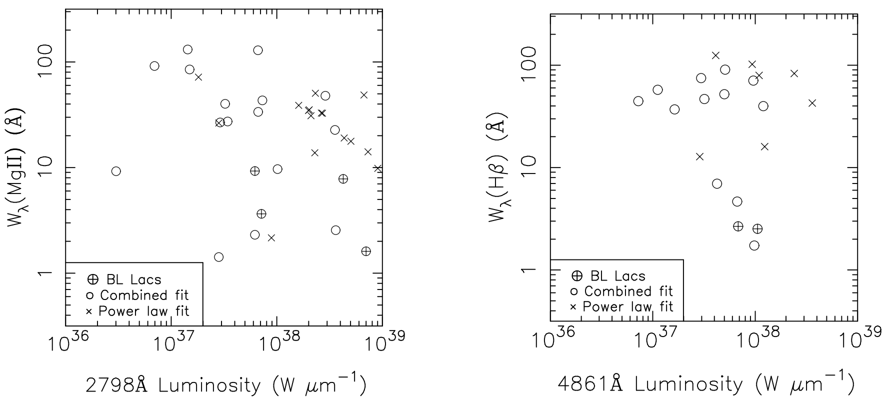

Figure 7.5: Equivalent width of emission lines as a function of the luminosity of the fitted model at the wavelength of the line. The different symbols show either if the source is a BL Lac or, if not, whether it was best fit by the combined model or the power law model.

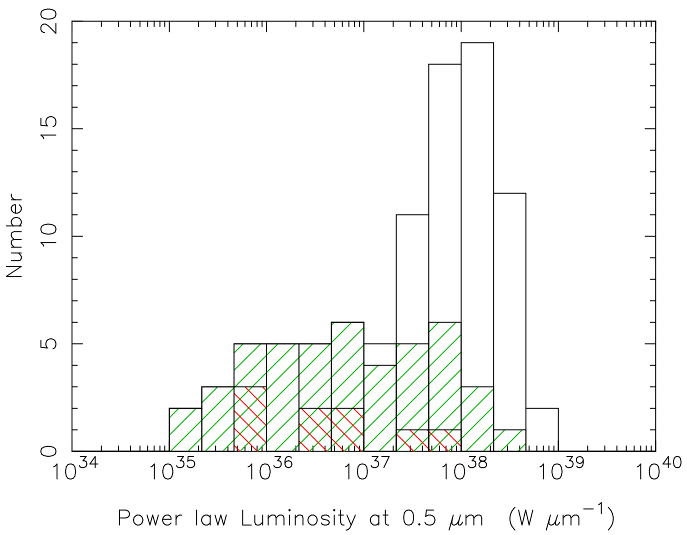

Figure 7.6: A histogram of luminosities of the fitted power law components, evaluated at a rest wavelength of 0.5μm (with H_0 = 75 km s^{-1} Mpc^{-1}and q_0 = 0.5). The open histogram is all sources with a good power law fit, the green is those sources best fit by the combined model, while the red is the BL Lacs.

An alternative explanation for the small equivalent widths is that the line fluxes in the BL Lacs are intrinsically small compared to the non-BL Lacs. This could be due to one of two reasons: there are no (or not enough) ionising photons present to provide the necessary excitation (for example, due to a small, or absent, accretion disk); or there is not enough emission line gas.

Do the BL Lacs have accretion disks? If so, are they as powerful as those seen in the non-BL Lac objects? These questions can be investigated by examining the strength of the power law component in the model fits. The luminosities of the power law components (either the BBB power law in the combined fit or the single power law from the power law fit) are shown in Fig 7.6, calculated at a rest wavelength of 0.5μm, with $H_0 = 75$ km s^{-1} Mpc^{-1}and $q_0 = 0.5$.

The BL Lac distribution is clearly different from that of the rest of the sample (and is significant at the 99% level). However, there is no difference between the BL Lac distribution and that of the rest of the sources best fit by the combined model, indicating that the BL Lacs do not have significantly smaller blue power laws than the non-BL Lac synchrotron-dominated sources. We get a similar result if the power law luminosity is calculated at a wavelength of 0.1μm (this is closer to the likely energies of the ionising photons). We do note, however, that visual inspection of the fits shows the presence of a significant power law component in only two sources (0537$-$441, which, as was noted in Section 4.5, is a highly variable source and may have an SED affected by short-term variability; and 2131$-$021). The rest of the BL Lacs have very small contributions from the power law component, even at the blue end of the SED. This is, of course, also the case for many of the non-BL Lac sources (although many of these have red SEDs that may be due to dust absorption rather than synchrotron emission), but is indicative of the fact that the BL Lacs have their optical SEDs dominated by synchrotron.

Nevertheless, the similarity of the power law strengths in the BL Lacs and some of the non-BL Lacs may indicate that the cause of the small emission lines in BL Lacs, rather than being a lack of ionising photons, is instead a simple lack of emission line gas.

7.4.2 UV spectra

A further way to differentiate between different causes of the small emission lines in BL Lacs would be to examine their ultra-violet spectra. If the emission lines are being swamped by a non-thermal (i.e. synchrotron) emission component, then, as is shown in the modelling in this thesis, this component will turn over at some wavelength. It is therefore likely to be far less important at the shorter wavelengths, near for instance the emission lines of Lyα and C IV. These lines need to be observed in the UV, as most BL Lacs are not of sufficient redshift for the lines to move into the optical region.

If the UV lines are strongly visible (i.e. do not seem to be reduced or swamped in any way), then this would indicate that the lack of emission lines at optical wavelengths can be explained by the swamping by a continuum that turns at longer wavelengths that the UV lines. If, however, the UV lines are either weak or absent, then either the swamping continuum extends past the UV, or the emission line region is intrinsically weak.

A large resource with which to perform this test is the catalogue of *IUE* spectra of quasars and BL Lacs by Lanzetta, Turnshek, and Sandoval (1993). This study contained 24 sources from the PHFS, including 7 sources classed as BL Lacs (namely 0048−097, 0118−272, 0301−243, 0422+004, 0537−441, 0829+046 and 1253−055 (3C 279)). None of the BL Lacs showed any significant emission lines in their spectra (that generally ranged from 1200Å to 3200Å), while many of the other PHFS quasars showed strong emission lines (typically Lyα, C IV, and sometimes C III]). This indicates that the lack of emission lines seen in BL Lacs in the optical extends to shorter wavelengths as well. This is confirmed by Kinney et al. (1991), who presented *IUE* spectra of 69 quasars and "blazars". The majority of the blazar objects presented showed no significant emission lines in their UV spectra.

We do note that Wills et al. (1995), who obtained UV spectra of 31 radio-loud quasars with *HST*, did observe emission lines (Lyα, C IV and C III]) in 1253−055. However, in each case these lines had the smallest equivalent widths of all objects observed. Quasars are very active in the ultraviolet (Kinney et al. 1991), and so it is likely that the synchrotron continuum (should that be present and responsible for diluting the emission lines) had varied in this source in the period between the two observations (1253−055 is seen to be very variable in other frequency bands).

7.4.3 Unification models

Orientation-based

What do these results tell us about possible unification models for radio-loud AGN? One of the main unification models is that describing BL Lacs and quasars respectively as beamed versions of FR I and FR II radio galaxies (i.e. viewed at small angles to the direction of propagation of the relativistic jet). Can we explain the observed differences (or similarities) between the BL Lacs and quasars in the PHFS in terms of this model? One difference between the two classes is their optical–NIR colour, with BL Lacs being redder. This is almost certainly due to the presence of a strong synchrotron component in all the BL Lacs (while there is not one in all the non-BL Lac quasars), and so does not relate to the nature of the parent population. The second, and major, difference is the distribution of equivalent widths, with BL Lacs having substantially weaker emission lines than the non-BL Lacs, due to a relative lack of emission line flux.

Is this compatible with the unification model? FR Is, the putative parent population of BL Lacs, do have significantly lower emission line luminosities than FR IIs of the same total radio power (Zirbel and Baum 1995), which is in accord with our finding here. We do note also that some FR IIs only show weak, low-excitation lines in their spectra (Laing et al. 1994), and so may also be included in the BL Lac parent population. Other than this finding (which is consistent with previous results), the modelling does not shed much light on the veracity or otherwise of this unification model.

Synchrotron-based

Another popular unification model is that of Fossati et al. (1998), which unifies all "flavours" of BL Lacs (from LBL to HBL) as well as FSRQs, on the basis of the peak of the synchrotron component. Under this scheme, the multi-wavelength SEDs of blazars are made up primarily of two broad peaks, representing the synchrotron emission (the low-frequency peak – roughly IR to soft X-rays) and the inverse-Compton emission (the high-frequency peak – roughly hard X-rays to gamma rays). The frequency of the synchrotron peak is related to the overall luminosity of the source, in the sense that the more luminous objects (which are generally the FSRQs) have lower frequency peaks, while the less luminous objects (HBLs) have higher frequency peaks.

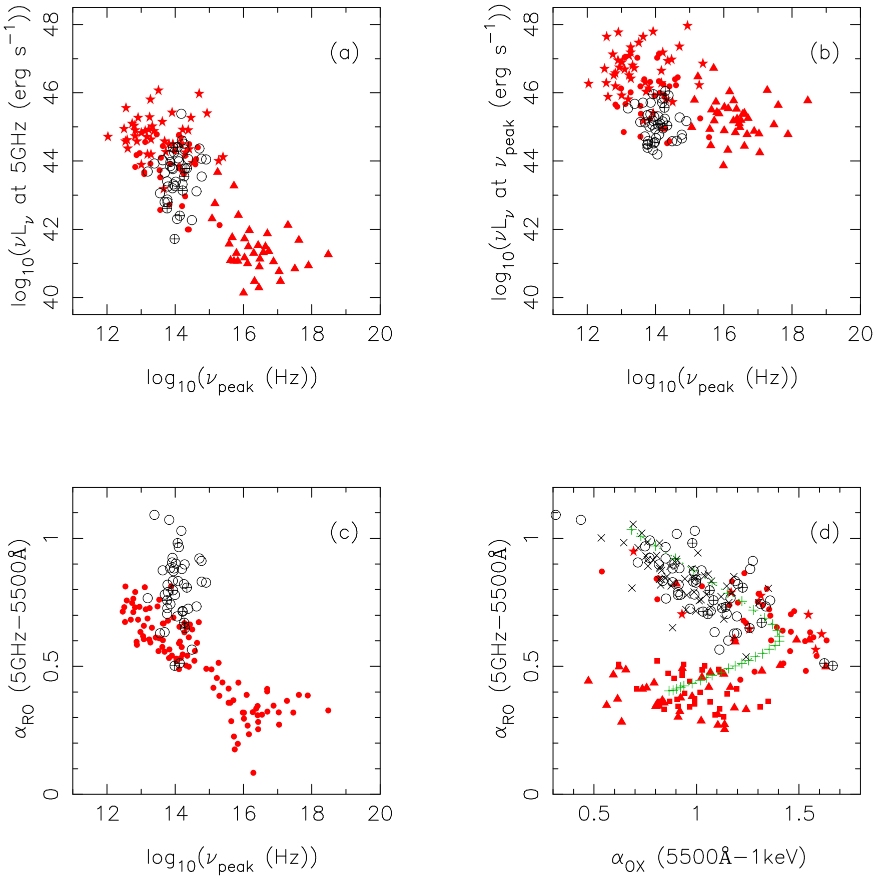

Figure 7.7: Comparison of the PHFS sources with the data from Fossati et al. (1998) and Fossati et al. (1997). a) Radio luminosity versus peak frequency. b) Peak luminosity versus peak frequency. c) Radio–optical slope versus peak frequency. d) Radio–optical slope versus optical–X-ray slope. The red points are data from Fossati et al. (1998) (for (a), (b) & (c)) and Fossati et al. (1997) ((d) only): star = FSRQs; circle = 1 Jy BL Lacs; triangle = Slew BL Lacs; square (in (d)) = EMSS BL Lacs. Green plus signs in (d) are from best fitting SED parametrisations of Fossati et al. (1997). The other points are PHFS sources, with symbols relating to their best fit from the model fitting: cross – best fit by power law; circle – best fit by combined model; circle with plus – BL Lac.

The objects on which this analysis was based were taken from three complete samples of blazars: the Slew survey (an X-ray survey made with the *Einstein* satellite (Elvis et al. 1992), from which was selected a sample of BL Lacs (Perlman et al. 1996)); the 1 Jy sample of BL Lacs (a radio survey, (Stickel et al. 1994)); and the 2 Jy survey of FSRQs (another radio survey – the sample is that of Padovani and Urry (1992), drawn from Wall and Peacock (1985)). The result of this sampling is that the sources that are analogous to the PHFS sources are all bright (either brighter than 1 Jy or 2 Jy depending on the survey, whereas the PHFS sources go down to 0.5 Jy), and the data used is non-simultaneous. We can therefore use the PHFS sources to explore whether the conclusions hold as the radio flux is reduced, and use the simultaneous photometry to get a better idea of where the synchrotron peak is.

Fossati et al. (1998) find a number of correlations between luminosity, synchrotron peak frequency, and radio–optical spectral slope. We show these in Fig. 7.7, and compare their data with that of the PHFS sources. We also compare the PHFS data with the model SEDs of Fossati et al. (1997) in a colour-colour diagram. The peak frequencies used for the PHFS sources are defined as $\nu_{\rm peak} = c/5\lambda_p$, which gives the approximate value of the peak of the νf_ν SED (this matches the $\nu_{\rm peak}$ values found by Fossati et al. (1998)). The radio fluxes used are either the contemporaneous fluxes from the ATCA, or, if these are not available, the fluxes from PKSCAT90 (Wright and Otrupcek 1990). The X-ray fluxes used in Fig 7.7d are from Siebert et al. (1998). (Note of course that neither the radio fluxes nor the X-ray fluxes are simultaneous with the optical photometry.)

The two luminosity–peak plots (Figs 7.7a&b) show that the sources from the PHFS are somewhat consistent with the data of Fossati et al. (1998), although the fact that the PHFS sources are of lower luminosity has resulted in lower luminosities at both the radio and peak frequencies. The correlation of peak luminosity with peak frequency is consequently reduced (Fig. 7.7b). The major difference is apparent in Fig. 7.7c. The PHFS sources have a greater range in optical fluxes and are generally lower in flux (see Fig. 7.8), and so even though the radio fluxes are generally less than the 1 Jy and 2 Jy sources, the radio–optical slope is still steeper for many sources (the slopes here are defined such that $F_\nu \propto \nu^{-\alpha}$). This moves the PHFS points away from the Fossati et al. points (and also away from the locus of points

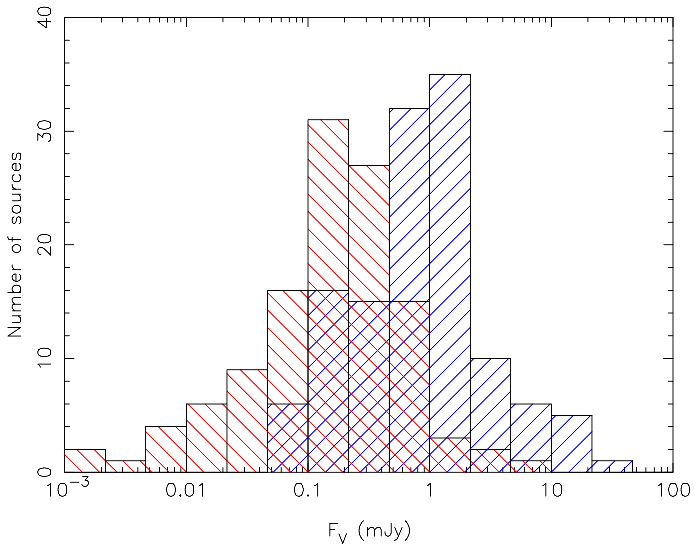

Figure 7.8: Comparison of optical fluxes (at V band) of PHFS sources (the red histogram) and sources from Fossati et al. (1998) (the blue histogram). The PHFS fluxes are calculated from the quasi-simultaneous photometry (Chapter 4).

predicted by their "synthetic" SEDs, which, although not shown in Fig. 7.7c, form a smooth curve through the middle of the red points).

Finally, Fig. 7.7d shows the radio–optical slope as a function of the optical–X-ray slope, for data from Fossati et al. (1997) (a slightly different data set from that of Fossati et al. (1998)), along with predictions from their SED parametrisation. The PHFS sources are also shown. They tend to fall in approximately the same region of the plot as the FSRQs and 1 Jy BL Lacs, as one would expect. However, on closer examination, we see that the majority of the points lie below the predicted points (in green), based on the "two-peak" SED model. This has two possible explanations, and both are important for the PHFS sources. Firstly, the radio flux will be slightly lower for many of the PHFS sources, since the radio flux limit is less, which will reduce the value of α. Secondly, from the fitting in Chapter 5, many of the PHFS sources have some power law emission present at optical wavelengths, which is not due to synchrotron emission. This component, which is not included in the Fossati et al. models, will contribute a substantial amount of the flux, thereby reducing the value of α from that expected of a pure synchrotron model.

7.5 Summary

The model-fitting performed in Chapter 5 provides an excellent way to compare the BL Lacs with the non-BL Lacs in the PHFS. We find that the BL Lacs are generally redder than the rest of the sample, particularly when compared with the sources best fit with a power law. However, this is the only significant different to arise out of the modelling. In all other model parameters, the BL Lacs are consistent with having the same distribution as the non-BL Lacs.

The main difference between the two classes is, not surprisingly, the equivalent widths of the emission lines. The BL Lacs have much smaller equivalent widths – on average an order of magnitude smaller. This seems to be caused by the emission lines having intrinsically low fluxes, as there is little difference between the continuum luminosities of the BL Lacs and the non-BL Lac sources, and no correlation between the continuum luminosity and the equivalent widths.

The low emission line fluxes in the BL Lacs are more likely to be due to a relative lack of emission line gas, since the luminosities of the power law component of the combined fit (which has been taken to represent the emission from the accretion disk, or big blue bump) are no different between the BL Lacs and non-BL Lacs. This suggests that both classes of sources have the same amount of ionising photons, but the BL Lacs have less gas to get ionised, resulting in lower emission line fluxes.

Finally, what can we learn about unification schemes from this analysis? The BL Lacs do tend to have relatively low emission line luminosities, which is consistent with them having FR I radio galaxies as their parent population. However, the fact that we find little difference (apart from emission line properties) between the BL Lacs and the other synchrotron-dominated quasars indicates that the region from which the optical synchrotron emission originates is similar in both types of objects. In the context of unification schemes (Urry and Padovani 1995), this probably indicates that the jets in FR Is and FR IIs have similar structure, particularly in the inner regions (where the optical synchrotron emission is more likely to originate).

The analysis of the "two-peak" unification model (Fossati et al. 1998) produced a couple of interesting conclusions. We have seen that by using less luminous objects (the PHFS has a lower flux cut-off than the samples used by Fossati et al. (1998), and the objects are often much fainter in the optical), the correlations found in the model are not as strong. Also, the Fossati et al. model does not account for the presence of the power law emission that is present (or indeed dominant) in many of the PHFS sources. This shows the need to account for all types of emission mechanisms when building models for radio-loud AGN.

Chapter 8

Micro-variability in PHFS Sources

One of the distinctive features of blazar AGN is rapid flux variability, which is seen in every region of the electromagnetic spectrum (Wagner and Witzel 1995). This variability can be on timescales as short as hours to minutes – in this case, it is termed "micro-variability". In the optical, these variations can be of the order of ~ 0.1 mag per night (see the review by Miller and Noble 1996). While some radio-quiet quasars have been shown to exhibit micro-variability (Jang and Miller 1997), it is seen most commonly in radio-loud (mostly blazar-type) AGN. The duty cycle[1] for radio-loud AGN is $\sim 68\%$, compared with $\sim 7\%$ for radio-quiet quasars (Romero et al. 1999) – the figure may be even higher ($\sim 80\%$) for radio-selected BL Lacs (Heidt and Wagner 1996).

Based on these numbers, it is reasonable to expect to see micro-variability in quasars and BL Lacs from the PHFS, and this chapter contains an investigation into the existence of micro-variability in three such sources. With the above figures, if three objects are observed there is a probability of $\gtrsim 97\%$ of seeing micro-variability in at least one source.

[1]The fraction of time that an object in a given class is variable. This figure is determined observationally by taking the ratio of the time for which objects of a given class are variable to the total observing time for objects in that class.

8.1 Observations

On the night of the 3rd of August, 1999, three PHFS AGN were observed[2] multiple times in three NIR filters over the course of $\sim$ 7.5 hours, in an attempt to detect short timescale micro-variability. The observations were made with the *CASPIR* near-infrared detector on the Australian National University's 2.3m telescope, at Siding Spring Observatory, NSW.

The three objects chosen were the following:

2243−123: A quasar, $z = 0.63$, that has been described as an optically variable quasar. Its optical/NIR SED takes the form of a blue power law ($B - K = 2.15$, fitted power law from Chapter 5 of $\alpha = -1.92$). Its optical spectrum shows strong broad Balmer lines and [O III] lines of small equivalent width (Tadhunter et al. 1993).

2240−260: A BL Lac object at $z = 0.774$. It has a redder optical/NIR SED ($B - K = 4.43$, fitted with a strong synchrotron component). High polarisation has been observed in this source (15.1%, Wills et al. (1992)), and only weak, if any, emission lines have been seen. This object was seen to exhibit intra-day variability by Heidt and Wagner (1996).

2233−148: A candidate for a BL Lac (according to Padovani and Giommi (1995)), at $z > 0.609$. This has a similar optical/NIR SED to 2240−260.

Three-colour images of each of these sources are shown in Fig. 8.1, indicating the location of the source and the comparison stars used.

These sources were chosen primarily on the basis of their position on the sky (to enable constant observations for the second half of a night, and to minimise the time required for the telescope to move between each source), and also to examine the potential for micro-variability in both BL Lacs (2240−260 and 2233−148) and blue radio-loud quasars (2243−123).

These objects were observed in three filters: J, H and K_n. Each source was observed eight times in each filter. 2240−260 was observed a ninth time

[2] By the author, with the assistance of Alicia Oshlack.

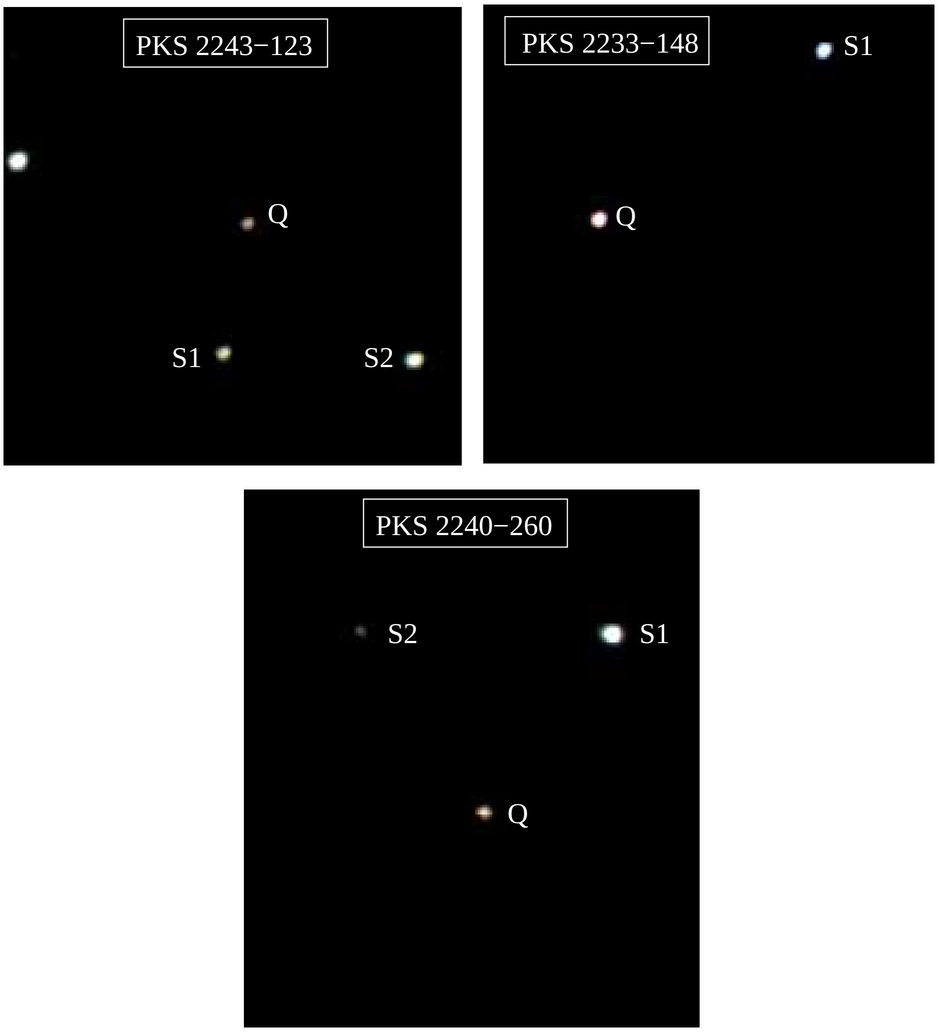

Figure 8.1: Three-colour composite NIR images of the sources used for the micro-variability analysis. The source in question is indicated by a "Q", while the comparison stars are indicated by "S1" and "S2". In all images, north is up and east is to the left.

as well, but a low altitude (and consequent high airmass) meant that the observations were unreliable. Standard stars were also observed several times during the night. This enables photometric calibration of the observations, and also calculation of fluxes and spectral indices.

Each of the images comprised of 2×2 dithered 60 second images, each made up of twelve averaged 5 sec exposures in K_n, six averaged 10 sec exposures in H, and two averaged 30 sec exposures in J. The flat field was created from the difference of dome exposures with the lamps on and off – this removes any telescope emission, improving greatly the photometric accuracy. The sky emission was removed by using a median of the four dithered images of the same band taken at the same time. The four images were then aligned and combined using the median (to remove any residual errors). The photometry was done with the *apphot* package in IRAF, using circular apertures with the sky background level determined by the median flux in an annulus around the source. The errors in the photometry shown on the light-curves are purely the random errors from the photometry calculations.

8.2 Measuring the variability

In order to construct light-curves for each of the sources, the differential magnitude of the quasar is measured relative to comparison stars in the same field. This differential magnitude is $\Delta m = m_q - m_c$, where m_q and m_c are the magnitudes of the quasar and the comparison star respectively. This differential magnitude is then compared to the comparison differential magnitude $\Delta m' = m_c - m_{c'}$, where $m_{c'}$ is the magnitude of a second comparison star in the same field. This second differential magnitude acts as a check – a change in flux in the quasar will change Δm but not $\Delta m'$, while a change that occurs in both will not be intrinsic to the quasar. The light-curves are presented in Fig. 8.2. For clarity, they are given an arbitrary offset – the offsets required to obtain the correct differential magnitudes are listed in Table 8.1.

It must be noted here that 2233−148 did not have a second comparison star in the small ($\sim 2'$) field of view of *CASPIR*. This means that the full variability analysis cannot be done for this source. However, a light-curve for Δm is presented, using the one available star.

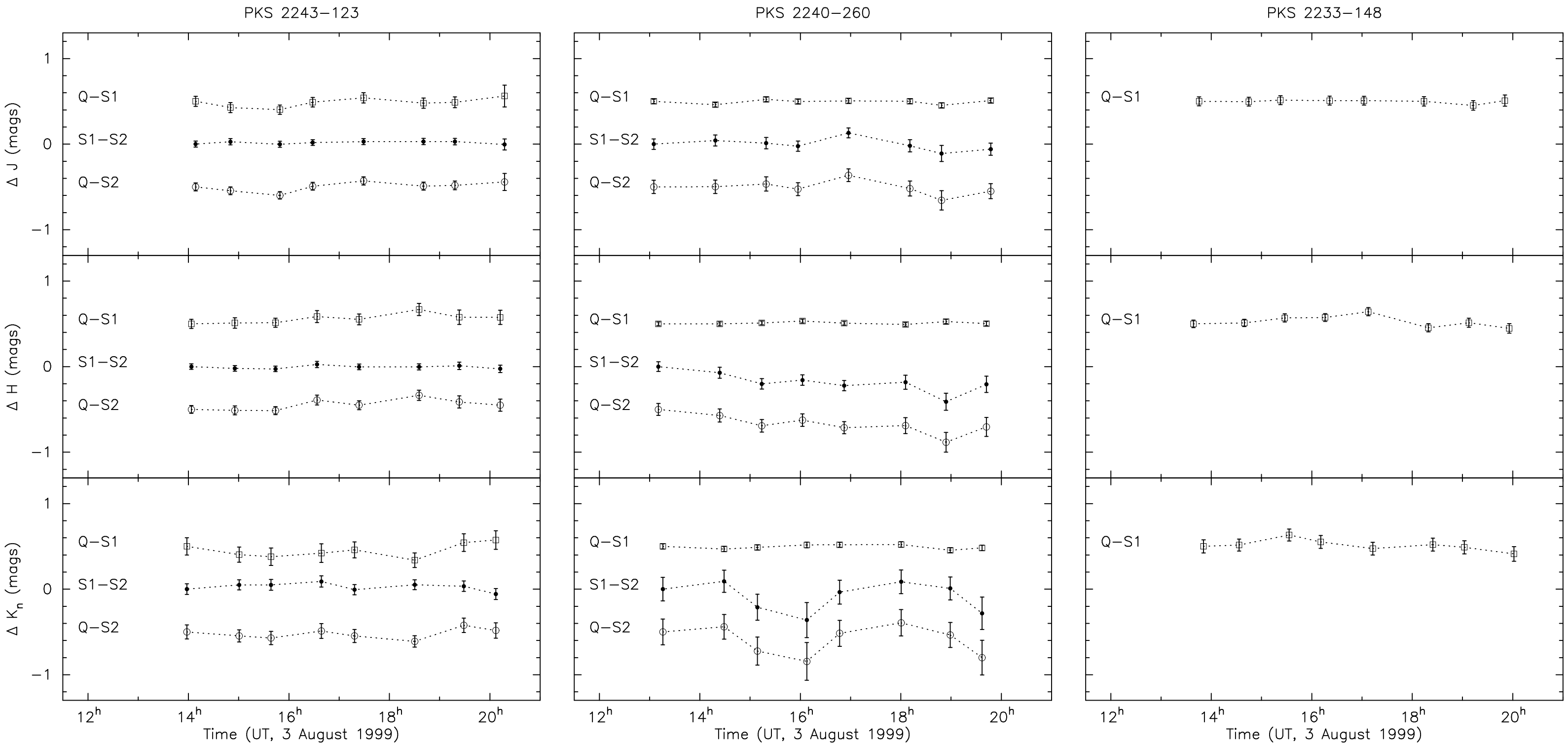

Figure 8.2: Differential light-curves for three PHFS sources. Shown are the quasar-star light-curves for each comparison star, and, where possible, the star-star comparison light-curve. The vertical offsets of each curve are set arbitrarily for clarity of presentation. The values of the offsets are given in Table 8.1.

Source	Band	Q−S1	Q−S2	S1−S2
2243−123	J	0.156	2.365	1.209
2243−123	H	0.292	2.227	0.935
2243−123	K_n	0.004	1.829	0.825
2240−260	J	2.102	−0.971	−4.073
2240−260	H	1.660	−0.964	−3.624
2240−260	K_n	0.990	−1.649	−3.639
2233−148	J	−0.116	–	–
2233−148	H	−0.423	–	–
2233−148	K_n	−1.022	–	–

Table 8.1: Offsets for the micro-variability light-curves presented in Fig. 8.2. To obtain the correct differential magnitude for each light-curve, add the corresponding number from the table to the values in the figure.

To determine whether a given source is variable, we use the 99% criterion from Jang and Miller (1997) and Romero et al. (1999). We define the variability confidence level $C = \sigma_T/\sigma$, where σ_T and σ are the standard deviations of the target (quasar-star) and comparison (star-star) light-curves. The variability criterion requires that, for a source to be variable, $C > 2.576$.

For a variable source, we also define (after Romero et al. (1999)) the variability amplitude to be

$$A = \frac{\sqrt{(D_{\rm max} - D_{\rm min})^2 - 2\sigma^2}}{\langle D \rangle},$$

where $D_{\rm min}$ and $D_{\rm max}$ are the minimum and maximum of the differential light-curve respectively. Table 8.2 shows the values for σ_T for each source with respect to each comparison star, as well as the confidence level C and, when the source is variable, the amplitude A.

8.3 Conclusions

8.3.1 Results

Clear micro-variability is detected in one source, 2243−123. There is strong variability in both J and H bands, while at K band, despite both the $Q - S$ curves showing variability, there is also significant noise present in the comparison light-curve, making it impossible to say with confidence that

Source Name	Band	σ_T (mag)		C		A (%)	
		Star 1	Star 2	Star 1	Star2	Star 1	Star 2
2243−123	J	0.049	0.051	3.39	3.49	24.55	8.98
2243−123	H	0.051	0.060	3.01	3.48	19.51	9.96
2243−123	K_n	0.077	0.055	1.80	1.30	–	–
2240−260	J	0.023	0.077	0.34	1.15	–	–
2240−260	H	0.013	0.106	0.12	0.95	–	–
2240−260	K_n	0.023	0.160	0.14	0.99	–	–
2233−148	J	0.060	–	–	–	–	–
2233−148	H	0.061	–	–	–	–	–
2233−148	K_n	0.018	–	–	–	–	–

Table 8.2: Micro-variability results for the three sources. The standard deviation of the comparison curves of the quasar with respect to each of the comparison stars, in each band. The values of the variability confidence level C are shown where there is more than one comparison star, and the variability amplitude A is shown for the cases where $C > 2.576$.

the quasar itself is varying.

The other two sources show at best only minimal evidence for variability. 2240−260, from its C values, shows no significant variability (in fact, the second comparison star is the cause for any variability seen in the light-curves – this may simply be because it is faint and subject to errors in the photometry). The lack of a second comparison star for 2233−148 means no conclusions can be drawn about the significance of its fluctuations.

It is interesting that the micro-variability was detected in the quasar, and not in either of the BL Lac objects. This quasar was described as an optically violent variable by Shen et al. (1998), although they did not give a reference for this classification (it possibly comes from the description as variable in Hewitt and Burbidge (1993)).

8.3.2 Interpretation

The origin of micro-variability in blazar AGN is not very well understood. There are two main types of models that have been developed to explain the observations. Firstly, there are models that use a shock-in-jet setup. This type of model has been used to explain the radio variability seen in blazars (Marscher and Gear 1985). To produce the optical micro-variability, a thin relativistic shock within a jet encounters a feature, such as a bend in the jet or an inhomogeneity in the density, which causes an enhancement of the observed jet emission (see, for example, Gopal-Krishna and Wiita 1992; Qian et al. 1991).

A second suggestion for the cause of micro-variability moves away from the jet and looks instead at the accretion disk. Perturbations or instabilities on the surface of an accretion disk (such as "hot-spots" – regions of high temperature and/or density) can create micro-variations in the emission (see Mangalam and Wiita 1993, and references therein). It is likely that both models are important for micro-variability in AGN, and the relative importance for individual sources depends on the relative strengths of the jet and disk emission.

The quasar 2243−123 has a blue optical/NIR SED (the photometry from these observations gives the same NIR slope as the photometry presented in Table B.1), and is modelled in Chapter 5 by a blue power law. It thus shows no evidence for synchrotron emission in its optical spectrum (a fact also supported by its observed strong emission lines). Hence, it is unlikely that fluctuations in the jet emission will cause the observed micro-variations, unless the jet is present at a very low level and experiences relatively large fluctuations. It seems that the micro-variability in this source is more likely to be explained by the accretion disk instability model. Such a scenario is consistent with observations of micro-variability in radio-quiet quasars (de Diego et al. 1998; Gopal-Krishna et al. 2000).

This is an important result that deserves following up. A good way to do so would be to select a small sample of quasars (and BL Lacs) that has some sources with synchrotron dominated SEDs (this part of the sample would contain the BL Lacs, based on the modelling in this thesis), and some with blue power law SEDs (in the manner of 2243−123). The observations would ideally cover a greater period of time than that described in this chapter, to increase the probability of seeing variability. The relative amounts of variability in the two types of sources could then be gauged accurately, hopefully giving an indication of how important each model is for micro-variability in radio-loud AGN.

Chapter 9

Conclusions and Discussion

9.1 Emission mechanisms

Synchrotron radiation is a very important emission process in quasars and AGN, due to its very broad band spectrum (extending over many decades of frequency) and its strong polarisation. It is the dominant process at radio frequencies in relativistic jets seen in radio galaxies and quasars, and in some jets (Chapter 2) this synchrotron emission is observed to extend to optical frequencies. Under unified models of AGN, such optical synchrotron jets are expected to exist in core-dominated quasars (such as those found in the PHFS), and this forms the basis for the modelling in this thesis.

A key observation that results from optical synchrotron jets is that the spectral index at optical frequencies is steeper than the average spectral index from the radio to the optical. This indicates that the synchrotron emission is turning over in the optical region – a feature that results from a cutoff or break in the energy distribution of the radiating electrons. This observation is supported by our modelling (see point ② below).

From the analytical theory of synchrotron emission, discussed in Chapter 3, we found that synchrotron emission from a highly ordered magnetic field will exhibit a strong dependence on the viewing angle. This dependence is of the form $L \propto (\sin\phi)^{2.5}$, where ϕ is the angle between the line of sight and the direction of the magnetic field. This finding is significant because it acts in the opposite sense to Doppler boosting. If plasma is moving with some relativistic bulk velocity in a direction close to the line of sight, then the observed flux will be strongly boosted. The amount of boosting will increase as the line of sight angle decreases.

Thus, the angular dependence of the synchrotron emission from an ordered field can decrease the effect of Doppler boosting, particularly at small angles to the line of sight. For such small angles, the bulk Lorentz factor Γ needs to be sufficiently large to be able to observe significant emission from the jet. Conversely, the fact that jets are visible at large angles to the line of sight (such as in radio galaxies), implies that the bulk velocities cannot be too great (else de-beaming occurs, resulting in a reduction of observed flux). The de-beaming is more pronounced for the ordered-field case, due to the relativistic aberration effect. This then places limits on how ordered the magnetic field in jets can be, in order for them to still be seen.

9.2 Data and modelling

It has to be emphasised that the modelling that was performed in Chapter 5 was made possible by the creation of the extraordinary data-set detailed in Francis et al. (2000) and Chapter 4. It is unprecedented in both the breadth and density of its coverage of the optical/NIR spectral region, and in the number of objects contained therein. Also, very importantly, all the observations are contemporaneous, which allows one to draw meaningful conclusions about the nature of the emission processes, confident that the effects of variability have been minimised (i.e. that, for each source, the ratio of fluxes in each pair of wave-bands is intrinsic to the source, and not because the source has varied during the interval between the observations).

The results of the modelling in this thesis can be summarised in the following points:

① Radio-loud quasars require at least two components to fit the rest-frame optical SEDs. These two components are well modelled by an optical power law, which in some sources is similar to the blue power law seen in optically-selected quasars, and a synchrotron component that turns over in the range $0.1\mu\mathrm{m} \lesssim \lambda_p \lesssim 3\mu\mathrm{m}$.

This is one of the very important results of the modelling in this thesis. Firstly, it shows that non-thermal radiation is important, or indeed dominant, at optical frequencies for a large fraction of the PHFS quasars. This synchrotron component is most likely connected with the radio synchrotron emission that comes from the relativistic jet, and so the jet emission extends over at least eight decades in frequency.

Secondly, the non-synchrotron sources are also important. In many studies performed on blazar AGN (including FSRQs), the dominant emission process that is used is synchrotron. It is very rare to see any other emission considered in the optical region, particularly when the broad-band SEDs (i.e. radio through X-ray) are considered (see Fossati et al. 1998, for example, as well as the discussion in Section 7.4.3). This work has shown that, for a large proportion of flat-spectrum radio quasars, synchrotron emission is in fact not dominant at all at optical wavelengths. It is undoubtedly present at some point in the spectrum, but the optical emission is dominated instead by emission that is most likely to be from the accretion disk region.

This draws out the fact that flat-spectrum radio quasars are quite heterogeneous at optical wavelengths – an observation caused, most likely, by the different cutoff wavelengths of the synchrotron component, and possibly by different strengths of the accretion disk as well.

② The model fits require the synchrotron component to have a break or turn-over at some wavelength λ_p in the observed wavelength range. A synchrotron spectrum with this break gives a much better fit to the data than a pure power law synchrotron model.

This break that is fitted to the data is a very sharp (exponential) cutoff. In this respect, the synchrotron emission is similar to that observed from optical jets in radio galaxies and quasars. These objects provide some of the only unambiguous detections of optical synchrotron emission (since the optical emission is coincident with the radio emission, is highly polarised, and is well fit by a synchrotron emission spectrum), and, as such, give strong support for the use of this type of spectrum.

The value of λ_p provides strong constraints on the modelling of particle acceleration and emission mechanisms. The sharp turnover is produced by an abrupt cutoff in the distribution of energies of the radiating particles. We have shown that such a cutoff is necessary to produce the required optical synchrotron spectra.

③ There is more than 4 orders of magnitude variation in the ratio of the synchrotron component to the power law component in those sources fit by the combined model. All the sources identified as BL Lacs lie at the high end of the distribution, although their distribution is not, statistically speaking, significantly different from that of the non-BL Lac objects.

This point again emphasises the heterogeneous nature of the PHFS at optical wavelengths. The sample includes blue quasars, dominated by power-law emission, through to red quasars and BL Lacs where the dominant emission component is synchrotron emission. Additionally, there is a continuum of variation between these two extremes, with many sources showing clear evidence of the presence of *both* components in the optical/NIR region. (A good example is 1510−089, which was found to have both accretion disk and “blazar” components in its optical spectrum by Malkan and Moore (1986), similar to the fit found in this thesis.)

④ The fits are statistically consistent with the data, and the fitting procedure is robust to reasonable changes in the values of the model parameters. Small changes in the assumed values of parameters such as the slope of the power law in the combined model do not change the overall complexion of the results (although the odd source may have a slightly different fit), and the conclusions drawn remain unchanged.

⑤ There may be an excess of red power law sources compared to optically-selected quasars. This will have implications for emission models of accretion disks.

These sources are quite puzzling. They do not appear to have any significant synchrotron emission in their optical spectra, nor do they show any evidence for dust reddening (due to their power law nature – a dust reddened source would be expected to show increasing curvature towards the blue). Yet they have redder slopes than typical blue quasars. Is this connected with their radio-loudness? Perhaps there is an interaction between the radio jet (or the outflow causing the jet) and the accretion disk region which produces this broader (and redder) range of colours. Closer spectroscopic analysis may be the best way to work out what is going on in these sources.

⑥ Sources which are well-fitted by power laws have a synchrotron component which may peak in the IR. In the optical, these sources are similar to optically-selected quasars.

All the PHFS sources have synchrotron emission dominating at radio frequencies. Yet the optical/NIR SEDs for the bluer sources show no evidence for synchrotron emission – they are well described simply by the blue power law seen in optically-selected quasars. Presumably the synchrotron emission must cut-off somewhere between the radio and the optical. These infrared (or even submillimetre) cutoffs would constitute the extension of the distribution of λ_p seen in Fig. 5.6.

On the other hand, the distribution of λ_p may not continue very far to shorter wavelengths than those investigated here. There are a few pieces of evidence to support this. Firstly, the redshift distributions of the sources with combined fits and power law fits (Fig. 5.10) indicated that there may be a lack of short-wavelength-peaking synchrotron components, thereby producing the observed redshift differences. Secondly, there are no observed synchrotron jets with synchrotron spectra that extend into the X-ray region. All observed optical jets show spectra that are steeper in the optical than the radio–optical slope, indicating that all these spectra are turning over in the optical region. Finally, the lack of power law synchrotron fits indicates that there are few, if any, sources with turn-overs at shorter wavelengths than those considered here. Thus, the distribution of λ_p values that we find from the modelling represents the short-wavelength end of the overall distribution.

⑦ Optical polarisation measurements (taken from the literature) support the synchrotron model fits to the SEDs. Firstly, there is a correlation between the polarisation and the colour, with the red sources being more highly polarised. Secondly, the highly polarised sources are fit with large amounts of synchrotron.

Near-infrared polarisation measurements lend some support to the fitted models, but, in general, the polarisation measurements do not cover a great enough range in wavelength to effectively discriminate between different models. The way to remedy this would be to obtain simultaneous optical and near-infrared polarisation measurements.

⑧ Both the power law emission (which is likely to be from the accretion disk) and the synchrotron emission can be variable. We observed micro-variability on timescales of hours in a source that showed no evidence for the presence of synchrotron (to which variability is usually attributed), indicating that the accretion disk emission can experience rapid flux variability.

⑨ Finally, the red component fitted to the data, which we have modelled as synchrotron emission with a turnover at some peak wavelength, cannot be hot dust. Emission from hot dust cannot peak at $\lambda_{\mathrm{rest}} < 1.66\mu$m as is required by the data. This establishes that the NIR emission in the PHFS is, at least in part, of a different origin to that seen in radio-quiet quasars (Sanders et al. 1989).

9.3 The nature of radio-loud AGN

9.3.1 BL Lacs

Due to the diverse nature of the AGN found in it, the PHFS provides us with a basis to study the relationship between the different classes of radio-loud AGN. We examined this in Chapter 7, by exploring the relationship of the BL Lac objects to the rest of the PHFS. We found that, optically, the only differences between the two classes were that BL Lacs were redder (particularly in comparison to the power law objects), and that the BL Lacs had smaller emission line equivalent widths. The distributions of all other fitted properties were consistent with being the same for all objects. We found that the most likely explanation for the small equivalent widths was a relative lack of gas in the BL Lacs to provide the emission line flux.

Under this picture, then, the BL Lacs are simply versions of synchrotron-dominated quasars that are relatively deficient in emission line gas. The emission that is observed from the BL Lacs is strongly dominated by the synchrotron emission (see Fig. 5.7), as is the emission in a number of quasars that show relatively large emission lines – only very weak, if any, power law emission is seen in these objects.

We note here that the synchrotron emission in the BL Lacs is observed in the optical only because it has not turned over at a longer wavelength. In other words, λ_p cannot be too great, else the synchrotron emission will not be seen. It is reasonable to expect, however, that this will not always be the case. It is likely that there are some BL Lacs (i.e. sources with very weak emission line fluxes) that have their synchrotron spectrum turning over at sufficiently long wavelengths that there is little contribution in the optical. At large enough redshifts, the host galaxy will not be seen, and so these sources will appear to be either very faint sources or empty fields.

Conversely, at low redshifts, the light from these BL Lacs will be dominated by the host galaxy. We therefore would expect that there are some BL Lacs buried at low luminosity inside a comparatively bright galaxy. According to definitions of BL Lacs (Marchã et al. 1996; Stocke et al. 1991), as well as having weak emission lines, the spectrum should not exhibit too strong a contrast across the 4000Å break. This assumes, however, that the BL Lac (as opposed to its host galaxy) has significant optical emission. These definitions, therefore, introduce a bias against BL Lacs that have their non-thermal component turning over before the optical region, yet still have low optical emission line fluxes.

How might these "optically-quiet" BL Lacs appear? Optically, they would seem to be a relatively normal galaxy (presumably elliptical, as are the host galaxies of most radio-loud AGN), whereas, at radio frequencies, they would have a flat spectrum core, and possibly similar extended emission to "normal" BL Lacs. Objects such as these may have been found in the 200 mJy flat-spectrum sample of Marchã et al. (1996) – they are discussed by Antón and Browne (1999), who interpret them in terms of an orientation model. It should be possible to search for such objects – for example, correlating galaxy and radio surveys to find otherwise unremarkable elliptical galaxies (or PEGs: passive elliptical galaxies, to use the acronym from Antón and Browne (1999)) that exhibit a flat-spectrum radio core.

9.3.2 Unification models

What can we say from the modelling presented in this thesis about possible unification models for radio-loud AGN? The discussion in Section 7.4.3 showed that these questions are largely unresolved, although this work can help shed some light on this area.

Firstly, the low emission line fluxes that we observe in the BL Lacs are consistent with them having FR I radio galaxies as their parent population (although we note that low-excitation FR IIs have also been suggested as possible parents of BL Lacs (Laing et al. 1994), and this is certainly not ruled out or in by our work). The other interesting point as far as these models are concerned is the observation that, apart from the emission line properties, there is little to distinguish the BL Lacs from the other synchrotron-dominated quasars. Does this have any implications for the idea of FR IIs being the parent population of FSRQs? The fact that the distribution of synchrotron peaks and strengths are very similar in both the BL Lacs and quasars probably indicates that the regions in the jets from where the optical synchrotron emission originates have similar properties. This may indicate that the jets themselves in FR Is and FR IIs have similar forms (e.g. velocity structures). We do note that many FR I sources show VLBI-scale jets that are similar to those seen in FR IIs (Giovannini et al. 1995; Parma et al. 1987), possibly indicating that the jets in both types of radio galaxies start off with relativistic velocities, but are then slowed down in FR Is (perhaps due to interactions with the ambient medium) (Laing et al. 1999).

Secondly, the comparison with the "two-peak" unification scheme (Fossati et al. 1998) raised a couple of points of interest. The scheme was developed using quite bright samples in both the X-ray and the radio, and by comparing these with the PHFS sources we have shown that the scheme is not as successful for the lower luminosity quasars. Also, this particular scheme did not account for the presence of the power law emission that is dominant in many of the PHFS sources. This was obvious in the colour-colour plot (Fig 7.7d), where most of the PHFS sources had radio–optical slopes below that predicted by the pure synchrotron model. This is consistent with there being an additional (non-synchrotron) component at optical wavelengths.

This last point demonstrates the importance of taking into account emission from the accretion disk in modelling radio-loud quasars. Our modelling presented in this thesis has shown that both the synchrotron emission *and* the accretion disk emission are important in explaining the optical emission of all types of radio-loud flat-spectrum objects. As we have seen, in most attempts at modelling the optical emission of radio-loud AGN, generally only one of these components is considered to be dominant. However, we have shown that, in a sample that is selected to be quite homogeneous at radio frequencies, both of these optical emission mechanisms are important.

9.4 Future directions

This section details how the work presented in this thesis could be extended, either by further observational campaigns, or via theoretical studies.

Polarisation: Polarimetry of quasars and BL Lacs in the optical and near-infrared provides an excellent way of determining the main emission components, due to the high intrinsic polarisation of synchrotron emission. The NIR polarisation data presented and discussed in this thesis, while somewhat supportive of the presence of synchrotron, did not have the necessary wavelength coverage to effectively discriminate between different models (such as the combined model or a pure synchrotron model).

It would be ideal to obtain contemporaneous optical *and* NIR polarisation measurements of a range of objects, in order to get an accurate idea of the wavelength dependence of the polarisation over a substantial range of wavelengths.

Micro-variability: The key finding of the micro-variability study is related to the last point of the previous section. Of the three sources examined, the one that we can confidently say exhibited significant micro-variability was the source that showed no evidence for synchrotron emission in its optical–NIR SED. This shows that the accretion disk emission can exhibit short-timescale variations, a property widely ascribed to synchrotron emission from a jet. Thus, both mechanisms will be important in describing blazar emission.

The relative importance of the micro-variability of the accretion disk and synchrotron emission will need to be gauged from a more thorough investigation of micro-variability properties of radio-loud AGN. A suitable sample to use would consist of sources both with and without optical synchrotron emission (also including BL Lac objects). By observing a larger sample of objects, the results will be able to be put on a more quantitative footing. This followup can be done either in the optical or near-infrared, although optical imaging is preferable due to the larger field of view (compare CCD imaging with the 1m with CASPIR on the 2.3m). This enables greater numbers of comparison stars to be observed, thereby providing greater accuracy in the light curve.

Multi-filter observations: The modelling presented in this thesis was made possible by the compilation of the large data set of optical and near-infrared photometry. This was a considerable undertaking[1], not least because each data point required a separate observation. In future, however, this problem may be (partially) circumvented by the advent of multi-filter cameras, such as those used in the surveys SDSS[2] and 2MASS[3]. These cameras can take images of the sky in a number of different filters at once, thereby providing totally simultaneous observations in all these bands (which, as we have seen, is crucial for studies of quasars and BL Lacs). The SDSS will provide images of one quarter of the sky in five broadband optical filters, and will thus provide a great resource for studying the optical emission of the hundreds of thousands of quasars that are expected to be found (100,000 of which will be followed up spectroscopically to determine redshift).

Jets: The examination of the different synchrotron emission models in Chapter 3 showed that emission from ordered magnetic fields has different properties to that from tangled fields – a key property being the strong angular dependence of the emission, which has implications for Doppler beaming of jets. These jet models, however, are quite simple, with the jet essentially being a uniform, straight tube. The next step in this modelling would be to construct models that are better representations of real jets, including properties such as a changing radial magnetic field strength.

Also, the relative importance of the ordered and tangled field models needs to be explored in the context of real jets. Polarimetry observations of the M87 jet (Perlman et al. 1999) have shown that the knots in the jet tend to be highly polarised, and so are likely to have highly ordered magnetic fields. There are other regions, however, that have relatively high emission but little polarisation – these regions are likely to have tangled fields. The relative strength of these types of regions, particularly as a function of jet power (in the sense of the FR I / FR II division) will have important consequences for orientation-dependent unification models.

Finally, we note that while the synchrotron models that were fitted to the data provided very good fits, the lower-frequency part of the spectrum was not constrained. It would be good, in future, to examine the connection between the optical synchrotron emission and the radio synchrotron emis-

[1] One for which Paul Francis deserves a great deal of praise!
[2] The Sloan Digital Sky Survey: http://www.sdss.org
[3] The Two Micron All Sky Survey: http://www.ipac.caltech.edu/2mass/

sion. A look at the broadband SEDs (Appendix D) shows that it is difficult in many cases to imagine a single synchrotron component (certainly of the simple forms discussed in Chapter 3) fitting both the radio and optical data points. (Remembering of course that these points are not simultaneous!) There are a number of key questions that remain unsolved in this area:

- Do the optical and radio emission come from a single component?
- If not, how is the optical emission connected with radio?
- Are there extra components in the radio that do not extend up to the higher frequencies? Where in the quasar/jet are these components from? How far in frequency do they go?
- Finally, what makes a flat radio spectrum (such as we see in the PHFS sources) flat?

Bibliography

J.R.P. Angel and H.S. Stockman. “Optical and infrared polarization of active extragalactic objects.”. *Ann. Rev. Astron. Astrophys.*, 8:321–361, 1980.

S. Antón and I. Browne. “Host galaxies of Flat Radio Spectrum Sources.”. In L.O. Takalo and A. Sillanpää, editors, *BL Lac Phenomenon*, volume 159 of *A.S.P. Conference Series*, pages 377–380, 1999.

R.R.J. Antonucci. “Polarization of active galactic nuclei and quasars”. In M. Kafatos, editor, *Supermassive Black Holes*, Proceedings of the 3rd George Mason Astrophysics Workshop, pages 26–38. Cambridge University Press, Cambridge, 1988.

R.R.J. Antonucci and J.S. Ulvestad. “Extended radio emission and the nature of blazars.”. *Astrophys. J.*, 294:158–182, 1985.

W. Baade. “Polarization in the jet of Messier 87.”. *Astrophys. J.*, 123:550–551, 1956.

J. N. Bahcall, S. Kirhakos, D. H. Saxe, and D. P. Schneider. “*Hubble Space Telescope* Images of a Sample of 20 Nearby Luminous Quasars”. *Astrophys. J.*, 479:642–658, 1997.

J.N. Bahcall, S. Kirhakos, D.P. Schneider, R.J. Davis, T.W.B. Muxlow, S.T. Garrington, R.G. Conway, and S.C. Unwin. “*HST* and *MERLIN* observations of the jet in 3C 273.”. *Astrophys. J., Lett.*, 452:L91–L93, 1995.

R. Barvainis. “Free-free emission and the big blue bump in Active Galactic Nuclei.”. *Astrophys. J.*, 412:513–523, 1993.

S. A. Baum, C. P. O'Dea, G. Giovannini, J. Biretta, W. B. Cotton, S. de Koff, L. Feretti, D. Golombek, L. Lara, F. D. Macchetto, G. K. Miley, W. B. Sparks, T. Venturi, and S. S. Komissarov. "*HST* and *MERLIN* observations of 3C 264 – A laboratory for jet physics and unified schemes.". *Astrophys. J.*, 483:178–193, 1997.

S.A. Baum and T. Heckman. "Extended optical line emitting gas in powerful radio galaxies - What is the radio emission-line connection?". *Astrophys. J.*, 336:702–721, 1989.

C.R. Benn, M. Vigotti, R. Carballo, J.I. Gonzalez-Serrano, and S.F. Sánchez. "Red quasars not so dusty.". *Mon. Not. R. Astron. Soc.*, 295: 451–456, 1998.

M. Bersanelli, P. Bouchet, and R. Falomo. "$JHKL'$ photometry on the ESO system: systematic effects and absolute calibration.". *Astron. Astrophys.*, 252:854–860, 1991.

M.S. Bessell, F. Castelli, and B. Plez. "Model atmospheres broad-band colours, bolometric corrections and temperature calibrations for O - M stars.". *Astron. Astrophys.*, 333:231–250, 1998.

J.A. Biretta, W.B. Sparks, and F. Machetto. "*HST* observations of superluminal motion in the M87 jet.". *Astrophys. J.*, 520:621–626, 1999.

J.A. Biretta, C.P. Stern, and D.E. Harris. "The radio to X-ray spectrum of the M87 jet and nucleus". *Astron. J.*, 101:1632–1646, 1991.

R.D. Blandford. *Active Galactic Nuclei.* Saas-Fee Advanced Course lecture notes. Springer-Verlag, 1990.

R.D. Blandford and M.J. Rees. "Some comments on radiation mechanisms in Lacertids". In A.N. Wolfe, editor, *"Pittsburgh Conference on BL Lac Objects"*, page 328. University of Pittsburgh Press, Pittsburgh, 1978.

B.J. Boyle, T. Shanks, S.M. Croom, R.J. Smith, L. Miller, N. Loaring, and C. Heymans. "The 2dF QSO Redshift Survey. I. The optical luminosity function of quasi-stellar objects". *Mon. Not. R. Astron. Soc.*, 317:1014–1022, 2000.

G.R. Burbidge, A.H. Crowne, and H.E. Smith. "An optical catalog of quasi-stellar objects". *Astrophys. J., Suppl. Ser.*, 33:113–188, 1977.

H.R. Butcher, W. van Breugel, and G.K. Miley. "Optical observations of radio jets.". *Astrophys. J.*, 235:749–754, 1980.

G. Chartas, D.M. Worrall, M. Birkinshaw, M. Cresitello-Dittmar, W. Cui, K.K. Ghosh, D.E. Harris, E.J. Hooper, D.L. Jauncey, D.-W. Kim, J. Lovell, H.L. Marshall, S. Mathur, D.A. Schwartz, S.J. Tingay, S.N. Virani, and B.J. Wilkes. "The *Chandra* X-ray Observatory resolves the X-ray morphology and spectra of a jet in PKS 0637−752.". *Astrophys. J.*, 542:655–666, 2000.

E.A. Corbett, A. Robinson, D.J. Axon, and J.H. Hough. "A Seyfert-like nucleus concealed in BL Lacertae?". *Mon. Not. R. Astron. Soc.*, 311: 485–492, 2000.

E.A. Corbett, A. Robinson, D.J. Axon, J.H. Hough, R.D. Jeffries, M.R. Thurston, and S. Young. "The appearance of broad Hα in BL Lacertae". *Mon. Not. R. Astron. Soc.*, 281:737–749, 1996.

P. Crane, R. Peletier, D. Baxter, W. B. Sparks, R. Albrecht, C. Barbieri, J. C. Blades, A. Boksenberg, J. M. Deharveng, M. J. Disney, P. Jakobsen, T. M. Kamperman, I. R. King, F. Macchetto, C. D. Mackay, F. Paresce, G. Weigelt, P. Greenfield, R. Jedrzejewski, and A. Nota. "Discovery of an optical synchrotron jet in 3C 264.". *Astrophys. J., Lett.*, 402:L37–L40, 1993.

H.D. Curtis. *Publ. Lick Obs.*, 13:31, 1918.

J.A. de Diego, D. Dultzin-Hacyan, A. Ramírez, and E. Benítez. "A Comparative Study of the Microvariability Properties in Radio-loud and Radio-quiet Quasars". *Astrophys. J.*, 501:69–81, 1998.

S. de Koff, S.A. Baum, W.B. Sparks, J. Biretta, D. Golombek, F. Macchetto, P. McCarthy, and G.K. Miley. "*HST* Snapshot survey of 3CR radio source counterparts. I. Intermediate redshifts.". *Astrophys. J., Suppl. Ser.*, 107: 621–660, 1996.

A. Dey and W. J. M. van Breugel. "Blue optical continuum associated with a radio knot in 3C346". *Astron. J.*, 107:1977–1983, 1994.

J.L.E Dreyer. "New General Catalogue of Nebulae and Clusters of stars.". *Mem. R. Astron. Soc.*, 49(I), 1888. (reprinted 1953, London: Royal Astronomical Society).

M.J. Drinkwater, R.L. Webster, P.J. Francis, J.J. Condon, S.L. Ellison, D.L. Jauncey, J. Lovell, B.A. Peterson, and A. Savage. "The Parkes Half-Jansky Flat-Spectrum Sample.". *Mon. Not. R. Astron. Soc.*, 284:85–125, 1997.

F.R. Elder, A.M. Gurewitsch, R.V. Langmuir, and H.C. Pollock. "Radiation from electrons in a synchrotron.". *Phys. Rev.*, 71:829–830, 1947.

F.R. Elder, R.V. Langmuir, and H.C. Pollock. "Radiation from electrons accelerated in a synchrotron.". *Phys. Rev.*, 74:52–56, 1948.

M. Elvis, D. Plummer, J. Schachter, and G. Fabbiano. "The *Einstein* Slew Survey". *Astrophys. J., Suppl. Ser.*, 80:257–303, 1992.

A.C. Fabian, I. Smail, K. Iwasawa, S.W. Allen, A.W. Blain, C.S. Crawford, S. Ettori, R.J. Ivison, R.M. Johnstone, J.-P. Kneib, and R.J. Wilman. "Testing the connection between the X-ray and submillimetre source populations using *Chandra*.". *Mon. Not. R. Astron. Soc.*, 315:L8–L12, 2000.

R. Falomo. "Redshifts of three BL Lacertae objects: PKS 0118−27, PKS 0829+04 and MC 1057+10". *Astron. J.*, 102(6):1991–1993, 1991.

B.L. Fanaroff and J.M. Riley. "The morphology of extragalactic radio sources of high and low luminosity.". *Mon. Not. R. Astron. Soc.*, 167: 31P–35P, 1974.

R. Fanti, C. Fanti, R.T. Schilizzi, R.E. Spencer, Nan Rendong, P. Parma, W.J.M. van Breugel, and T. Venturi. "On the nature of compact steep spectrum radio sources". *Astron. Astrophys.*, 231:333–346, 1990.

H.C. Ford, R.J. Harms, Z.I. Tsvetanov, G.F. Hartig, L.L. Dressel, G.A. Kriss, R.C. Bohlin, A.F. Davidsen, B. Margon, and A.K. Kochhar. "Narrowband *HST* images of M87: Evidence for a disk of ionised gas around a massive black hole.". *Astrophys. J., Lett.*, 435:L27–L30, 1994.

G. Fossati, A. Celotti, G. Ghisellini, and L. Maraschi. "Unifying models for X-ray selected and radio selected BL Lacs". *Mon. Not. R. Astron. Soc.*, 289:136–150, 1997. (astro-ph/9704113).

G. Fossati, L. Maraschi, A. Celotti, A. Comastri, and G. Ghisellini. "A unifying view of the spectral energy distributions of blazars". *Mon. Not. R. Astron. Soc.*, 299:433–448, 1998.

D. Fraix-Burnet. "An optical counterjet in 3C 66B?". *Mon. Not. R. Astron. Soc.*, 284:911–914, 1997.

A. Franceschini, L. Bassani, M. Cappi, G.L. Granato, G. Malaguti, E. Palazzi, and M. Persic. "*BeppoSAX* uncovers a type-2 QSO in the hyperluminous infrared galaxy IRAS 09104+4109". *Astron. Astrophys.*, 353:910–916, 2000.

P.J. Francis. "The continuum slopes of optically-selected QSOs.". *Publ. Astron. Soc. Aust.*, 13:212–217, 1996.

P.J. Francis, C. Drake, M.T. Whiting, M.J. Drinkwater, and R.L. Webster. "The spectra of red quasars.". *Publ. Astron. Soc. Aust.*, 2001. In press.

P.J. Francis, M.T. Whiting, and R.L. Webster. "The Optical/Near-IR Colours of Red Quasars.". *Publ. Astron. Soc. Aust.*, 17:56–71, 2000.

G. Ghisellini, A. Celotti, G. Fossati, L. Maraschi, and A. Comastri. "A theoretical unifying scheme for gamma-ray bright blazars". *Mon. Not. R. Astron. Soc.*, 301:451–468, 1998.

G. Ghisellini, P. Padovani, A. Celotti, and L. Maraschi. "Relativistic bulk motion in AGN.". *Astrophys. J.*, 407:65–82, 1993.

V.L. Ginzburg and S.I. Syrovatskii. "Cosmic magnetobremsstrahlung (synchrotron radiation)". *Ann. Rev. Astron. Astrophys.*, 3:297–350, 1965.

V.L. Ginzburg and S.I. Syrovatskii. "Developments in the theory of synchrotron radiation and its reabsorption". *Ann. Rev. Astron. Astrophys.*, 7:375–420, 1969.

G. Giovannini, W.D. Cotton, L. Feretti, L. Lara, T. Venturi, and J.M. Marcaide. "Very-long-baseline radio interferometry observations of low power radio galaxies.". *Proc. Nat. Acad. Sci.*, 92:11356–11359, 1995.

Gopal-Krishna, A.C. Gupta, R. Sagar, P.J. Wiita, U.S. Chaubey, and C.S. Stalin. "Rapid optical variability in radio-quiet QSOs". *Mon. Not. R. Astron. Soc.*, 314:815–825, 2000.

Gopal-Krishna and P.J. Wiita. "Swinging jets and the variability of active galactic nuclei.". *Astron. Astrophys.*, 259:109–117, 1992.

R.F. Green, M. Schmidt, and J. Liebert. "The Palomar-Green catalog of ultraviolet-excess stellar objects". *Astrophys. J., Suppl. Ser.*, 61:305–352, 1986.

J.L. Greenstein and T.A. Matthews. "Red-shift of the unusual radio source: 3C 48". *Nature*, 197:1041–1042, 1963.

J.L. Greenstein and M. Schmidt. "The Quasi-Stellar Radio Sources 3C 48 and 3C 273.". *Astrophys. J.*, 140:1–34, 1964.

J.P. Halpern, T.J. Turner, and I.M. George. "Are there any Type 2 QSOs? The case of AXJ0341.4-4453". *Mon. Not. R. Astron. Soc.*, 307:L47–L50, 1999.

R.J. Harms, H.C. Ford, Z.I. Tsvetanov, G.F. Hartig, L.L. Dressel, G.A. Kriss, R.C. Bohlin, A.F. Davidsen, B. Margon, and A.K. Kochhar. "*HST FOS* spectroscopy of M87: Evidence for a disk of ionised gas around a massive black hole.". *Astrophys. J., Lett.*, 435:L35–l38, 1994.

D.E Harris, K.M. Leighly, and J.P. Leahy. "X-ray emission from a radio hot spot in 3C 390.3: Evidence for the deflection of a radio jet by a neighboring galaxy.". *Astrophys. J., Lett.*, 499:L149–L152, 1998.

R.C. Hartman, D.L. Bertsch, S.D. Bloom, A.W. Chen, P. Deines-Jones, J.A. Esposito, C.E. Fichtel, D.P. Friedlander, S.D. Hunter, L.M. McDonald, P. Sreekumar, D.J. Thompson, B.B. Jones, Y.C. Lin, P.F. Michelson, P.L. Nolan, W.F. Tompkins, G. Kanbach, H.A. Mayer-Hasselwander, A. Mücke, M. Pohl, O. Reimer, D.A. Kniffen, E.J. Schneid, C. von Montigny, R. Mukherjee, and B.L. Dingus. "The Third *EGRET* Catalog of High-Energy Gamma-Ray Sources". *Astrophys. J., Suppl. Ser.*, 123:79–202, 1999.

C. Hazard, M.B. Mackey, and A.J. Shimmins. " Investigation of the radio source 3C 273 by the method of lunar occultations.". *Nature*, 197:1037–1039, 1963.

T.M. Heckman. "An optical and radio survey of the nuclei of bright galaxies - Activity in normal galactic nuclei". *Astron. Astrophys.*, 87:152–164, 1980.

J. Heidt and S.J. Wagner. "Statistics of optical intraday variability in a complete sample of radio-selected BL Lacertae objects.". *Astron. Astrophys.*, 305:42–52, 1996.

S. Heinz and M.C. Begelman. "Analysis of the synchrotron emission from the M87 jet.". *Astrophys. J.*, 490:653–663, 1997.

J.R. Herrnstein, J.M. Moran, L.J. Greenhill, P.J. Diamond, M. Miyoshi, N. Nakai, and M. Inoue. "Discovery of a Subparsec Jet 4000 Radii away from the Central Schwarzschild engine of NGC 4258.". *Astrophys. J., Lett.*, 475:L17–L20, 1997.

R. Hes, P.D. Barthel, and R.A.E. Fosbury. "Support for a unified model of radio galaxies and quasars from isotropic [O II] emission.". *Nature*, 362: 326–328, 1993.

P.C. Hewett, C.B. Foltz, and F.H. Chaffee. "The Large Bright Quasar Survey. VI. Quasar catalog and survey parameters". *Astron. J.*, 109:1498–1521, 1995.

A. Hewitt and G. Burbidge. "A revised and updated catalog of quasi-stellar objects". *Astrophys. J., Suppl. Ser.*, 87:451–947, 1993.

P.R. Hiltner, K. Meisenheimer, H.-J. Roeser, R.A. Laing, and R.A. Perley. "Hot spot 3C20 west: an optical synchrotron source". *Astron. Astrophys.*, 286:25–36, 1994.

J. Hjorth, A.N. Vestergaard, A.N. Sørensen, and F. Grundahl. "Detection of a faint optical jet in 3C 120.". *Astrophys. J., Lett.*, 452:L17–L20, 1995.

C.D. Impey, C.R. Lawrence, and S. Tapia. "Optical polarization of a complete sample of radio sources". *Astrophys. J.*, 375:46–68, 1991.

C.D. Impey and G. Neugebauer. "Energy distributions of blazars.". *Astron. J.*, 95:307–351, 1988.

C.D. Impey and S. Tapia. "The optical polarisation properties of quasars.". *Astrophys. J.*, 354:124–139, 1990.

M. Jang and H.R. Miller. "The microvariability of selected radio-quiet and radio-loud QSOs.". *Astron. J.*, 114:565–574, 1997.

L. Kedziora-Chudczer. *"The study of intraday variability of extragalactic compact radio sources."*. PhD thesis, University of Sydney, 1998.

A.L. Kinney, R.C. Bohlin, J.C. Blades, and D.G. York. "An ultraviolet atlas of quasar and blazar spectra.". *Astrophys. J., Suppl. Ser.*, 75:645–717, 1991.

Y.Y. Kovalev, N.A. Nizhelsky, Y.A. Kovalev, A.B. Berlin, G.V. Zhekanis, M.G. Mingaliev, and A.V. Bogdantsov. "Survey of instantaneous 1-22 GHz spectra of 550 compact extragalactic objects with declinations from $-30°$ to $+43°$". *Astron. Astrophys. Suppl. Ser.*, 139:545–554, 1999.

J.H. Krolik. *"Active Galactic Nuclei: from the central black hole to the galactic environment."*. Princeton University Press, 1999.

R. Laing, P. Parma, H.R. de Ruiter, and R. Fanti. "Asymmetries in the jets of weak radio galaxies". *Mon. Not. R. Astron. Soc.*, 306:513–530, 1999.

R.A. Laing, C.R. Jenkins, J.V. Wall, and S.W. Unger. "Spectrophotometry of a complete sample of 3CR radio sources: Implications for unified models.". In *The First Stromlo Symposium: The physics of active galaxies.*, volume 54 of *A.S.P. Conference Series*, pages 201–208, 1994.

K.M. Lanzetta, D.A. Turnshek, and J. Sandoval. "Ultraviolet spectra of quasars, BL Lacertæ objects, and Seyfert galaxies.". *Astrophys. J., Suppl. Ser.*, 84:109–184, 1993.

A. Laor and B.T. Draine. "Spectroscopic constraints on the properties of dust in active galactic nuclei". *Astrophys. J.*, 402:441–468, 1993.

L. Lara, L. Feretti, G. Giovannini, S. Baum, W.D. Cotton, C.P. O'Dea, and T. Venturi. "The radio-optical jet in NGC 3862 (3C 264) from parsec to sub-kiloparsec scales.". *Astrophys. J.*, 513:197–206, 1999.

S.A. Laurent-Muehleisen, R.I. Kollgaard, E.D. Feigelson, W. Brinkmann, and J. Siebert. "The RGB Sample of Intermediate BL Lacertae Objects". *Astrophys. J.*, 525:127–143, 1999.

K.R. Lind and R.D. Blandford. "Semidynamical models of radio jets: relativistic beaming and source counts.". *Astrophys. J.*, 295:358–367, 1985.

M.S. Longair. *"High energy astrophysics."*. Cambridge University Press, Cambridge, 2nd edition, 1994.

F. Macchetto, R. Albrecht, C. Barbieri, J. C. Blades, A. Boksenberg, P. Crane, J. M. Deharveng, M. J. Disney, P. Jakobsen, T. M. Kamperman, I. R. King, C. D. Mackay, F. Paresce, G. Weigelt, D. Baxter, P. Greenfield, R. Jedrzejewski, A. Nota, W. B. Sparks, and G. K. Miley. "*HST* observations of 3C 66B: A double-stranded optical jet.". *Astrophys. J., Lett.*, 373:L55–L58, 1991a.

F. Macchetto, R. Albrecht, C. Barbieri, J. C. Blades, A. Boksenberg, P. Crane, J. M. Deharveng, M. J. Disney, P. Jakobsen, T. M. Kamperman, I. R. King, C. D. Mackay, F. Paresce, G. Weigelt, D. Baxter, P. Greenfield, R. Jedrzejewski, A. Nota, and W. B. Sparks. "First results from the faint object camera: observations of PKS 0521−36.". *Astrophys. J., Lett.*, 369:L55–L57, 1991b.

M. Maesano, F. Montagni, E. Massaro, and R. Nesci. "*BVRI* photometry of BL Lacertæ in 1993–1995.". *Astron. Astrophys. Suppl. Ser.*, 122:267–270, 1997.

M.A. Malkan and R.L. Moore. "The ultraviolet excess of quasars. III. The highly polarized quasars PKS 0736+017 and PKS 1510−089.". *Astrophys. J.*, 300:216–223, 1986.

A.V. Mangalam and P.J. Wiita. "Accretion disk models for optical and ultraviolet microvariability in active galactic nuclei.". *Astrophys. J.*, 406: 420–429, 1993.

L. Maraschi, L. Chiappetti, R. Falomo, B. Garilli, M. Malkan, G. Tagliaferri, E.G. Tanzi, and A. Treves. "Coordinated X-ray ultraviolet and optical observations of 3C 120". *Astrophys. J.*, 368:138–151, 1991.

M.J.M. Marchã, I.W.A. Browne, C.D. Impey, and P.S. Smith. "Optical spectroscopy and polarization of a new sample of optically bright flat radio spectrum sources.". *Mon. Not. R. Astron. Soc.*, 281:425–448, 1996.

A.P. Marscher and W.K. Gear. "Models for high-frequency radio outbursts in extragalactic sources, with application to the early 1983 millimeter-to-infrared flare of 3C 273". *Astrophys. J.*, 298:114–127, 1985.

H.L. Marshall, J.J. Drake, A. Fruscione, J. Grimes, D. Harris, M. Juda, R. Kraft, S. Mathur, S.S. Murray, P.M. Ogle, D. Pease, A. Siemiginowska, S. Vrtilek, and B.J. Wargelin. "Structure of the X-ray emission from the jet of 3C 273.". *Astrophys. J., Lett.*, 2000. In press.

A.R. Martel, S.A. Baum, W.B. Sparks, E. Wyckoff, J.A. Biretta, D. Golombek, F.D. Macchetto, S. de Koff, P.J. McCarthy, and G.K. Miley. "*Hubble Space Telescope* Snapshot Survey of 3CR Radio Source Counterparts. III. Radio Galaxies with $z < 0.1$". *Astrophys. J., Suppl. Ser.*, 122: 81–108, 1999.

A.R. Martel, W.B. Sparks, F.D. Macchetto, J.A. Biretta, S.A. Baum, D. Golombek, P.J. McCarthy, S. de Koff, and G.K. Miley. "Discovery of an optical synchrotron jet in 3C 15.". *Astrophys. J.*, 496:203–209, 1998.

F.J. Masci. *"Obscuration of quasars by dust and the reddening mechanism in Parkes-quasars."*. PhD thesis, School of Physics, University of Melbourne, 1997.

F.J. Masci, R.L. Webster, and P.J. Francis. "Host galaxy contribution to the colours of 'Red' quasars.". *Mon. Not. R. Astron. Soc.*, 301:975–984, 1998.

W.G. Mathews. "The enormous mass of the elliptical galaxy M87 - A model for the extended X-ray source". *Astrophys. J.*, 219:413–423, 1978.

P. McGregor, J. Hart, M. Downing, D. Hoadley, and G. Bloxham. . In I.S. McLean, editor, *Infrared Astronomy with Arrays: The Next Generation*, page 299. Dordrecht: Kluwer, 1994.

K. Meisenheimer, H.-J. Röser, P.R. Hiltner, M.G. Yates, M.S. Longair, R. Chini, and R.A. Perley. "The synchrotron spectra of radio hot spots.". *Astron. Astrophys.*, 219:63–86, 1989.

K. Meisenheimer, H.-J. Röser, and M. Schlötelburg. "The synchrotron spectrum of the jet of M87". *Astron. Astrophys.*, 307:61–79, 1996.

C. Messier. "Catalogue des nebuleuses et des amas d'étoiles.". *Connaissance des Temps*, 1784:227–269, 1781.

H.R. Miller and J.C. Noble. "The microvariability of Blazars and related AGN.". In H.R. Miller, J.R. Webb, and J.C. Noble, editors, *Blazar Continuum Variability*, volume 110 of *A.S.P. Conference Series*, pages 17–29, 1996.

J.S. Miller, R.W. Goodrich, and W.G. Mathews. "Multidirectional views of the active nucleus of NGC 1068". *Astrophys. J.*, 378:47–64, 1991.

P. Morrison and A. Sadun. "The optical jet of 3C 273: an electron-positron plasma beam viewed by the light of its quasar?". *Mon. Not. R. Astron. Soc.*, 254:488–492, 1992.

H. Netzer and B.M. Peterson. "Reverberation Mapping and the Physics of Active Galactic Nuclei". In *Astronomical Time Series*, pages 85–108, 1997.

M. Neumann, K. Meisenheimer, H.-J. Roeser, and H.H. Fink. "*ROSAT-HRI* observations of the jet in M 87.". *Astron. Astrophys.*, 318:383–389, 1997.

K. Nilsson, J. Heidt, T. Pursimo, A. Sillanpää, L.O. Takalo, and K. Jäger. "Discovery of an optical jet in the BL Lacertae object 3C 371.". *Astrophys. J., Lett.*, 484:L107–L111, 1997.

C.P. O'Dea, W. De Vries, J.A. Biretta, and S.A. Baum. "*HST* and VLA observations of two optical continuum knots in the jet of 3C 380.". *Astron. J.*, 117:1143–1150, 1999.

J.B. Oke. "Absolute energy distribution in the optical spectrum of 3C 273.". *Nature*, 197:1040–1041, 1963.

F.N. Owen and M.J. Ledlow. "The FR I/II break and the bivariate luminosity function in Abell clusters of galaxies.". In G.V. Bicknell, M.A. Dopita, and P.J. Quinn, editors, *The First Stromlo Symposium: The physics of active galaxies.*, volume 54 of *A.S.P. Conference Series*, pages 319–323, 1994.

A.G. Pacholczyk. *"Radio Astrophysics"*. W.H.Freeman and Company, San Francisco, 1970.

P. Padovani and P. Giommi. "A sample-oriented catalogue of BL Lacertae objects". *Mon. Not. R. Astron. Soc.*, 277:1477–1490, 1995.

P. Padovani and C.M. Urry. "Luminosity functions, relativistic beaming, and unified theories of high-luminosity radio sources". *Astrophys. J.*, 387: 449–457, 1992.

P. Parma, H.R. de Ruiter, C. Fanti, R. Fanti, and R. Morganti. "VLA observations of low-luminosity radio galaxies. VI. Discussion of radio jets". *Astron. Astrophys.*, 181:244–264, 1987.

E.S. Perlman, J.A. Biretta, F. Zhou, W.B. Sparks, and F.D. Macchetto. "Optical and radio polarimetry of the M87 jet at 0.2$''$ resolution.". *Astron. J.*, 117:2185–2198, 1999.

E.S. Perlman, J.T. Stocke, J.F. Schachter, M. Elvis, E. Ellingson, C.M. Urry, M. Potter, C.D. Impey, and P. Kolchinsky. "The *Einstein* Slew Survey Sample of BL Lacertae Objects". *Astrophys. J., Suppl. Ser.*, 104: 251–285, 1996.

B.M. Peterson. *"Introduction to Active Galactic Nuclei"*. Cambridge University Press, Cambridge, 1997.

D. Petry. "Observations of Blazars with the HEGRA Cherenkov telescopes.". In L.O. Takalo and A. Sillanpää, editors, *BL Lac Phenomenon*, volume 159 of *A.S.P. Conference Series*, pages 235–238, 1999.

E. Pian, G. Vacanti, G. Tagliaferri, G. Ghisellini, L. Maraschi, A. Treves, M. Urry, F. Fiore, P. Giommi, E. Palazzi, L. Chiappetti, and R.M. Sambruna. "*BeppoSAX* Observations of Unprecedented Synchrotron Activity in the BL Lacertae Object Markarian 501.". *Astrophys. J., Lett.*, 492: L17–L20, 1998.

W.H. Press, S.A. Teukolsky, W.T. Vetterling, and B.P. Flannery. *Numerical Recipes in C.* Cambridge University Press, second edition, 1997.

S.J. Qian, A. Quirrenbach, A. Witzel, T.P. Krichbaum, C.A. Hummel, and J.A. Zensus. "A model for the rapid radio variability in the quasar 0917+624". *Astron. Astrophys.*, 241:15–21, 1991.

S. Rawlings, R. Saunders, S.A. Eales, and C.D. Mackay. "The relations between radio and forbidden [O III] emission line luminosities in FR II radiogalaxies". *Mon. Not. R. Astron. Soc.*, 240:701–722, 1989.

S.E. Ridgway and A. Stockton. "Deep WFPC2 and ground-based imaging of a complete sample of 3C quasars and galaxies.". *Astron. J.*, 114:511–543,862–874(plates), 1997.

G.E. Romero, S.A. Cellone, and J.A. Combi. "Optical microvariability of southern AGNs.". *Astron. Astrophys. Suppl. Ser.*, 135:477–486, 1999.

G.E. Romero, S.A. Cellone, and J.A. Combi. "Two-colour photometry with high temporal resolution of the extremely variable blazar PKS 0537−441.". *Astron. J.*, 120:1192–1197, 2000.

G.B. Rybicki and A.P. Lightman. *"Radiative processes in astrophysics."*. Wiley, New York, 1979.

D.B. Sanders, E.S. Phinney, G. Neugebauer, B.T. Soifer, and K. Matthews. "Continuum energy distributions of quasars: Shapes and origins.". *Astrophys. J.*, 347:29–51, 1989.

R. Scarpa and R. Falomo. "Are high polarization quasars and BL Lacertae objects really different? A study of the optical spectral properties.". *Astron. Astrophys.*, 325:109–123, 1997.

R. Scarpa and C.M. Urry. "On the Physical conditions in AGN Optical jets.". *New Astron. Rev.*, In press, 2001. Proceedings of "Life Cycle of Radio Galaxies" workshop.

R. Scarpa, C.M. Urry, R. Falomo, and A. Treves. "*HST* Observations of the Optical Jets of PKS 0521−365, 3C371, and PKS 2201+044.". *Astrophys. J.*, 526:643–648, 1999.

D.J. Schlegel, D.P. Finkbeiner, and M. Davis. "Maps of Dust Infrared Emission for Use in Estimation of Reddening and Cosmic Microwave Background Radiation Foregrounds". *Astrophys. J.*, 500:525–553, 1998.

M. Schmidt. "3C 273: A star-like object with a large red-shift.". *Nature*, 197:1040, 1963.

M. Schmidt and R.F. Green. "Quasar evolution derived from the Palomar bright quasar survey and other complete quasar surveys". *Astrophys. J.*, 269:352–374, 1983.

J.L. Schmitt. "BL Lac identified as a Radio Source.". *Nature*, 218:663, 1968.

E.J. Schreier, P. Gorenstein, and E.D. Feigelson. "High-resolution X-ray observations of M87 - Nucleus, jet and radio halo". *Astrophys. J.*, 261: 42–50, 1982.

D.A. Schwartz, H.L. Marshall, J.E.J. Lovell, B.G. Piner, S.J. Tingay, M. Birkinshaw, G. Chartas, M. Elvis, E.D. Feigelson, K.K. Ghosh, D.E. Harris, H. Hirabayashi, E.J. Hooper, D.L. Jauncey, K.M. Lanzetta, S. Mathur, R.A. Preston, W.H. Tucker, S.N. Virani, B.J. Wilkes, and D.M. Worrall. "*Chandra* discovery of a 100 kpc X-ray jet in PKS 0637−752.". *Astrophys. J., Lett.*, 540:L69–L72, 2000.

J. Schwinger. "On the classical radiation of accelerated electrons.". *Phys. Rev.*, 75(12):1912–1925, 1949.

S. Serjeant and S. Rawlings. "Hidden quasars reddened by dust?". *Nature*, 379:304, 1996.

Z.-. Shen, T.-. Wan, J.M. Moran, D.L. Jauncey, J.E. Reynolds, A.K. Tzioumis, R.G. Gough, R.H. Ferris, M.W. Sinclair, D.-. Jiang, X.-. Hong, S.-. Liang, P.G. Edwards, M.E. Costa, S.J. Tingay, P.M. McCulloch, J.E.J. Lovell, E.A. King, G.D. Nicolson, D.W. Murphy, D.L. Meier, T.D. van Ommen, and G.L. White. "A 5 GHz Southern Hemisphere VLBI Survey of Compact Radio Sources. II.". *Astron. J.*, 115:1357–1370, 1998.

I.S. Shklovsky. . *Doklady Akad. Nauk. U.S.S.R.*, 90:983, 1953.

J. Siebert, W. Brinkmann, M.J. Drinkwater, W. Yuan, P.J. Francis, B.A. Peterson, and R.L. Webster. "X-ray properties of the Parkes sample of flat-spectrum radio sources: dust in radio-loud quasars?". *Mon. Not. R. Astron. Soc.*, 301:261–279, 1998.

P.S. Smith, R. Elston, G. Berriman, R.G. Allen, and T.J. Balonek. "Evidence for accretion disks in highly polarised quasars.". *Astrophys. J., Lett.*, 326:L39–L44, 1988.

P.S. Smith, G.D. Schmidt, B.T. Jannuzi, and R. Elston. "The synchrotron continuum of the highly polarized quasar PKS 1546+027.". *Astrophys. J.*, 426:535–541, 1994.

W.B. Sparks, S.A. Baum, J. Biretta, F.D. Macchetto, and A.R. Martel. "Face-on dust disks in galaxies with optical jets.". *Astrophys. J.*, 542: 667–672, 2000.

W.B. Sparks, D. Golombek, S.A. Baum, J. Biretta, S. de Koff, F. Macchetto, P. McCarthy, and G.K. Miley. "Discovery of an optical synchrotron jet in 3C 78.". *Astrophys. J., Lett.*, 450:L55–L58, 1995.

M. Stickel, K. Meisenheimer, and H. Kühr. "The optical identification status of the 1 Jy radio source catalogue". *Astron. Astrophys. Suppl. Ser.*, 105: 211–234, 1994.

J.T. Stocke, S.L. Morris, I.M. Gioia, T. Maccacaro, R. Schild, A. Wolter, T.A. Fleming, and J.P. Henry. "The Einstein Observatory Extended Medium-Sensitivity Survey. II - The optical identifications". *Astrophys. J., Suppl. Ser.*, 76:813–874, 1991.

H.S. Stockman, R.L. Moore, and J.R.P. Angel. "The optical polarization properties of 'normal' quasars". *Astrophys. J.*, 279:485–498, 1984.

A. Stockton and S.E. Ridgway. "Deep spectroscopy in the field of 3C 212.". *Astron. J.*, 115:1340–1347, 1998.

C.N. Tadhunter, R. Morganti, S. di Serego-Alighieri, R.A.E. Fosbury, and I.J. Danziger. "Optical Spectroscopy of a Complete Sample of Southern 2 Jy Radio Sources". *Mon. Not. R. Astron. Soc.*, 263:999–1022, 1993.

R.C. Thomson, C.D. Mackay, and A.E. Wright. "Internal structure and polarization of the optical jet of the quasar 3C273.". *Nature*, 365:133–135, 1993.

S.J. Tingay, D.W. Murphy, J.E.J. Lovell, M.E. Costa, P. McCulloch, P.G. Edwards, D.L. Jauncey, J.E. Reynolds, A.K. Tzioumis, E.A. King, D.L. Jones, R.A. Preston, D.L. Meier, T.D. van Ommen, G.D. Nicolson, and J.F.H. Quick. "VLBI Observations of Gamma-Ray-quiet Active Galactic Nuclei: Comparing Radio-Core Brightness Temperatures". *Astrophys. J.*, 497:594+, 1998.

C.M. Urry and P. Padovani. "Unified schemes for radio-loud AGN". *Publ. Astron. Soc. Pac.*, 107:803–845, 1995.

R.C. Vermeulen, P.M. Ogle, H.D. Tran, I.W.A. Browne, M.H. Cohen, A.C.S. Readhead, G.B. Taylor, and R.W. Goodrich. "When Is BL Lac Not a BL Lac?". *Astrophys. J., Lett.*, 452:L5–L8, 1995.

M.P. Véron-Cetty and P. Véron. "Quasars and Active Galactic Nuclei (9th Ed.).". *ESO Sci. Rep.*, 19:1, 2000.

M. Vigotti, G. Vettolani, R. Merighi, J.F. Lahulla, and M. Pedani. "The B3-VLA quasar sample". *Astron. Astrophys. Suppl. Ser.*, 123:219–239, 1997.

S.J. Wagner and A. Witzel. "Intraday variability in quasars and BL Lac objects.". *Ann. Rev. Astron. Astrophys.*, 33:163–197, 1995.

R.C. Walker, M.A. Walker, and J.M. Benson. "Evidence for superluminal motion on kiloparsec scales in 3C 120". *Astrophys. J.*, 335:668–676, 1988.

J.V. Wall and J.A. Peacock. "Bright extragalactic radio sources at 2.7 GHz. III - The all-sky catalogue". *Mon. Not. R. Astron. Soc.*, 216:173–192, 1985.

R.L. Webster, P.J. Francis, B.A. Peterson, M.J. Drinkwater, and F.J. Masci. "Evidence for a large undetected population of dust-reddened quasars.". *Nature*, 375:469–471, 1995.

K.C. Westfold. "The polarization of synchrotron radiation.". *Astrophys. J.*, 130:241–258, 1959.

M.T. Whiting, R.L. Webster, and P.J. Francis. "Red synchrotron jets in Parkes quasars". *Mon. Not. R. Astron. Soc.*, 323:718–732, 2001.

B.J. Wilkes, A.E. Wright, D.L. Jauncey, and B.A. Peterson. "An atlas of QSO spectra". *Publ. Astron. Soc. Aust.*, 5:2–83, 1983.

B.J. Wills, K.L. Thompson, M. Han, H. Netzer, D. Wills, J.A. Baldwin, G.J. Ferland, I.W.A. Browne, and M.S. Brotherton. "The *Hubble Space Telescope* sample of radio-loud quasars: Ultraviolet spectra of the first 31 quasars.". *Astrophys. J.*, 447:139–158, 1995.

B.J. Wills, D. Wills, M. Breger, R.R.J. Antonucci, and R. Barvainis. "A survey for high optical polarization in quasars with core-dominant radio structure: Is there a beamed optical continuum?". *Astrophys. J.*, 398: 454–475, 1992.

A.E. Wright and R.E. Otrupcek. "Parkes Catalogue (PKSCAT90)". Australia Telescope National Facility, 1990.

T. Yaqoob and P. Serlemitsos. "A broad Fe Kα emission line in the X-ray spectrum of the quasar 3C 273.". *Astrophys. J., Lett.*, 544:L95–L99, 2000.

E.L. Zirbel and S.A. Baum. "On the FR I/FR II Dichotomy in Powerful Radio Sources: Analysis of Their Emission-Line and Radio Luminosities". *Astrophys. J.*, 448:521–547, 1995.

Appendix A

Glossary

The following is a list of abbreviations and acronyms used throughout this thesis.

3C/3CR: 3rd Cambridge catalogue of radio sources / revised version (prefix in name of sources from this catalogue)

AGN: Active Galactic Nucleus/Nuclei

ANU: Australian National University

ATCA: Australia Telescope Compact Array

BBB: Big Blue Bump

BL Lac: BL Lacertæ object

CASPIR: Cryogenic Array Spectrometer/Imager – near-infrared detector on the Australian National University's 2.3m telescope

EGRET: Energetic Gamma Ray Experiment Telescope

FR I / II: Fanaroff-Riley radio galaxy type I / type II

FSRQ: Flat-Spectrum Radio Quasar

HPQ: High-Polarisation Quasar

HST: Hubble Space Telescope

IDV: Intra-Day Variability

IRAS: Infrared Astronomical Satellite

IRIS: Infrared Imager and Spectrometer – near-infrared instrument used on the Anglo-Australian Telescope

IUE: International Ultraviolet Explorer

LBQS: Large Bright Quasar Survey

LINER: Low Ionisation Nuclear Emission line Region

LPQ: Low-Polarisation Quasar

NGC: New General Catalogue (of nebulæand clusters of stars) (Dreyer 1888)

NIR: Near-Infrared (usually defined roughly as the wavelength region 1–5 μm)

NOT: Nordic Optical Telescope

OVV: Optically-Violent Variable

PHFS: Parkes Half-Jansky Flat-spectrum Sample (Drinkwater et al. 1997)

PKS: Parkes (used in names of sources taken from the survey of the sky made with the Parkes radio telescope)

QSO: Quasi-Stellar Object

SED: Spectral Energy Distribution

VLA: Very Large Array

VLBI: Very Long Baseline Interferometry

Appendix B

Photometry

This appendix contains the tables of photometry, taken from Francis et al. (2000), with the errors changed according to the method described in Section 4.5. Please note that, as is the case for the rest of the thesis, the 'PKS' designation that usually appears at the beginning of each source name has been omitted for brevity.

The first table, Table B.1, contains the photometry for all sources that were used in the modelling described in Chapter 5. The errors given are 1σ errors, while the upper limits (that is, upper limits to the flux, or lower limits to the magnitudes) are 3σ.

The second table gives the photometry for the sources that were excluded from the modelling. The reason(s) for their exclusion are given in the table. These are:

- Photometry: not enough data points to perform the modelling.
- No z: the source has no measured redshift.
- Galaxy: the source is at low redshift and shows evidence for the host galaxy in the SED.
- $z > 3$: all sources with redshift above 3 were discarded due to the presence of the strong Lyα emission line.

Name	B	V	R	I	J	H	K
0038−020	18.74 ± 0.11	18.44 ± 0.11	18.11 ± 0.11	18.01 ± 0.12	17.44 ± 0.17	16.82 ± 0.16	16.16 ± 0.16
0048−071	20.74 ± 0.20	20.32 ± 0.16	19.84 ± 0.13	19.53 ± 0.17	18.73 ± 0.22	17.93 ± 0.18	17.54 ± 0.40
0048−427	18.62 ± 0.11	18.45 ± 0.11	18.15 ± 0.10	17.75 ± 0.11	17.21 ± 0.15	16.86 ± 0.16	16.19 ± 0.16
0056−001	17.73 ± 0.10	17.55 ± 0.10	17.43 ± 0.10	—	16.49 ± 0.12	15.66 ± 0.11	14.92 ± 0.11
0131−001	23.34 ± 0.70	22.50 ± 0.50	20.78 ± 0.16	20.17 ± 0.19	17.95 ± 0.16	17.24 ± 0.15	16.78 ± 0.27
0202−172	17.46 ± 0.10	17.33 ± 0.10	17.11 ± 0.10	16.74 ± 0.10	16.27 ± 0.11	15.67 ± 0.11	15.35 ± 0.12
0213−026	21.33 ± 0.22	20.82 ± 0.16	19.99 ± 0.12	18.87 ± 0.11	17.48 ± 0.17	16.40 ± 0.13	15.17 ± 0.11
0216+011	20.33 ± 0.16	20.36 ± 0.16	19.54 ± 0.12	19.02 ± 0.13	18.14 ± 0.21	17.55 ± 0.15	17.38 ± 0.35
0220−349	21.73 ± 0.39	21.32 ± 0.28	20.83 ± 0.22	19.88 ± 0.20	18.72 ± 0.22	17.77 ± 0.16	16.82 ± 0.23
0221+067	19.85 ± 0.13	18.97 ± 0.11	18.24 ± 0.10	17.36 ± 0.10	16.29 ± 0.11	15.26 ± 0.11	14.47 ± 0.11
0226−038	17.56 ± 0.10	17.38 ± 0.10	17.17 ± 0.10	16.79 ± 0.10	16.40 ± 0.11	15.86 ± 0.11	15.13 ± 0.11
0229−398	19.74 ± 0.11	20.31 ± 0.13	19.90 ± 0.12	19.46 ± 0.13	18.86 ± 0.20	17.55 ± 0.15	17.51 ± 0.39
0232−042	15.73 ± 0.10	16.27 ± 0.10	15.93 ± 0.10	15.63 ± 0.10	15.22 ± 0.10	14.38 ± 0.10	14.28 ± 0.10
0237+040	18.33 ± 0.10	17.88 ± 0.10	17.53 ± 0.10	17.14 ± 0.10	16.49 ± 0.11	15.97 ± 0.11	15.15 ± 0.11
0240−060	19.07 ± 0.11	18.87 ± 0.11	18.61 ± 0.11	18.07 ± 0.11	17.50 ± 0.15	17.33 ± 0.18	16.35 ± 0.25
0537−441	17.93 ± 0.10	17.34 ± 0.10	16.92 ± 0.10	16.35 ± 0.10	14.76 ± 0.10	13.85 ± 0.10	13.02 ± 0.10
0829+046	16.28 ± 0.10	15.61 ± 0.10	15.11 ± 0.10	14.49 ± 0.10	13.45 ± 0.10	12.52 ± 0.10	11.80 ± 0.10
0912+029	18.75 ± 0.10	18.59 ± 0.11	18.29 ± 0.10	17.87 ± 0.11	16.97 ± 0.11	16.01 ± 0.10	15.29 ± 0.11
1016−311	18.32 ± 0.11	18.01 ± 0.10	17.82 ± 0.10	17.51 ± 0.11	16.70 ± 0.12	16.42 ± 0.13	15.59 ± 0.16
1020−103	17.10 ± 0.10	16.70 ± 0.10	16.30 ± 0.10	15.62 ± 0.10	14.85 ± 0.10	14.11 ± 0.10	13.27 ± 0.10
1032−199	18.92 ± 0.11	18.83 ± 0.11	18.60 ± 0.11	18.16 ± 0.12	17.35 ± 0.15	16.80 ± 0.14	16.04 ± 0.13
1034−293	18.83 ± 0.11	18.26 ± 0.10	17.71 ± 0.10	17.01 ± 0.10	15.76 ± 0.11	14.83 ± 0.10	13.70 ± 0.11
1036−154	20.54 ± 0.14	20.07 ± 0.13	19.43 ± 0.12	18.62 ± 0.12	17.23 ± 0.14	16.32 ± 0.11	15.63 ± 0.17
1045−188	18.55 ± 0.10	18.26 ± 0.10	17.76 ± 0.10	17.08 ± 0.10	16.30 ± 0.11	15.30 ± 0.11	14.59 ± 0.10

Table B.1: Magnitudes of PHFS sources used in modelling. Errors quoted are 1σ, while upper limits are 3σ.

Name	B	V	R	I	J	H	K
1101−325	15.54 ± 0.10	15.54 ± 0.10	15.31 ± 0.10	14.97 ± 0.10	14.55 ± 0.10	13.93 ± 0.10	13.16 ± 0.10
1107−187	22.44 ± 0.36	21.10 ± 0.16	19.30 ± 0.11	18.74 ± 0.11	17.46 ± 0.11	17.21 ± 0.11	15.95 ± 0.12
1133−172	22.32 ± 0.36	21.54 ± 0.21	20.52 ± 0.14	19.41 ± 0.13	18.37 ± 0.23	17.69 ± 0.21	16.63 ± 0.28
1136−135	16.65 ± 0.10	16.52 ± 0.10	16.39 ± 0.10	16.06 ± 0.10	15.54 ± 0.10	14.90 ± 0.10	14.40 ± 0.10
1244−255	17.42 ± 0.10	16.99 ± 0.10	16.63 ± 0.10	16.11 ± 0.10	15.43 ± 0.10	14.66 ± 0.10	13.85 ± 0.11
1256−229	18.43 ± 0.11	17.68 ± 0.10	17.11 ± 0.10	16.39 ± 0.10	15.16 ± 0.10	14.21 ± 0.10	13.44 ± 0.10
1313−333	18.17 ± 0.11	17.63 ± 0.10	17.16 ± 0.10	16.50 ± 0.10	15.46 ± 0.10	14.36 ± 0.10	13.69 ± 0.11
1404−342	17.37 ± 0.10	16.78 ± 0.10	16.56 ± 0.10	16.35 ± 0.10	15.67 ± 0.11	15.13 ± 0.11	14.57 ± 0.12
1430−155	> 22.70	23.24 ± 0.48	22.91 ± 0.48	20.73 ± 0.18	19.07 ± 0.28	17.97 ± 0.16	17.50 ± 0.38
1430−178	19.14 ± 0.11	18.92 ± 0.11	18.55 ± 0.11	18.14 ± 0.12	17.75 ± 0.25	16.78 ± 0.19	15.69 ± 0.24
1435−218	19.20 ± 0.11	18.54 ± 0.11	18.04 ± 0.10	17.75 ± 0.11	17.64 ± 0.23	17.18 ± 0.24	16.77 ± 0.53
1437−153	19.94 ± 0.14	19.01 ± 0.11	18.47 ± 0.11	17.68 ± 0.11	16.29 ± 0.12	15.11 ± 0.11	14.24 ± 0.12
1438−347	17.80 ± 0.10	17.31 ± 0.10	16.98 ± 0.10	16.72 ± 0.10	16.36 ± 0.13	15.86 ± 0.13	15.24 ± 0.18
1450−338	22.52 ± 0.38	20.40 ± 0.13	19.39 ± 0.11	18.69 ± 0.12	16.99 ± 0.12	16.03 ± 0.11	15.23 ± 0.13
1454−060	18.36 ± 0.11	17.84 ± 0.10	17.45 ± 0.10	17.08 ± 0.10	16.56 ± 0.13	15.86 ± 0.13	15.16 ± 0.17
1504−166	20.28 ± 0.15	19.75 ± 0.14	19.35 ± 0.13	18.46 ± 0.13	16.33 ± 0.12	15.59 ± 0.11	14.01 ± 0.11
1508−055	17.37 ± 0.10	16.94 ± 0.10	16.66 ± 0.10	16.28 ± 0.10	15.56 ± 0.11	14.87 ± 0.11	14.29 ± 0.12
1510−089	17.26 ± 0.10	17.12 ± 0.10	16.72 ± 0.10	16.17 ± 0.10	15.24 ± 0.10	14.09 ± 0.10	13.27 ± 0.10
1511−100	18.18 ± 0.10	18.00 ± 0.10	17.50 ± 0.10	17.07 ± 0.10	16.46 ± 0.11	15.60 ± 0.11	14.70 ± 0.12
1511−210	22.01 ± 0.26	21.45 ± 0.21	20.65 ± 0.14	20.30 ± 0.18	18.62 ± 0.33	17.81 ± 0.26	16.79 ± 0.37
1514−241	15.18 ± 0.10	14.50 ± 0.10	13.98 ± 0.10	13.31 ± 0.10	11.95 ± 0.10	11.10 ± 0.10	10.50 ± 0.10
1519−273	18.21 ± 0.11	17.74 ± 0.10	17.18 ± 0.10	16.55 ± 0.10	15.65 ± 0.11	14.84 ± 0.11	14.08 ± 0.11
1532+016	19.12 ± 0.12	18.92 ± 0.11	18.44 ± 0.11	17.98 ± 0.12	17.40 ± 0.20	16.22 ± 0.14	15.48 ± 0.21
1542+042	18.75 ± 0.11	18.54 ± 0.11	18.21 ± 0.11	17.61 ± 0.11	17.38 ± 0.15	16.46 ± 0.13	15.82 ± 0.19
1546+027	17.43 ± 0.10	17.14 ± 0.10	16.75 ± 0.10	16.16 ± 0.10	14.97 ± 0.10	13.88 ± 0.10	13.02 ± 0.10

Table B.1: PHFS magnitudes (cont'd)

Name	B	V	R	I	J	H	K
1548+056	19.37 ± 0.11	18.65 ± 0.11	18.13 ± 0.11	17.42 ± 0.11	16.30 ± 0.11	15.13 ± 0.11	14.30 ± 0.11
1550−269	20.24 ± 0.16	19.67 ± 0.13	19.18 ± 0.12	18.58 ± 0.13	17.63 ± 0.17	17.01 ± 0.16	16.07 ± 0.14
1555+001	20.34 ± 0.13	19.95 ± 0.12	20.00 ± 0.11	18.72 ± 0.12	17.73 ± 0.18	16.90 ± 0.15	16.24 ± 0.25
1556−245	18.89 ± 0.11	19.02 ± 0.11	18.82 ± 0.11	18.30 ± 0.12	17.59 ± 0.16	16.97 ± 0.16	16.58 ± 0.32
1602−001	17.66 ± 0.10	17.57 ± 0.10	17.10 ± 0.10	16.66 ± 0.10	16.28 ± 0.11	15.41 ± 0.11	15.19 ± 0.12
1615+029	18.01 ± 0.10	17.75 ± 0.10	17.31 ± 0.10	17.00 ± 0.10	16.66 ± 0.10	16.04 ± 0.10	15.89 ± 0.12
1616+063	19.45 ± 0.12	18.97 ± 0.11	18.76 ± 0.11	18.27 ± 0.12	17.87 ± 0.23	17.54 ± 0.25	16.52 ± 0.19
1635−035	21.58 ± 0.33	21.00 ± 0.22	20.75 ± 0.20	20.73 ± 0.34	19.11 ± 0.20	18.84 ± 0.23	17.48 ± 0.33
1654−020	23.51 ± 0.68	23.90 ± 0.87	23.05 ± 0.52	23.02 ± 0.88	> 20.00	19.92 ± 0.64	18.25 ± 0.56
1655+077	20.18 ± 0.13	19.88 ± 0.11	19.36 ± 0.11	18.42 ± 0.11	17.50 ± 0.16	16.59 ± 0.13	15.38 ± 0.15
1656+053	17.33 ± 0.10	16.86 ± 0.10	16.64 ± 0.10	16.10 ± 0.10	15.54 ± 0.11	15.04 ± 0.11	14.39 ± 0.13
1705+018	19.07 ± 0.11	18.66 ± 0.11	18.37 ± 0.11	17.86 ± 0.11	17.14 ± 0.13	16.44 ± 0.13	15.92 ± 0.13
1706+006	22.15 ± 0.30	20.59 ± 0.15	19.95 ± 0.13	18.95 ± 0.13	17.52 ± 0.18	16.38 ± 0.13	15.63 ± 0.19
1725+044	17.92 ± 0.10	17.46 ± 0.10	16.97 ± 0.10	16.37 ± 0.10	15.76 ± 0.10	14.91 ± 0.10	14.13 ± 0.10
1933−400	18.46 ± 0.11	18.03 ± 0.10	17.72 ± 0.10	17.43 ± 0.11	16.26 ± 0.11	15.79 ± 0.11	15.00 ± 0.13
1953−325	19.60 ± 0.13	18.91 ± 0.11	18.52 ± 0.11	18.00 ± 0.11	17.32 ± 0.18	16.78 ± 0.18	15.92 ± 0.27
1954−388	17.99 ± 0.10	17.55 ± 0.10	17.28 ± 0.10	16.89 ± 0.10	16.27 ± 0.12	15.28 ± 0.11	14.39 ± 0.12
1958−179	19.48 ± 0.12	18.89 ± 0.11	18.34 ± 0.11	17.54 ± 0.11	16.26 ± 0.12	14.97 ± 0.11	14.39 ± 0.12
2002−185	19.39 ± 0.11	18.82 ± 0.11	18.55 ± 0.11	18.05 ± 0.11	17.03 ± 0.13	16.87 ± 0.13	16.92 ± 0.34
2004−447	19.52 ± 0.13	18.74 ± 0.11	18.18 ± 0.11	17.35 ± 0.11	16.48 ± 0.11	15.46 ± 0.11	14.70 ± 0.11
2008−159	17.50 ± 0.10	17.07 ± 0.10	16.76 ± 0.10	16.33 ± 0.10	16.18 ± 0.12	15.58 ± 0.11	14.97 ± 0.15
2021−330	19.50 ± 0.12	19.06 ± 0.11	18.70 ± 0.11	18.31 ± 0.12	17.70 ± 0.15	16.82 ± 0.13	16.49 ± 0.20
2022−077	19.10 ± 0.11	18.55 ± 0.10	18.44 ± 0.10	18.50 ± 0.12	18.11 ± 0.31	16.61 ± 0.16	16.08 ± 0.31
2037−253	19.69 ± 0.13	19.56 ± 0.13	19.21 ± 0.12	19.24 ± 0.18	18.52 ± 0.35	18.01 ± 0.35	17.40 ± 0.66
2044−168	17.70 ± 0.10	17.55 ± 0.10	17.18 ± 0.10	17.05 ± 0.10	16.48 ± 0.13	15.99 ± 0.13	15.18 ± 0.17

Table B.1: PHFS magnitudes (cont'd)

Name	B	V	R	I	J	H	K
2053−044	18.86 ± 0.11	18.47 ± 0.11	18.18 ± 0.11	17.99 ± 0.11	17.81 ± 0.22	16.96 ± 0.17	16.13 ± 0.26
2058−297	18.85 ± 0.11	18.68 ± 0.11	18.29 ± 0.11	18.09 ± 0.11	17.52 ± 0.17	17.00 ± 0.17	16.22 ± 0.36
2059+034	18.09 ± 0.10	17.65 ± 0.10	17.40 ± 0.10	17.20 ± 0.11	16.34 ± 0.11	16.18 ± 0.12	15.63 ± 0.17
2106−413	19.57 ± 0.13	18.85 ± 0.11	18.45 ± 0.11	17.76 ± 0.11	16.77 ± 0.12	15.74 ± 0.11	14.81 ± 0.12
2120+099	19.65 ± 0.13	19.24 ± 0.12	18.96 ± 0.12	18.36 ± 0.13	17.98 ± 0.24	17.66 ± 0.27	16.52 ± 0.35
2121+053	19.86 ± 0.13	19.22 ± 0.11	18.68 ± 0.11	17.93 ± 0.11	16.52 ± 0.11	15.49 ± 0.11	14.71 ± 0.12
2127−096	19.43 ± 0.11	18.65 ± 0.11	18.00 ± 0.11	17.39 ± 0.11	16.38 ± 0.11	15.41 ± 0.11	14.61 ± 0.12
2128−123	15.28 ± 0.10	15.13 ± 0.10	15.00 ± 0.10	14.70 ± 0.10	14.58 ± 0.10	13.89 ± 0.10	13.22 ± 0.10
2131−021	20.61 ± 0.16	20.16 ± 0.17	19.58 ± 0.14	19.11 ± 0.19	17.58 ± 0.16	16.71 ± 0.14	15.85 ± 0.19
2134+004	17.04 ± 0.10	16.80 ± 0.10	16.56 ± 0.10	16.11 ± 0.10	15.67 ± 0.11	15.18 ± 0.11	14.73 ± 0.12
2135−248	19.64 ± 0.13	19.23 ± 0.12	18.96 ± 0.12	18.41 ± 0.13	17.50 ± 0.16	16.76 ± 0.14	15.89 ± 0.20
2140−048	17.22 ± 0.10	17.18 ± 0.10	16.87 ± 0.10	16.44 ± 0.10	15.59 ± 0.10	14.76 ± 0.10	13.95 ± 0.11
2143−156	18.02 ± 0.10	17.69 ± 0.10	17.55 ± 0.10	17.09 ± 0.11	16.61 ± 0.12	15.91 ± 0.11	15.24 ± 0.14
2144+092	18.78 ± 0.11	18.36 ± 0.11	18.01 ± 0.11	17.68 ± 0.11	16.37 ± 0.11	15.69 ± 0.11	14.82 ± 0.13
2145−176	19.43 ± 0.13	19.11 ± 0.12	18.85 ± 0.11	18.23 ± 0.13	17.74 ± 0.21	17.25 ± 0.21	16.41 ± 0.33
2145+067	16.15 ± 0.10	15.80 ± 0.10	15.56 ± 0.10	15.29 ± 0.10	14.54 ± 0.10	14.17 ± 0.10	13.48 ± 0.11
2149−307	18.00 ± 0.10	17.75 ± 0.10	17.31 ± 0.10	17.20 ± 0.11	16.60 ± 0.12	16.02 ± 0.12	15.24 ± 0.16
2149+056	> 23.50	22.05 ± 0.24	20.85 ± 0.14	19.54 ± 0.13	18.26 ± 0.25	17.42 ± 0.20	17.17 ± 0.49
2149+069	18.79 ± 0.11	18.48 ± 0.11	17.99 ± 0.11	17.74 ± 0.11	16.90 ± 0.13	15.82 ± 0.11	15.76 ± 0.21
2155−152	18.42 ± 0.10	17.90 ± 0.10	17.45 ± 0.10	16.88 ± 0.10	15.67 ± 0.10	14.72 ± 0.10	13.92 ± 0.10
2200−238	18.45 ± 0.11	18.36 ± 0.11	18.10 ± 0.11	17.64 ± 0.11	17.27 ± 0.14	16.72 ± 0.14	15.82 ± 0.13
2203−188	18.85 ± 0.11	18.52 ± 0.11	18.10 ± 0.11	17.46 ± 0.11	16.69 ± 0.12	15.93 ± 0.11	15.25 ± 0.11
2208−137	16.79 ± 0.10	16.70 ± 0.10	16.42 ± 0.10	16.10 ± 0.10	15.13 ± 0.10	14.34 ± 0.10	13.40 ± 0.10
2210−257	18.74 ± 0.11	18.76 ± 0.11	18.53 ± 0.11	17.95 ± 0.11	17.34 ± 0.15	16.42 ± 0.13	15.65 ± 0.12
2212−299	17.47 ± 0.10	17.36 ± 0.10	17.12 ± 0.10	16.81 ± 0.10	15.92 ± 0.11	15.19 ± 0.11	14.59 ± 0.11

Table B.1: PHFS magnitudes (cont'd)

Name	B	V	R	I	J	H	K
2216−038	17.03 ± 0.10	16.49 ± 0.10	16.14 ± 0.10	15.80 ± 0.10	14.81 ± 0.10	14.42 ± 0.10	13.96 ± 0.10
2223−052	18.59 ± 0.11	18.33 ± 0.11	17.89 ± 0.10	17.43 ± 0.11	16.45 ± 0.11	15.51 ± 0.11	14.69 ± 0.11
2227−088	18.31 ± 0.11	18.15 ± 0.11	17.81 ± 0.10	17.39 ± 0.11	16.47 ± 0.11	15.70 ± 0.11	15.06 ± 0.13
2227−399	17.94 ± 0.10	17.77 ± 0.10	17.19 ± 0.10	16.69 ± 0.10	15.87 ± 0.11	15.02 ± 0.10	14.11 ± 0.11
2229−172	21.26 ± 0.21	21.14 ± 0.20	21.34 ± 0.31	19.83 ± 0.19	18.88 ± 0.28	17.71 ± 0.23	16.77 ± 0.19
2233−148	19.24 ± 0.11	18.61 ± 0.11	18.06 ± 0.10	17.27 ± 0.10	16.38 ± 0.11	15.42 ± 0.11	14.57 ± 0.10
2239+096	19.00 ± 0.11	18.68 ± 0.11	18.34 ± 0.11	17.91 ± 0.11	17.42 ± 0.15	16.73 ± 0.13	16.01 ± 0.20
2240−260	17.95 ± 0.10	17.37 ± 0.10	16.95 ± 0.10	16.36 ± 0.10	15.15 ± 0.10	14.32 ± 0.10	13.52 ± 0.10
2243−123	16.65 ± 0.10	16.50 ± 0.10	16.32 ± 0.10	16.04 ± 0.10	15.51 ± 0.10	15.00 ± 0.10	14.50 ± 0.11
2245−328	19.08 ± 0.11	18.82 ± 0.11	18.51 ± 0.11	18.31 ± 0.12	17.61 ± 0.16	17.20 ± 0.16	16.08 ± 0.21
2252−090	22.03 ± 0.25	21.51 ± 0.18	20.49 ± 0.15	19.48 ± 0.14	18.98 ± 0.49	17.02 ± 0.18	16.48 ± 0.34
2312−319	18.10 ± 0.10	17.86 ± 0.10	17.50 ± 0.10	17.09 ± 0.10	16.82 ± 0.13	16.04 ± 0.12	15.63 ± 0.13
2313−438	19.89 ± 0.14	19.53 ± 0.12	19.10 ± 0.11	18.60 ± 0.13	17.97 ± 0.21	17.37 ± 0.20	16.72 ± 0.19
2314−409	18.33 ± 0.11	18.08 ± 0.10	17.75 ± 0.10	17.36 ± 0.11	16.74 ± 0.12	16.15 ± 0.12	15.59 ± 0.12
2329−415	19.40 ± 0.12	19.17 ± 0.11	18.89 ± 0.11	18.41 ± 0.13	17.58 ± 0.16	16.67 ± 0.13	15.67 ± 0.12
2345−167	17.23 ± 0.10	16.79 ± 0.10	16.44 ± 0.10	15.88 ± 0.10	14.53 ± 0.10	13.57 ± 0.10	12.76 ± 0.10
2351−154	18.97 ± 0.11	18.71 ± 0.11	18.46 ± 0.11	18.42 ± 0.13	17.88 ± 0.20	17.06 ± 0.16	16.37 ± 0.27
2354−117	18.81 ± 0.11	18.03 ± 0.10	17.80 ± 0.10	17.44 ± 0.11	16.56 ± 0.11	15.96 ± 0.11	15.06 ± 0.11

Table B.1: PHFS magnitudes (cont'd)

Name	B	V	R	I	J	H	K	Explanation
0036−216	21.20 ± 0.22	19.36 ± 0.11	18.33 ± 0.10	17.46 ± 0.10	16.20 ± 0.11	15.39 ± 0.11	14.46 ± 0.11	no z, galaxy
0048−097	16.12 ± 0.10	15.75 ± 0.10	15.39 ± 0.10	14.92 ± 0.10	13.99 ± 0.10	13.24 ± 0.10	12.51 ± 0.10	no z
0153−410	19.81 ± 0.13	18.15 ± 0.11	17.41 ± 0.10	16.69 ± 0.10	15.49 ± 0.11	14.81 ± 0.11	14.14 ± 0.11	galaxy
0238−084	12.03 ± 0.10	11.04 ± 0.10	10.44 ± 0.10	9.77 ± 0.10	8.70 ± 0.10	7.92 ± 0.10	7.68 ± 0.10	galaxy
0240−217	19.20 ± 0.13	17.93 ± 0.11	17.07 ± 0.10	16.34 ± 0.10	—	14.23 ± 0.10	13.63 ± 0.11	galaxy
0256+075	21.32 ± 0.20	20.68 ± 0.16	19.92 ± 0.12	18.92 ± 0.12	—	—	—	photometry
0301−243	16.51 ± 0.10	16.10 ± 0.10	15.69 ± 0.10	15.22 ± 0.10	—	—	—	photometry, no z
0316−444	16.07 ± 0.10	14.76 ± 0.10	14.12 ± 0.10	13.51 ± 0.10	—	—	—	photometry, galaxy
0922+005	—	—	17.09 ± 0.10	16.58 ± 0.10	—	—	—	photometry
1021−006	18.38 ± 0.11	18.25 ± 0.10	18.03 ± 0.10	17.61 ± 0.11	17.12 ± 0.13	—	—	photometry
1038+064	17.10 ± 0.10	16.92 ± 0.10	16.63 ± 0.10	16.43 ± 0.10	—	—	—	photometry
1042+071	20.38 ± 0.14	19.87 ± 0.14	19.12 ± 0.12	18.27 ± 0.12	—	—	—	photometry
1048−313	20.19 ± 0.13	20.19 ± 0.16	19.70 ± 0.14	19.21 ± 0.18	—	—	—	photometry
1055−243	19.13 ± 0.11	18.71 ± 0.11	18.40 ± 0.11	17.94 ± 0.11	—	—	—	photometry
1055+018	18.17 ± 0.10	17.63 ± 0.10	17.15 ± 0.10	16.47 ± 0.10	—	—	—	photometry
1110−217	24.41 ± 1.08	23.01 ± 0.43	21.57 ± 0.16	21.10 ± 0.23	19.06 ± 0.21	17.82 ± 0.14	16.74 ± 0.17	no z
1156−094	21.95 ± 0.34	21.43 ± 0.23	20.47 ± 0.14	20.22 ± 0.19	18.16 ± 0.23	17.51 ± 0.22	16.87 ± 0.22	no z
1330+022	19.02 ± 0.11	17.89 ± 0.10	17.24 ± 0.10	16.47 ± 0.10	15.23 ± 0.10	14.43 ± 0.10	13.71 ± 0.11	galaxy
1353−341	19.20 ± 0.11	17.46 ± 0.10	16.74 ± 0.10	15.94 ± 0.10	15.20 ± 0.11	14.38 ± 0.10	13.62 ± 0.11	galaxy
1411+094	18.64 ± 0.13	17.56 ± 0.11	16.77 ± 0.10	16.15 ± 0.11	15.10 ± 0.11	14.36 ± 0.11	13.78 ± 0.11	galaxy

Table B.2: Magnitudes of PHFS sources excluded from the modelling, and reasons for their exlusion. Errors are 1σ, while upper limits are 3σ.

Name	B	V	R	I	J	H	K	Explanation
1456+044	—	—	18.83 ± 0.10	18.12 ± 0.10	16.17 ± 0.10	15.71 ± 0.10	14.30 ± 0.10	photometry
1509+022	19.75 ± 0.15	18.27 ± 0.11	—	—	16.04 ± 0.11	15.12 ± 0.11	14.31 ± 0.12	photometry, galaxy
1518+045	16.11 ± 0.10	14.84 ± 0.10	14.20 ± 0.10	13.45 ± 0.10	12.06 ± 0.10	11.31 ± 0.10	11.02 ± 0.10	galaxy
1535+004	> 21.70	—	> 22.30	> 21.50	—	> 19.73	—	photometry
1555−140	18.28 ± 0.10	16.93 ± 0.10	16.28 ± 0.10	15.47 ± 0.10	14.25 ± 0.10	13.43 ± 0.10	13.08 ± 0.10	galaxy
1601−222	—	—	> 22.90	> 22.40	—	> 20.02	> 19.49	photometry
1614+051	20.38 ± 0.14	19.38 ± 0.11	19.31 ± 0.12	18.93 ± 0.13	18.04 ± 0.25	17.83 ± 0.31	17.31 ± 0.33	$z > 3$
1648+015	21.87 ± 0.32	21.14 ± 0.20	20.41 ± 0.14	19.50 ± 0.13	17.84 ± 0.12	16.85 ± 0.11	16.56 ± 0.16	no z
1649−062	—	—	> 23.20	> 23.30	> 18.88	> 17.77	> 17.03	photometry
1732+094	> 23.50	21.15 ± 0.14	19.74 ± 0.11	19.33 ± 0.11	18.40 ± 0.22	17.44 ± 0.16	16.37 ± 0.22	no z
2000−330	18.90 ± 0.11	17.48 ± 0.10	16.92 ± 0.10	16.71 ± 0.10	16.10 ± 0.11	15.64 ± 0.11	15.10 ± 0.12	$z > 3$
2047+098	—	—	> 22.99	> 22.19	—	> 19.92	—	photometry
2056−369	—	> 23.50	23.45 ± 0.61	22.22 ± 0.45	19.55 ± 0.40	19.07 ± 0.40	18.21 ± 0.42	no z
2058−135	15.88 ± 0.10	14.76 ± 0.10	14.15 ± 0.10	13.45 ± 0.10	12.35 ± 0.10	11.58 ± 0.10	11.39 ± 0.10	galaxy
2126−158	17.97 ± 0.10	16.92 ± 0.10	16.63 ± 0.10	16.23 ± 0.10	15.45 ± 0.10	14.89 ± 0.10	14.30 ± 0.10	$z > 3$
2206−237	17.41 ± 0.11	16.25 ± 0.10	15.70 ± 0.10	15.04 ± 0.10	13.94 ± 0.10	13.23 ± 0.10	12.87 ± 0.11	galaxy
2215+020	21.84 ± 0.32	20.42 ± 0.13	20.14 ± 0.15	20.00 ± 0.22	19.20 ± 0.50	18.21 ± 0.30	19.34 ± 1.78	$z > 3$
2245+029	21.71 ± 0.23	21.00 ± 0.19	20.26 ± 0.13	19.48 ± 0.14	17.45 ± 0.16	16.63 ± 0.15	15.49 ± 0.17	no z
2337−334	22.93 ± 0.60	21.89 ± 0.28	21.40 ± 0.22	20.51 ± 0.16	19.88 ± 0.54	18.42 ± 0.33	16.39 ± 0.22	no z
2344−192	23.52 ± 0.68	—	21.68 ± 0.26	20.96 ± 0.28	18.71 ± 0.16	17.64 ± 0.13	17.25 ± 0.22	no z

Table B.2: Magnitudes of excluded PHFS sources. (cont'd)

Appendix C

Model fitting results

This appendix contains the results of the modelling described in Chapter 5. Each source from Table B.1 is shown here, with the following entries:

- ID: Identification from Drinkwater et al. (1997).
- BL?: This is 'Y' if the source is a BL Lac object, and '—' if not.
- $B - K$: The colour from the photometry in Table B.1.
- Model: The best-fit model – 'C' for the combined model, 'P' for the power law model, or '—' for sources without a good fit for either model.
- α_{PL}: Index of the power law (either from the power law model, or the $\lambda^{-1.7}$ power law component of the combined model).
- λ_p: Peak wavelength of the synchrotron component (for those sources best fit by the combined model).
- $R_{0.5}$: Ratio of synchrotron flux to total flux at a rest-frame wavelength of 0.5μm.

Note that no data is given for sources that do not have a good fit for either of the two models (see Chapter 5 for definition of a good fit).

Name	z	ID	BL?	$B-K$	Model	$\chi^2_{\rm P}/\nu$	$\chi^2_{\rm C}/\nu$	α_{PL}	$\lambda_p(\mu\rm m)$	$R_{0.5}$
PKS 0038−020	1.1780	s	—	2.58	P	1.24	1.53	−1.74	—	—
PKS 0048−071	1.9740	f	—	3.20	P	0.80	0.87	−1.21	—	—
PKS 0048−427	1.7490	s	—	2.43	P	1.61	2.06	−1.74	—	—
PKS 0056−001	0.7170	s	—	2.07	C	1.41	0.54	−1.70	3.82	0.001
PKS 0131−001	0.8790	f	—	6.56	—	—	—	—	—	—
PKS 0202−172	1.7400	s	—	2.11	P	1.44	—	−1.88	—	—
PKS 0213−026	1.1780	f	—	6.16	C	1.43	0.87	−1.70	0.85	0.910
PKS 0216+011	1.6100	f	—	2.95	—	—	—	—	—	—
PKS 0220−349	1.4900	f	—	4.91	C	0.29	0.20	−1.70	0.47	0.875
PKS 0221+067	0.5100	s	—	5.38	C	—	1.22	−1.70	0.61	0.987
PKS 0226−038	2.0660	s	—	2.43	P	1.54	2.72	−1.82	—	—
PKS 0229−398	1.6460	m	—	2.23	—	—	—	—	—	—
PKS 0232−042	1.4370	s	—	1.45	—	—	—	—	—	—
PKS 0237+040	0.9780	s	—	3.18	P	2.34	2.87	−1.42	—	—
PKS 0240−060	1.8000	s	—	2.72	P	2.39	2.75	−1.61	—	—
PKS 0537−441	0.8930	s	Y	4.91	C	1.27	1.11	−1.70	0.69	0.754
PKS 0829+046	0.1800	s	Y	4.48	C	2.24	0.46	−1.70	0.44	0.978
PKS 0912+029	0.4270	s	—	3.46	C	0.84	0.50	−1.70	1.03	0.155
PKS 1016−311	0.7940	s	—	2.73	P	1.08	1.34	−1.64	—	—
PKS 1020−103	0.1966	s	—	3.83	C	1.35	1.10	−1.70	0.19	0.959
PKS 1032−199	2.1980	s	—	2.88	P	0.34	0.40	−1.47	—	—
PKS 1034−293	0.3120	s	—	5.13	P	0.27	0.51	−0.23	—	—
PKS 1036−154	0.5250	s	—	4.91	C	1.77	0.77	−1.70	0.68	0.841
PKS 1045−188	0.5950	s	—	3.96	P	1.48	1.50	−0.83	—	—

Table C.1: Sources that have been fitted by the three models, and the resulting model parameters.

Name	z	ID	BL?	$B-K$	Model	χ^2_{P}/ν	χ^2_{C}/ν	α_{PL}	$\lambda_p(\mu\mathrm{m})$	$R_{0.5}$
PKS 1101−325	0.3554	s	—	2.38	P	1.77	2.90	−1.81	—	—
PKS 1107−187	0.4970	f	—	6.49	—	—	—	—	—	—
PKS 1133−172	1.0240	f	—	5.69	C	—	2.87	−1.70	0.58	0.973
PKS 1136−135	0.5566	s	—	2.25	P	0.43	1.84	−1.85	—	—
PKS 1244−255	0.6380	s	—	3.57	P	1.33	1.41	−1.16	—	—
PKS 1256−229	1.3650	s	Y	4.99	C	2.82	0.17	−1.70	0.31	0.999
PKS 1313−333	1.2100	s	—	4.48	C	1.21	0.80	−1.70	0.33	0.874
PKS 1404−342	1.1220	s	—	2.80	—	—	—	—	—	—
PKS 1430−155	1.5730	f	—	> 5.20	C	—	3.22	−1.70	0.90	0.982
PKS 1430−178	2.3260	s	—	3.45	P	1.48	1.72	−1.29	—	—
PKS 1435−218	1.1870	s	—	2.43	—	—	—	—	—	—
PKS 1437−153	0.2540	s	Y	5.70	C	1.62	0.75	−1.70	1.04	0.770
PKS 1438−347	1.1590	s	—	2.56	—	—	—	—	—	—
PKS 1450−338	0.3680	f	—	7.29	—	—	—	—	—	—
PKS 1454−060	1.2490	s	—	3.20	—	—	—	—	—	—
PKS 1504−166	0.8760	m	—	6.27	C	—	3.22	−1.70	1.39	0.731
PKS 1508−055	1.1850	s	—	3.08	P	1.15	1.45	−1.40	—	—
PKS 1510−089	0.3620	s	—	3.99	C	1.92	1.28	−1.70	1.21	0.209
PKS 1511−100	1.5130	s	—	3.48	P	1.96	2.40	−1.19	—	—
PKS 1511−210	1.1790	s	—	5.22	P	0.60	0.75	−0.16	—	—
PKS 1514−241	0.0486	g	Y	4.68	C	—	1.28	−1.70	0.62	0.973
PKS 1519−273	0.5100	s	Y	4.13	C	1.99	0.98	−1.70	0.27	0.940
PKS 1532+016	1.4350	s	—	3.64	P	1.38	1.70	−1.03	—	—
PKS 1542+042	2.1840	s	—	2.93	P	2.85	—	−1.47	—	—
PKS 1546+027	0.4150	s	—	4.41	C	0.83	0.28	−1.70	1.04	0.387

Table C.1: Results of modelling (cont'd)

Name	z	ID	BL?	$B-K$	Model	χ^2_{P}/ν	χ^2_{C}/ν	α_{PL}	$\lambda_p(\mu\mathrm{m})$	$R_{0.5}$
PKS 1548+056	1.4220	s	—	5.07	C	1.20	0.83	−1.70	0.38	0.929
PKS 1550−269	2.1450	s	—	4.17	C	1.25	0.74	−1.70	0.12	0.973
PKS 1555+001	1.7700	f	—	4.10	—	—	—	—	—	—
PKS 1556−245	2.8179	s	—	2.31	P	1.46	1.71	−1.63	—	—
PKS 1602−001	1.6241	s	—	2.47	—	—	—	—	—	—
PKS 1615+029	1.3410	s	—	2.12	—	—	—	—	—	—
PKS 1616+063	2.0880	s	—	2.93	P	2.84	—	−1.54	—	—
PKS 1635−035	2.8560	s	—	4.10	P	1.16	1.31	−1.00	—	—
PKS 1654−020	2.0000	f	—	5.26	C	0.54	0.24	−1.70	2.45	0.665
PKS 1655+077	0.6210	s	—	4.80	P	1.63	1.91	−0.38	—	—
PKS 1656+053	0.8873	s	—	2.94	P	2.79	—	−1.51	—	—
PKS 1705+018	2.5765	s	—	3.15	P	1.29	1.53	−1.32	—	—
PKS 1706+006	0.4490	f	—	6.52	C	—	1.58	−1.70	1.01	0.957
PKS 1725+044	0.2960	m	—	3.79	C	2.67	2.49	−1.70	0.14	0.995
PKS 1933−400	0.9650	s	—	3.46	P	0.89	0.94	−1.17	—	—
PKS 1953−325	1.2420	s	—	3.68	—	—	—	—	—	—
PKS 1954−388	0.6260	s	—	3.60	P	2.06	2.55	−1.18	—	—
PKS 1958−179	0.6520	s	—	5.09	C	2.37	1.53	−1.70	0.71	0.824
PKS 2002−185	0.8590	s	—	2.47	—	—	—	—	—	—
PKS 2004−447	0.2400	s	—	4.82	C	—	1.51	−1.70	0.53	0.982
PKS 2008−159	1.1780	s	—	2.53	—	—	—	—	—	—
PKS 2021−330	1.4710	s	—	3.01	P	2.01	2.39	−1.34	—	—
PKS 2022−077	1.3880	s	—	3.02	—	—	—	—	—	—
PKS 2037−253	1.5740	s	—	2.29	P	0.67	0.95	−1.80	—	—
PKS 2044−168	1.9370	s	—	2.52	P	1.43	2.15	−1.80	—	—

Table C.1: Results of modelling (cont'd)

Name	z	ID	BL?	$B-K$	Model	χ^2_{P}/ν	χ^2_{C}/ν	α_{PL}	$\lambda_p(\mu\mathrm{m})$	$R_{0.5}$
PKS 2053−044	1.1770	s	—	2.73	—	—	—	—	—	—
PKS 2058−297	1.4920	s	—	2.63	P	1.15	1.40	−1.68	—	—
PKS 2059+034	1.0120	s	—	2.46	—	—	—	—	—	—
PKS 2106−413	1.0550	s	—	4.76	C	0.97	0.88	−1.70	0.32	0.935
PKS 2120+099	0.9320	s	—	3.13	P	2.63	2.95	−1.39	—	—
PKS 2121+053	1.9410	s	—	5.15	C	1.21	0.34	−1.70	0.40	0.928
PKS 2127−096	0.7800	f	—	4.82	C	—	1.04	−1.70	0.37	0.987
PKS 2128−123	0.4990	s	—	2.06	—	—	—	—	—	—
PKS 2131−021	1.2850	s	Y	4.76	C	0.37	0.30	−1.70	0.51	0.819
PKS 2134+004	1.9370	s	—	2.31	P	2.25	—	−1.82	—	—
PKS 2135−248	0.8210	s	—	3.75	C	0.13	0.12	−1.70	0.10	0.950
PKS 2140−048	0.3440	s	—	3.27	C	1.07	0.64	−1.70	1.22	0.084
PKS 2143−156	0.6980	s	—	2.78	P	1.04	1.30	−1.61	—	—
PKS 2144+092	1.1130	s	—	3.96	P	0.49	0.61	−0.87	—	—
PKS 2145−176	2.1300	s	—	3.02	P	1.48	1.78	−1.40	—	—
PKS 2145+067	0.9990	s	—	2.67	P	1.37	1.70	−1.68	—	—
PKS 2149−307	2.3450	s	—	2.76	P	1.86	2.17	−1.66	—	—
PKS 2149+056	0.7400	f	—	> 6.33	—	—	—	—	—	—
PKS 2149+069	1.3640	s	—	3.03	—	—	—	—	—	—
PKS 2155−152	0.6720	s	—	4.50	C	0.34	0.13	−1.70	0.49	0.768
PKS 2200−238	2.1200	s	—	2.63	P	1.85	1.91	−1.69	—	—
PKS 2203−188	0.6190	s	—	3.60	C	1.32	1.13	−1.70	0.10	0.981
PKS 2208−137	0.3920	s	—	3.39	C	1.50	0.29	−1.70	1.67	0.050
PKS 2210−257	1.8330	s	—	3.09	C	1.66	1.39	−1.70	0.65	0.301
PKS 2212−299	2.7030	s	—	2.88	C	0.34	0.30	−1.70	0.25	0.330

Table C.1: Results of modelling (cont'd)

Name	z	ID	BL?	$B-K$	Model	χ^2_{P}/ν	χ^2_{C}/ν	α_{PL}	$\lambda_p(\mu\mathrm{m})$	$R_{0.5}$
PKS 2216−038	0.9010	s	—	3.07	—	—	—	—	—	—
PKS 2223−052	1.4040	s	—	3.90	P	0.36	0.42	−0.88	—	—
PKS 2227−088	1.5610	s	—	3.25	P	0.31	0.35	−1.21	—	—
PKS 2227−399	0.3230	s	—	3.83	P	1.39	1.72	−0.94	—	—
PKS 2229−172	1.7800	f	—	4.49	C	2.94	1.99	−1.70	0.75	0.749
PKS 2233−148	0.6090	s	Y	4.67	C	2.47	1.01	−1.70	0.36	0.987
PKS 2239+096	1.7070	s	—	2.99	P	1.57	1.95	−1.47	—	—
PKS 2240−260	0.7740	s	Y	4.43	C	0.76	0.08	−1.70	0.33	0.910
PKS 2243−123	0.6300	s	—	2.15	P	0.55	—	−1.92	—	—
PKS 2245−328	2.2680	s	—	3.00	P	1.31	—	−1.60	—	—
PKS 2252−090	0.6064	s	—	5.55	C	—	2.41	−1.70	0.73	0.986
PKS 2312−319	1.3230	s	—	2.47	—	—	—	—	—	—
PKS 2313−438	1.8470	s	—	3.17	P	1.52	1.77	−1.31	—	—
PKS 2314−409	2.4480	s	—	2.74	P	1.17	1.52	−1.57	—	—
PKS 2329−415	0.6710	s	—	3.73	C	0.81	0.51	−1.70	0.98	0.224
PKS 2345−167	0.5760	s	—	4.47	C	0.54	0.33	−1.70	0.83	0.532
PKS 2351−154	2.6750	s	—	2.60	P	1.11	1.48	−1.76	—	—
PKS 2354−117	0.9600	s	—	3.75	C	—	3.02	−1.70	0.07	0.925

Table C.1: Results of modelling (cont'd)

Appendix D

Fits to data

The figures in this Appendix show the fits to the photometry for the models detailed in Chapter 5. The fits for the sources that were modelled in Chapter 5 are shown from page 188. Page 247 shows the fits to the two extra sources from the near-infrared polarimetry of Chapter 6, and the fits for the sources without redshifts (as discussed in Section 5.8) are shown from page 248. Each figure contains a number of sections, showing different observations and different model fitting results.

The panel at the top-right shows the basic data for the source. There is an entry in the "other name" section if there is another common name that the source is known by. The classification is that given by Drinkwater et al. (1997). If the source is a BL Lac or BL Lac candidate, this is also stated, together with a reference for this status. This reference is either PG95, representing Padovani and Giommi (1995) (the primary source of BL Lac classifications) or VV00, representing Véron-Cetty and Véron (2000). The galactic extinction from Schlegel et al. (1998) is given, and is converted into a B-band absorption. The B magnitude and $B - K$ colour are given, as is the absolute magnitude M_V (calculated according to Section 4.4).

The photometry is shown in the centre-left panel. The magnitudes from Table B.1 have been converted into fluxes according to the zero magnitude fluxes from Table 4.1, and plotted on a log-log scale against wavelength. The two models – the power law fit and the combined fit – are also shown. The best fit is plotted with a solid line, while the other (if it is a viable fit – see Chapter 5 for details) is plotted with a dashed line. If the best fit model is the combined model, the two individual components are shown with dotted lines. Locations of well-known emission lines, placed at the redshift of the source, are shown along the top.

The centre-right panel has two parts. The plot shows the values of χ^2/ν for each value of λ_p that was considered for the combined fit. If the fit was viable (i.e. if the normalisations of the two fitted components were both positive), then the symbol used is a circle, while a dot is used if the fit is not viable. The χ^2/ν value of the power law fit is shown by the (lower) horizontal line. If the source was too blue to fit the combined model to, then a second horizontal line shows the χ^2/ν value from a fit with just the BBB power law (i.e. $\lambda^{-1.7}$) component. This plot then provides a graphical way of seeing which model was better, and how well constrained the peak wavelength is. Next to this plot are the basic details of the best model fit. This includes the fitted model parameters (the power law index and the peak wavelength), the χ^2/ν value and ν, the number of degrees of freedom. Also shown, for combined fits, are the ratio of the synchrotron to the power law component and to the total flux, at 0.5μm (rest frame).

At the top-left is a graph of any polarisation measurements. These are either the NIR polarisation measurements from Chapter 6 (shown in circles), measurements from Wills et al. (1992) (squares), or measurements from Impey and Tapia (1990) (diamonds). The latter two, being un-filtered optical measurements, are plotted at an arbitrary wavelength of 0.5μm, and thus are for illustrative purposes only (they are not simultaneous with any of the other observations – see Chapter 6). The polarisation is plotted on a linear scale, against wavelength on the same log scale as the photometry.

The bottom-left shows the optical spectrum, where one exists in our data-base (the analysis of these spectra is presented in Francis et al. (2001)). This is plotted on a log-log scale with f_λ against λ (again to match the scales on the photometry plot). Locations of prominent emission lines, placed at the redshift of the source, are shown along the top.

Finally, the broad-band SED is shown in the bottom-right. The observations are from a number of sources:

RADIO: The radio observations come from three sources: the circles are the four simultaneous fluxes obtained made with the ATCA; the triangles are the two PKSCAT90 fluxes (Wright and Otrupcek 1990) used to define the PHFS; and finally, the crosses are simultaneous observations from the large survey by Kovalev et al. (1999).

IRAS: Fluxes from the *IRAS* Point Source Catalog are shown. The symbols indicate the level of confidence of the detection: circles and squares indicate detections (of high and moderate quality), while crosses indicate upper limits.

OPT: The optical–NIR photometry discussed in this thesis is shown in the optical region. Also shown in this region is the best fit model, plotted between 10^{13} Hz and $10^{15.5}$ Hz, together with the individual components for the combined fits.

X-RAY: The X-ray fluxes are taken from Siebert et al. (1998). The X-ray slope used is either that explicitly given therein, or the average values for quasars, galaxies or BL Lacs that they calculate. The error in the X-ray slope is also shown. If the source is not detected (i.e. the flux is an upper limit), the bow-tie is plotted with a dotted line.

EGRET: Fluxes from the Third *EGRET* Catalogue (Hartman et al. 1999) are shown, either as a square (for detections) or a triangle (for upper limits).

Finally, please note that the combined fit shown for PKS 2245−328 is clearly unphysical, and should be disregarded. We take the best fit to be the power law fit given in Table C.1.

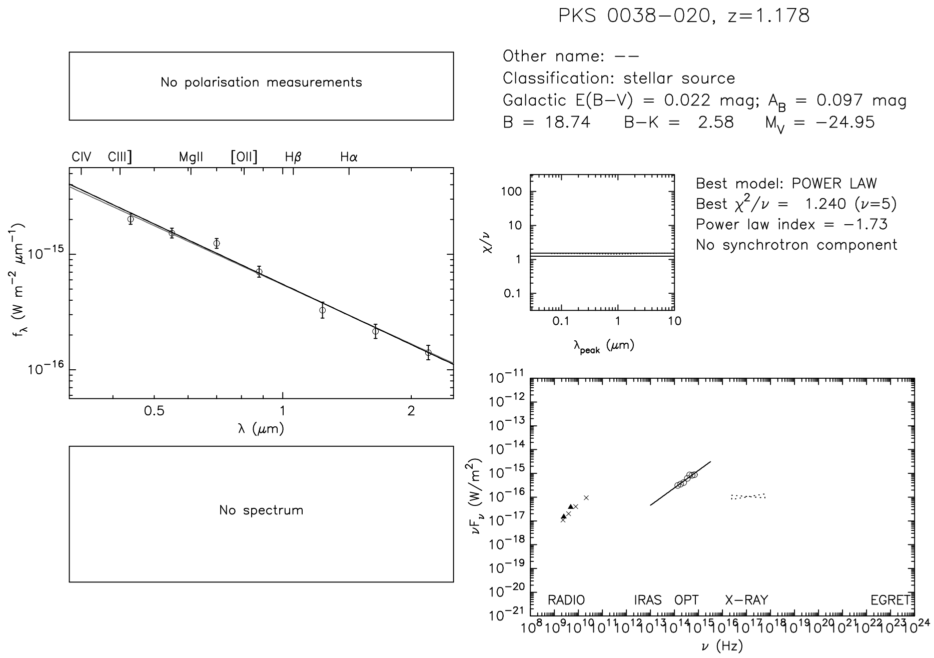
PKS 0038−020, z=1.178
Other name: −−
Classification: stellar source
Galactic E(B−V) = 0.022 mag; A_B = 0.097 mag
B = 18.74 B−K = 2.58 M_V = −24.95
No polarisation measurements
Best model: POWER LAW
Best χ^2/ν = 1.240 (ν=5)
Power law index = −1.73
No synchrotron component
No spectrum
RADIO
IRAS
OPT
X-RAY
EGRET
ν (Hz)
λ (μm)
λ_{peak} (μm)

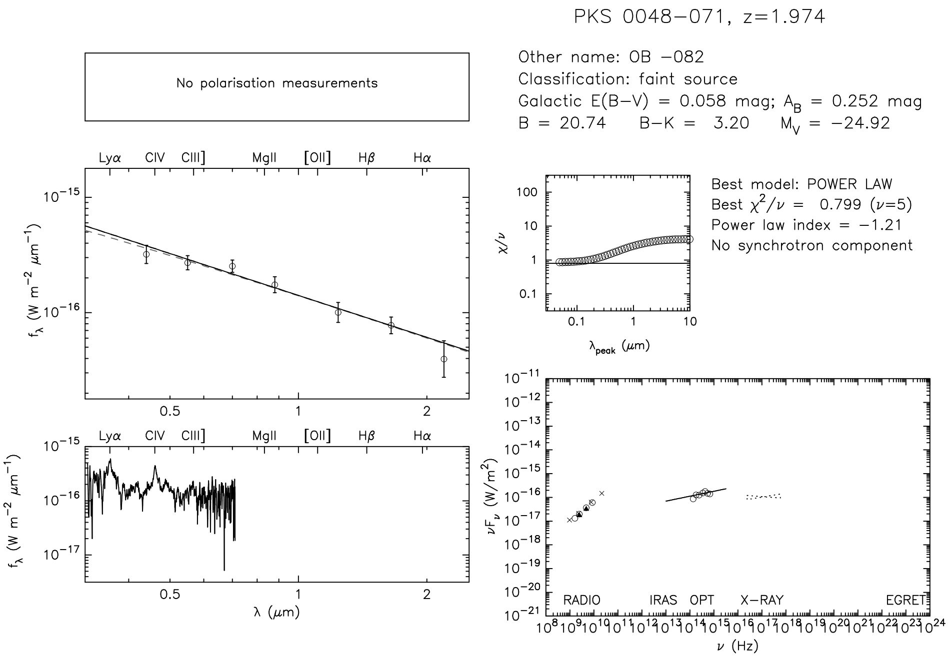
PKS 0048−071, z=1.974
Other name: OB −082
Classification: faint source
Galactic E(B−V) = 0.058 mag; A_B = 0.252 mag
B = 20.74 B−K = 3.20 M_V = −24.92
No polarisation measurements
Best model: POWER LAW
Best χ^2/ν = 0.799 (ν=5)
Power law index = −1.21
No synchrotron component
RADIO
IRAS
OPT
X-RAY
EGRET
ν (Hz)
λ (μm)
λ_{peak} (μm)

PKS 0048−427, z=1.749

No polarisation measurements

Other name: −−
Classification: stellar source
Galactic E(B−V) = 0.012 mag; A_B = 0.052 mag
B = 18.62   B−K = 2.43 M_V = −25.94

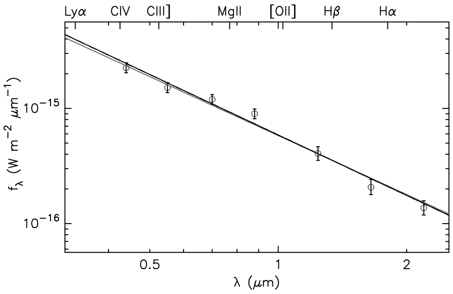

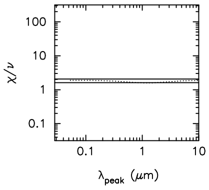

Best model: POWER LAW
Best χ^2/ν = 1.614 (ν=5)
Power law index = −1.74
No synchrotron component

No spectrum

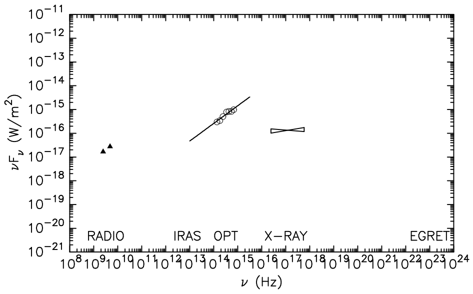

PKS 0056−001, z=0.717

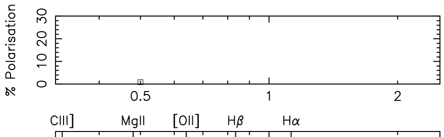

Other name: LBQS 0056−0009
Classification: stellar source
Galactic E(B−V) = 0.027 mag; A_B = 0.115 mag
B = 17.73   B−K = 2.81 M_V = −24.54

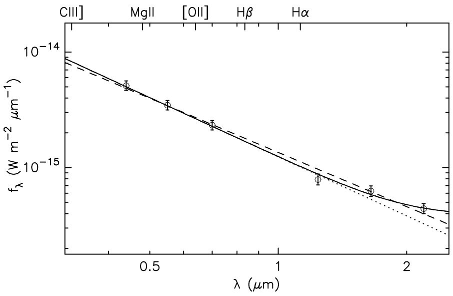

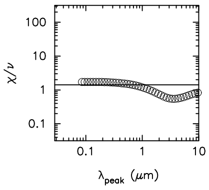

Best model: COMBINED
Best χ^2/ν = 0.544 (ν=3)
Power law index = −1.70
λ_{peak} (synch.) = 3.82 μm
0.5 μm ratio = 0.00
0.5 μm fraction = 0.1%

No spectrum

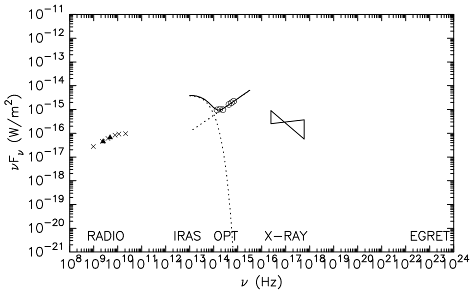

PKS 0131−001, z=0.879

No polarisation measurements

Other name: 4C −00.11
Classification: faint source
Galactic E(B−V) = 0.037 mag; A_B = 0.159 mag
B = 23.34 B−K = 6.56 M_V = −22.06

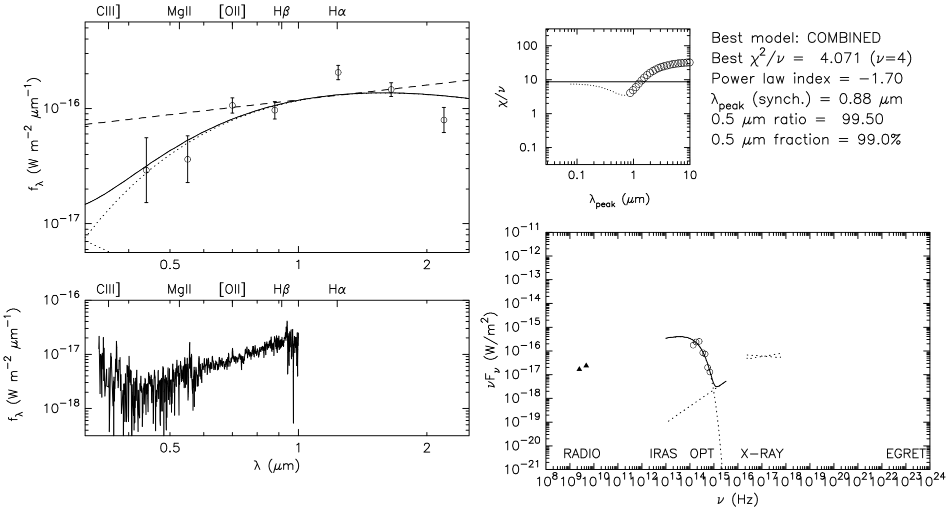

Best model: COMBINED
Best χ^2/ν = 4.071 (ν=4)
Power law index = −1.70
λ_{peak} (synch.) = 0.88 μm
0.5 μm ratio = 99.50
0.5 μm fraction = 99.0%

PKS 0202−172, z=1.74

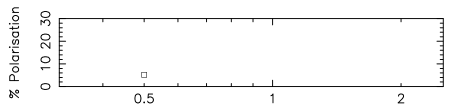

Other name: −−
Classification: stellar source
Galactic E(B−V) = 0.031 mag; A_B = 0.135 mag
B = 17.46 B−K = 2.11 M_V = −26.81

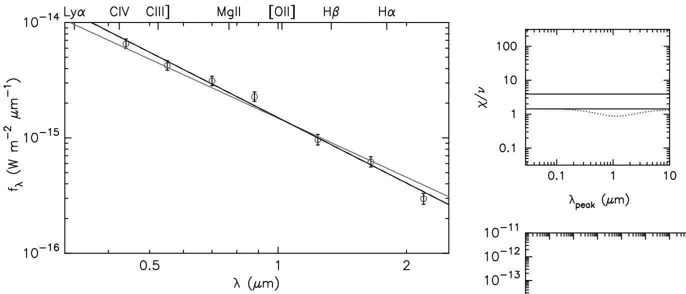

Best model: POWER LAW
Best χ^2/ν = 1.437 (ν=5)
Power law index = −1.88
No synchrotron component

No spectrum

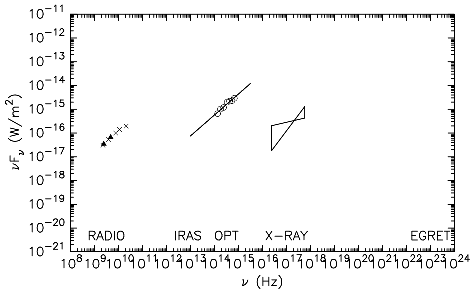

PKS 0213−026, z=1.178

No polarisation measurements

Other name: 4C −02.09
Classification: faint source
Galactic E(B−V) = 0.026 mag; A_B = 0.111 mag
B = 21.33   B−K = 6.16 M_V = −24.61

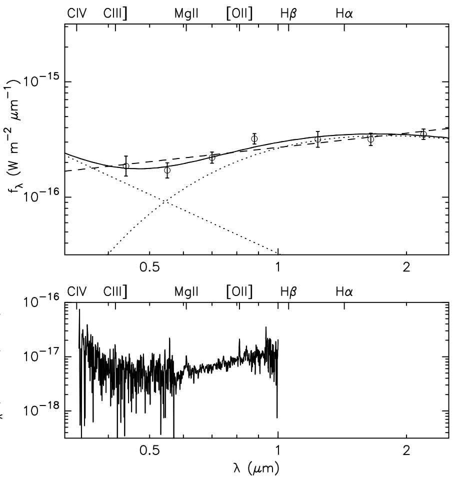

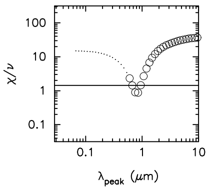

Best model: COMBINED
Best χ^2/ν = 0.870 (ν=4)
Power law index = −1.70
λ_{peak} (synch.) = 0.85 μm
0.5 μm ratio = 10.16
0.5 μm fraction = 91.0%

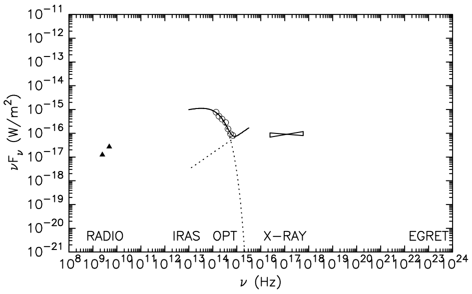

PKS 0216+011, z=1.61

No polarisation measurements

Other name: --
Classification: faint source
Galactic E(B−V) = 0.034 mag; A_B = 0.146 mag
B = 20.33   B−K = 2.95 M_V = −24.64

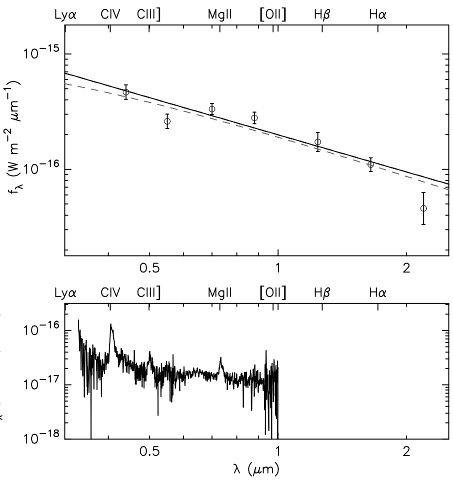

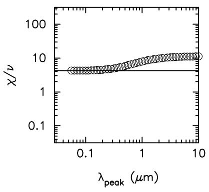

Best model: POWER LAW
Best χ^2/ν = 4.221 (ν=5)
Power law index = −1.07
No synchrotron component

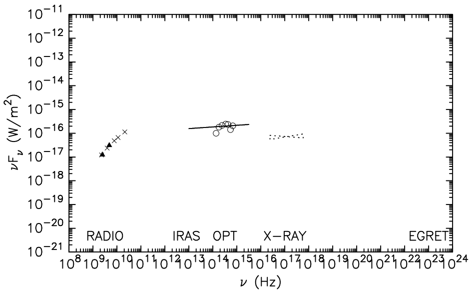

PKS 0220−349, z=1.49

No polarisation measurements

Other name: −−
Classification: faint source
Galactic E(B−V) = 0.018 mag; A_B = 0.078 mag
B = 21.73 B−K = 4.91 M_V = −24.10

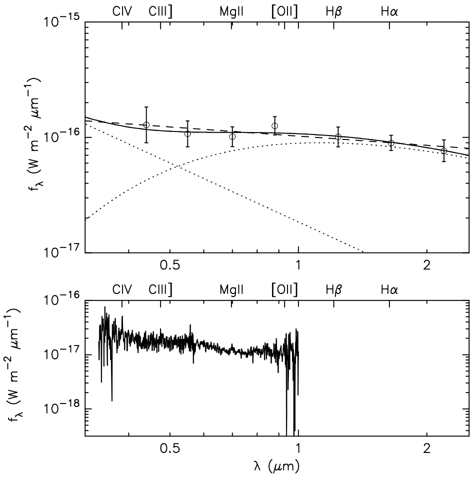

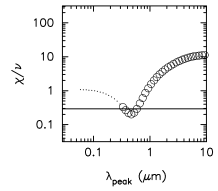

Best model: COMBINED
Best χ^2/ν = 0.201 (ν=4)
Power law index = −1.70
λ_{peak} (synch.) = 0.47 μm
0.5 μm ratio = 7.01
0.5 μm fraction = 87.5%

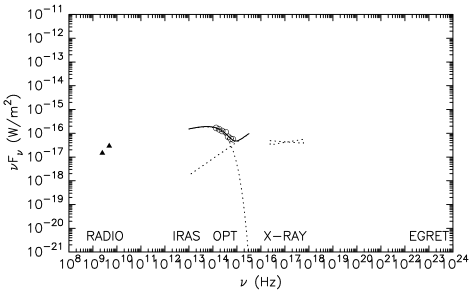

PKS 0221+067, z=0.51

No polarisation measurements

Other name: 4C +06.11
Classification: stellar source
Galactic E(B−V) = 0.074 mag; A_B = 0.321 mag
B = 19.85 B−K = 5.38 M_V = −23.59

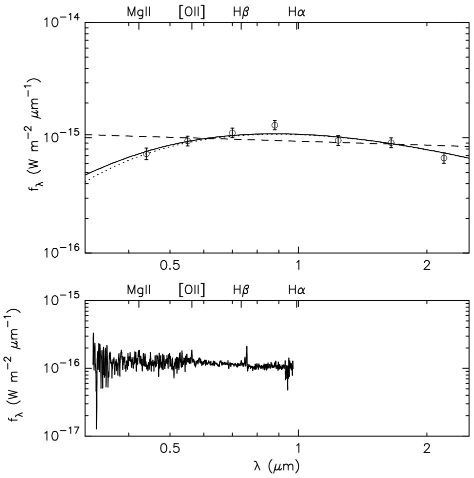

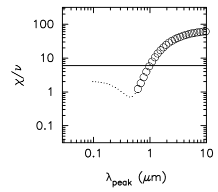

Best model: COMBINED
Best χ^2/ν = 1.223 (ν=4)
Power law index = −1.70
λ_{peak} (synch.) = 0.61 μm
0.5 μm ratio = 76.95
0.5 μm fraction = 98.7%

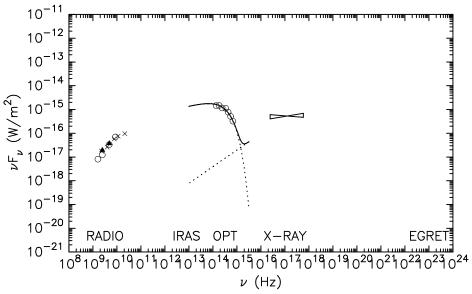

PKS 0226−038, z=2.066

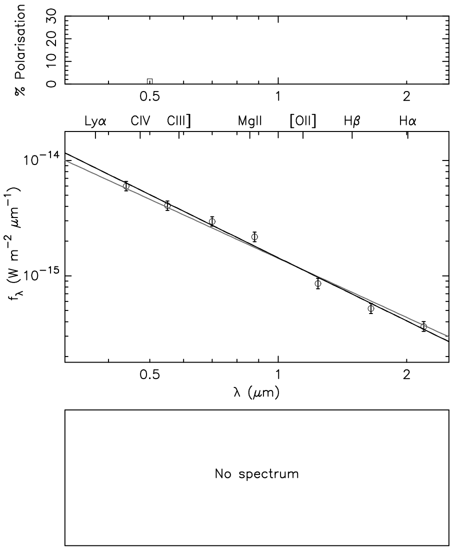

Other name: 4C −03.07
Classification: stellar source
Galactic E(B−V) = 0.030 mag; A_B = 0.130 mag
B = 17.56 B−K = 2.43 M_V = −27.19

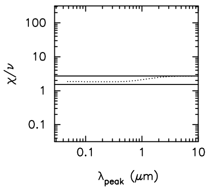

Best model: POWER LAW
Best χ^2/ν = 1.536 (ν=5)
Power law index = −1.82
No synchrotron component

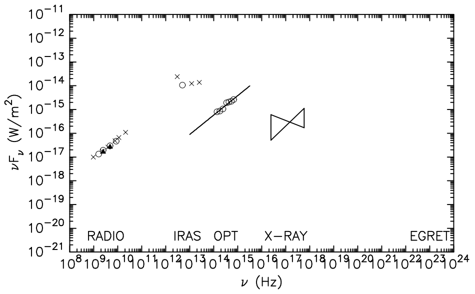

PKS 0229−398, z=1.646

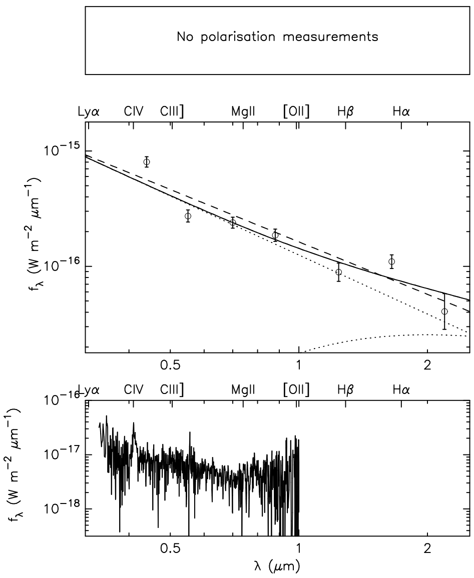

Other name: −−
Classification: merger
Galactic E(B−V) = 0.019 mag; A_B = 0.082 mag
B = 19.74 B−K = 2.23 M_V = −23.14

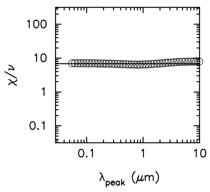

Best model: COMBINED
Best χ^2/ν = 6.452 (ν=4)
Power law index = −1.70
λ_{peak} (synch.) = 0.78 μm
0.5 μm ratio = 0.29
0.5 μm fraction = 22.5%

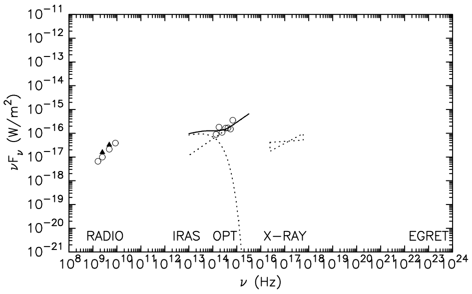

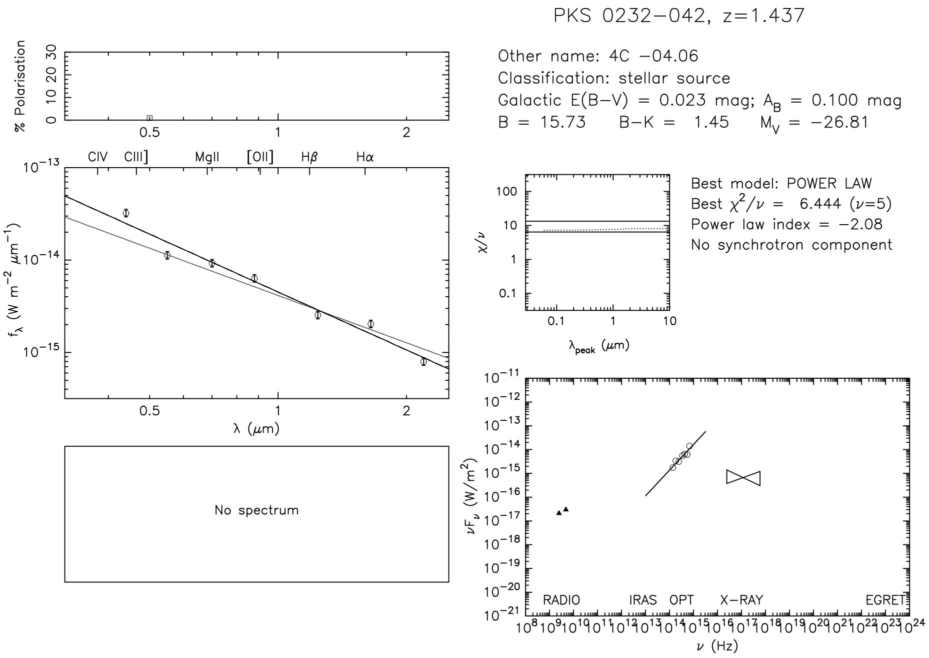
PKS 0232−042, z=1.437
Other name: 4C −04.06
Classification: stellar source
Galactic E(B−V) = 0.023 mag; A_B = 0.100 mag
B = 15.73 B−K = 1.45 M_V = −26.81
Best model: POWER LAW
Best χ^2/ν = 6.444 (ν=5)
Power law index = −2.08
No synchrotron component
% Polarisation
CIV CIII] MgII [OII] Hβ Hα
f_λ (W m^{-2} μm^{-1})
λ (μm)
No spectrum
χ/ν
λ_{peak} (μm)
νF_ν (W/m^2)
RADIO IRAS OPT X-RAY EGRET
ν (Hz)

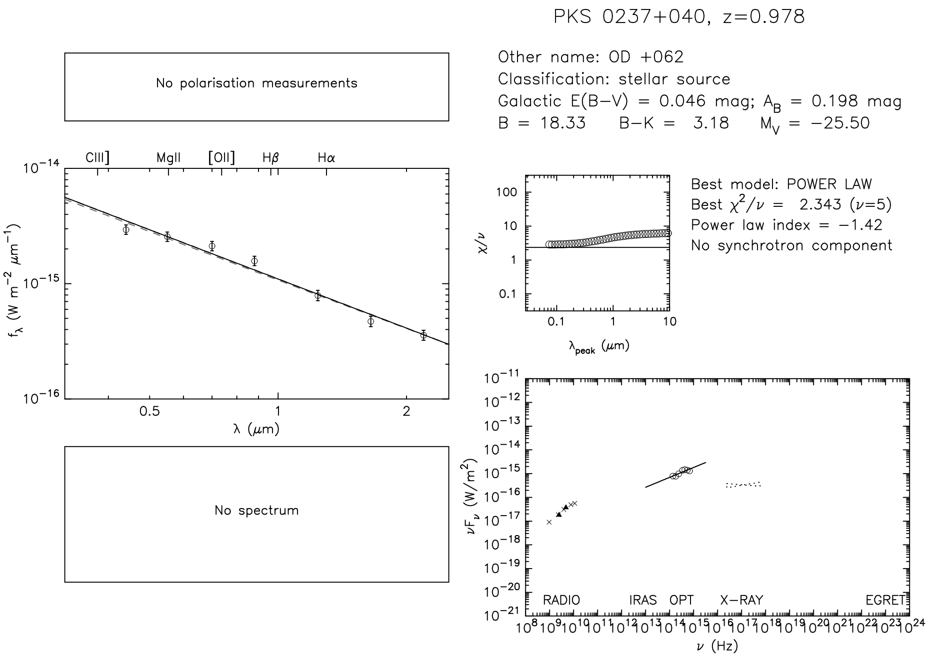
PKS 0237+040, z=0.978
Other name: OD +062
Classification: stellar source
Galactic E(B−V) = 0.046 mag; A_B = 0.198 mag
B = 18.33 B−K = 3.18 M_V = −25.50
No polarisation measurements
Best model: POWER LAW
Best χ^2/ν = 2.343 (ν=5)
Power law index = −1.42
No synchrotron component
CIII] MgII [OII] Hβ Hα
f_λ (W m^{-2} μm^{-1})
λ (μm)
No spectrum
χ/ν
λ_{peak} (μm)
νF_ν (W/m^2)
RADIO IRAS OPT X-RAY EGRET
ν (Hz)

PKS 0240−060, z=1.8

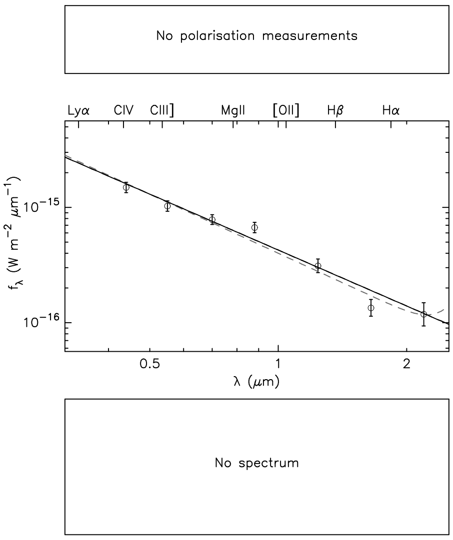

Other name: OD −068
Classification: stellar source
Galactic E(B−V) = 0.031 mag; A_B = 0.133 mag
B = 19.07 B−K = 2.72 M_V = −25.73

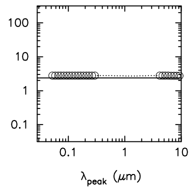

Best model: POWER LAW
Best χ^2/ν = 2.392 (ν=5)
Power law index = −1.61
No synchrotron component

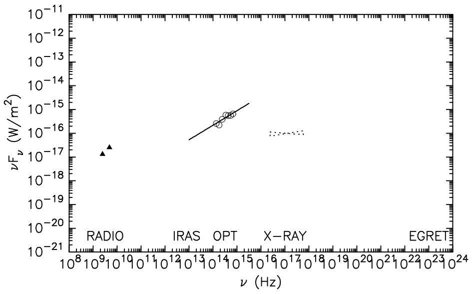

PKS 0537−441, z=0.893

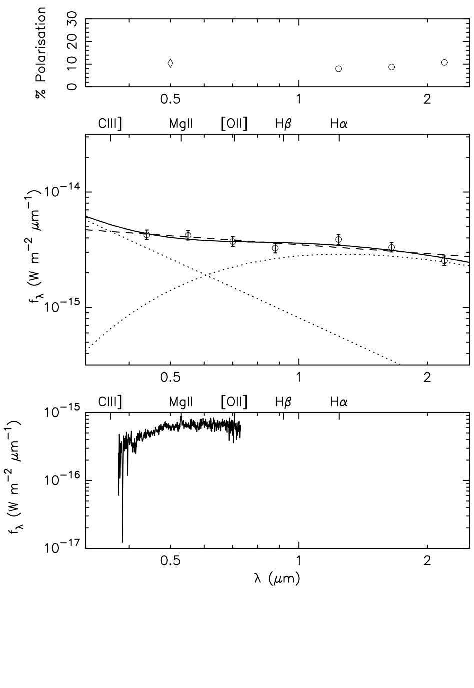

Other name: −−
Classification: stellar source, BL Lac (PG95)
Galactic E(B−V) = 0.038 mag; A_B = 0.163 mag
B = 17.93 B−K = 4.91 M_V = −26.16

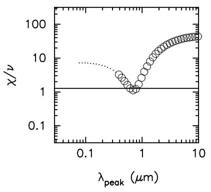

Best model: COMBINED
Best χ^2/ν = 1.114 (ν=4)
Power law index = −1.70
λ_{peak} (synch.) = 0.69 μm
0.5 μm ratio = 3.07
0.5 μm fraction = 75.4%

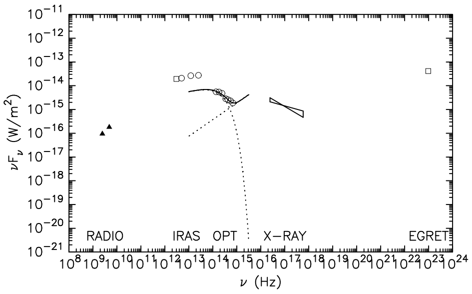

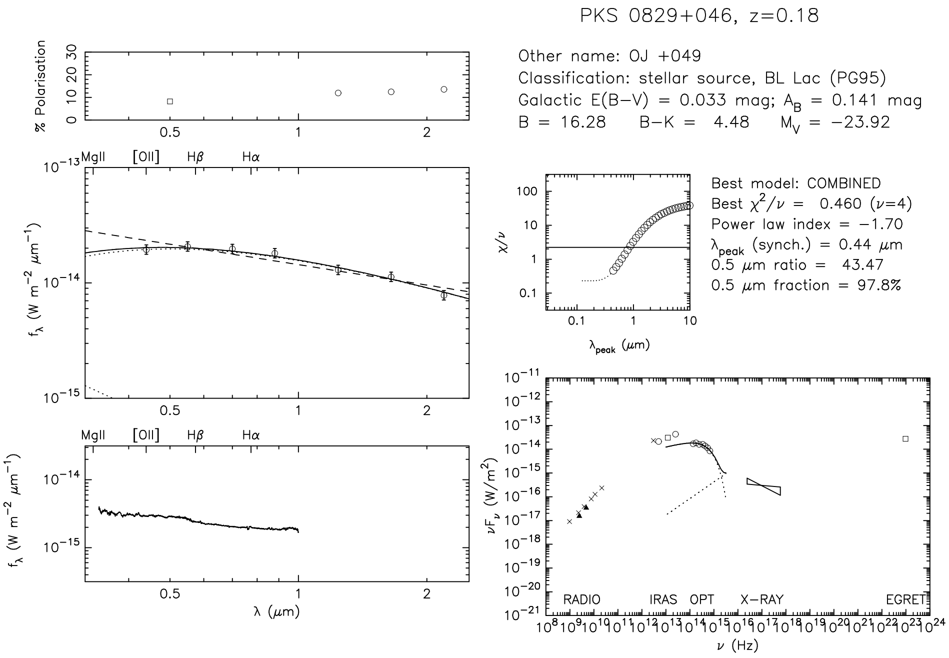
PKS 0829+046, z=0.18
Other name: OJ +049
Classification: stellar source, BL Lac (PG95)
Galactic E(B−V) = 0.033 mag; A_B = 0.141 mag
B = 16.28 B−K = 4.48 M_V = −23.92
Best model: COMBINED
Best χ²/ν = 0.460 (ν=4)
Power law index = −1.70
λ_peak (synch.) = 0.44 μm
0.5 μm ratio = 43.47
0.5 μm fraction = 97.8%
% Polarisation
MgII [OII] Hβ Hα
f_λ (W m⁻² μm⁻¹)
λ (μm)
χ/ν
λ_peak (μm)
νF_ν (W/m²)
RADIO IRAS OPT X-RAY EGRET
ν (Hz)

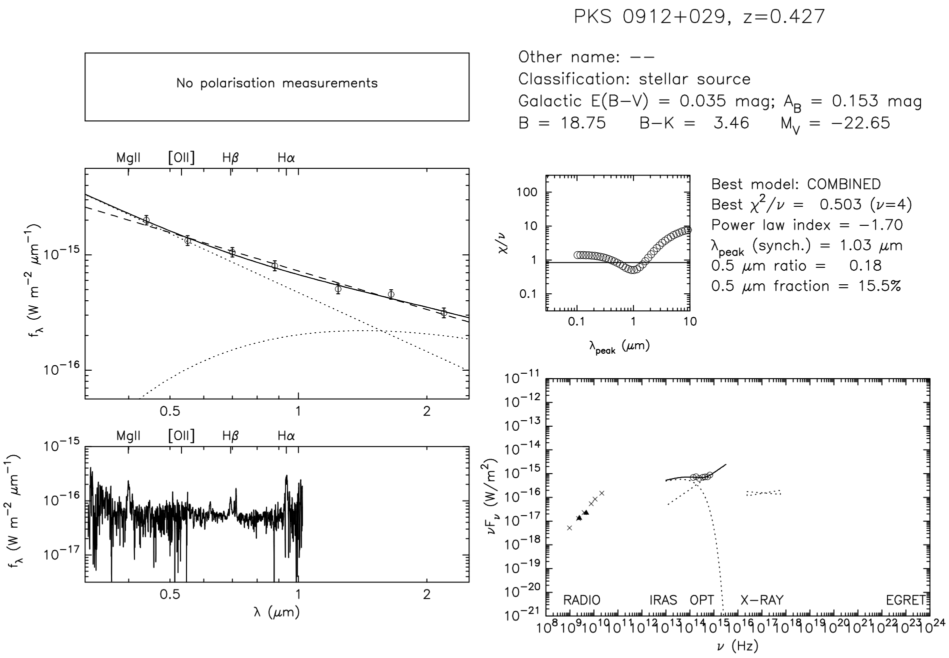
PKS 0912+029, z=0.427
Other name: --
Classification: stellar source
Galactic E(B−V) = 0.035 mag; A_B = 0.153 mag
B = 18.75 B−K = 3.46 M_V = −22.65
No polarisation measurements
Best model: COMBINED
Best χ²/ν = 0.503 (ν=4)
Power law index = −1.70
λ_peak (synch.) = 1.03 μm
0.5 μm ratio = 0.18
0.5 μm fraction = 15.5%
MgII [OII] Hβ Hα
f_λ (W m⁻² μm⁻¹)
λ (μm)
χ/ν
λ_peak (μm)
νF_ν (W/m²)
RADIO IRAS OPT X-RAY EGRET
ν (Hz)

PKS 1016−311, z=0.794

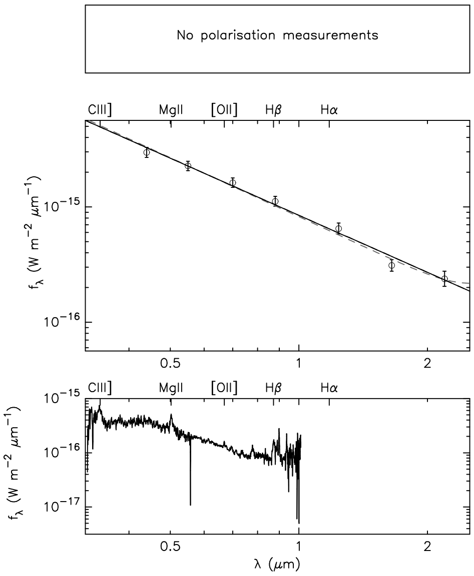

Other name: −−
Classification: stellar source
Galactic E(B−V) = 0.056 mag; A_B = 0.241 mag
B = 18.32 B−K = 2.73 M_V = −24.53

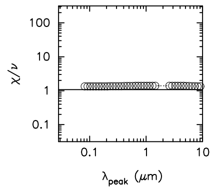

Best model: POWER LAW
Best χ^2/ν = 1.080 (ν=5)
Power law index = −1.65
No synchrotron component

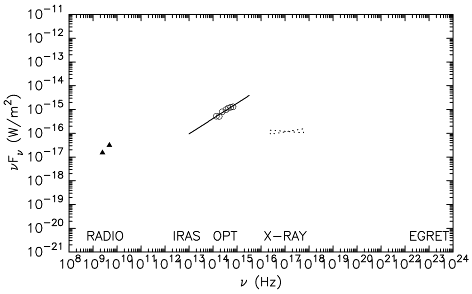

PKS 1020−103, z=0.1966

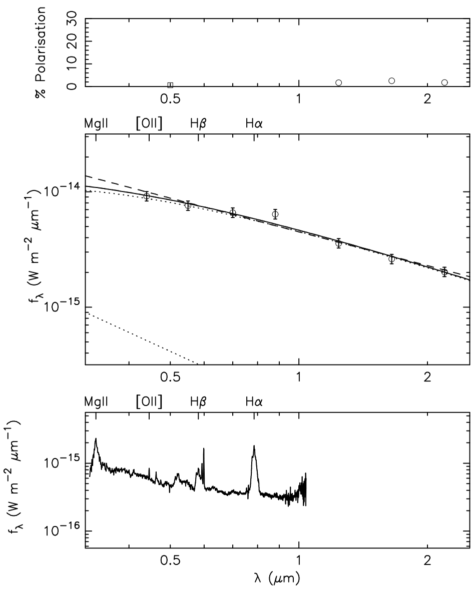

Other name: OL −133
Classification: stellar source
Galactic E(B−V) = 0.046 mag; A_B = 0.200 mag
B = 17.10 B−K = 3.83 M_V = −22.96

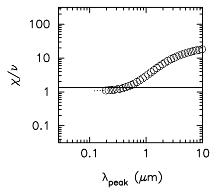

Best model: COMBINED
Best χ^2/ν = 1.102 (ν=4)
Power law index = −1.70
λ_{peak} (synch.) = 0.19 μm
0.5 μm ratio = 23.22
0.5 μm fraction = 95.9%

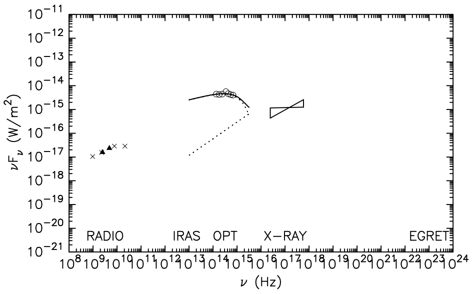

PKS 1032−199, z=2.198

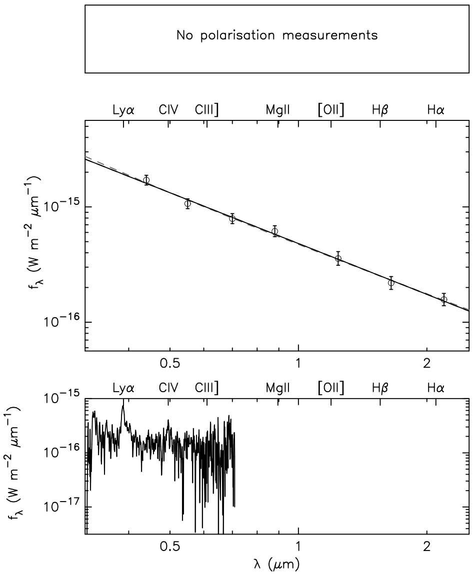

Other name: --
Classification: stellar source
Galactic E(B−V) = 0.044 mag; A_B = 0.192 mag
B = 18.92 B−K = 2.88 M_V = −25.85

Best model: POWER LAW
Best χ^2/ν = 0.343 (ν=5)
Power law index = −1.46
No synchrotron component

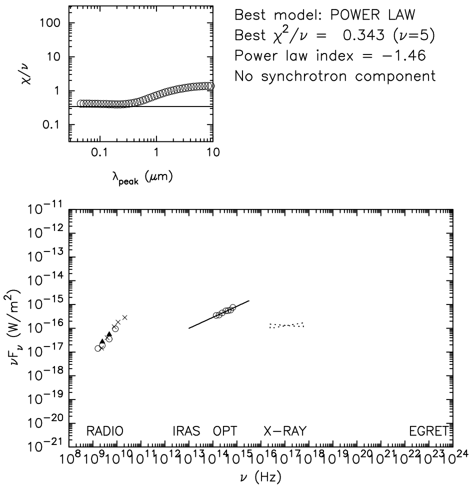

PKS 1034−293, z=0.312

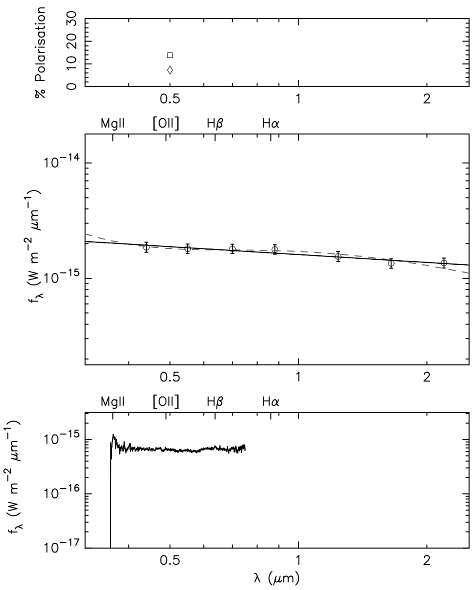

Other name: OL −259
Classification: stellar source
Galactic E(B−V) = 0.051 mag; A_B = 0.222 mag
B = 18.83 B−K = 5.13 M_V = −22.64

Best model: POWER LAW
Best χ^2/ν = 0.274 (ν=5)
Power law index = −0.23
No synchrotron component

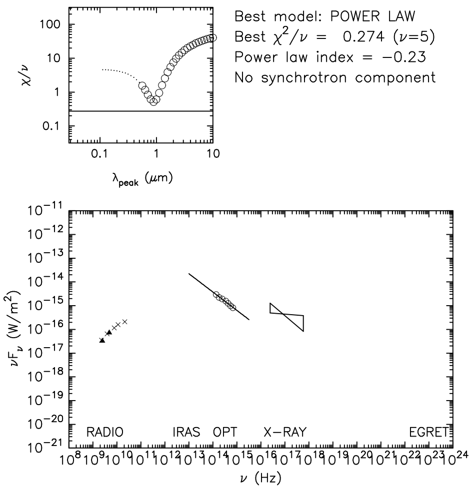

PKS 1036−154, z=0.525

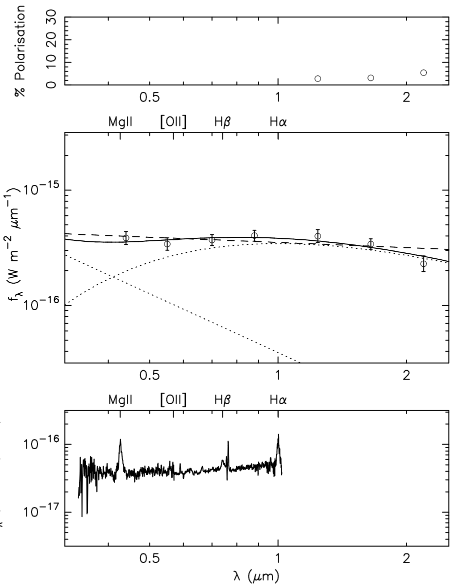

Other name: OL −161
Classification: stellar source
Galactic E(B−V) = 0.065 mag; A_B = 0.283 mag
B = 20.54 B−K = 4.91 M_V = −22.27

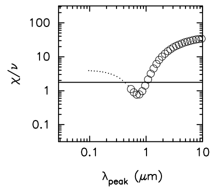

Best model: COMBINED
Best χ^2/ν = 0.767 (ν=4)
Power law index = −1.70
λ_{peak} (synch.) = 0.68 μm
0.5 μm ratio = 5.30
0.5 μm fraction = 84.1%

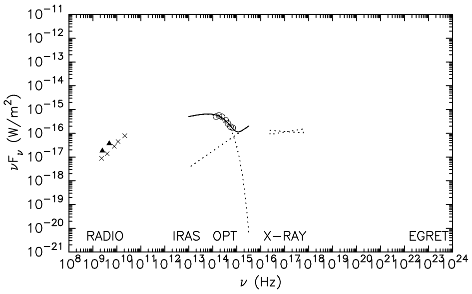

PKS 1045−188, z=0.595

No polarisation measurements

Other name: OL −176
Classification: stellar source
Galactic E(B−V) = 0.038 mag; A_B = 0.165 mag
B = 18.55 B−K = 3.96 M_V = −24.12

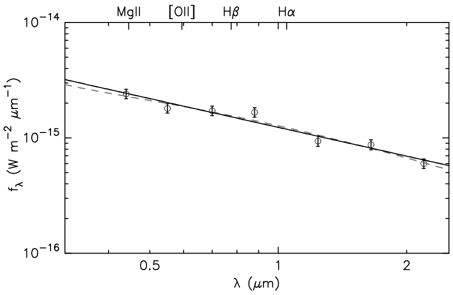

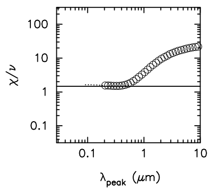

Best model: POWER LAW
Best χ^2/ν = 1.477 (ν=5)
Power law index = −0.83
No synchrotron component

No spectrum

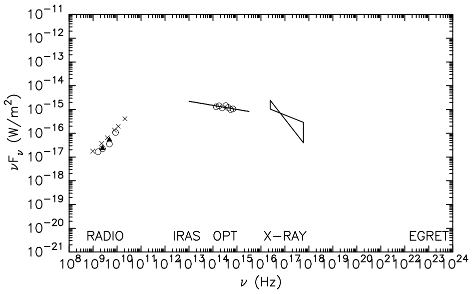

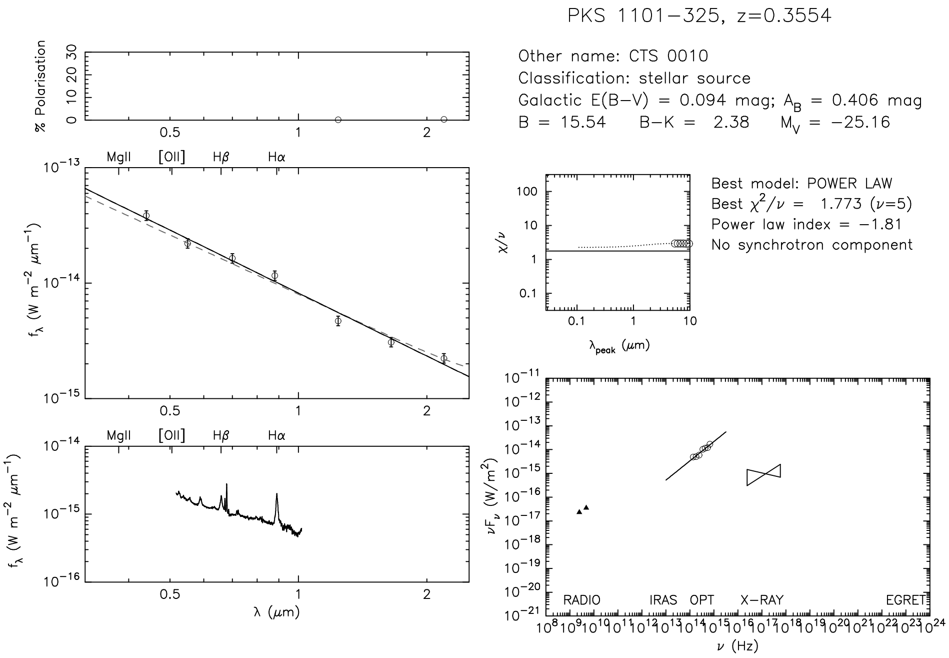
PKS 1101−325, z=0.3554
Other name: CTS 0010
Classification: stellar source
Galactic E(B−V) = 0.094 mag; A_B = 0.406 mag
B = 15.54 B−K = 2.38 M_V = −25.16
Best model: POWER LAW
Best χ^2/ν = 1.773 (ν=5)
Power law index = −1.81
No synchrotron component
% Polarisation
MgII [OII] Hβ Hα
f_λ (W m^{-2} μm^{-1})
λ (μm)
χ/ν
λ_{peak} (μm)
νF_ν (W/m^2)
ν (Hz)
RADIO IRAS OPT X-RAY EGRET

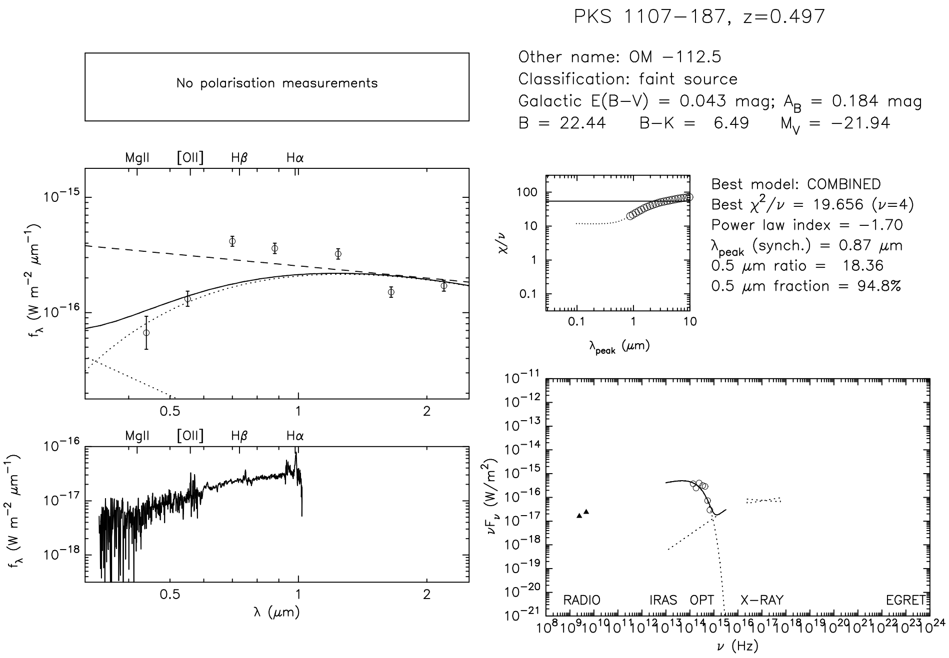
PKS 1107−187, z=0.497
Other name: OM −112.5
Classification: faint source
Galactic E(B−V) = 0.043 mag; A_B = 0.184 mag
B = 22.44 B−K = 6.49 M_V = −21.94
No polarisation measurements
Best model: COMBINED
Best χ^2/ν = 19.656 (ν=4)
Power law index = −1.70
λ_{peak} (synch.) = 0.87 μm
0.5 μm ratio = 18.36
0.5 μm fraction = 94.8%
MgII [OII] Hβ Hα
f_λ (W m^{-2} μm^{-1})
λ (μm)
χ/ν
λ_{peak} (μm)
νF_ν (W/m^2)
ν (Hz)
RADIO IRAS OPT X-RAY EGRET

PKS 1133−172, z=1.024

No polarisation measurements

Other name: OM −156
Classification: faint source
Galactic E(B−V) = 0.033 mag; A_B = 0.143 mag
B = 22.32 B−K = 5.69 M_V = −23.82

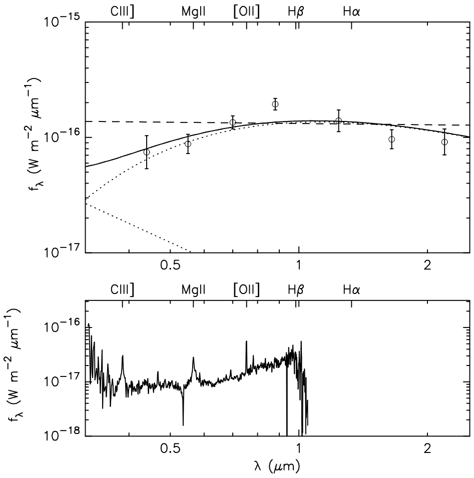

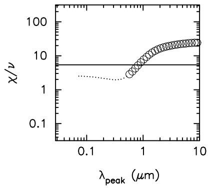

Best model: COMBINED
Best χ^2/ν = 2.865 (ν=4)
Power law index = −1.70
λ_{peak} (synch.) = 0.58 μm
0.5 μm ratio = 36.42
0.5 μm fraction = 97.3%

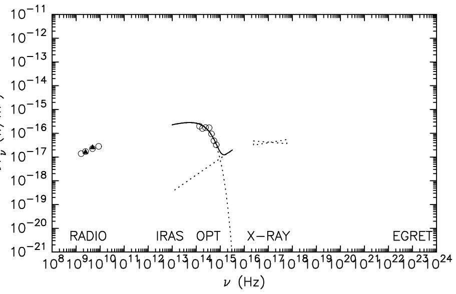

PKS 1136−135, z=0.5566

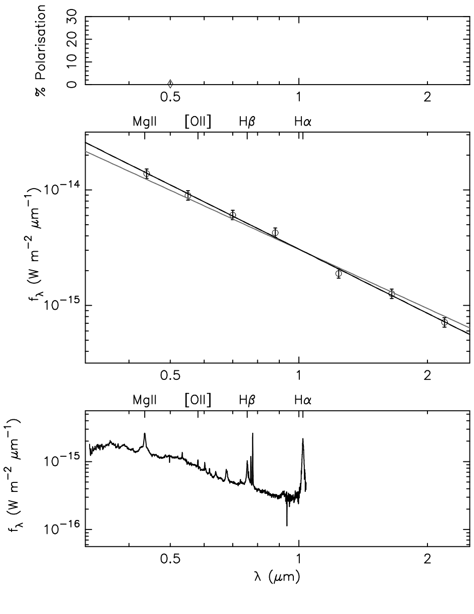

Other name: CTS 0667
Classification: stellar source
Galactic E(B−V) = 0.039 mag; A_B = 0.170 mag
B = 16.65 B−K = 2.25 M_V = −25.11

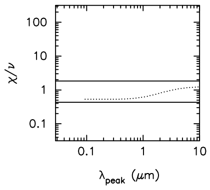

Best model: POWER LAW
Best χ^2/ν = 0.431 (ν=5)
Power law index = −1.85
No synchrotron component

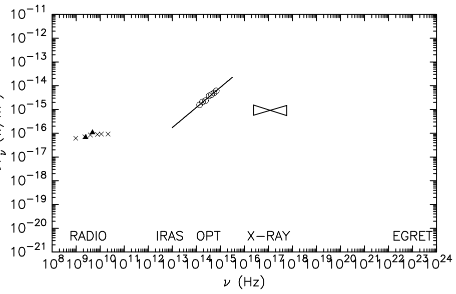

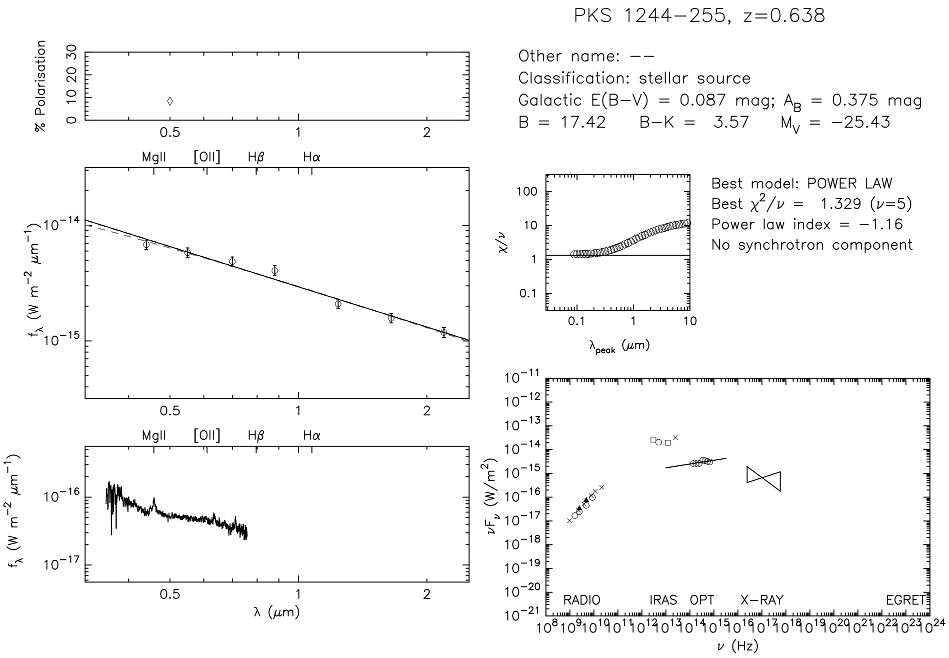

PKS 1244−255, z=0.638
Other name: −−
Classification: stellar source
Galactic E(B−V) = 0.087 mag; A_B = 0.375 mag
B = 17.42 B−K = 3.57 M_V = −25.43
Best model: POWER LAW
Best χ²/ν = 1.329 (ν=5)
Power law index = −1.16
No synchrotron component
% Polarisation
MgII [OII] Hβ Hα
f_λ (W m⁻² μm⁻¹)
λ (μm)
χ/ν
λ_peak (μm)
νF_ν (W/m²)
RADIO IRAS OPT X−RAY EGRET
ν (Hz)

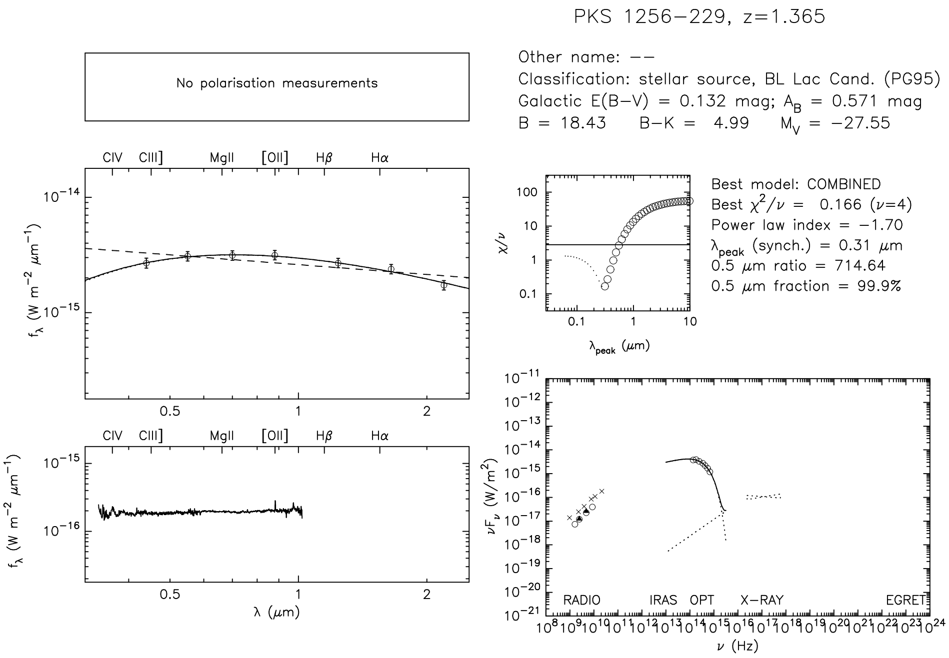

PKS 1256−229, z=1.365
No polarisation measurements
Other name: −−
Classification: stellar source, BL Lac Cand. (PG95)
Galactic E(B−V) = 0.132 mag; A_B = 0.571 mag
B = 18.43 B−K = 4.99 M_V = −27.55
Best model: COMBINED
Best χ²/ν = 0.166 (ν=4)
Power law index = −1.70
λ_peak (synch.) = 0.31 μm
0.5 μm ratio = 714.64
0.5 μm fraction = 99.9%
CIV CIII] MgII [OII] Hβ Hα
f_λ (W m⁻² μm⁻¹)
λ (μm)
χ/ν
λ_peak (μm)
νF_ν (W/m²)
RADIO IRAS OPT X−RAY EGRET
ν (Hz)

PKS 1313−333, z=1.21

Other name: OP −322
Classification: stellar source
Galactic E(B−V) = 0.062 mag; A_B = 0.266 mag
B = 18.17 B−K = 4.48 M_V = −26.81

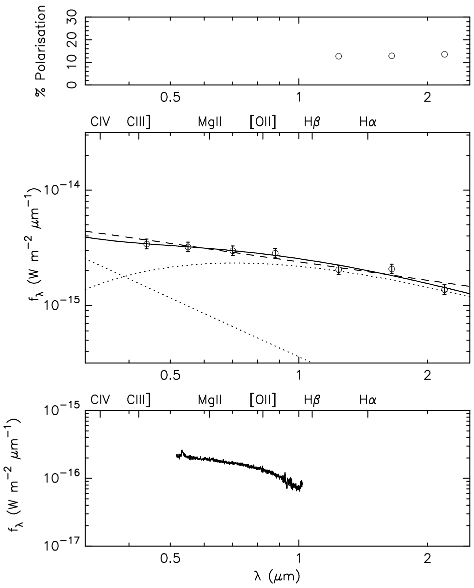

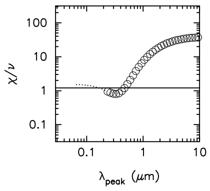

Best model: COMBINED
Best χ^2/ν = 0.801 (ν=4)
Power law index = −1.70
λ_{peak} (synch.) = 0.33 μm
0.5 μm ratio = 6.94
0.5 μm fraction = 87.4%

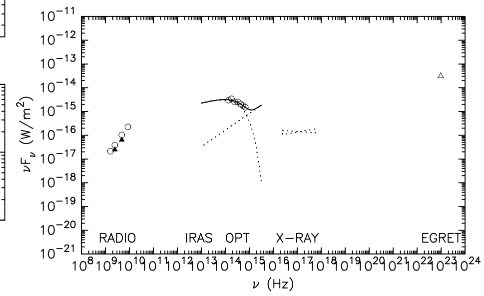

PKS 1404−342, z=1.122

Other name: −−
Classification: stellar source
Galactic E(B−V) = 0.066 mag; A_B = 0.287 mag
B = 17.37 B−K = 2.80 M_V = −26.73

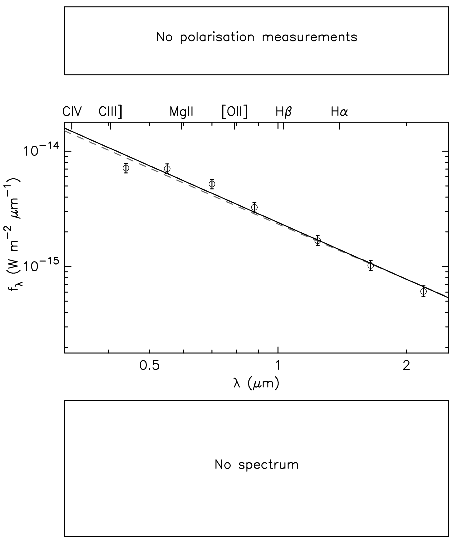

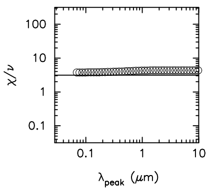

Best model: POWER LAW
Best χ^2/ν = 3.132 (ν=5)
Power law index = −1.63
No synchrotron component

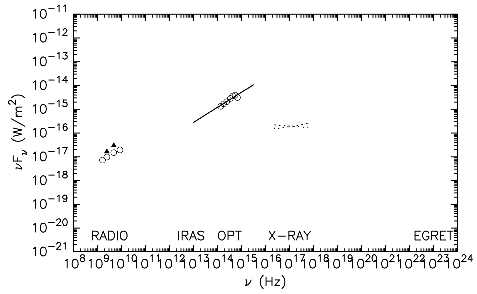

PKS 1430−155, z=1.573

No polarisation measurements

Other name: OQ −150.2
Classification: faint source
Galactic E(B−V) = 0.142 mag; A_B = 0.616 mag
B > 22.70 B−K > 5.20 M_V = −25.30

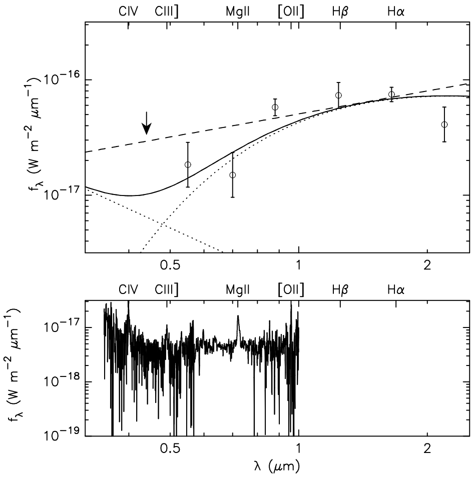

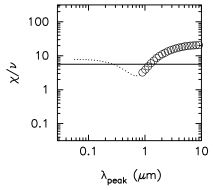

Best model: COMBINED
Best χ^2/ν = 3.220 (ν=4)
Power law index = −1.70
λ_{peak} (synch.) = 0.90 μm
0.5 μm ratio = 55.11
0.5 μm fraction = 98.2%

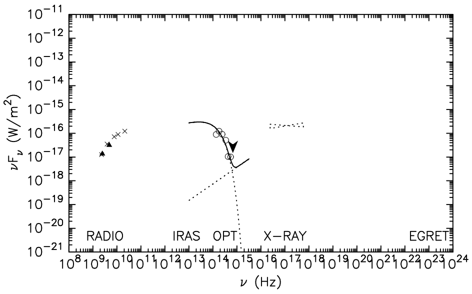

PKS 1430−178, z=2.326

No polarisation measurements

Other name: OQ −151
Classification: stellar source
Galactic E(B−V) = 0.075 mag; A_B = 0.324 mag
B = 19.14 B−K = 3.45 M_V = −26.35

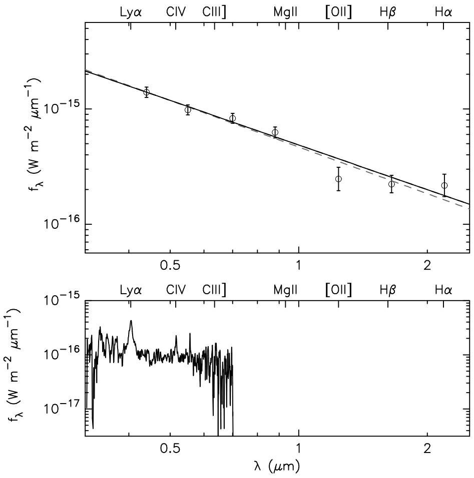

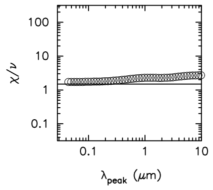

Best model: POWER LAW
Best χ^2/ν = 1.482 (ν=5)
Power law index = −1.29
No synchrotron component

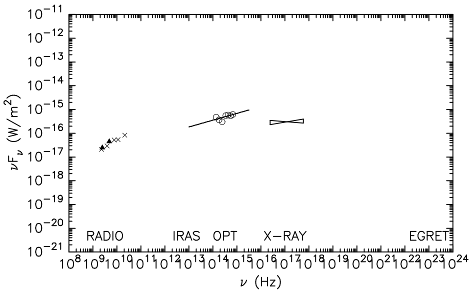

PKS 1435−218, z=1.187

No polarisation measurements

Other name: OQ −259
Classification: stellar source
Galactic E(B−V) = 0.085 mag; A_B = 0.366 mag
B = 19.20 B−K = 2.43 M_V = −25.63

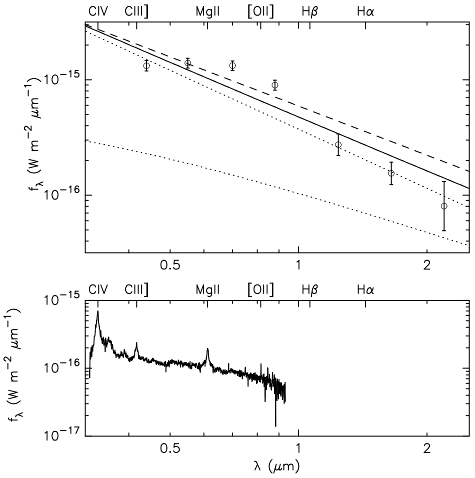

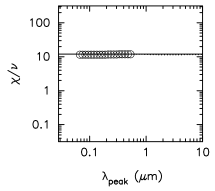

Best model: COMBINED
Best χ^2/ν = 11.467 (ν=4)
Power law index = −1.70
λ_{peak} (synch.) = 0.07 μm
0.5 μm ratio = 0.29
0.5 μm fraction = 22.7%

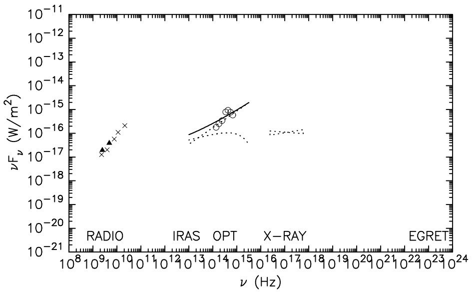

PKS 1437−153, z=0.254

No polarisation measurements

Other name: OQ −162
Classification: stellar source, BL Lac (VV97)
Galactic E(B−V) = 0.127 mag; A_B = 0.550 mag
B = 19.94 B−K = 5.70 M_V = −21.49

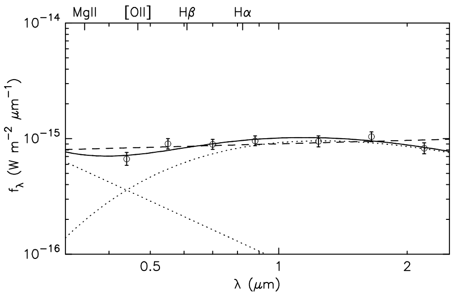

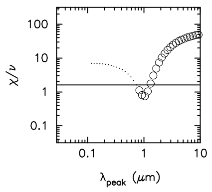

Best model: COMBINED
Best χ^2/ν = 0.747 (ν=4)
Power law index = −1.70
λ_{peak} (synch.) = 1.04 μm
0.5 μm ratio = 3.34
0.5 μm fraction = 77.0%

No spectrum

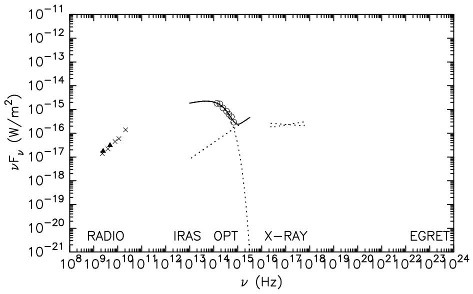

PKS 1438−347, z=1.159

No polarisation measurements

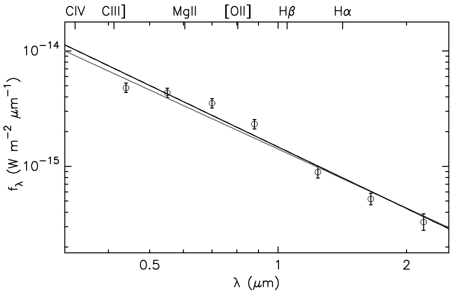

No spectrum

Other name: −−
Classification: stellar source
Galactic E(B−V) = 0.097 mag; A_B = 0.419 mag
B = 17.80 B−K = 2.56 M_V = −26.37

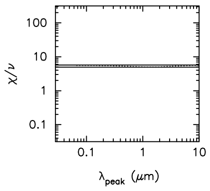

Best model: POWER LAW
Best χ^2/ν = 4.946 (ν=5)
Power law index = −1.77
No synchrotron component

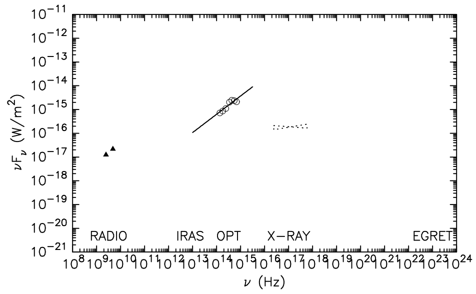

PKS 1450−338, z=0.368

No polarisation measurements

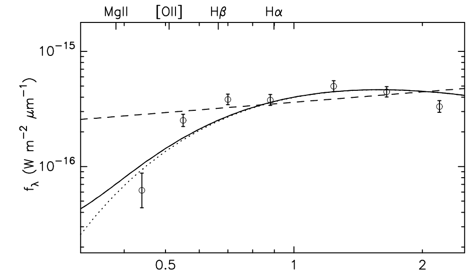

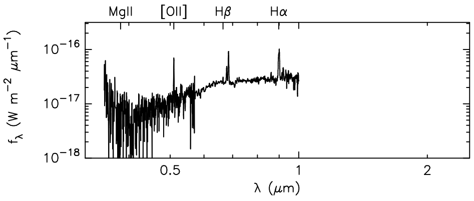

Other name: −−
Classification: faint source
Galactic E(B−V) = 0.095 mag; A_B = 0.412 mag
B = 22.52 B−K = 7.29 M_V = −21.39

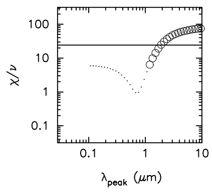

Best model: COMBINED
Best χ^2/ν = 6.441 (ν=4)
Power law index = −1.70
λ_{peak} (synch.) = 1.20 μm
0.5 μm ratio = 55.57
0.5 μm fraction = 98.2%

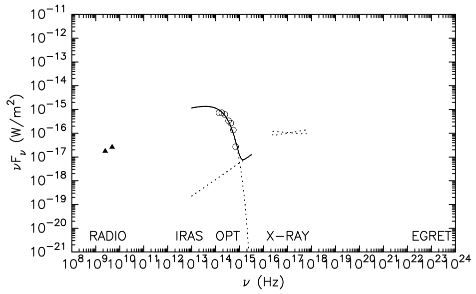

PKS 1454−060, z=1.249

No polarisation measurements

Other name: 4C −05.62
Classification: stellar source
Galactic E(B−V) = 0.080 mag; A_B = 0.345 mag
B = 18.36   B−K = 3.20 M_V = −26.25

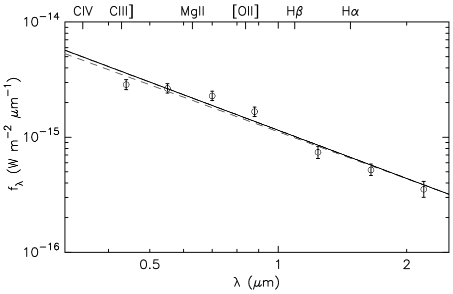

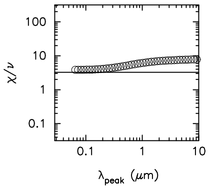

Best model: POWER LAW
Best χ^2/ν = 3.260 (ν=5)
Power law index = −1.39
No synchrotron component

No spectrum

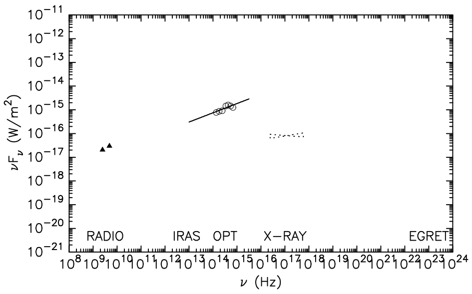

PKS 1504−166, z=0.876

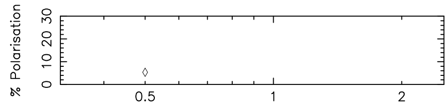

Other name: OR −102/−107
Classification: merger
Galactic E(B−V) = 0.095 mag; A_B = 0.411 mag
B = 20.28   B−K = 6.27 M_V = −23.89

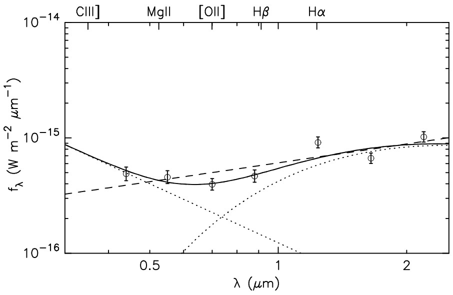

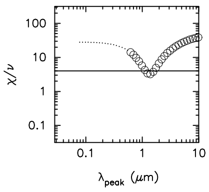

Best model: COMBINED
Best χ^2/ν = 3.219 (ν=4)
Power law index = −1.70
λ_{peak} (synch.) = 1.39 μm
0.5 μm ratio = 2.71
0.5 μm fraction = 73.1%

No spectrum

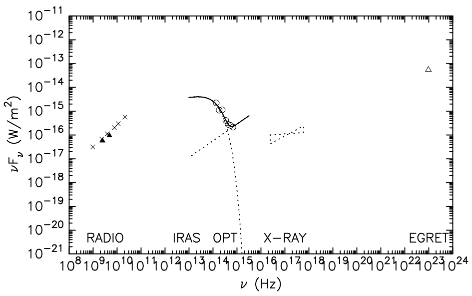

PKS 1508−055, z=1.185

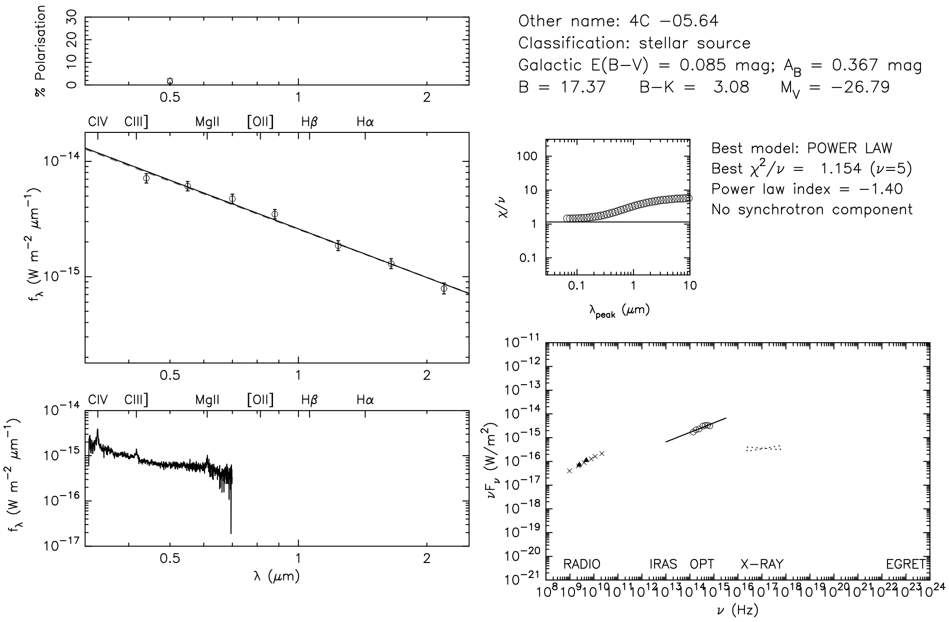

PKS 1510−089, z=0.362

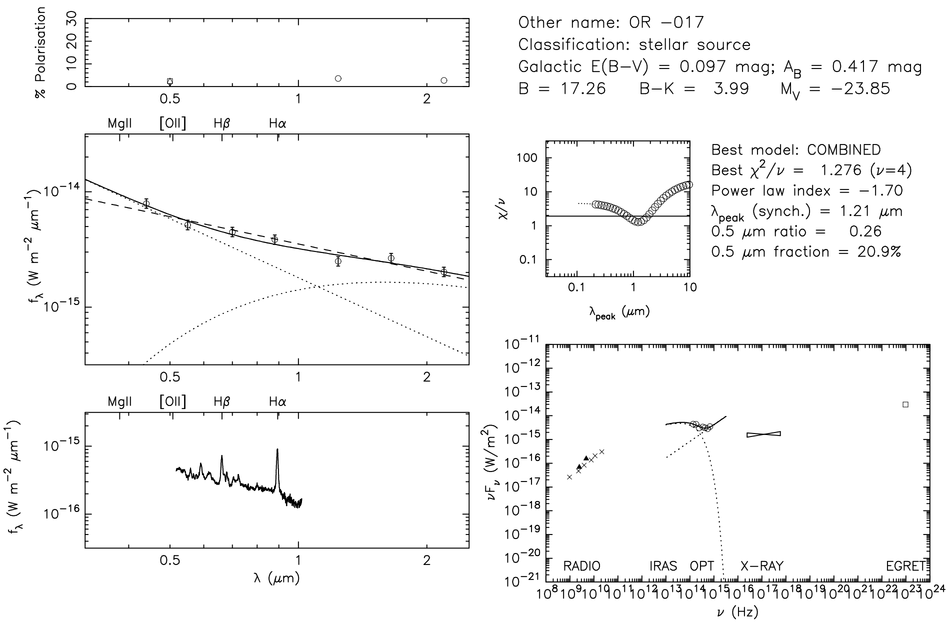

PKS 1511−100, z=1.513

No polarisation measurements

Other name: OR −118
Classification: stellar source
Galactic E(B−V) = 0.106 mag; A_B = 0.457 mag
B = 18.18 B−K = 3.48 M_V = −26.43

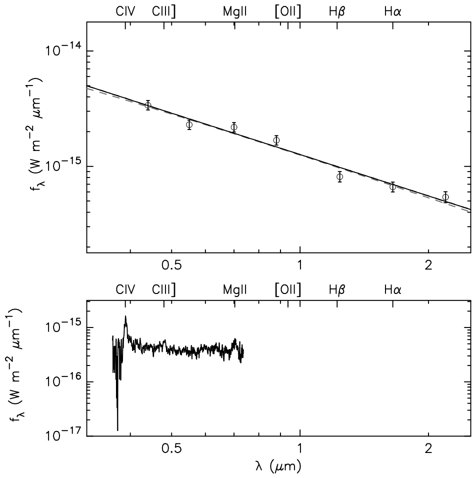

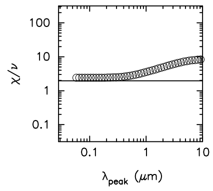

Best model: POWER LAW
Best χ^2/ν = 1.957 (ν=5)
Power law index = −1.19
No synchrotron component

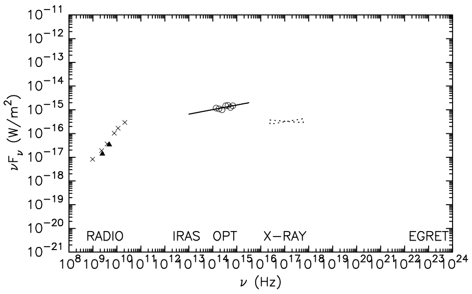

PKS 1511−210, z=1.179

No polarisation measurements

Other name: OR −218
Classification: stellar source
Galactic E(B−V) = 0.159 mag; A_B = 0.686 mag
B = 22.01 B−K = 5.22 M_V = −23.05

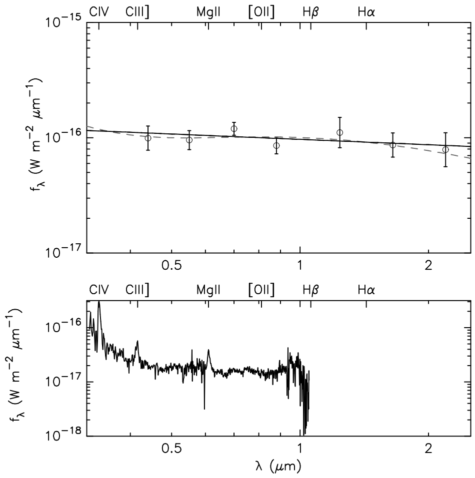

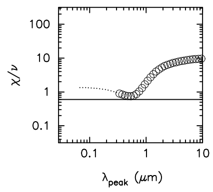

Best model: POWER LAW
Best χ^2/ν = 0.600 (ν=5)
Power law index = −0.15
No synchrotron component

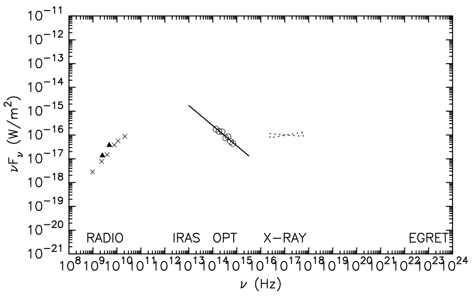

PKS 1514−241, z=0.0486

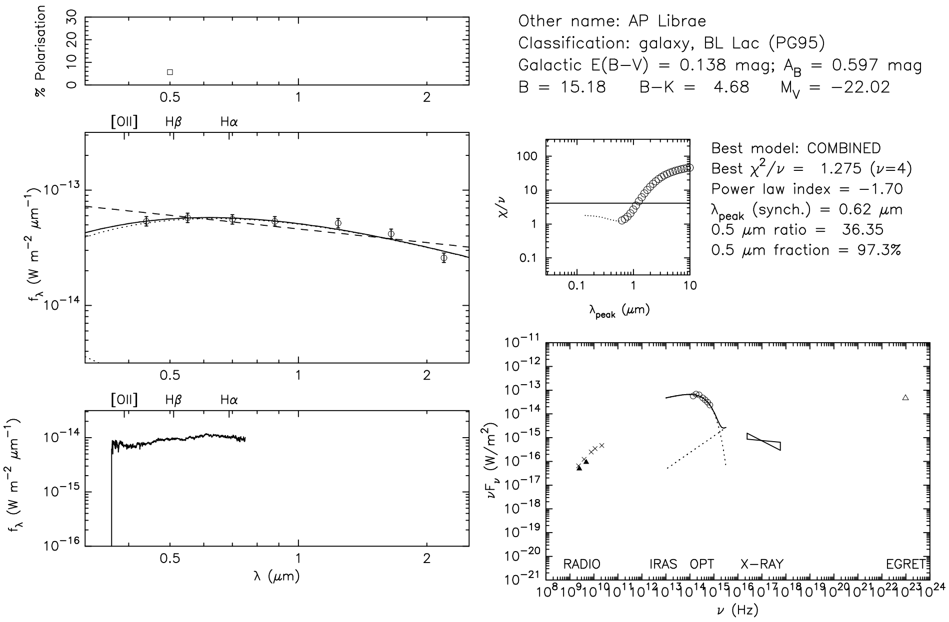

PKS 1519−273, z=0.51

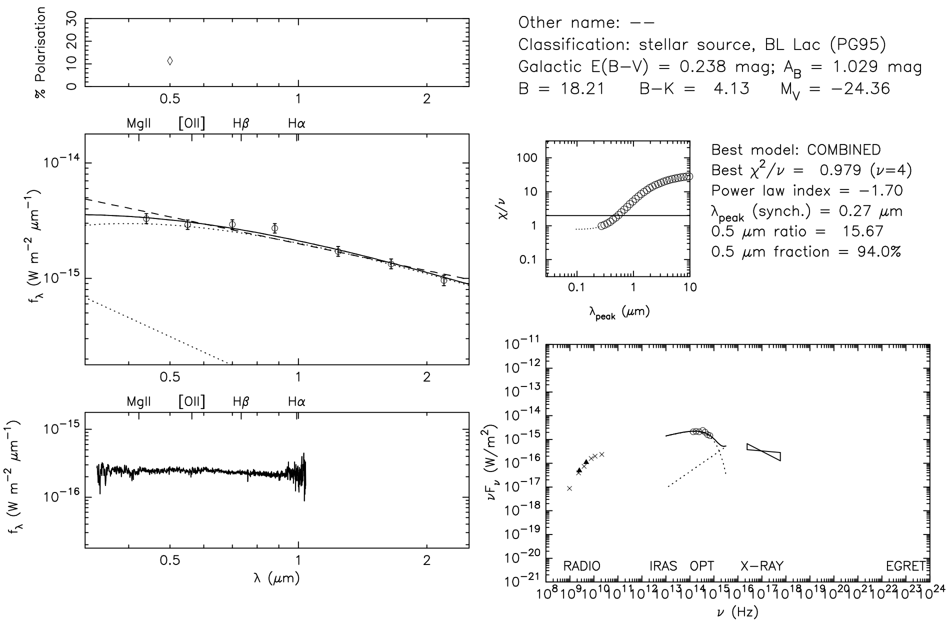

PKS 1532+016, z=1.435

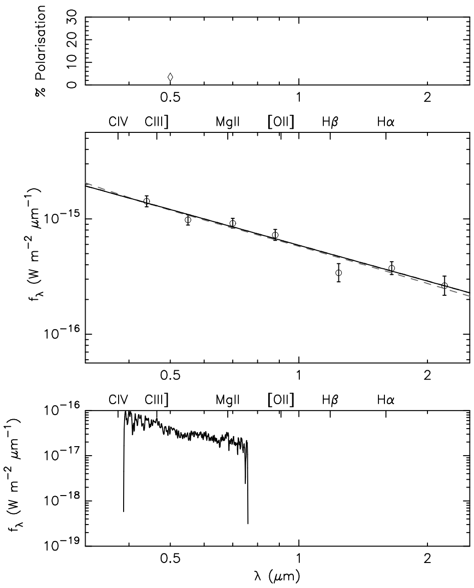

Other name: --
Classification: stellar source
Galactic E(B−V) = 0.051 mag; A_B = 0.219 mag
B = 19.12 B−K = 3.64 M_V = −25.41

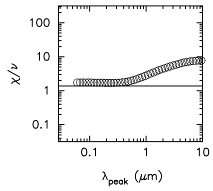

Best model: POWER LAW
Best χ^2/ν = 1.384 (ν=5)
Power law index = −1.03
No synchrotron component

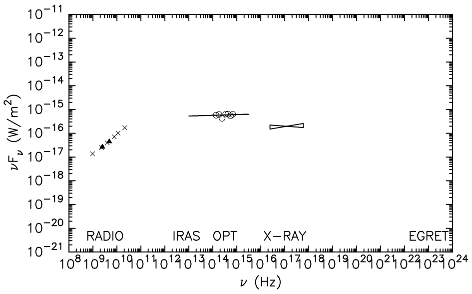

PKS 1542+042, z=2.184

No polarisation measurements

Other name: --
Classification: stellar source
Galactic E(B−V) = 0.084 mag; A_B = 0.362 mag
B = 18.75 B−K = 2.93 M_V = −26.76

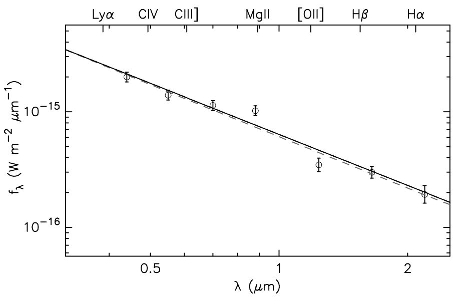

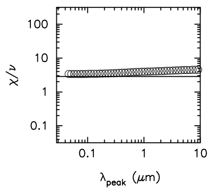

Best model: POWER LAW
Best χ^2/ν = 2.854 (ν=5)
Power law index = −1.47
No synchrotron component

No spectrum

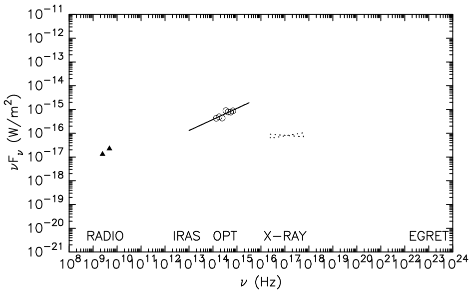

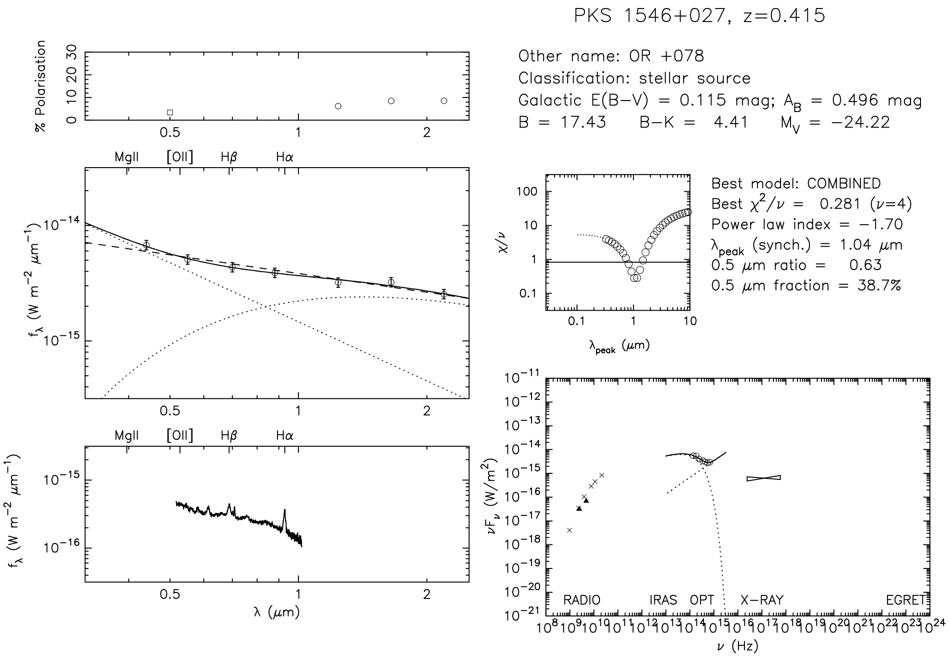
PKS 1546+027, z=0.415
Other name: OR +078
Classification: stellar source
Galactic E(B−V) = 0.115 mag; A_B = 0.496 mag
B = 17.43 B−K = 4.41 M_V = −24.22
Best model: COMBINED
Best χ^2/ν = 0.281 (ν=4)
Power law index = −1.70
λ_{peak} (synch.) = 1.04 μm
0.5 μm ratio = 0.63
0.5 μm fraction = 38.7%
% Polarisation
MgII [OII] Hβ Hα
f_λ (W m^{-2} μm^{-1})
λ (μm)
χ/ν
λ_{peak} (μm)
νF_ν (W/m^2)
RADIO IRAS OPT X-RAY EGRET
ν (Hz)

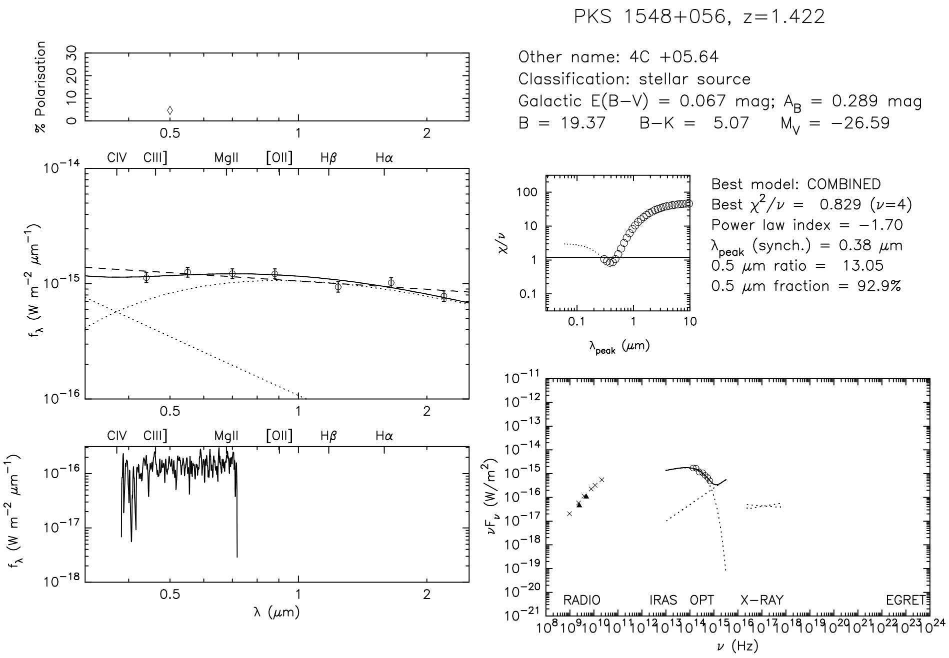
PKS 1548+056, z=1.422
Other name: 4C +05.64
Classification: stellar source
Galactic E(B−V) = 0.067 mag; A_B = 0.289 mag
B = 19.37 B−K = 5.07 M_V = −26.59
Best model: COMBINED
Best χ^2/ν = 0.829 (ν=4)
Power law index = −1.70
λ_{peak} (synch.) = 0.38 μm
0.5 μm ratio = 13.05
0.5 μm fraction = 92.9%
% Polarisation
CIV CIII] MgII [OII] Hβ Hα
f_λ (W m^{-2} μm^{-1})
λ (μm)
χ/ν
λ_{peak} (μm)
νF_ν (W/m^2)
RADIO IRAS OPT X-RAY EGRET
ν (Hz)

PKS 1550−269, z=2.145

No polarisation measurements

Other name: −−
Classification: stellar source
Galactic E(B−V) = 0.155 mag; A_B = 0.669 mag
B = 20.24 B−K = 4.17 M_V = −26.42

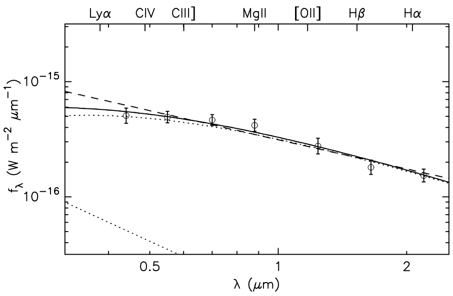

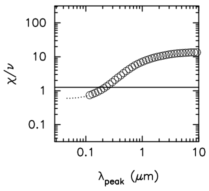

Best model: COMBINED
Best χ^2/ν = 0.739 (ν=4)
Power law index = −1.70
λ_{peak} (synch.) = 0.12 μm
0.5 μm ratio = 36.07
0.5 μm fraction = 97.3%

No spectrum

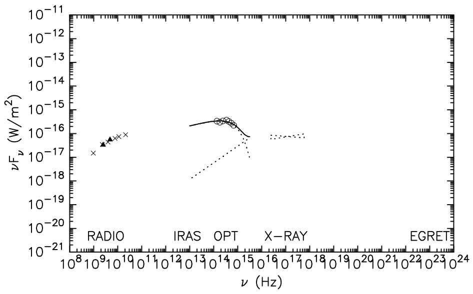

PKS 1555+001, z=1.77

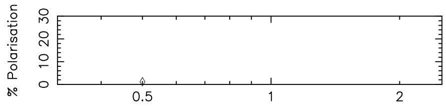

Other name: −−
Classification: faint source
Galactic E(B−V) = 0.139 mag; A_B = 0.603 mag
B = 20.34 B−K = 4.10 M_V = −25.31

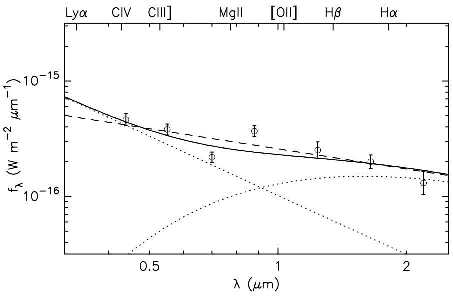

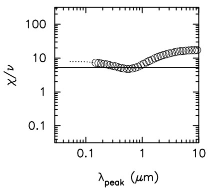

Best model: COMBINED
Best χ^2/ν = 4.818 (ν=4)
Power law index = −1.70
λ_{peak} (synch.) = 0.59 μm
0.5 μm ratio = 2.52
0.5 μm fraction = 71.6%

No spectrum

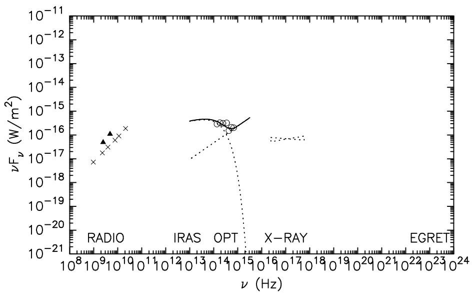

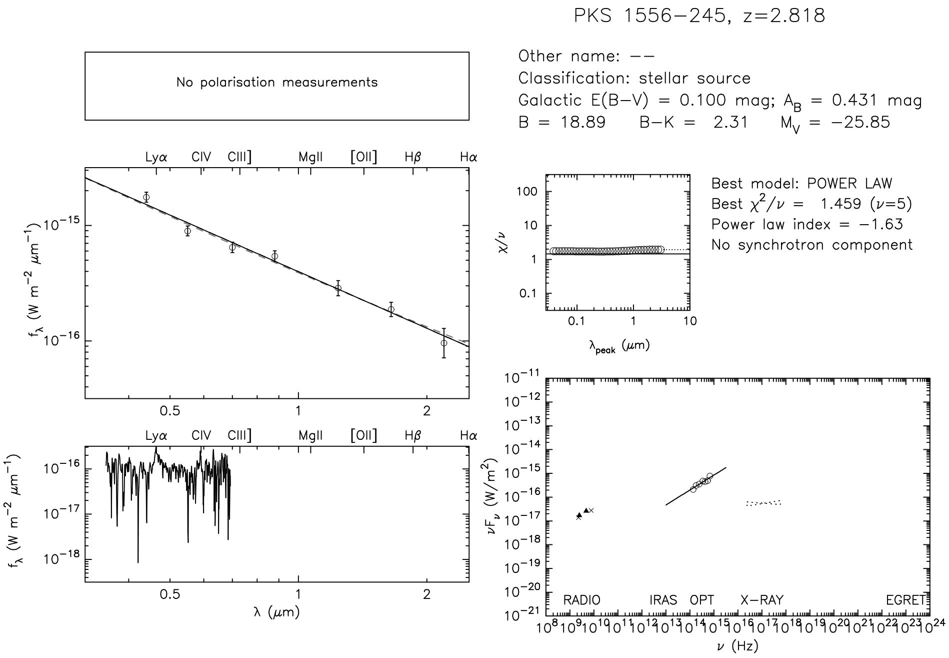
PKS 1556−245, z=2.818
Other name: −−
Classification: stellar source
Galactic E(B−V) = 0.100 mag; A_B = 0.431 mag
B = 18.89 B−K = 2.31 M_V = −25.85
No polarisation measurements
Best model: POWER LAW
Best χ²/ν = 1.459 (ν=5)
Power law index = −1.63
No synchrotron component
Lyα CIV CIII] MgII [OII] Hβ Hα
f_λ (W m^−2 μm^−1)
λ (μm)
χ/ν
λ_peak (μm)
νF_ν (W/m²)
ν (Hz)
RADIO IRAS OPT X−RAY EGRET

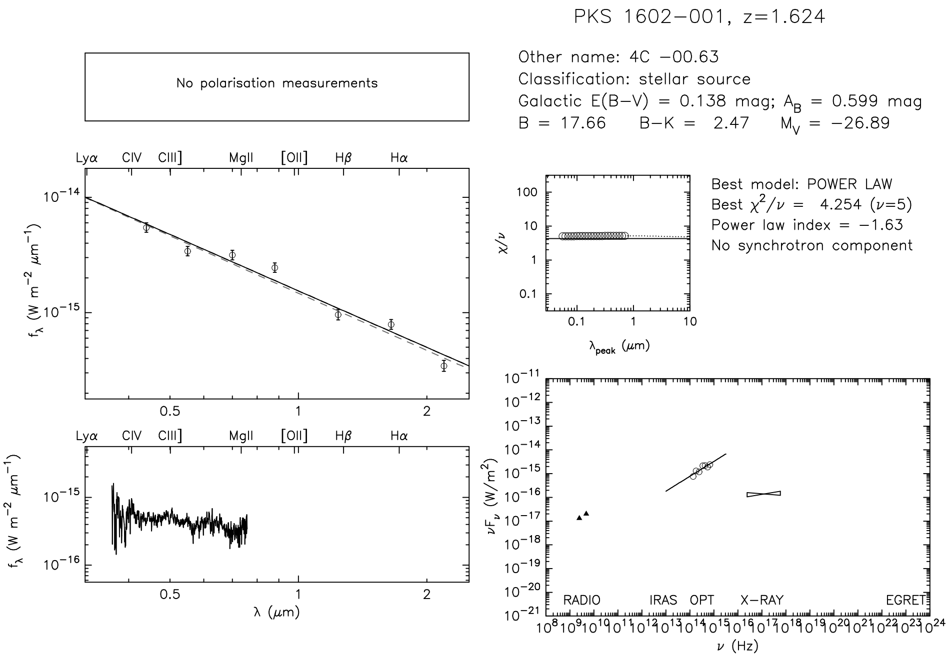
PKS 1602−001, z=1.624
Other name: 4C −00.63
Classification: stellar source
Galactic E(B−V) = 0.138 mag; A_B = 0.599 mag
B = 17.66 B−K = 2.47 M_V = −26.89
No polarisation measurements
Best model: POWER LAW
Best χ²/ν = 4.254 (ν=5)
Power law index = −1.63
No synchrotron component
Lyα CIV CIII] MgII [OII] Hβ Hα
f_λ (W m^−2 μm^−1)
λ (μm)
χ/ν
λ_peak (μm)
νF_ν (W/m²)
ν (Hz)
RADIO IRAS OPT X−RAY EGRET

PKS 1615+029, z=1.341

No polarisation measurements

Other name: OS +028
Classification: stellar source
Galactic E(B−V) = 0.067 mag; A_B = 0.292 mag
B = 18.01   B−K = 2.12 M_V = −26.25

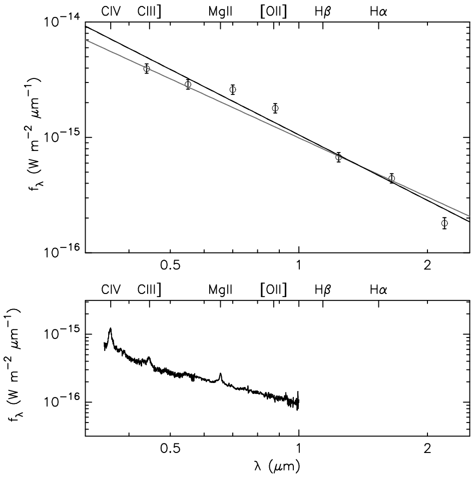

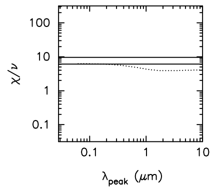

Best model: POWER LAW
Best χ^2/ν = 6.124 (ν=5)
Power law index = −1.89
No synchrotron component

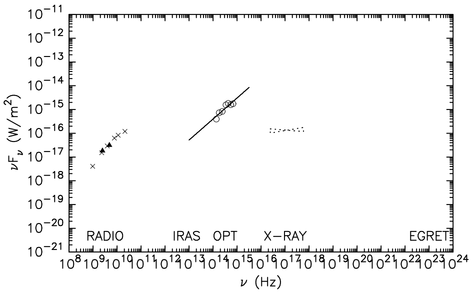

PKS 1616+063, z=2.088

No polarisation measurements

Other name: −−
Classification: stellar source
Galactic E(B−V) = 0.059 mag; A_B = 0.255 mag
B = 19.45   B−K = 2.93 M_V = −26.20

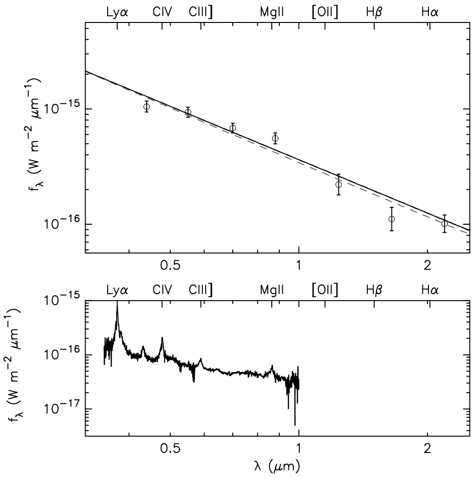

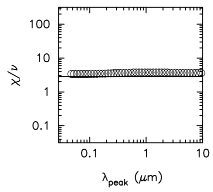

Best model: POWER LAW
Best χ^2/ν = 2.840 (ν=5)
Power law index = −1.54
No synchrotron component

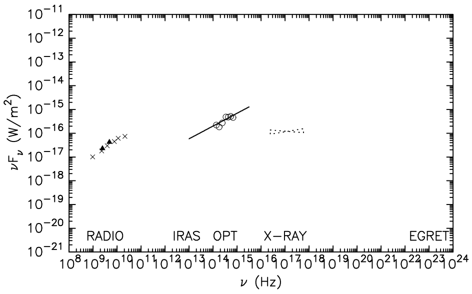

PKS 1635−035, z=2.856

No polarisation measurements

Other name: −−
Classification: stellar source
Galactic E(B−V) = 0.353 mag; A_B = 1.527 mag
B = 21.58 B−K = 4.10 M_V = −24.48

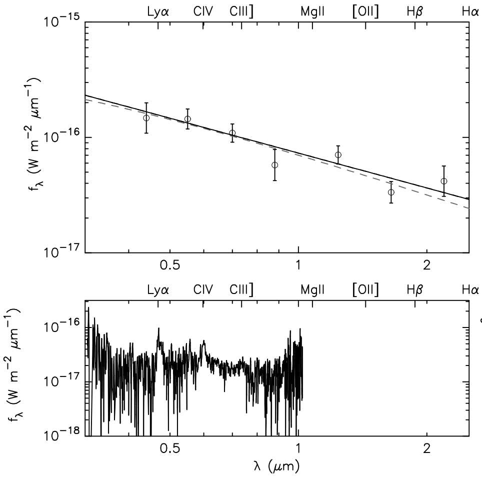

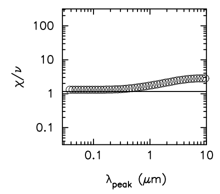

Best model: POWER LAW
Best χ^2/ν = 1.157 (ν=5)
Power law index = −1.00
No synchrotron component

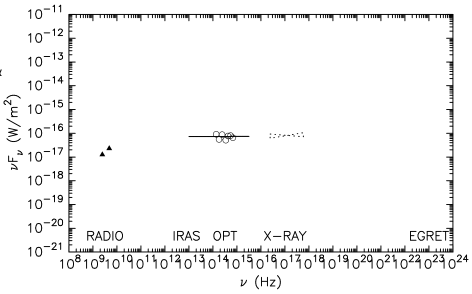

PKS 1654−020, z= 2

No polarisation measurements

Other name: 4C −01.39
Classification: faint source
Galactic E(B−V) = 0.223 mag; A_B = 0.963 mag
B = 23.51 B−K = 5.26 M_V = −20.56

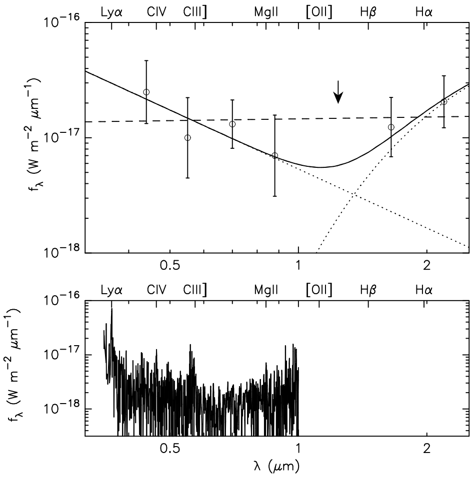

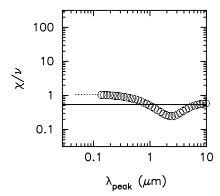

Best model: COMBINED
Best χ^2/ν = 0.244 (ν=4)
Power law index = −1.70
λ_{peak} (synch.) = 2.45 μm
0.5 μm ratio = 1.98
0.5 μm fraction = 66.5%

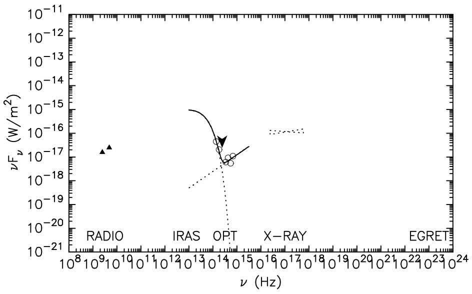

PKS 1655+077, z=0.621

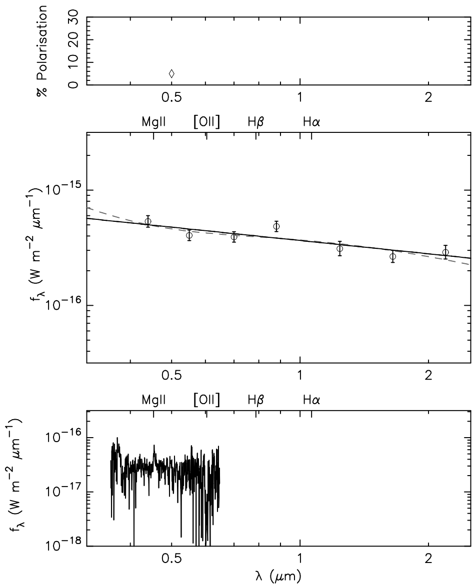

Other name: OS +092
Classification: stellar source
Galactic E(B−V) = 0.153 mag; A_B = 0.662 mag
B = 20.18 B−K = 4.80 M_V = −22.81

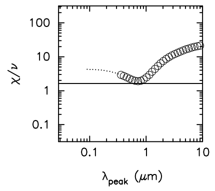

Best model: POWER LAW
Best χ^2/ν = 1.627 (ν=5)
Power law index = −0.38
No synchrotron component

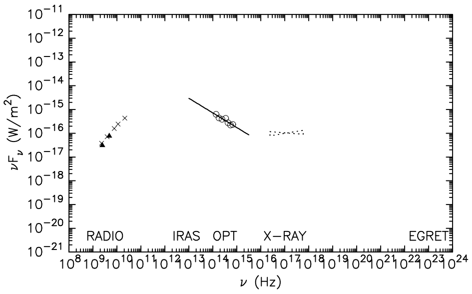

PKS 1656+053, z=0.8873

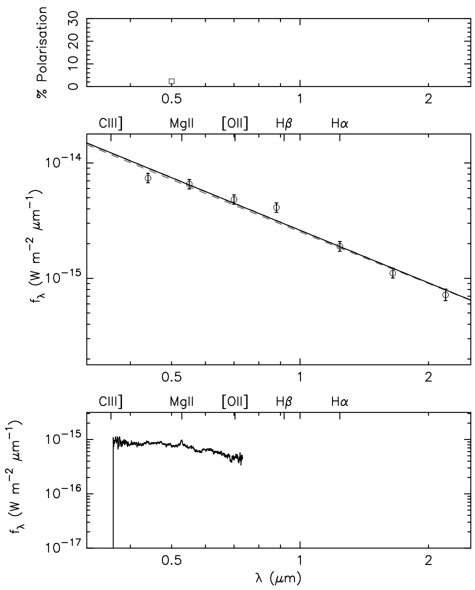

Other name: OS +094
Classification: stellar source
Galactic E(B−V) = 0.159 mag; A_B = 0.686 mag
B = 17.33 B−K = 2.94 M_V = −26.28

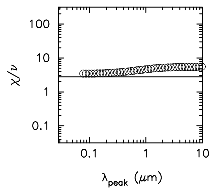

Best model: POWER LAW
Best χ^2/ν = 2.792 (ν=5)
Power law index = −1.51
No synchrotron component

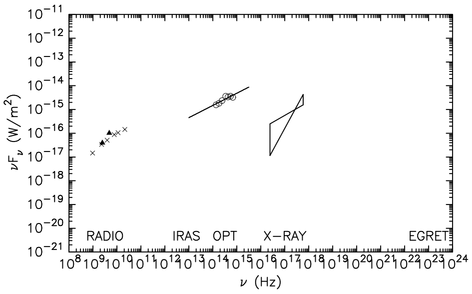

PKS 1705+018, z=2.576

No polarisation measurements

Other name: −−
Classification: stellar source
Galactic E(B−V) = 0.177 mag; A_B = 0.767 mag
B = 19.07 B−K = 3.15 M_V = −27.14

Best model: POWER LAW
Best χ^2/ν = 1.291 (ν=5)
Power law index = −1.32
No synchrotron component

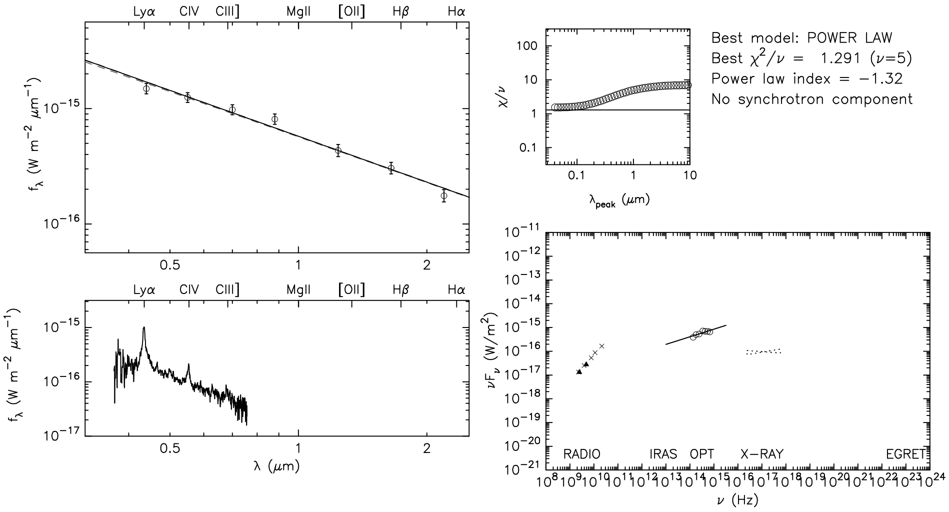

PKS 1706+006, z=0.449

No polarisation measurements

Other name: −−
Classification: faint source
Galactic E(B−V) = 0.229 mag; A_B = 0.990 mag
B = 22.15 B−K = 6.52 M_V = −21.74

Best model: COMBINED
Best χ^2/ν = 1.575 (ν=4)
Power law index = −1.70
λ_{peak} (synch.) = 1.01 μm
0.5 μm ratio = 22.32
0.5 μm fraction = 95.7%

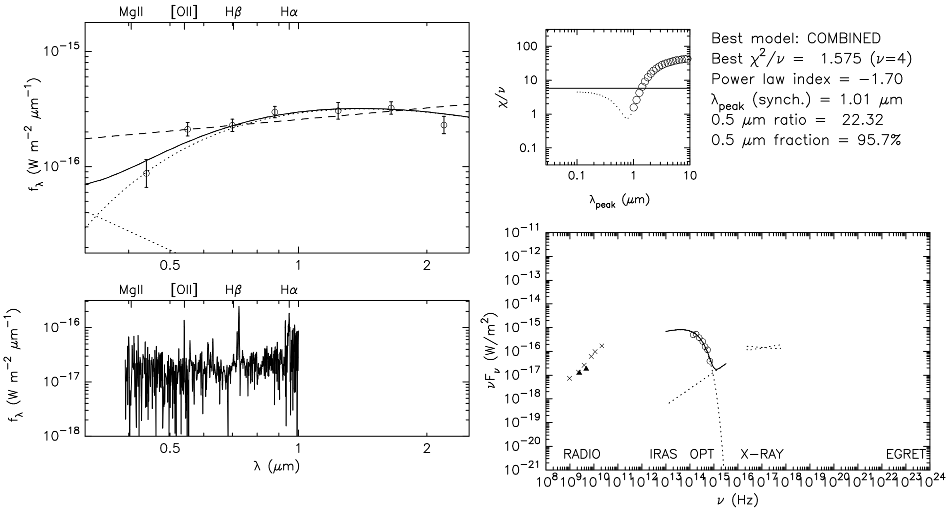

PKS 1725+044, z=0.296

No polarisation measurements

Other name: --
Classification: merger
Galactic E(B−V) = 0.143 mag; A_B = 0.618 mag
B = 17.92 B−K = 3.79 M_V = −23.21

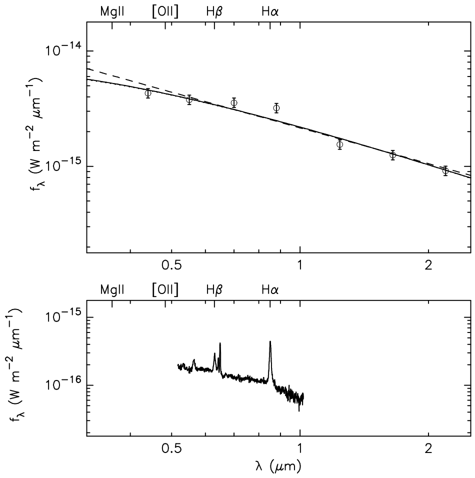

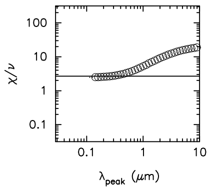

Best model: COMBINED
Best χ^2/ν = 2.494 (ν=4)
Power law index = −1.70
λ_{peak} (synch.) = 0.14 μm
0.5 μm ratio = 194.25
0.5 μm fraction = 99.5%

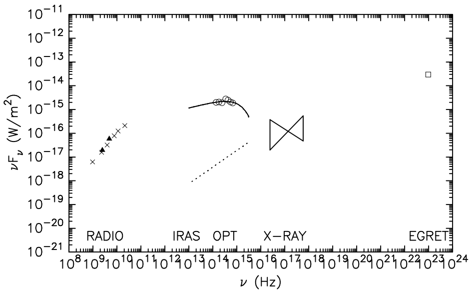

PKS 1933−400, z=0.965

No polarisation measurements

Other name: --
Classification: stellar source
Galactic E(B−V) = 0.148 mag; A_B = 0.641 mag
B = 18.46 B−K = 3.46 M_V = −25.17

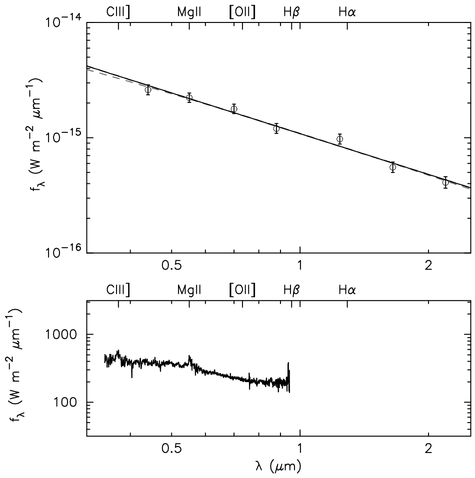

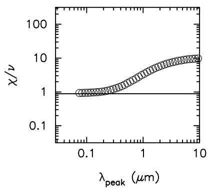

Best model: POWER LAW
Best χ^2/ν = 0.887 (ν=5)
Power law index = −1.17
No synchrotron component

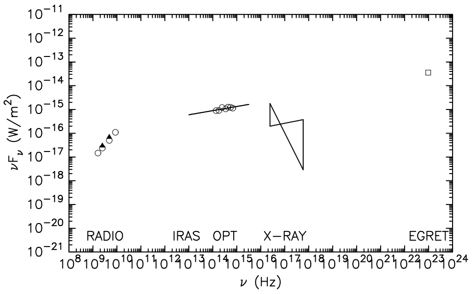

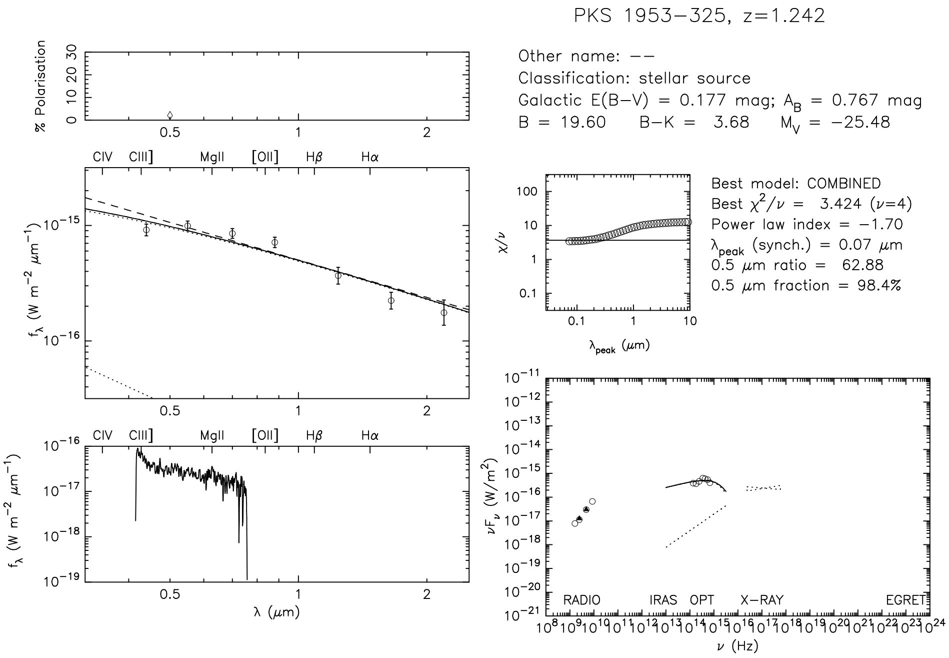
PKS 1953−325, z=1.242
Other name: −−
Classification: stellar source
Galactic E(B−V) = 0.177 mag; A_B = 0.767 mag
B = 19.60   B−K = 3.68 M_V = −25.48
Best model: COMBINED
Best χ^2/ν = 3.424 (ν=4)
Power law index = −1.70
λ_{peak} (synch.) = 0.07 μm
0.5 μm ratio = 62.88
0.5 μm fraction = 98.4%
% Polarisation
CIV CIII] MgII [OII] Hβ Hα
f_λ (W m^{-2} μm^{-1})
λ (μm)
χ/ν
λ_{peak} (μm)
νF_ν (W/m^2)
RADIO IRAS OPT X-RAY EGRET
ν (Hz)

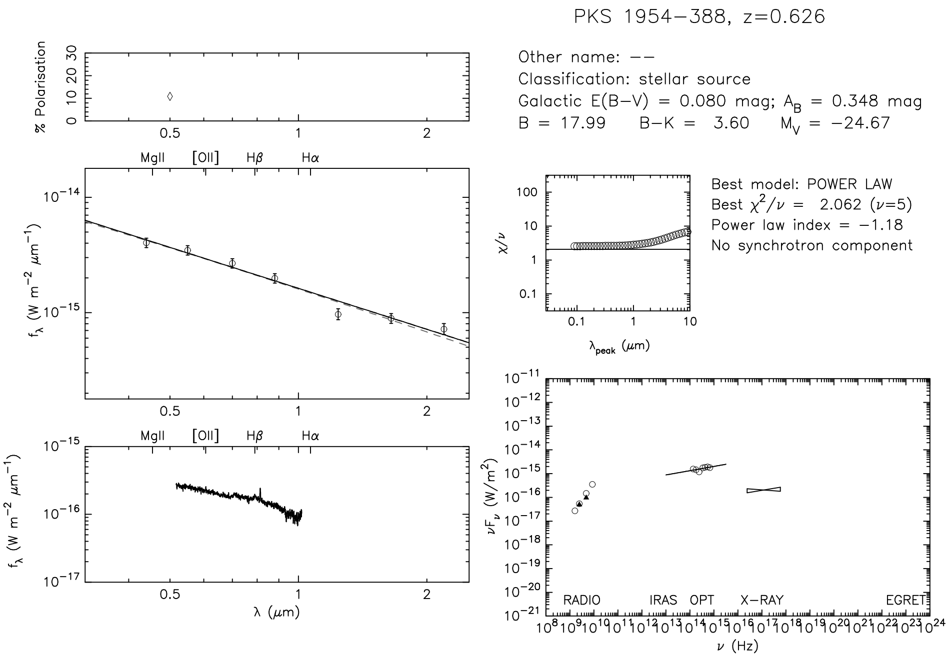
PKS 1954−388, z=0.626
Other name: −−
Classification: stellar source
Galactic E(B−V) = 0.080 mag; A_B = 0.348 mag
B = 17.99   B−K = 3.60 M_V = −24.67
Best model: POWER LAW
Best χ^2/ν = 2.062 (ν=5)
Power law index = −1.18
No synchrotron component
% Polarisation
MgII [OII] Hβ Hα
f_λ (W m^{-2} μm^{-1})
λ (μm)
χ/ν
λ_{peak} (μm)
νF_ν (W/m^2)
RADIO IRAS OPT X-RAY EGRET
ν (Hz)

PKS 1958−179, z=0.652

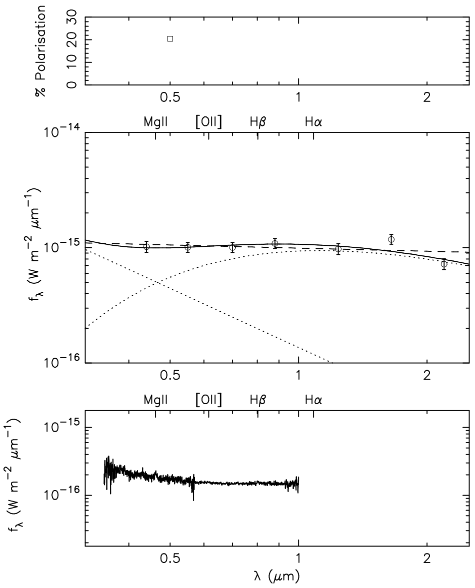

Other name: OV −198
Classification: stellar source
Galactic E(B−V) = 0.133 mag; A_B = 0.574 mag
B = 19.48 B−K = 5.09 M_V = −24.04

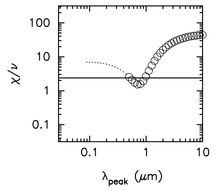

Best model: COMBINED
Best χ^2/ν = 1.528 (ν=4)
Power law index = −1.70
λ_{peak} (synch.) = 0.71 μm
0.5 μm ratio = 4.69
0.5 μm fraction = 82.4%

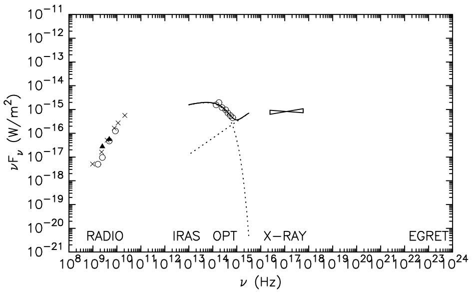

PKS 2002−185, z=0.859

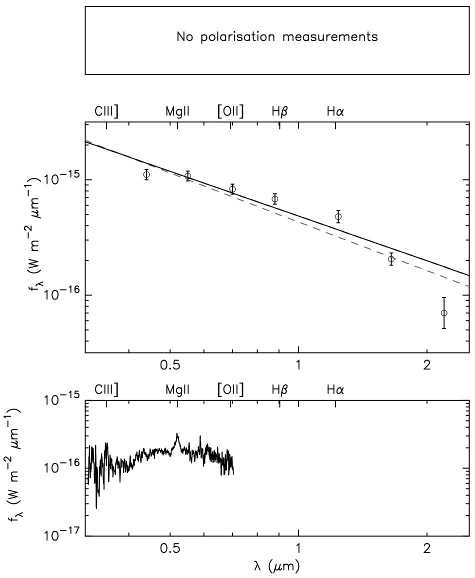

Other name: OW −105
Classification: stellar source
Galactic E(B−V) = 0.146 mag; A_B = 0.632 mag
B = 19.39 B−K = 2.47 M_V = −24.34

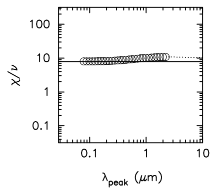

Best model: POWER LAW
Best χ^2/ν = 7.941 (ν=5)
Power law index = −1.29
No synchrotron component

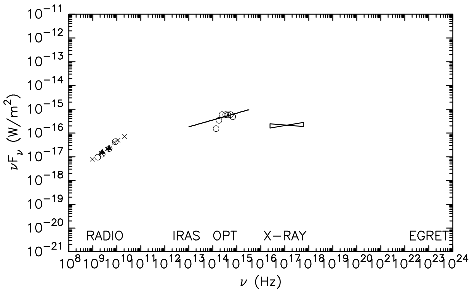

PKS 2004−447, z=0.24

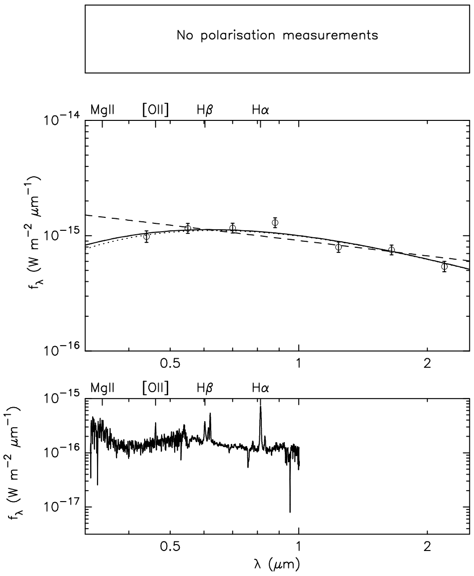

Other name: −−
Classification: stellar source
Galactic E(B−V) = 0.034 mag; A_B = 0.146 mag
B = 19.52 B−K = 4.82 M_V = −21.60

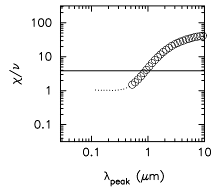

Best model: COMBINED
Best χ^2/ν = 1.515 (ν=4)
Power law index = −1.70
λ_{peak} (synch.) = 0.53 μm
0.5 μm ratio = 55.79
0.5 μm fraction = 98.2%

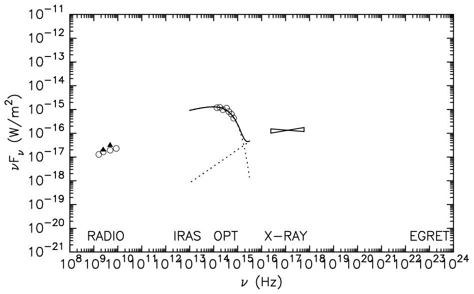

PKS 2008−159, z=1.178

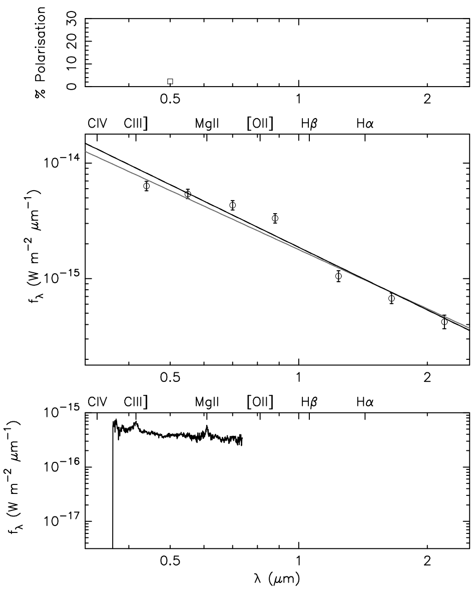

Other name: OW −115
Classification: stellar source
Galactic E(B−V) = 0.142 mag; A_B = 0.614 mag
B = 17.50 B−K = 2.53 M_V = −26.74

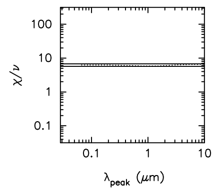

Best model: POWER LAW
Best χ^2/ν = 5.668 (ν=5)
Power law index = −1.80
No synchrotron component

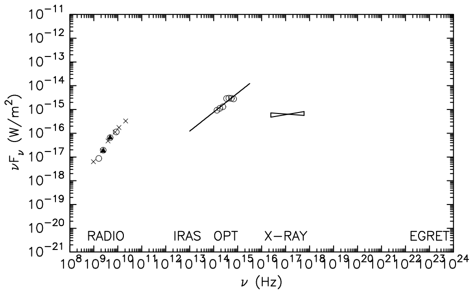

PKS 2021−330, z=1.471

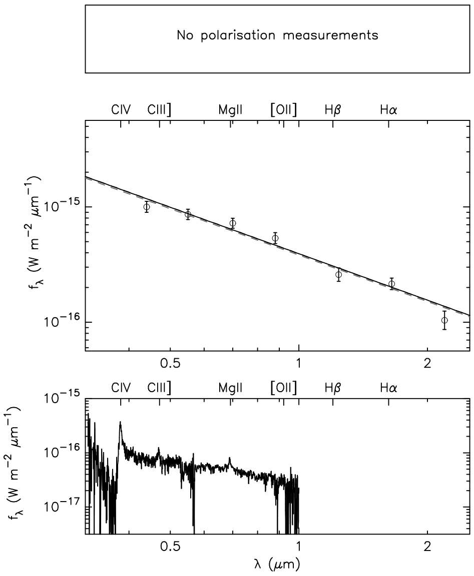

Other name: −−
Classification: stellar source
Galactic E(B−V) = 0.075 mag; A_B = 0.325 mag
B = 19.50 B−K = 3.01 M_V = −25.34

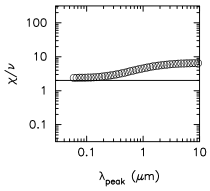

Best model: POWER LAW
Best χ^2/ν = 2.006 (ν=5)
Power law index = −1.34
No synchrotron component

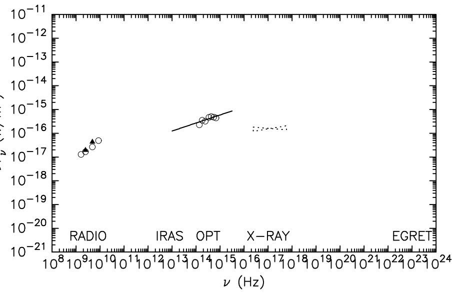

PKS 2022−077, z=1.388

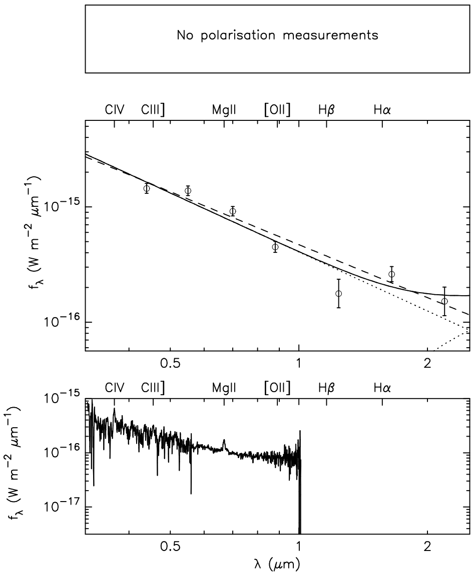

Other name: NRAO 0629
Classification: stellar source
Galactic E(B−V) = 0.039 mag; A_B = 0.168 mag
B = 19.10 B−K = 3.02 M_V = −24.98

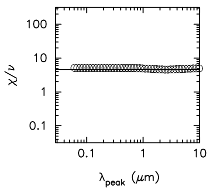

Best model: COMBINED
Best χ^2/ν = 4.585 (ν=4)
Power law index = −1.70
λ_{peak} (synch.) = 2.74 μm
0.5 μm ratio = 0.02
0.5 μm fraction = 2.4%

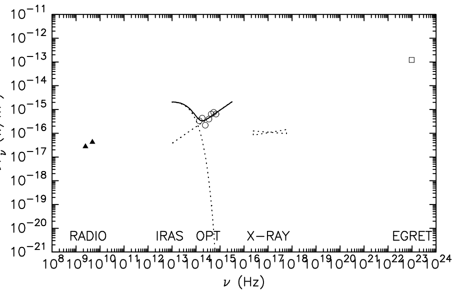

PKS 2037−253, z=1.574

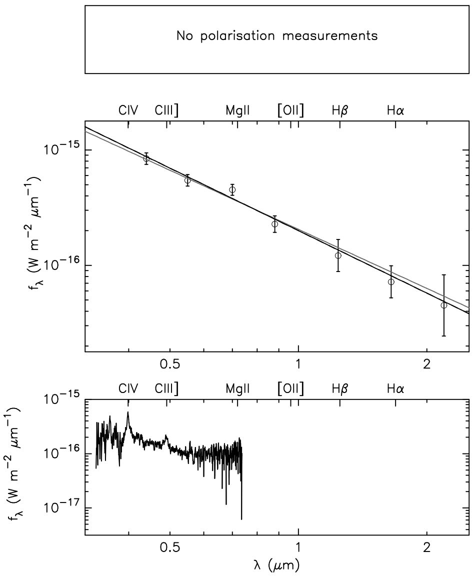

Other name: −−
Classification: stellar source
Galactic E(B−V) = 0.048 mag; A_B = 0.206 mag
B = 19.69 B−K = 2.29 M_V = −24.22

Best model: POWER LAW
Best χ^2/ν = 0.672 (ν=5)
Power law index = −1.80
No synchrotron component

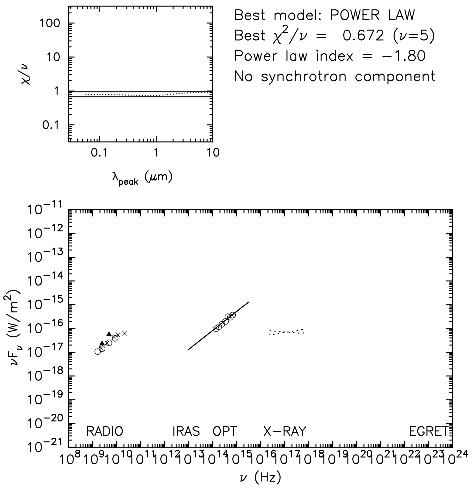

PKS 2044−168, z=1.937

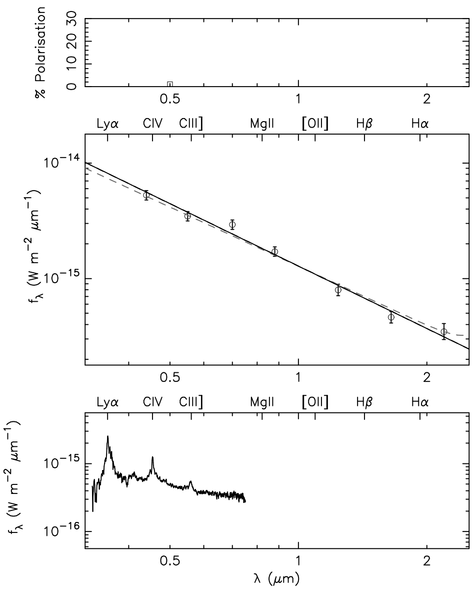

Other name: OW −174
Classification: stellar source
Galactic E(B−V) = 0.072 mag; A_B = 0.311 mag
B = 17.70 B−K = 2.52 M_V = −26.79

Best model: POWER LAW
Best χ^2/ν = 1.430 (ν=5)
Power law index = −1.80
No synchrotron component

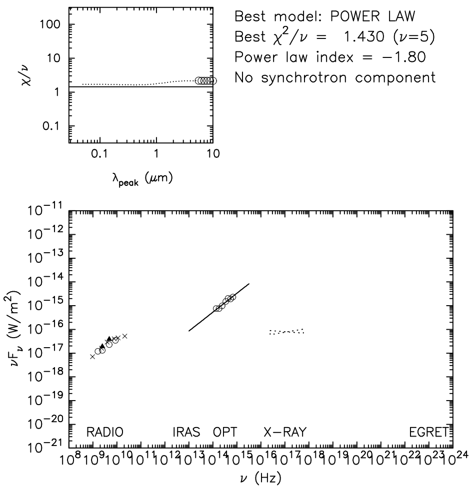

PKS 2053−044, z=1.177

No polarisation measurements

Other name: 4C −04.80
Classification: stellar source
Galactic E(B−V) = 0.076 mag; A_B = 0.329 mag
B = 18.86   B−K = 2.73 M_V = −25.03

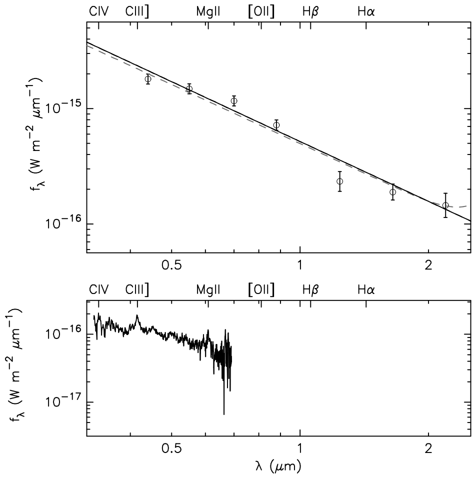

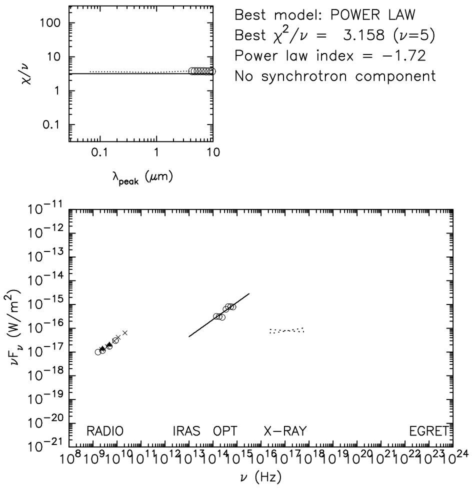

Best model: POWER LAW
Best χ^2/ν = 3.158 (ν=5)
Power law index = −1.72
No synchrotron component

PKS 2058−297, z=1.492

No polarisation measurements

Other name: IC 1347
Classification: stellar source
Galactic E(B−V) = 0.101 mag; A_B = 0.437 mag
B = 18.85   B−K = 2.63 M_V = −25.26

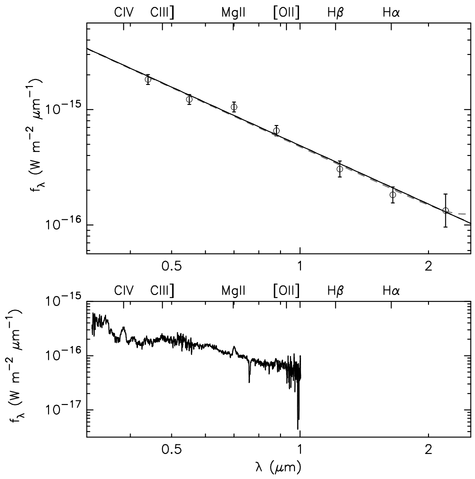

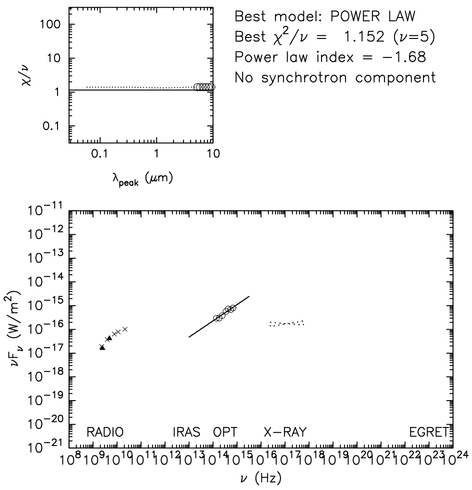

Best model: POWER LAW
Best χ^2/ν = 1.152 (ν=5)
Power law index = −1.68
No synchrotron component

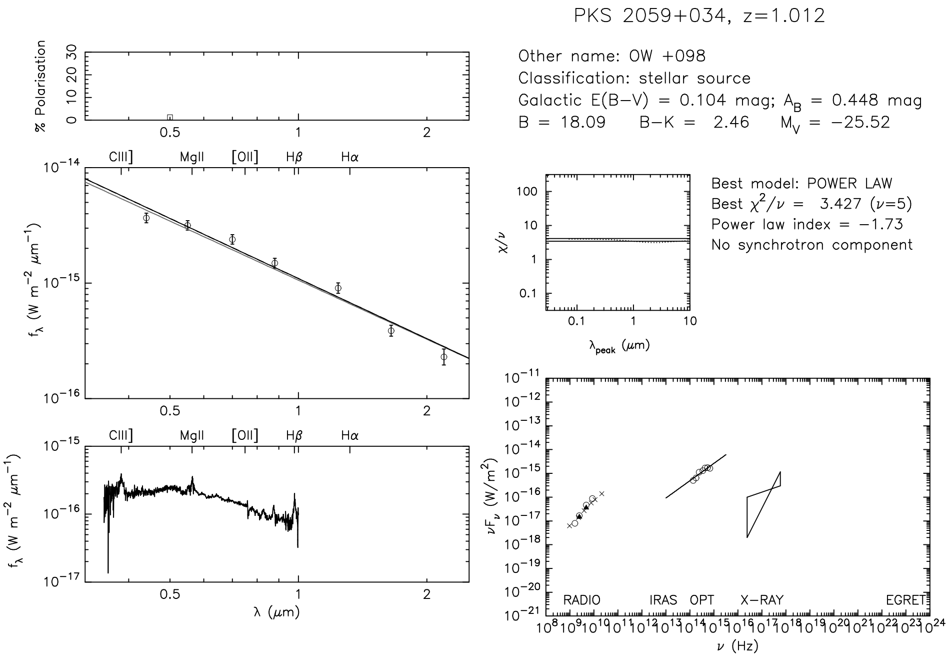
PKS 2059+034, z=1.012
Other name: OW +098
Classification: stellar source
Galactic E(B−V) = 0.104 mag; A_B = 0.448 mag
B = 18.09 B−K = 2.46 M_V = −25.52
Best model: POWER LAW
Best χ^2/ν = 3.427 (ν=5)
Power law index = −1.73
No synchrotron component
% Polarisation
CIII] MgII [OII] Hβ Hα
f_λ (W m^{-2} μm^{-1})
λ (μm)
χ/ν
λ_{peak} (μm)
νF_ν (W/m^2)
RADIO IRAS OPT X-RAY EGRET
ν (Hz)

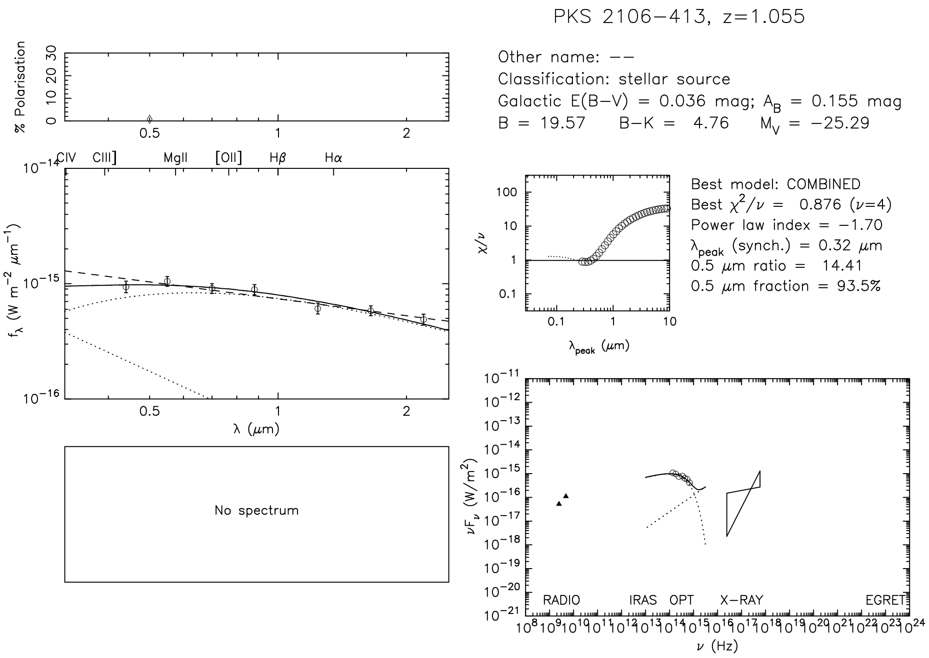
PKS 2106−413, z=1.055
Other name: −−
Classification: stellar source
Galactic E(B−V) = 0.036 mag; A_B = 0.155 mag
B = 19.57 B−K = 4.76 M_V = −25.29
Best model: COMBINED
Best χ^2/ν = 0.876 (ν=4)
Power law index = −1.70
λ_{peak} (synch.) = 0.32 μm
0.5 μm ratio = 14.41
0.5 μm fraction = 93.5%
% Polarisation
CIV CIII] MgII [OII] Hβ Hα
f_λ (W m^{-2} μm^{-1})
λ (μm)
No spectrum
χ/ν
λ_{peak} (μm)
νF_ν (W/m^2)
RADIO IRAS OPT X-RAY EGRET
ν (Hz)

PKS 2120+099, z=0.932

Other name: --
Classification: stellar source
Galactic E(B−V) = 0.057 mag; A_B = 0.245 mag
B = 19.65 B−K = 3.13 M_V = −24.08

No polarisation measurements

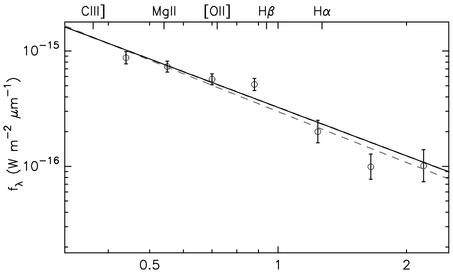

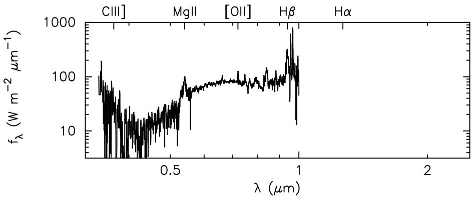

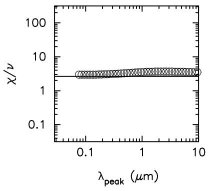

Best model: POWER LAW
Best χ^2/ν = 2.631 (ν=5)
Power law index = −1.39
No synchrotron component

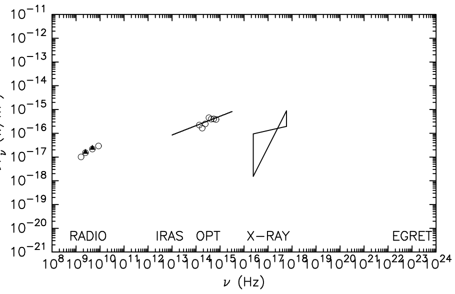

PKS 2121+053, z=1.941

Other name: OX +036
Classification: stellar source
Galactic E(B−V) = 0.073 mag; A_B = 0.314 mag
B = 19.86 B−K = 5.15 M_V = −26.98

No polarisation measurements

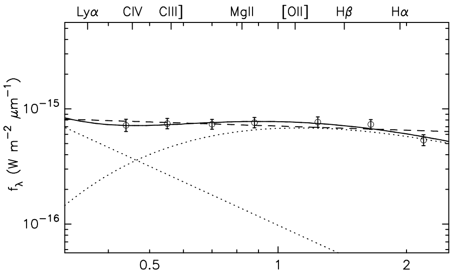

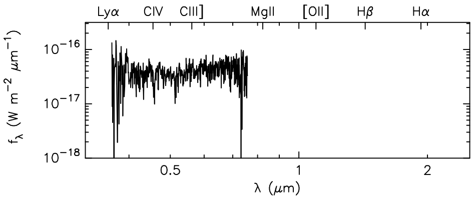

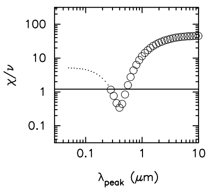

Best model: COMBINED
Best χ^2/ν = 0.342 (ν=4)
Power law index = −1.70
λ_{peak} (synch.) = 0.40 μm
0.5 μm ratio = 12.95
0.5 μm fraction = 92.8%

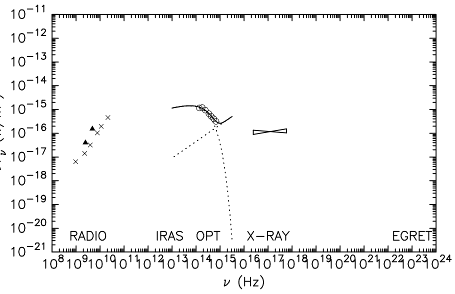

PKS 2127−096, z=0.78

No polarisation measurements

Other name: −−
Classification: faint source
Galactic E(B−V) = 0.046 mag; A_B = 0.200 mag
B = 19.43 B−K = 4.82 M_V = −24.88

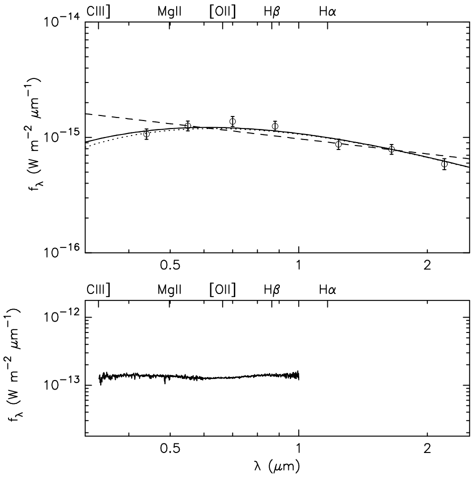

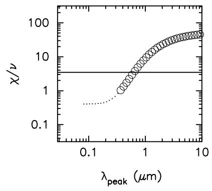

Best model: COMBINED
Best χ^2/ν = 1.036 (ν=4)
Power law index = −1.70
λ_{peak} (synch.) = 0.37 μm
0.5 μm ratio = 74.26
0.5 μm fraction = 98.7%

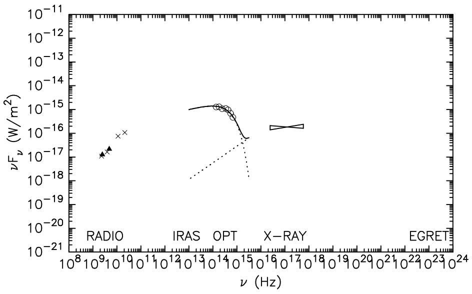

PKS 2128−123, z=0.499

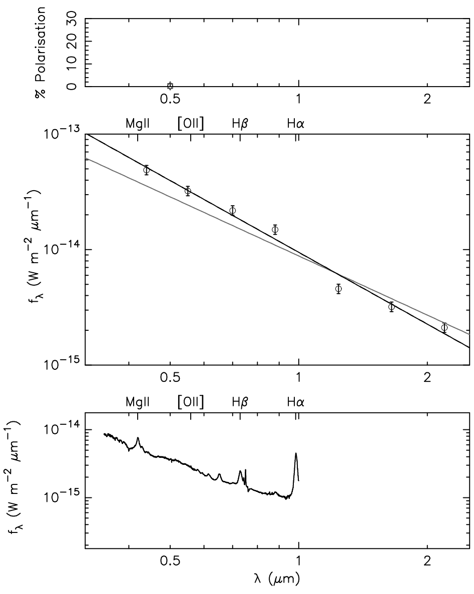

Other name: PHL 1598
Classification: stellar source
Galactic E(B−V) = 0.062 mag; A_B = 0.266 mag
B = 15.28 B−K = 2.06 M_V = −26.27

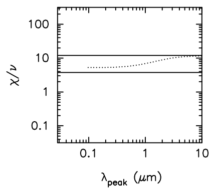

Best model: POWER LAW
Best χ^2/ν = 3.735 (ν=5)
Power law index = −2.07
No synchrotron component

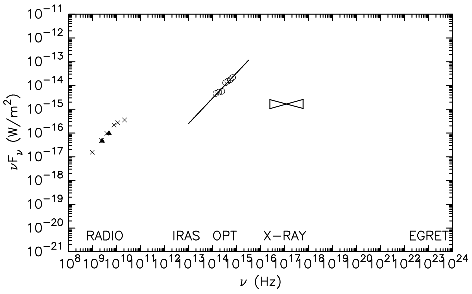

PKS 2131−021, z=1.285

Other name: 4C −02.81
Classification: stellar source, BL Lac (PG95)
Galactic E(B−V) = 0.055 mag; A_B = 0.238 mag
B = 20.61   B−K = 4.76 M_V = −24.34

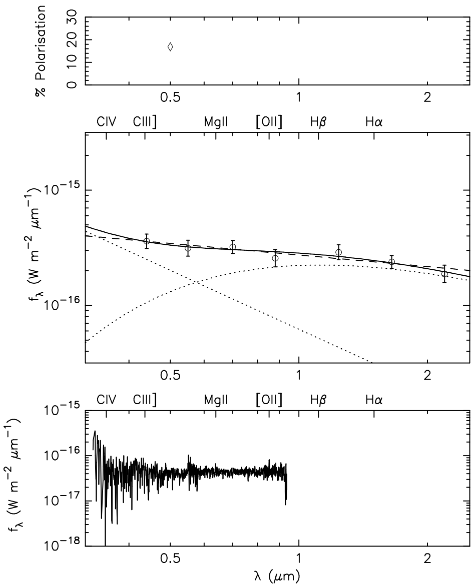

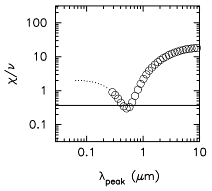

Best model: COMBINED
Best χ^2/ν = 0.302 (ν=4)
Power law index = −1.70
λ_{peak} (synch.) = 0.51 μm
0.5 μm ratio = 4.52
0.5 μm fraction = 81.9%

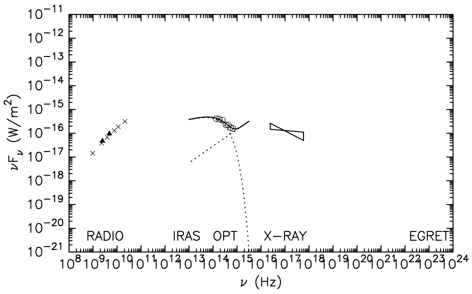

PKS 2134+004, z=1.937

Other name: PHL 0061
Classification: stellar source
Galactic E(B−V) = 0.065 mag; A_B = 0.282 mag
B = 17.04   B−K = 2.31 M_V = −27.87

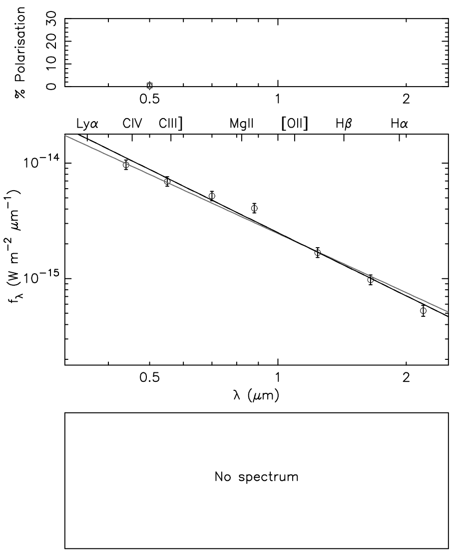

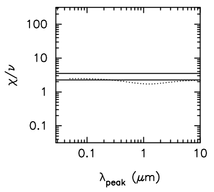

Best model: POWER LAW
Best χ^2/ν = 2.248 (ν=5)
Power law index = −1.82
No synchrotron component

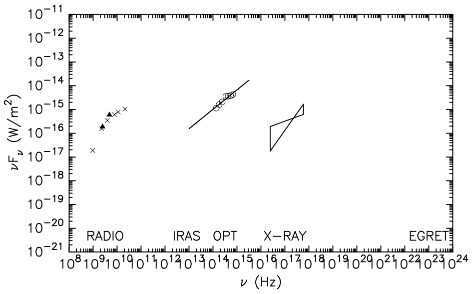

PKS 2135−248, z=0.821

No polarisation measurements

Other name: −−
Classification: stellar source
Galactic E(B−V) = 0.052 mag; A_B = 0.224 mag
B = 19.64 B−K = 3.75 M_V = −23.73

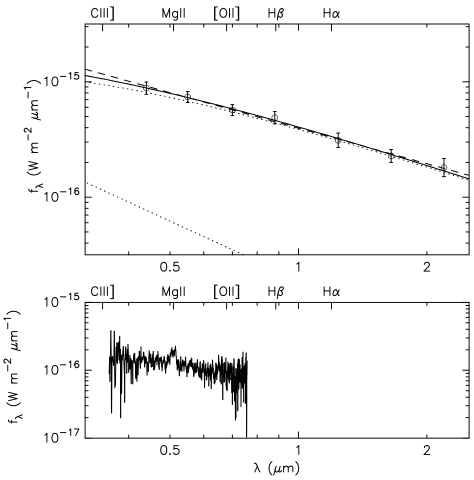

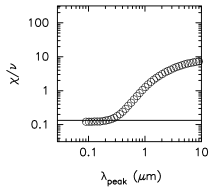

Best model: COMBINED
Best χ^2/ν = 0.122 (ν=4)
Power law index = −1.70
λ_{peak} (synch.) = 0.10 μm
0.5 μm ratio = 18.98
0.5 μm fraction = 95.0%

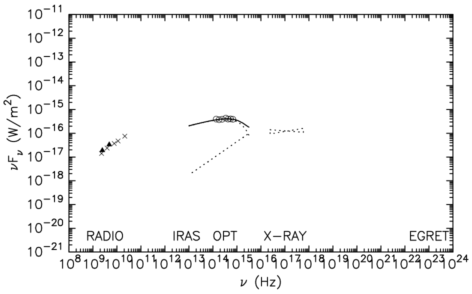

PKS 2140−048, z=0.344

No polarisation measurements

Other name: PHL 0109
Classification: stellar source
Galactic E(B−V) = 0.032 mag; A_B = 0.140 mag
B = 17.22 B−K = 3.27 M_V = −23.54

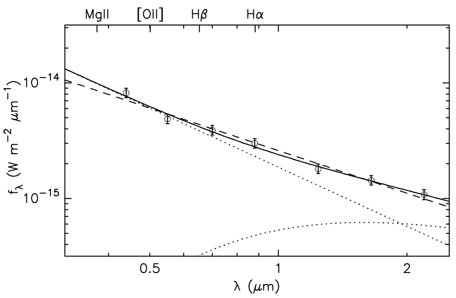

No spectrum

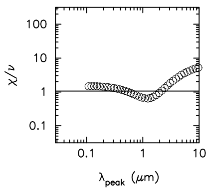

Best model: COMBINED
Best χ^2/ν = 0.643 (ν=4)
Power law index = −1.70
λ_{peak} (synch.) = 1.22 μm
0.5 μm ratio = 0.09
0.5 μm fraction = 8.4%

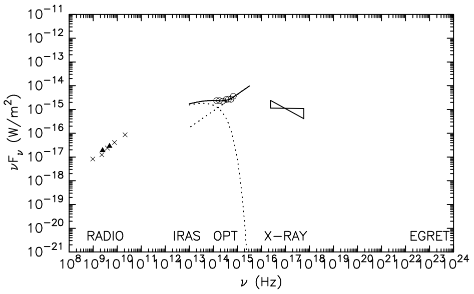

PKS 2143−156, z=0.698

No polarisation measurements

Other name: OX −173
Classification: stellar source
Galactic E(B−V) = 0.098 mag; A_B = 0.422 mag
B = 18.02 B−K = 2.78 M_V = −24.64

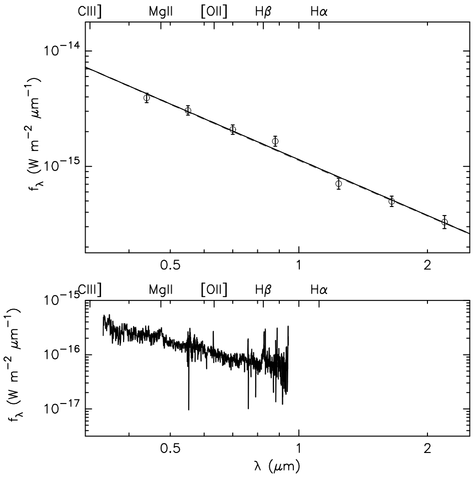

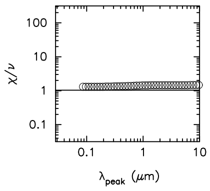

Best model: POWER LAW
Best χ^2/ν = 1.041 (ν=5)
Power law index = −1.60
No synchrotron component

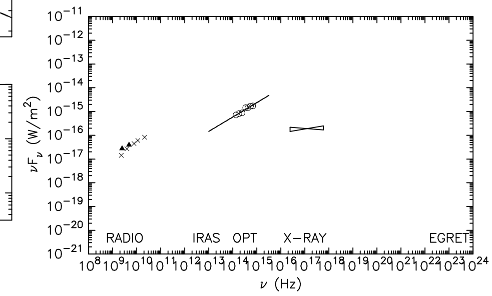

PKS 2144+092, z=1.113

No polarisation measurements

Other name: OX +074
Classification: stellar source
Galactic E(B−V) = 0.072 mag; A_B = 0.311 mag
B = 18.78 B−K = 3.96 M_V = −25.25

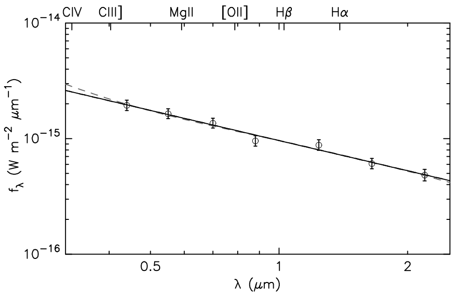

No spectrum

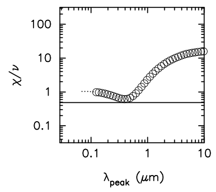

Best model: POWER LAW
Best χ^2/ν = 0.488 (ν=5)
Power law index = −0.87
No synchrotron component

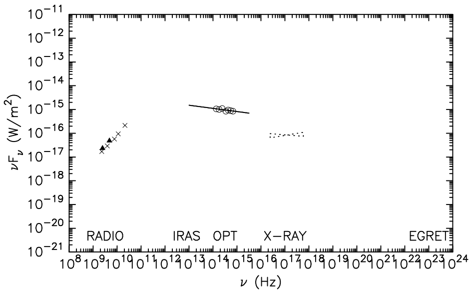

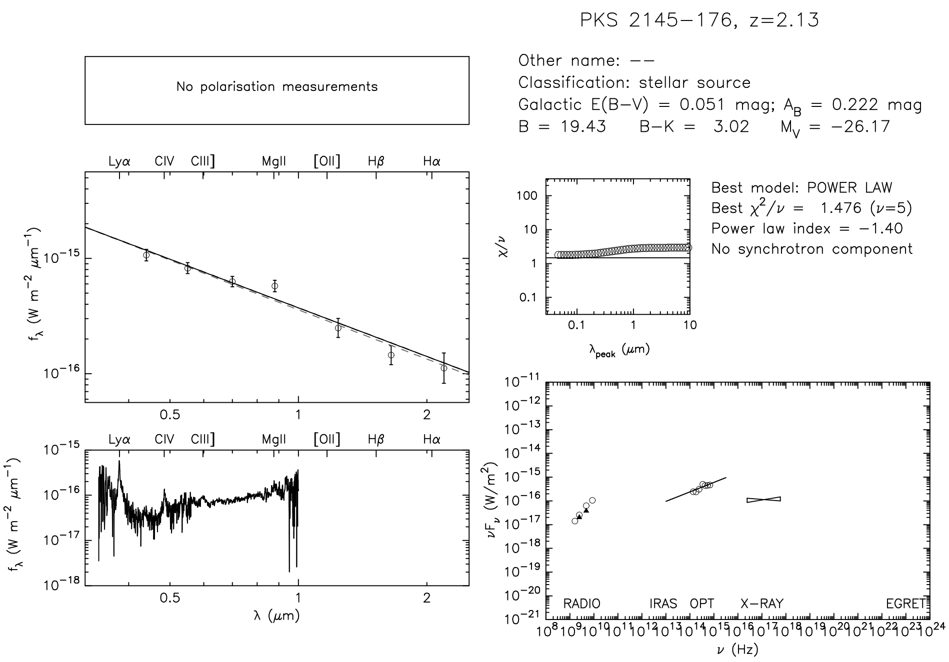
PKS 2145−176, z=2.13
No polarisation measurements
Other name: −−
Classification: stellar source
Galactic E(B−V) = 0.051 mag; A_B = 0.222 mag
B = 19.43 B−K = 3.02 M_V = −26.17
Best model: POWER LAW
Best χ^2/ν = 1.476 (ν=5)
Power law index = −1.40
No synchrotron component
Lyα CIV CIII] MgII [OII] Hβ Hα
f_λ (W m^{-2} μm^{-1})
λ (μm)
χ/ν
λ_{peak} (μm)
νF_ν (W/m^2)
RADIO IRAS OPT X-RAY EGRET
ν (Hz)

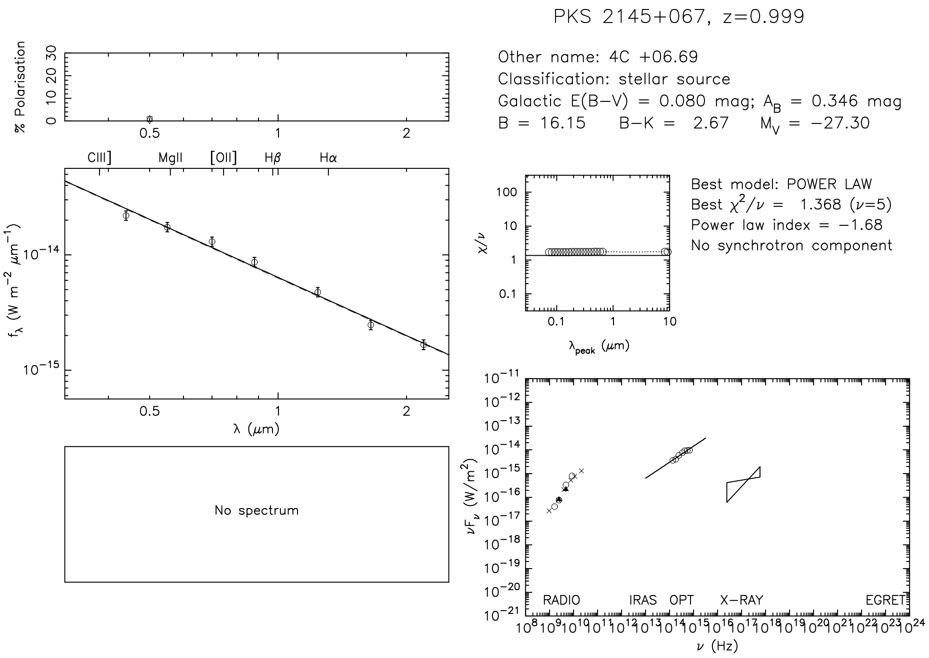
PKS 2145+067, z=0.999
% Polarisation
Other name: 4C +06.69
Classification: stellar source
Galactic E(B−V) = 0.080 mag; A_B = 0.346 mag
B = 16.15 B−K = 2.67 M_V = −27.30
Best model: POWER LAW
Best χ^2/ν = 1.368 (ν=5)
Power law index = −1.68
No synchrotron component
CIII] MgII [OII] Hβ Hα
f_λ (W m^{-2} μm^{-1})
λ (μm)
No spectrum
χ/ν
λ_{peak} (μm)
νF_ν (W/m^2)
RADIO IRAS OPT X-RAY EGRET
ν (Hz)

PKS 2149−307, z=2.345

No polarisation measurements

Other name: −−
Classification: stellar source
Galactic E(B−V) = 0.025 mag; A_B = 0.109 mag
B = 18.00   B−K = 2.76 M_V = −27.27

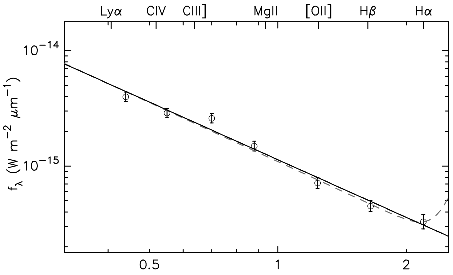

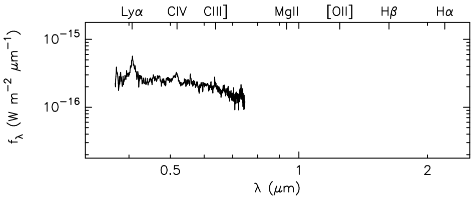

Best model: POWER LAW
Best χ^2/ν = 1.862 (ν=5)
Power law index = −1.66
No synchrotron component

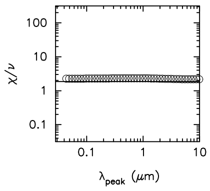

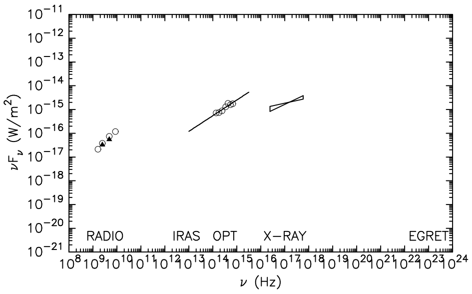

PKS 2149+056, z=0.74

No polarisation measurements

Other name: OX +082
Classification: faint source
Galactic E(B−V) = 0.057 mag; A_B = 0.246 mag
B > 23.50   B−K > 6.33 M_V = −22.65

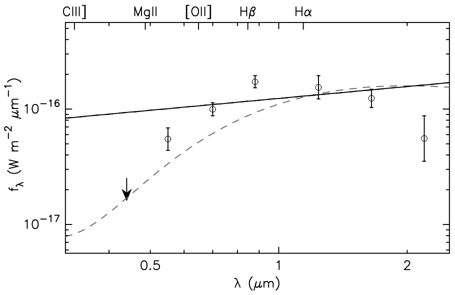

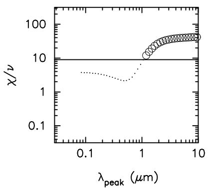

Best model: POWER LAW
Best χ^2/ν = 9.053 (ν=5)
Power law index = 0.34
No synchrotron component

No spectrum

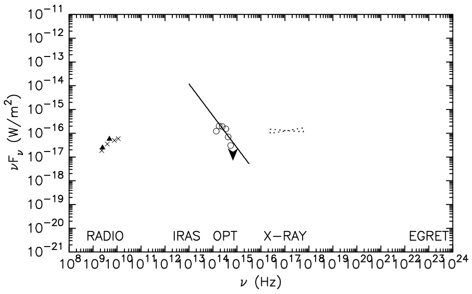

PKS 2149+069, z=1.364

Other name: OX +081
Classification: stellar source
Galactic E(B−V) = 0.052 mag; A_B = 0.226 mag
B = 18.79 B−K = 3.03 M_V = −25.62

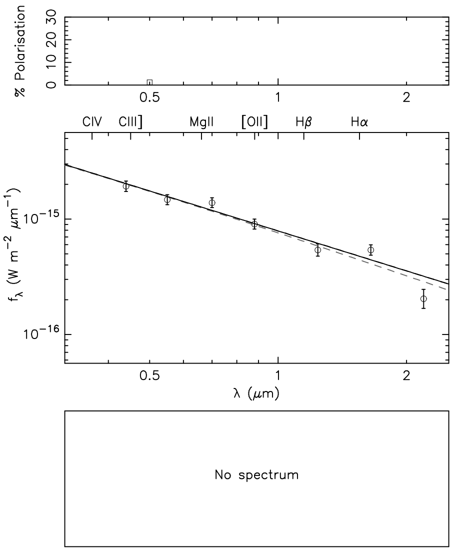

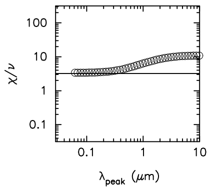

Best model: POWER LAW
Best χ^2/ν = 3.205 (ν=5)
Power law index = −1.15
No synchrotron component

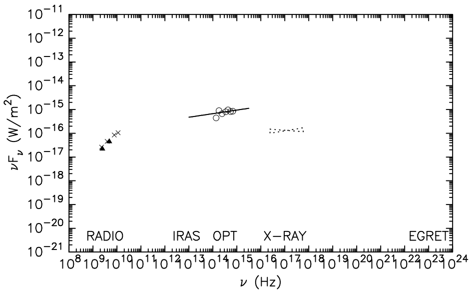

PKS 2155−152, z=0.672

Other name: OX −192
Classification: stellar source
Galactic E(B−V) = 0.048 mag; A_B = 0.208 mag
B = 18.42 B−K = 4.50 M_V = −24.82

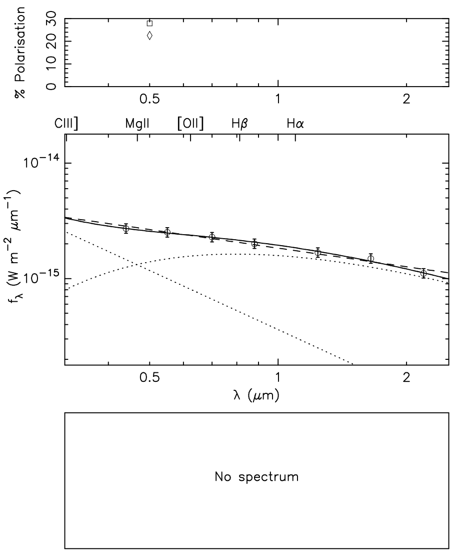

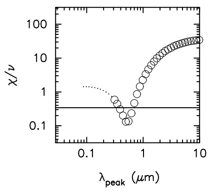

Best model: COMBINED
Best χ^2/ν = 0.133 (ν=4)
Power law index = −1.70
λ_{peak} (synch.) = 0.49 μm
0.5 μm ratio = 3.32
0.5 μm fraction = 76.8%

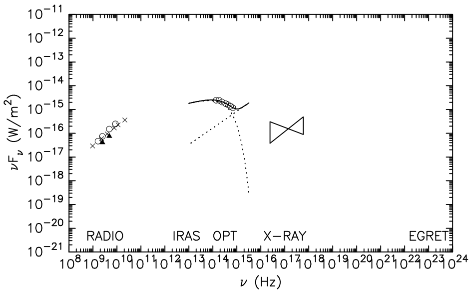

PKS 2200−238, z=2.12

No polarisation measurements

Other name: −−
Classification: stellar source
Galactic E(B−V) = 0.030 mag; A_B = 0.130 mag
B = 18.45   B−K = 2.63 M_V = −26.34

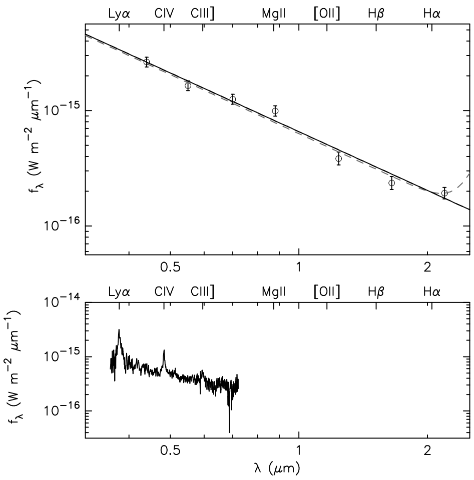

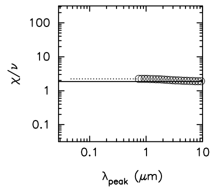

Best model: POWER LAW
Best χ^2/ν = 1.851 (ν=5)
Power law index = −1.69
No synchrotron component

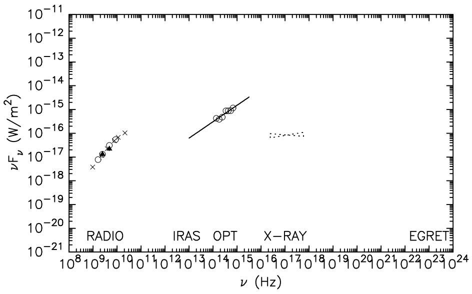

PKS 2203−188, z=0.619

Other name: OY −106
Classification: stellar source
Galactic E(B−V) = 0.027 mag; A_B = 0.116 mag
B = 18.85   B−K = 3.60 M_V = −23.89

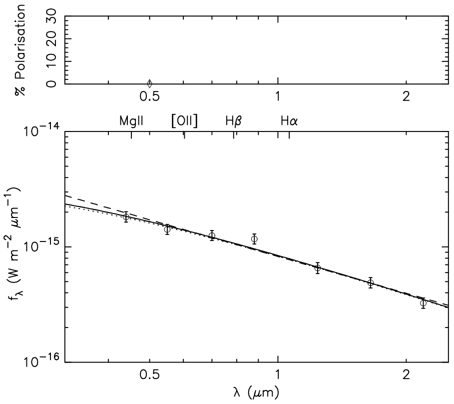

No spectrum

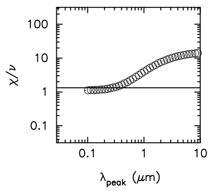

Best model: COMBINED
Best χ^2/ν = 1.126 (ν=4)
Power law index = −1.70
λ_{peak} (synch.) = 0.10 μm
0.5 μm ratio = 51.89
0.5 μm fraction = 98.1%

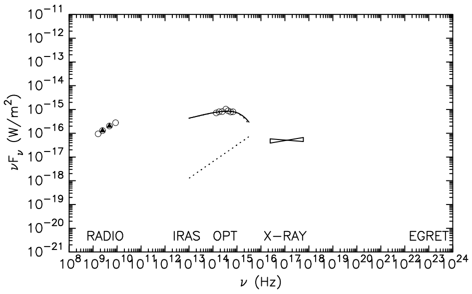

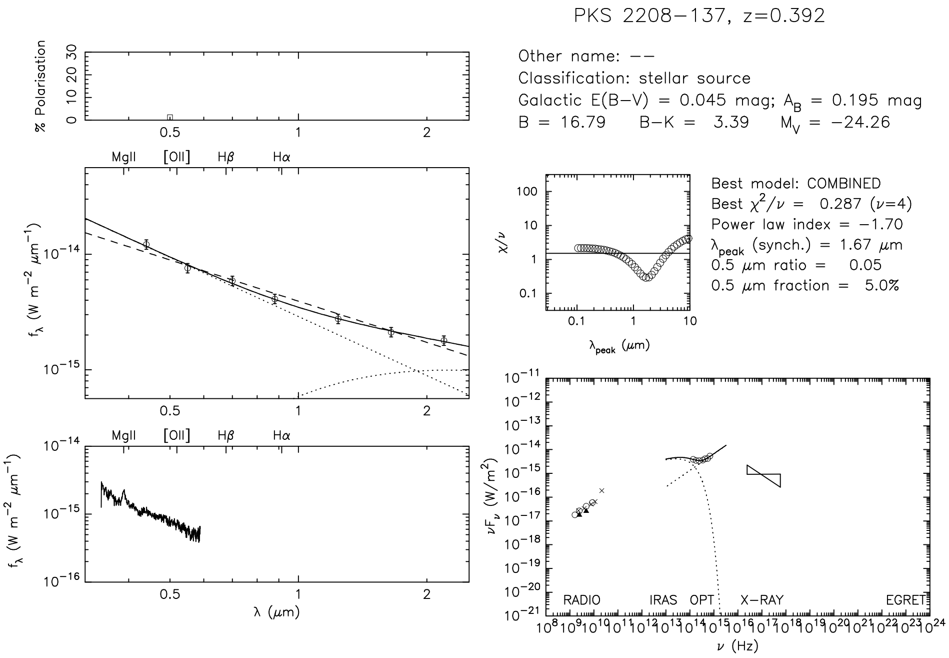
PKS 2208−137, z=0.392
Other name: −−
Classification: stellar source
Galactic E(B−V) = 0.045 mag; A_B = 0.195 mag
B = 16.79 B−K = 3.39 M_V = −24.26
Best model: COMBINED
Best χ²/ν = 0.287 (ν=4)
Power law index = −1.70
λ_peak (synch.) = 1.67 μm
0.5 μm ratio = 0.05
0.5 μm fraction = 5.0%
% Polarisation
MgII [OII] Hβ Hα
f_λ (W m⁻² μm⁻¹)
λ (μm)
χ/ν
λ_peak (μm)
νF_ν (W/m²)
RADIO IRAS OPT X−RAY EGRET
ν (Hz)

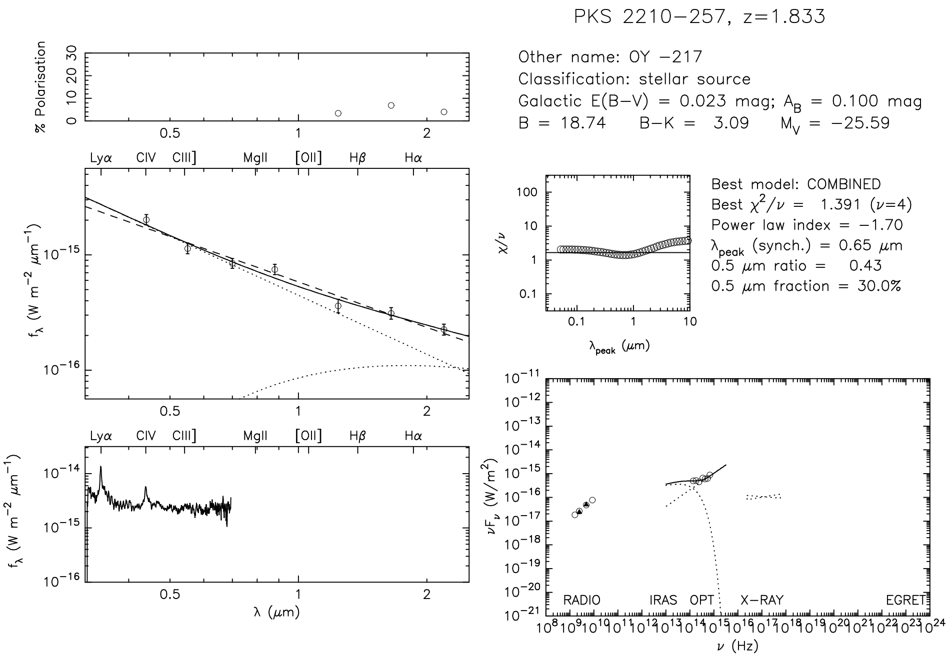
PKS 2210−257, z=1.833
Other name: OY −217
Classification: stellar source
Galactic E(B−V) = 0.023 mag; A_B = 0.100 mag
B = 18.74 B−K = 3.09 M_V = −25.59
Best model: COMBINED
Best χ²/ν = 1.391 (ν=4)
Power law index = −1.70
λ_peak (synch.) = 0.65 μm
0.5 μm ratio = 0.43
0.5 μm fraction = 30.0%
% Polarisation
Lyα CIV CIII] MgII [OII] Hβ Hα
f_λ (W m⁻² μm⁻¹)
λ (μm)
χ/ν
λ_peak (μm)
νF_ν (W/m²)
RADIO IRAS OPT X−RAY EGRET
ν (Hz)

PKS 2212−299, z=2.703

No polarisation measurements

Other name: OY −221
Classification: stellar source
Galactic E(B−V) = 0.015 mag; A_B = 0.064 mag
B = 17.47 B−K = 2.88 M_V = −27.61

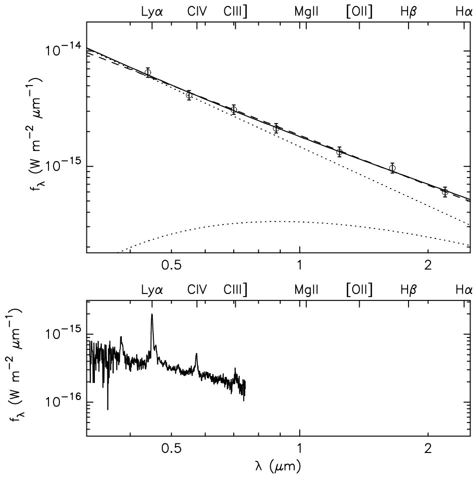

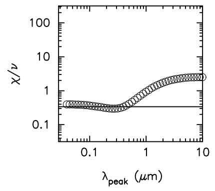

Best model: COMBINED
Best χ^2/ν = 0.296 (ν=4)
Power law index = −1.70
λ_{peak} (synch.) = 0.25 μm
0.5 μm ratio = 0.49
0.5 μm fraction = 33.0%

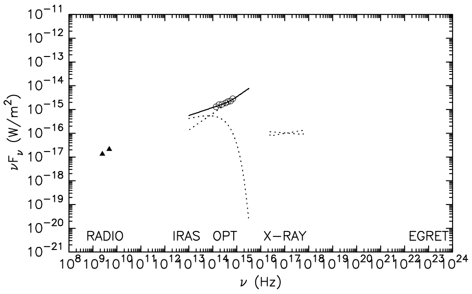

PKS 2216−038, z=0.901

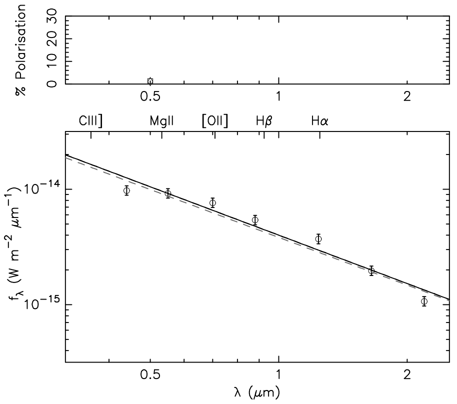

Other name: 4C −03.79
Classification: stellar source
Galactic E(B−V) = 0.095 mag; A_B = 0.410 mag
B = 17.03 B−K = 3.07 M_V = −26.72

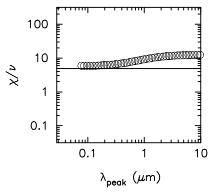

Best model: POWER LAW
Best χ^2/ν = 4.968 (ν=5)
Power law index = −1.39
No synchrotron component

No spectrum

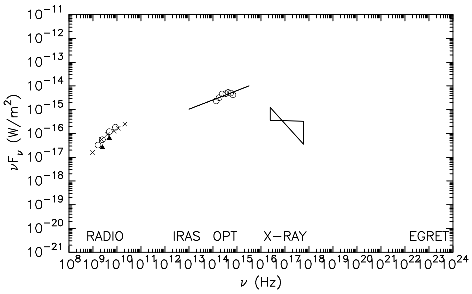

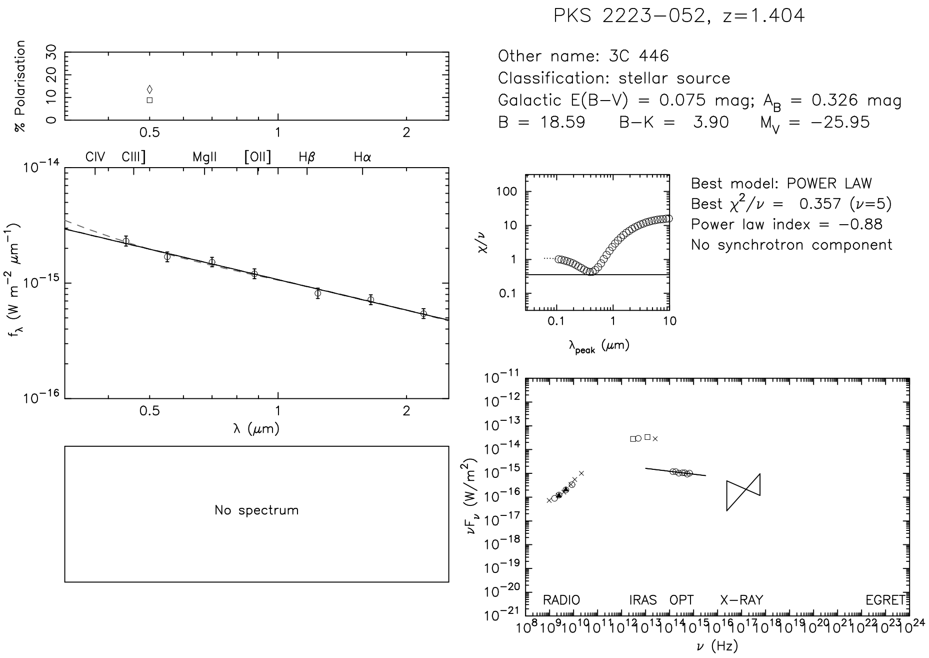
PKS 2223−052, z=1.404
Other name: 3C 446
Classification: stellar source
Galactic E(B−V) = 0.075 mag; A_B = 0.326 mag
B = 18.59 B−K = 3.90 M_V = −25.95
Best model: POWER LAW
Best χ^2/ν = 0.357 (ν=5)
Power law index = −0.88
No synchrotron component
No spectrum
% Polarisation
CIV CIII] MgII [OII] Hβ Hα
f_λ (W m^{-2} μm^{-1})
λ (μm)
χ/ν
λ_{peak} (μm)
νF_ν (W/m^2)
RADIO IRAS OPT X−RAY EGRET
ν (Hz)

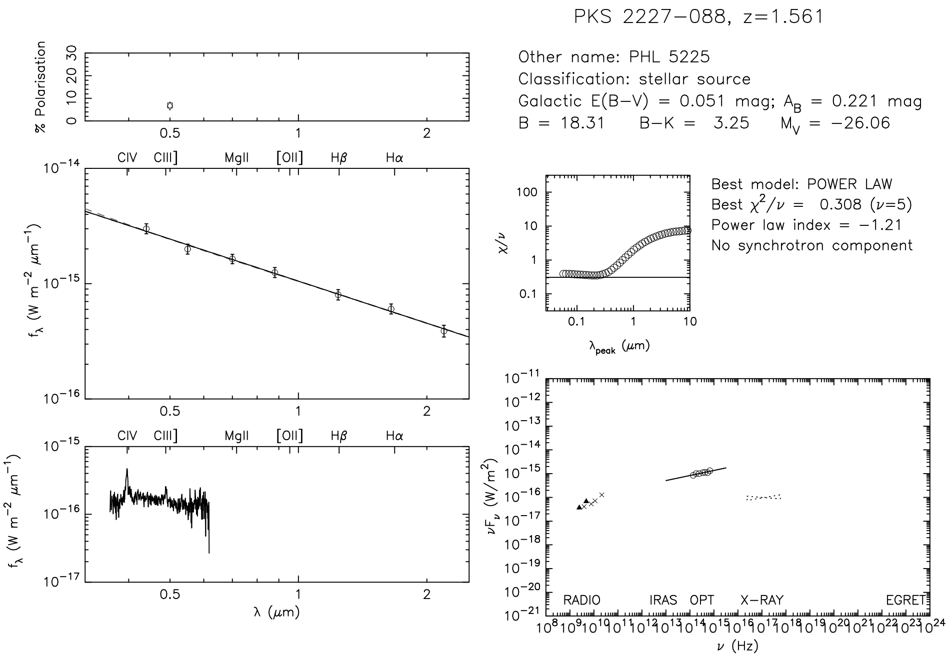
PKS 2227−088, z=1.561
Other name: PHL 5225
Classification: stellar source
Galactic E(B−V) = 0.051 mag; A_B = 0.221 mag
B = 18.31 B−K = 3.25 M_V = −26.06
Best model: POWER LAW
Best χ^2/ν = 0.308 (ν=5)
Power law index = −1.21
No synchrotron component
% Polarisation
CIV CIII] MgII [OII] Hβ Hα
f_λ (W m^{-2} μm^{-1})
λ (μm)
χ/ν
λ_{peak} (μm)
νF_ν (W/m^2)
RADIO IRAS OPT X−RAY EGRET
ν (Hz)

PKS 2227−399, z=0.323

No polarisation measurements

Other name: --
Classification: stellar source
Galactic E(B−V) = 0.018 mag; A_B = 0.077 mag
B = 17.94 B−K = 3.83 M_V = −23.02

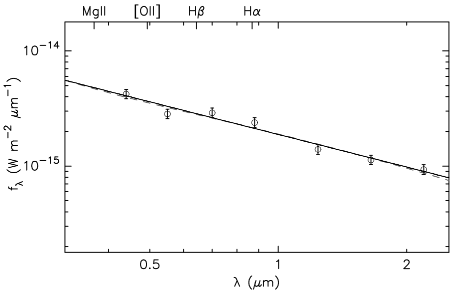

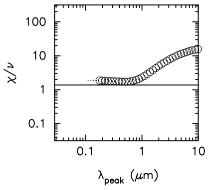

Best model: POWER LAW
Best χ^2/ν = 1.386 (ν=5)
Power law index = −0.94
No synchrotron component

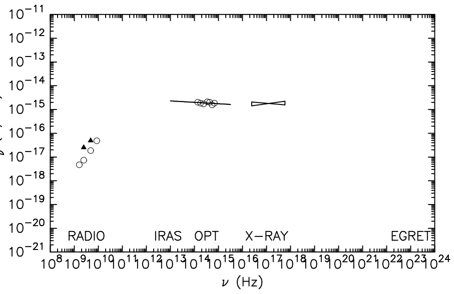

No spectrum

PKS 2229−172, z=1.78

No polarisation measurements

Other name: OY −150
Classification: faint source
Galactic E(B−V) = 0.035 mag; A_B = 0.152 mag
B = 21.26 B−K = 4.49 M_V = −24.04

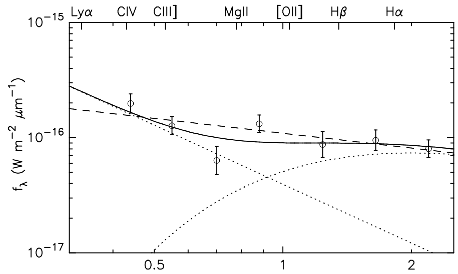

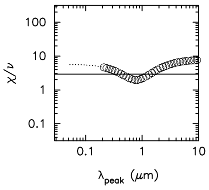

Best model: COMBINED
Best χ^2/ν = 1.994 (ν=4)
Power law index = −1.70
λ_{peak} (synch.) = 0.75 μm
0.5 μm ratio = 2.98
0.5 μm fraction = 74.9%

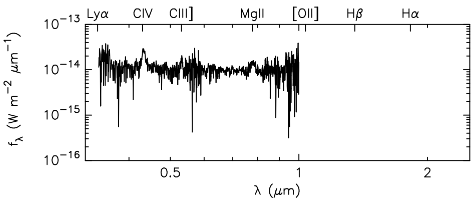

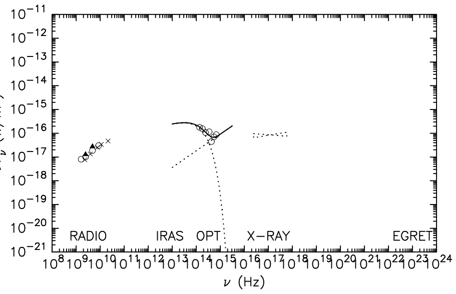

PKS 2233−148, z=0.609

Other name: OY −156
Classification: stellar source, BL Lac Cand. (PG95)
Galactic E(B−V) = 0.043 mag; A_B = 0.186 mag
B = 19.24 B−K = 4.67 M_V = −24.14

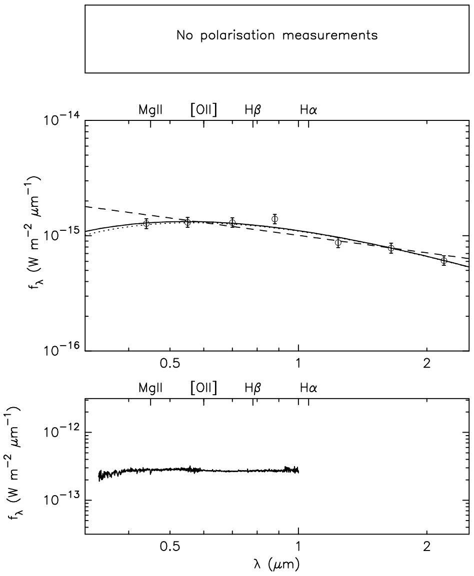

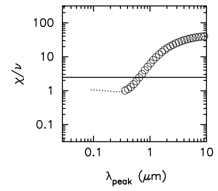

Best model: COMBINED
Best χ^2/ν = 1.013 (ν=4)
Power law index = −1.70
λ_{peak} (synch.) = 0.36 μm
0.5 μm ratio = 74.68
0.5 μm fraction = 98.7%

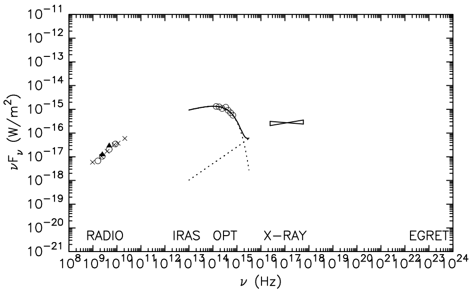

PKS 2239+096, z=1.707

Other name: −−
Classification: stellar source
Galactic E(B−V) = 0.078 mag; A_B = 0.335 mag
B = 19.00 B−K = 2.99 M_V = −25.95

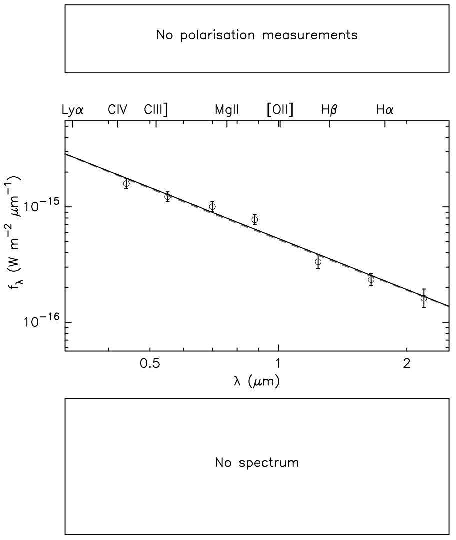

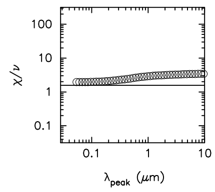

Best model: POWER LAW
Best χ^2/ν = 1.565 (ν=5)
Power law index = −1.47
No synchrotron component

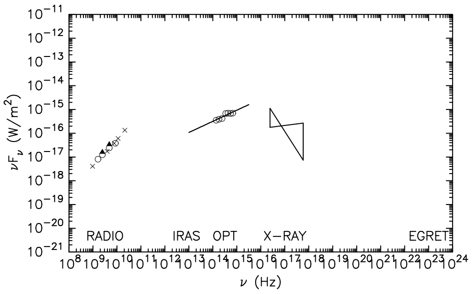

PKS 2240−260, z=0.774

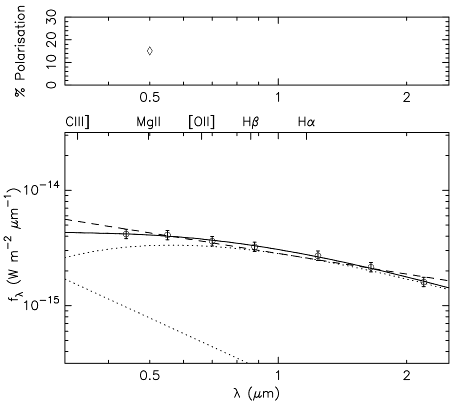

No spectrum

Other name: OY −268
Classification: stellar source, BL Lac (PG95)
Galactic E(B−V) = 0.021 mag; A_B = 0.092 mag
B = 17.95 B−K = 4.43 M_V = −25.75

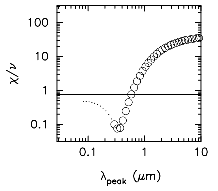

Best model: COMBINED
Best χ^2/ν = 0.076 (ν=4)
Power law index = −1.70
λ_{peak} (synch.) = 0.33 μm
0.5 μm ratio = 10.16
0.5 μm fraction = 91.0%

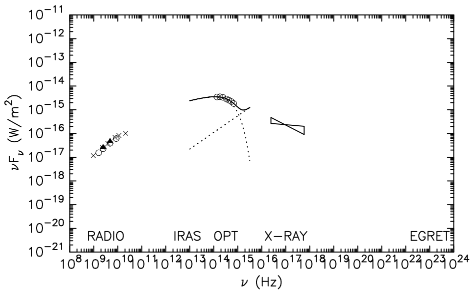

PKS 2243−123, z=0.63

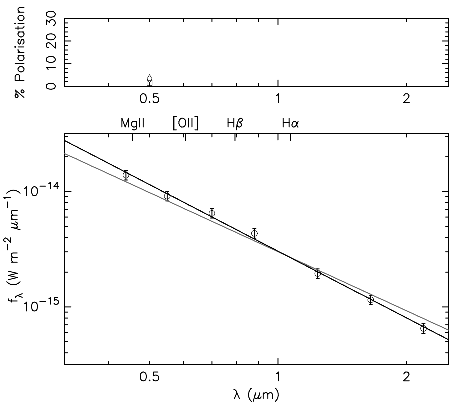

No spectrum

Other name: PB 07192
Classification: stellar source
Galactic E(B−V) = 0.050 mag; A_B = 0.216 mag
B = 16.65 B−K = 2.15 M_V = −25.41

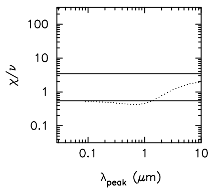

Best model: POWER LAW
Best χ^2/ν = 0.548 (ν=5)
Power law index = −1.92
No synchrotron component

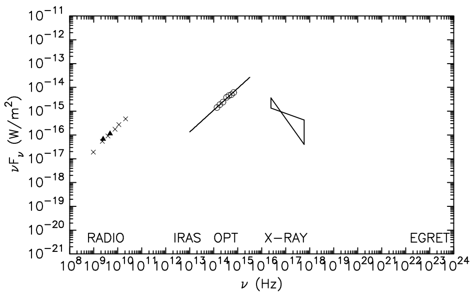

PKS 2245−328, z=2.268

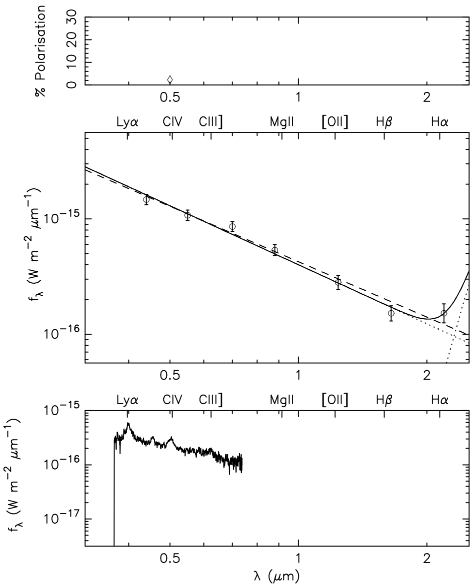

Other name: OY −376
Classification: stellar source
Galactic E(B−V) = 0.019 mag; A_B = 0.080 mag
B = 19.08 B−K = 3.00 M_V = −26.01

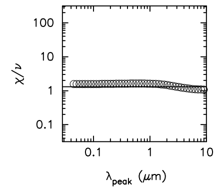

Best model: COMBINED
Best χ^2/ν = 1.077 (ν=4)
Power law index = −1.70
λ_{peak} (synch.) = 8.95 μm
0.5 μm ratio = 0.00
0.5 μm fraction = 0.2%

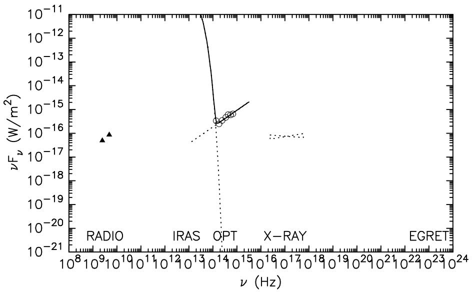

PKS 2252−090, z=0.6064

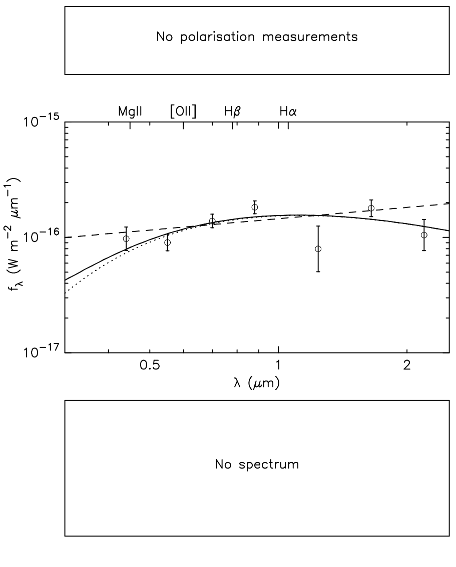

Other name: --
Classification: stellar source
Galactic E(B−V) = 0.043 mag; A_B = 0.187 mag
B = 22.03 B−K = 5.55 M_V = −21.76

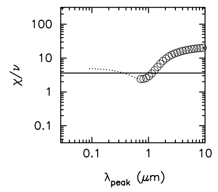

Best model: COMBINED
Best χ^2/ν = 2.410 (ν=4)
Power law index = −1.70
λ_{peak} (synch.) = 0.73 μm
0.5 μm ratio = 72.21
0.5 μm fraction = 98.6%

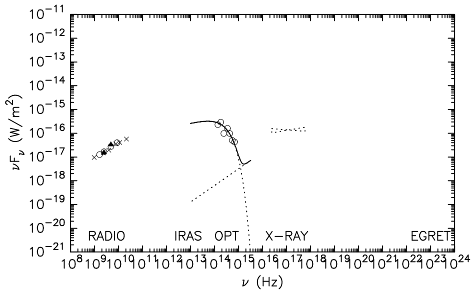

PKS 2312−319, z=1.323

No polarisation measurements

Other name: −−
Classification: stellar source
Galactic E(B−V) = 0.016 mag; A_B = 0.069 mag
B = 18.10 B−K = 2.47 M_V = −26.08

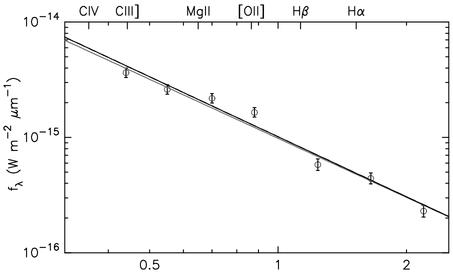

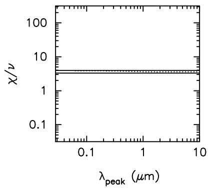

Best model: POWER LAW
Best χ^2/ν = 3.292 (ν=5)
Power law index = −1.73
No synchrotron component

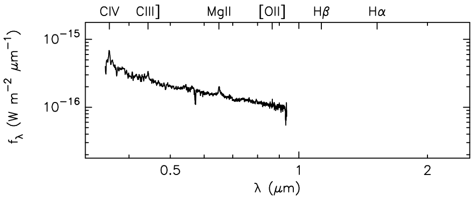

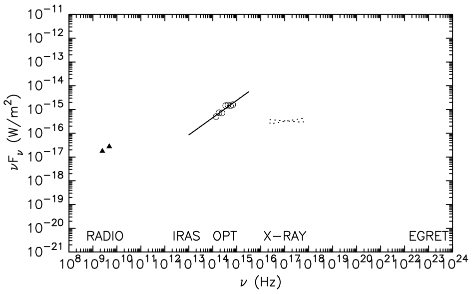

PKS 2313−438, z=1.847

No polarisation measurements

Other name: −−
Classification: stellar source
Galactic E(B−V) = 0.010 mag; A_B = 0.044 mag
B = 19.89 B−K = 3.17 M_V = −25.62

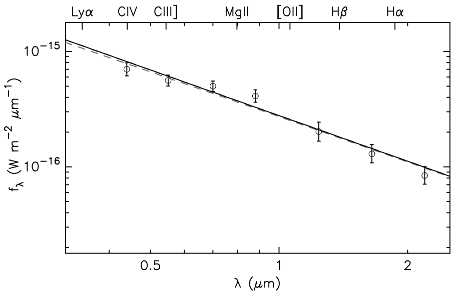

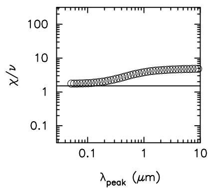

Best model: POWER LAW
Best χ^2/ν = 1.516 (ν=5)
Power law index = −1.31
No synchrotron component

No spectrum

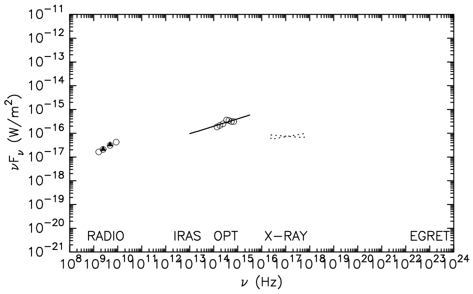

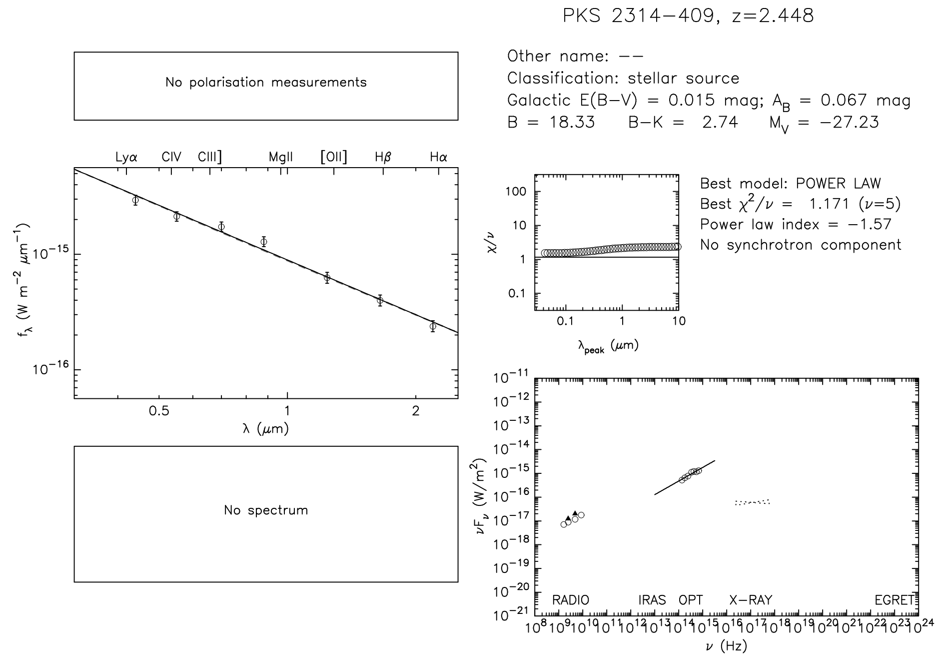
PKS 2314−409, z=2.448
Other name: −−
Classification: stellar source
Galactic E(B−V) = 0.015 mag; A_B = 0.067 mag
B = 18.33 B−K = 2.74 M_V = −27.23
No polarisation measurements
Best model: POWER LAW
Best χ²/ν = 1.171 (ν=5)
Power law index = −1.57
No synchrotron component
No spectrum
Lyα CIV CIII] MgII [OII] Hβ Hα
λ (μm)
λ_peak (μm)
ν (Hz)
RADIO IRAS OPT X-RAY EGRET

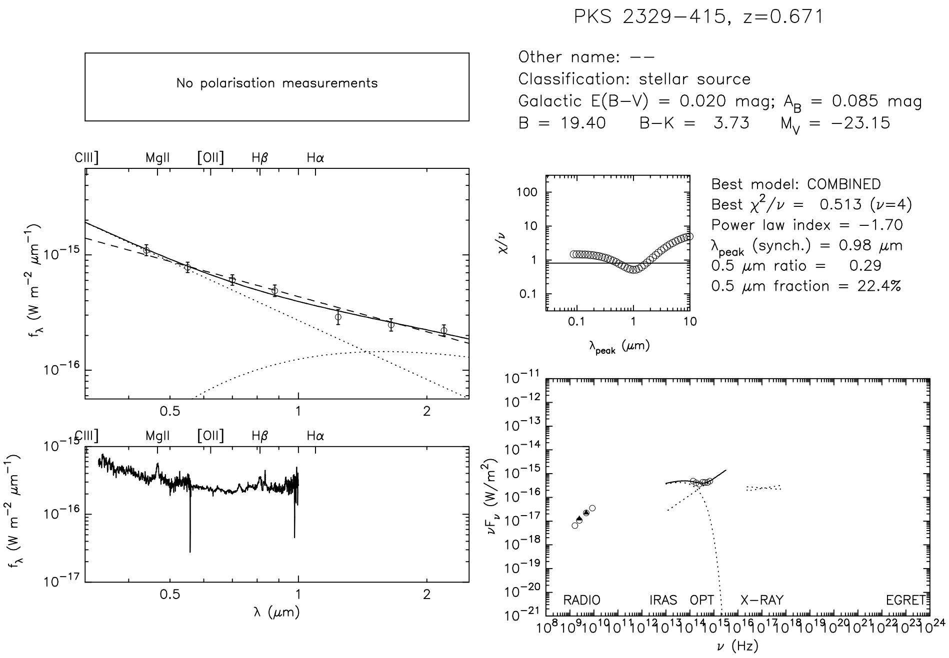
PKS 2329−415, z=0.671
Other name: −−
Classification: stellar source
Galactic E(B−V) = 0.020 mag; A_B = 0.085 mag
B = 19.40 B−K = 3.73 M_V = −23.15
No polarisation measurements
Best model: COMBINED
Best χ²/ν = 0.513 (ν=4)
Power law index = −1.70
λ_peak (synch.) = 0.98 μm
0.5 μm ratio = 0.29
0.5 μm fraction = 22.4%
CIII] MgII [OII] Hβ Hα
λ (μm)
λ_peak (μm)
ν (Hz)
RADIO IRAS OPT X-RAY EGRET

PKS 2345−167, z=0.576

Other name: OZ −176
Classification: stellar source
Galactic E(B−V) = 0.026 mag; A_B = 0.112 mag
B = 17.23 B−K = 4.47 M_V = −25.40

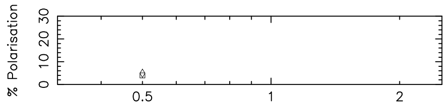

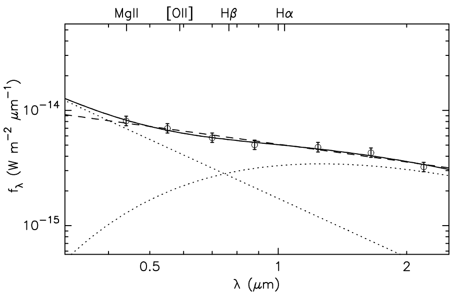

No spectrum

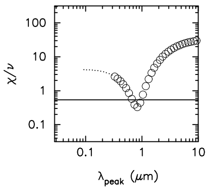

Best model: COMBINED
Best χ^2/ν = 0.328 (ν=4)
Power law index = −1.70
λ_{peak} (synch.) = 0.83 μm
0.5 μm ratio = 1.14
0.5 μm fraction = 53.2%

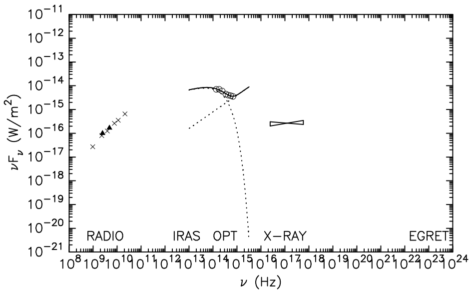

PKS 2351−154, z=2.675

Other name: OZ −187
Classification: stellar source
Galactic E(B−V) = 0.034 mag; A_B = 0.145 mag
B = 18.97 B−K = 2.60 M_V = −26.12

No polarisation measurements

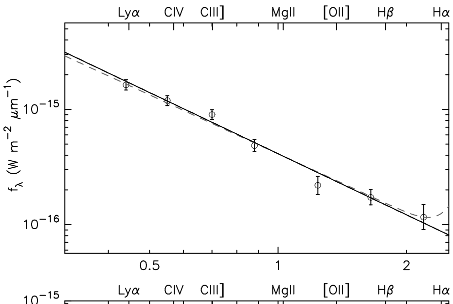

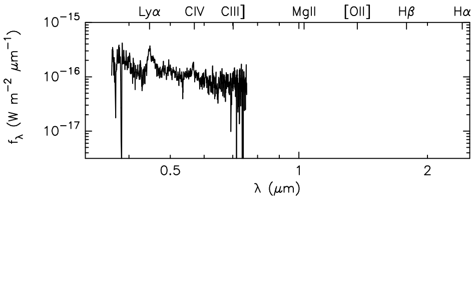

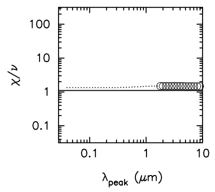

Best model: POWER LAW
Best χ^2/ν = 1.110 (ν=5)
Power law index = −1.76
No synchrotron component

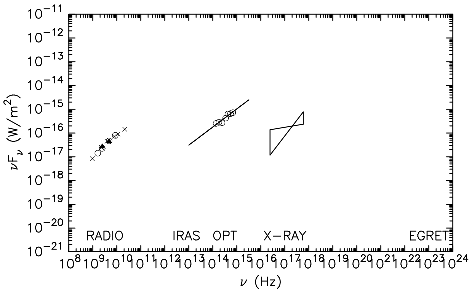

PKS 2354−117, z=0.96

Other name: −−
Classification: stellar source
Galactic E(B−V) = 0.032 mag; A_B = 0.136 mag
B = 18.81 B−K = 3.75 M_V = −25.41

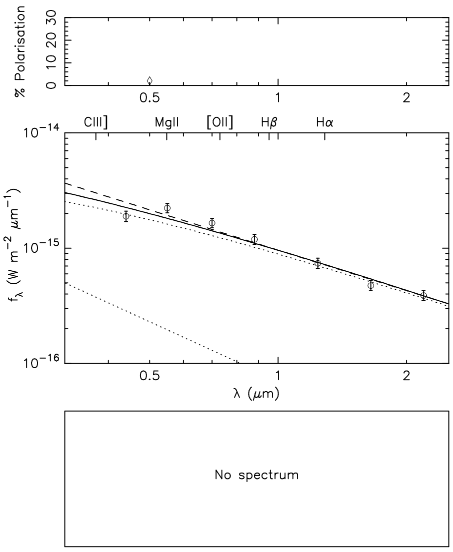

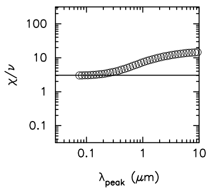

Best model: COMBINED
Best χ^2/ν = 3.025 (ν=4)
Power law index = −1.70
λ_{peak} (synch.) = 0.07 μm
0.5 μm ratio = 12.40
0.5 μm fraction = 92.5%

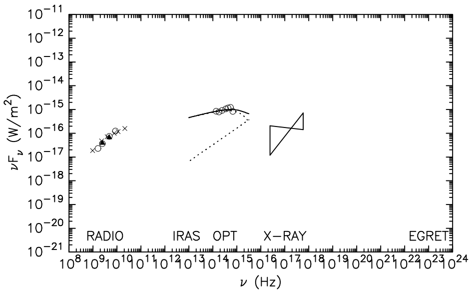

PKS 0118−272, z=0.556

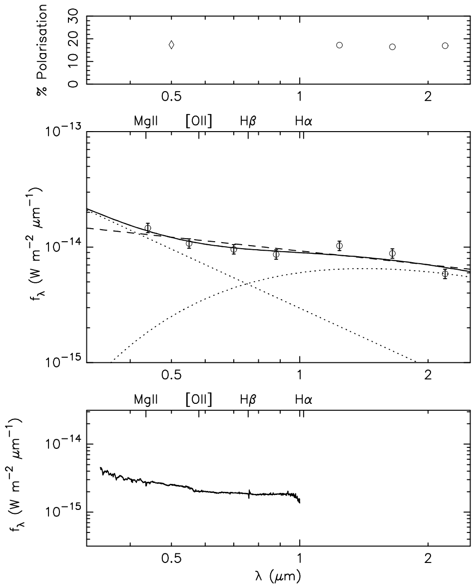

Other name: OC −230.4
Classification: stellar source, BL Lac (PG95)
Galactic E(B−V) = 0.014 mag; A_B = 0.059 mag
B = 16.59 B−K = 4.48 M_V = −25.77

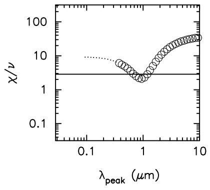

Best model: COMBINED
Best χ^2/ν = 2.099 (ν=4)
Power law index = −1.70
λ_{peak} (synch.) = 0.94 μm
0.5 μm ratio = 1.10
0.5 μm fraction = 52.4%

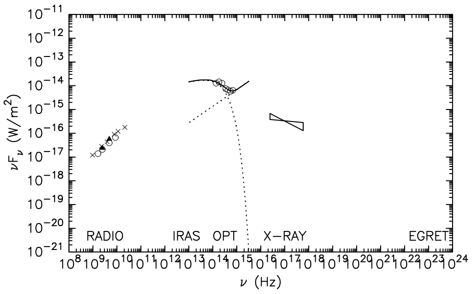

PKS 0454+066, z=0.405

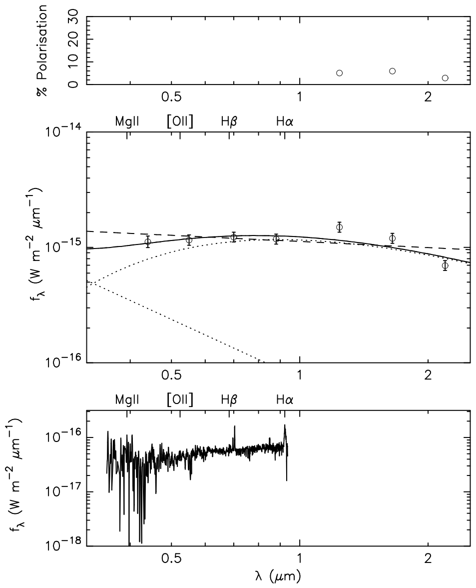

Other name: 4C +06.21
Classification: stellar source
Galactic E(B−V) = 0.081 mag; A_B = 0.349 mag
B = 19.38 B−K = 4.96 M_V = −22.88

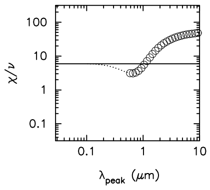

Best model: COMBINED
Best χ^2/ν = 3.078 (ν=4)
Power law index = −1.70
λ_{peak} (synch.) = 0.66 μm
0.5 μm ratio = 8.45
0.5 μm fraction = 89.4%

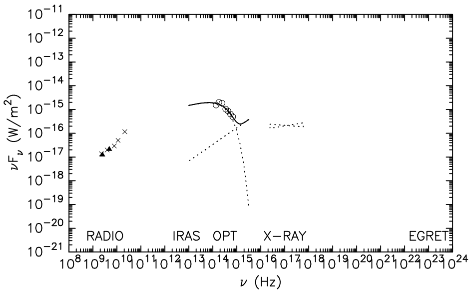

PKS 0048−097, no redshift

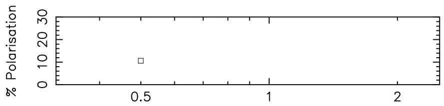

Other name: PHL 0856
Classification: stellar source, BL Lac (PG95)
Galactic E(B−V) = 0.032 mag; A_B = 0.139 mag
B = 16.12 B−K = 3.61

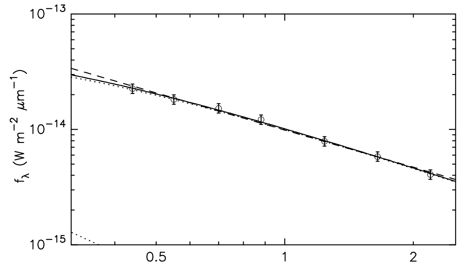

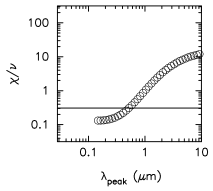

Best model: COMBINED
Best χ^2/ν = 0.132 (ν=4)
Power law index = −1.70
λ_{peak} (synch.) = 0.15 μm
0.5 μm ratio = 33.44
0.5 μm fraction = 97.1%

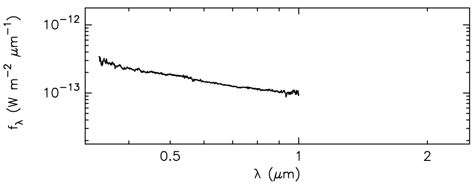

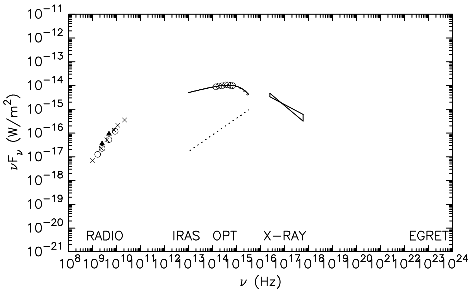

PKS 1110−217, no redshift

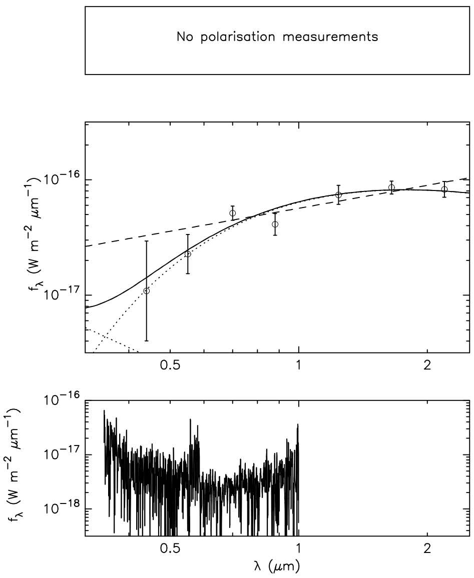

Other name: OM −218
Classification: faint source
Galactic E(B−V) = 0.041 mag; A_B = 0.179 mag
B = 24.41 B−K = 7.67

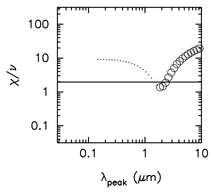

Best model: COMBINED
Best χ^2/ν = 1.378 (ν=4)
Power law index = −1.70
λ_{peak} (synch.) = 1.85 μm
0.5 μm ratio = 7.15
0.5 μm fraction = 87.7%

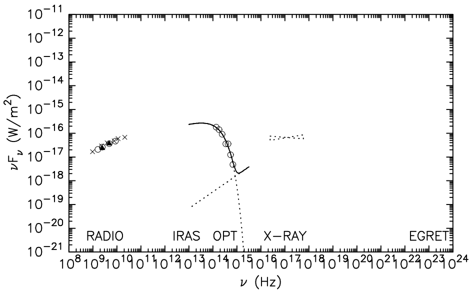

PKS 1156−094, no redshift

No polarisation measurements

Other name: OM −094
Classification: faint source
Galactic E(B−V) = 0.040 mag; A_B = 0.173 mag
B = 21.95   B−K = 5.08

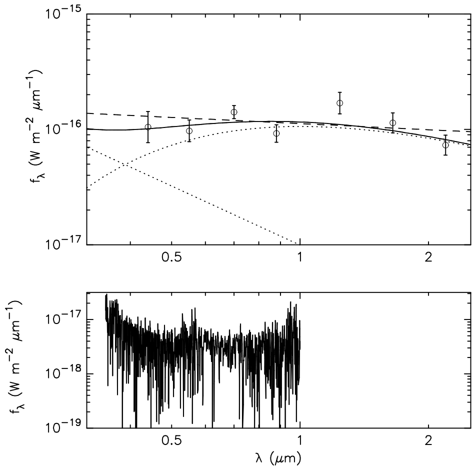

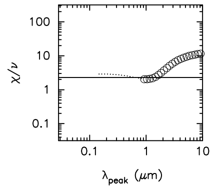

Best model: COMBINED
Best χ^2/ν = 2.040 (ν=4)
Power law index = −1.70
λ_{peak} (synch.) = 1.04 μm
0.5 μm ratio = 2.26
0.5 μm fraction = 69.3%

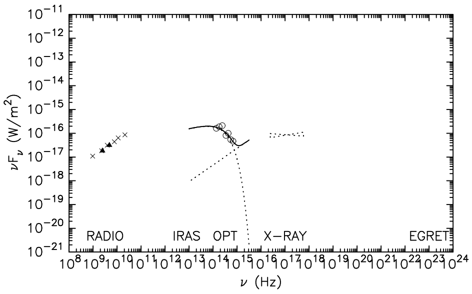

PKS 1648+015, no redshift

No polarisation measurements

Other name: −−
Classification: faint source
Galactic E(B−V) = 0.076 mag; A_B = 0.327 mag
B = 21.87   B−K = 5.31

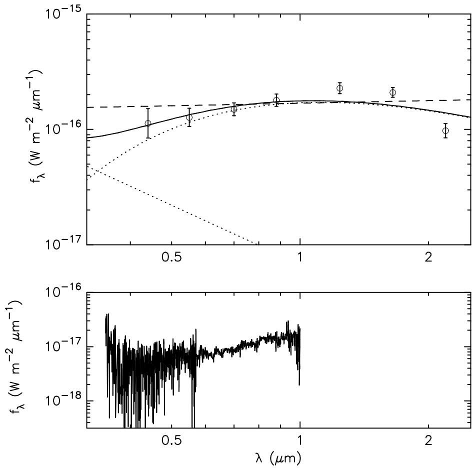

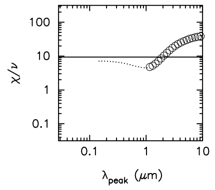

Best model: COMBINED
Best χ^2/ν = 4.764 (ν=4)
Power law index = −1.70
λ_{peak} (synch.) = 1.17 μm
0.5 μm ratio = 4.58
0.5 μm fraction = 82.1%

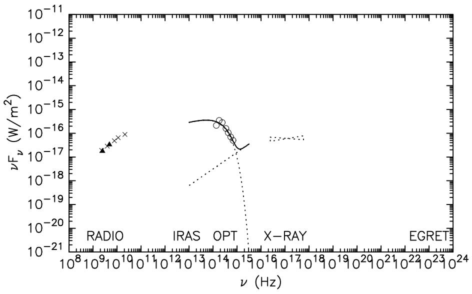

PKS 1732+094, no redshift

No polarisation measurements

Other name: OT +054
Classification: faint source
Galactic E(B−V) = 0.161 mag; A_B = 0.697 mag
B > 23.50 B−K > 7.13

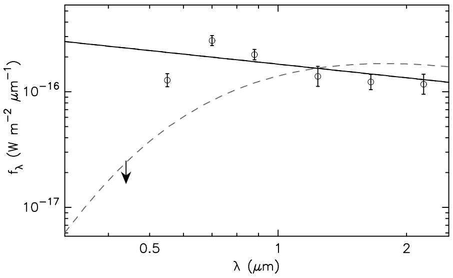

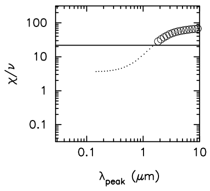

Best model: POWER LAW
Best χ^2/ν = 21.855 (ν=5)
Power law index = −0.39
No synchrotron component

No spectrum

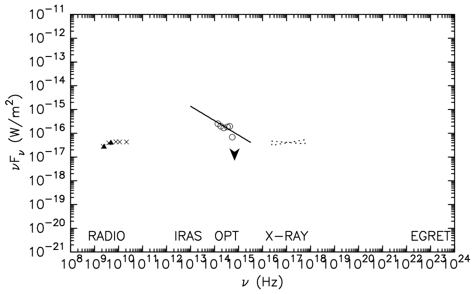

PKS 2056−369, no redshift

No polarisation measurements

Other name: −−
Classification: faint source
Galactic E(B−V) = 0.068 mag; A_B = 0.294 mag
V > 23.50 V−K > 5.29

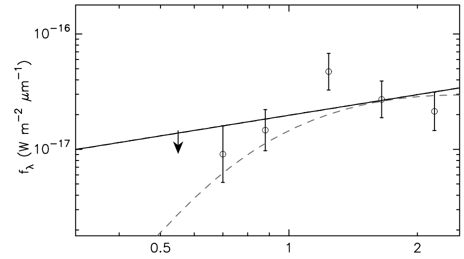

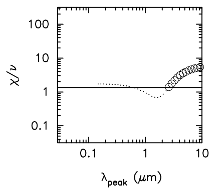

Best model: POWER LAW
Best χ^2/ν = 1.348 (ν=4)
Power law index = 0.59
No synchrotron component

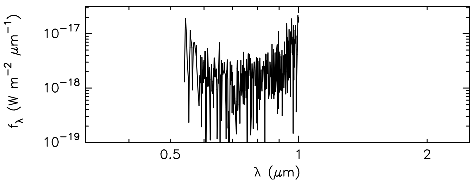

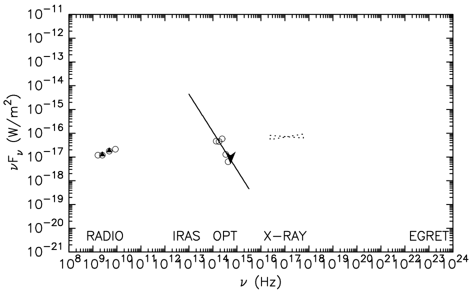

PKS 2245+029, no redshift

No polarisation measurements

Other name: --
Classification: stellar source
Galactic E(B−V) = 0.057 mag; A_B = 0.248 mag
B = 21.71 B−K = 6.22

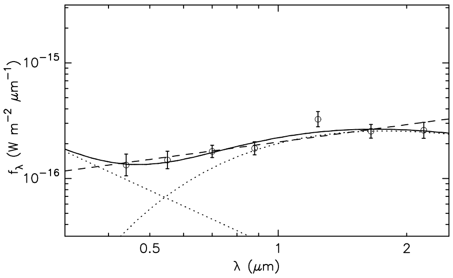

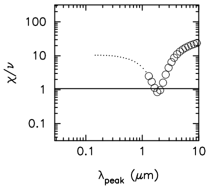

Best model: COMBINED
Best χ^2/ν = 0.847 (ν=4)
Power law index = −1.70
λ_{peak} (synch.) = 1.85 μm
0.5 μm ratio = 0.69
0.5 μm fraction = 40.8%

No spectrum

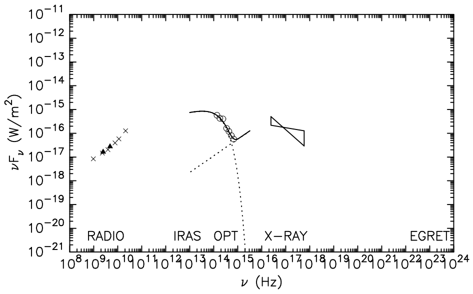

PKS 2337−334, no redshift

No polarisation measurements

Other name: --
Classification: faint source
Galactic E(B−V) = 0.013 mag; A_B = 0.055 mag
B = 22.93 B−K = 6.54

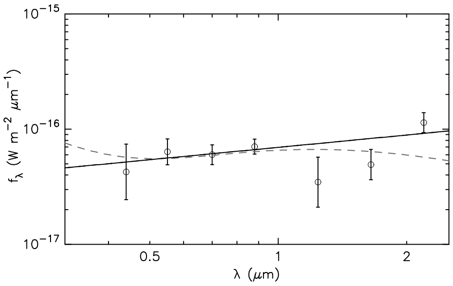

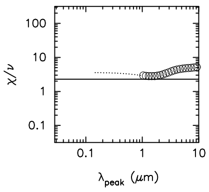

Best model: POWER LAW
Best χ^2/ν = 2.276 (ν=5)
Power law index = 0.36
No synchrotron component

No spectrum

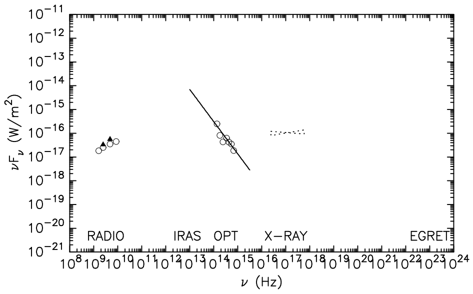

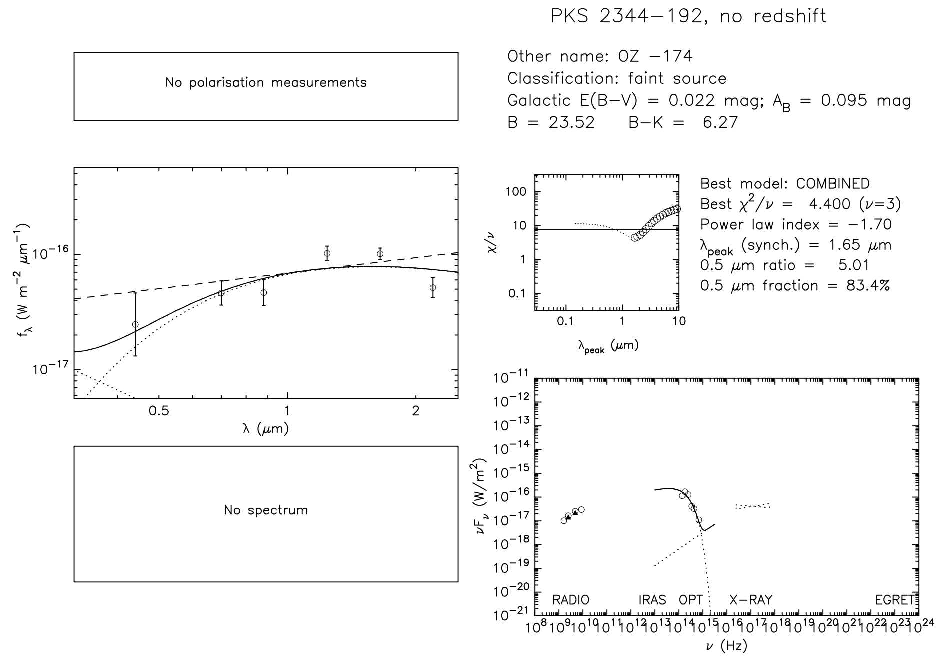
PKS 2344−192, no redshift
No polarisation measurements
Other name: OZ −174
Classification: faint source
Galactic E(B−V) = 0.022 mag; A_B = 0.095 mag
B = 23.52 B−K = 6.27
Best model: COMBINED
Best χ^2/ν = 4.400 (ν=3)
Power law index = −1.70
λ_{peak} (synch.) = 1.65 μm
0.5 μm ratio = 5.01
0.5 μm fraction = 83.4%
f_λ (W m^{-2} μm^{-1})
λ (μm)
χ/ν
λ_{peak} (μm)
No spectrum
νF_ν (W/m^2)
RADIO
IRAS
OPT
X−RAY
EGRET
ν (Hz)